ScuDo
Scuola di Dottorato ~ Doctoral School
WHAT YOU ARE, TAKES YOU FAR

INRiM
ISTITUTO NAZIONALE
DI RICERCA METROLOGICA

Doctoral Dissertation
Doctoral Program in Electrical, Electronics and Communications Engineering
(31.th cycle)

Experimental and computational EM analysis of MRI RF coils and of their interaction with implanted conductive objects

Umberto Zanovello

* * * * * *

Supervisors
Prof. Carlo Ragusa, Supervisor
Dr. Michele Borsero, Co-supervisor
Prof. Mario Chiampi, Co-Supervisor

Doctoral Examination Committee:
Prof. Carlo Carobbi, Referee, Università degli Studi di Firenze, Italy
Dr. Matt Hall, Referee, National Physical Laboratory (NPL), England
Dr. Fabio Baruffaldi, Istituto Ortopedico Rizzoli, Italy
Prof. Luca Giaccone, Politecnico di Torino, Italy
Dr. Marta Parazzini, CNR - IEIIT, Italy

Politecnico di Torino
???

I hereby declare that, the contents and organisation of this dissertation constitute my own original work and does not compromise in any way the rights of third parties, including those relating to the security of personal data.

Umberto Zanovello
Turin, ???

Summary

Radio frequency (RF) coils are employed in Magnetic Resonance Imaging (MRI) to excite and detect the signal from nuclear spins at Larmor frequency. The intrinsic complexity of the phenomena involved inside an MR scanner leads to strong requirements on the magnetic field $\boldsymbol{B}_1$ generated by the RF coil which should be fulfilled to ensure reliable results. Nevertheless, the presence of an external conductive object, such as a metallic implant, strongly interacts with the $\boldsymbol{B}_1$ field and potentially affects the performance of an even ideal RF coil.

Whereas the $\boldsymbol{B}_1$ magnetic field prevalently impacts on the quality of the MRI result, the electric field generated by the RF coil has important safety consequences and should be accounted for as well.

This thesis is developed in the framework of the evaluation of the electromagnetic fields generated by MRI RF coils and of their interaction with conductive passive objects.

In this context, the third chapter of the thesis describes the realization of a dosimetric experimental set-up, able to generate and measure RF electromagnetic fields in a "tissues mimicking" phantom. The generation equipment consists of an RF synthesizer whose amplified signal is used to supply suitable antennas. The acquisition system is based on two power meters (connected to a directional coupler to measure the incident and reflected power), an electromagnetic field acquisition station and a tri-axial automatic system for specific field probes positioning.

The first characterization of the set-up is described and has been obtained employing a self-made shielded loop antenna. Its validation has been performed both in terms of magnetic and electric fields by comparing the experimental measurements with numerical simulation results. In such a context, an uncertainty budget has been studied and it has been associated to the relevant dosimetric set-up.

A second activity is presented in the same chapter and involved a double-tuned (23Na/1H) loop coil specifically designed for a 7 T MRI scanner and provided by the IMAGO7 foundation, Pisa. The experimental electromagnetic measurements have been compared to the numerical results carried out by the IMAGO7 research group by means of the same simulation codes they use for coil design routine evaluations.

The plan for the implementation of a realistic scaled-down 3 T MR body coil, conceived to increase the versatility of the dosimetric set-up, led to the design of a 16-leg high-pass

birdcage coil. A detailed theoretical study of the coil structure represents the topic of the second chapter, whereas the coil design and fabrication become part of the chapter devoted to the experimental set-up.

The distortion of the RF coil sensitivities due to the presence of elongated passive implants, which leads to RF inhomogeneity artefacts, is evaluated through numerical simulations and represents the subject of the fourth chapter. The simulation set-up includes a birdcage volume resonator and a proper phantom inside which the metallic objects (i.e. a metallic cylinder and a realistic hip prosthesis stem model) are plunged. Special attention is given to the achievement of an easy but reliable description of the physical phenomenon. On the basis of these results, a solution is hence proposed to reduce the impact of RF artefacts in MRI exams. This proposal consists in covering the metallic objects with a suitable dielectric coating to make them invisible to the radiating antenna. The optimum coating parameters and the general effectiveness of the coating are studied using different commercial electromagnetic numerical codes both at 64 MHz and 128 MHz.

Finally, following a specific request from an MRI medical staff, the possible interactions between body-art tattoos and MRI electromagnetic fields are evaluated. The study is developed especially from a safety point of view. The tattoo inks and pigments electrical and magnetic properties experimental characterization is performed to assess electromagnetic and thermal simulations. The results are reported and discussed in the fifth chapter of the thesis.

Acknowledgements

Firstly, I would like to sincerely thank my advisors Dr. Michele Borsero and Prof. Mario Chiampi for their endless support and faith in me. I'm extremely grateful to them for sharing with me their knowledge and to have been like friends.

I would like to express my gratitude to my thesis commettee, especially to Prof. Carlo Carobbi and Dr. Matt Hall whose insightful comments and suggestions definitely improved my work.

I would like to thank also Prof. Ladislau Matekovits who revealed to be one of the best and most important figures during my Ph.D. career. Without him my research would have been substantially different and certainly not better.

A huge thank to my collegues in INRIM, especially to Dr. Luca Zilberti, Dr. Domenico Giordano and Dr. Gabriella Crotti. They have been extremely helpful for me and I know I could always rely on them.

A sincere thank also goes to my Ph.D. mates. In particular to Dr. Alessandro Arduino who helped me in many occasions and to Dr. Mohammad Modarres who supported me to weld copper leads to more than thirty surface-mounting capacitors.

I express my gratitude to all my friends that in these last four years shared with me wonderful moments. In particular to Alberto who, among other countless things, hosted me in Paris after 2018 ISMRM Annual Meeting, and to my old friend Gian Pietro.

Finally, I would like to thank my family: my parents, my sister, her boyfriend and Rossella who always gave me everything I needed.

Contents

Chapter 1

Introduction

In the present thesis, the Magnetic Resonance Imaging (MRI) Radio Frequency (RF) coils represent the common link between the different issues investigated through the chapters. Given the centrality of such a topic for the thesis, it is appropriate to introduce a general overview of the subject aimed to better contextualise the results presented in the main body of the work. The overview reported below is followed by a section in which the thesis programme is described together with the original contributions achieved.

RF Coils

The Radio Frequency (RF) coil is the component responsible for the MRI signal stimulation (*i.e* the generation of the $\boldsymbol{B}_1$ field at Larmor frequency which rotates the net magnetization from its longitudinal position) and reception. It follows that a proper selection, design and realization of such a device is critical to a safe and successful MRI scan [1]. For example, the geometry of an RF coil always represents an important aspect in obtaining optimum results. Whereas it should be large enough to fit around the patient and to reach satisfactory field-of-view (FOV), the larger it is, the less sensitive it will be as receiver leading to a signal-to-noise ratio (SNR) that could be too low. On the other hand, the closer the coil is to the patient, the stronger the received signal will be at the expense of a smaller FOV. For that reason, optimal coil design strongly depends on the body part that has to be imaged [2].

Whereas, thanks to the Principle of Reciprocity (see Appendix A), a generic RF coil that is capable of transmitting the RF signal will also be able to receive the signal emitted from nuclear spins, not necessarily it does it efficiently for the considered application. As a consequence, RF coils are generally divided in three different categories: transmit and receive coils (transceivers), transmit-only coils, receive-only coils [3]. The first category is used to both transmit the $\boldsymbol{B}_1$ field and to receive the RF energy from the imaged object. Transmit-only coils are used exclusively to generate the B_1 field and receive-only coils to detect the MR signal. Although transceiver coils were once the norm, today modern scanners generally adopt separate transmit and receive systems. However, some of them, such those used for head and knee imaging, are still in use [4].

Transmit coils have to efficiently (*i.e.* absorbing the less active power as possible) generate an homogeneous $\boldsymbol{B}_1$ magnetic field inside the region-of-interest (ROI). The $\boldsymbol{B}_1$ homogeneity represents a key point in MRI and it is one of the fundamental conditions to guarantee a connection between the MR signal and the properties of a specific tissue. Maxwell equations show that time-varying magnetic fields are necessarily related to the electrical counterparts. Due to the non-zero conductivity value of the human tissues, the presence of the electric field results in a power deposition that may be responsible of dangerous temperature increases.

The power per unit mass (power density) due to an electric field $\boldsymbol{E}$ over a sample with mass density equal to ρ and electrical conductivity equal to σ can be obtained as:

$$P = \frac{\sigma|\boldsymbol{E}|^2}{\rho} \tag{1.1}$$

From the power density distribution, it is possible to obtain the specific absorption rate (SAR) defined as the power density value averaged on a sample volume V_s:

$$SAR = \frac{1}{V_s}\int_{V_s} P(\boldsymbol{r})dr^3 \tag{1.2}$$

The maximum SAR values, admitted during an MRI session, are limited by standards. In particular, different limits are imposed if the whole human body (whole body SAR) or only a fraction (local body SAR) is considered for averaging [5]. In the context of the present thesis, for practical reasons, the power density evaluated in a point identified by the position vector $\boldsymbol{r}$ will be referred as $SAR(\boldsymbol{r})$.

A linearly polarized magnetic field can be seen as the superposition of two counter-rotating magnetic fields with an amplitude equal to half that of the linear field[1]. Since spins are mainly affected by the magnetic field that rotates according to their precession direction ($\boldsymbol{B}_1^+$) [6, 7] (see also Appendix A), the other rotating component ($\boldsymbol{B}_1^-$) constitutes "wasted" RF-power that creates the adverse affect of increasing SAR [6, 8]. Hence, the advantage to select transmitting coils that can be fed in "quadrature operation mode" (*i.e.* supplying the coil by means of two or more voltage generators whose phase shift and positions are opportunely arranged) to generate a rotating magnetic field in the ROI.

Receiving coils have to detect the signal emitted from the precessing spins with a

---

[1] This can be seen considering the summation of two vectors with an amplitude equal to 1/2 which rotate in opposite directions with an angluar frequency equal to ω. In a static Agrand plane it gives: $\frac{1}{2}e^{-j\omega t} + \frac{1}{2}e^{j\omega t} = \cos\omega t$.

spatial sensitivity that should be as homogeneous as possible to avoid an unwanted correlation between the measured MR signal and the position from which it is emitted. Furthermore, their geometry has to be properly designed to obtain optimum SNR values. Whereas with a simple loop receiving coil (linear coil), it would be possible, by means of a dual channel demodulation (see Appendix A), to obtain the useful MRI complex signal, the detection with quadrature coils (the simpler quadrature coil is represented by two linear coils placed 90° apart) and a quadrature combiner to conveniently mix the signals into one channel[2], permits to improve the receiver sensitivity, and therefore the SNR, by a factor of $\sqrt{2}$ [2, 9].

Generally, RF coils are divided in two categories: Surface coils and Volume coils. The surface coils can be placed adjacent to a surface of a ROI in an MRI sample. Due to their reduced dimension they are able to localize a near-surface ROI with high transmit efficiency and/or receive sensitivity. In general, the sensitivity of a surface coil drops off quickly as the distance from the coil increases. Thus, they are particularly suitable only for imaging of a small surface ROI and they have to be gathered in so-called phased arrays to cover efficiently wider anatomical human parts. Phased arrays are a large group of small overlapped coils (to minimize coupling between nearest-neighbor coils) connected to low input impedance preamplifiers (to guarantee decoupling between non-nearest neighbors) [10]. N independent (where noise correlation can be neglected) phased array coils, will ideally increase the SNR by a factor of $\sqrt{N}$. Unfortunately, as the number of coils increases, the elements have to become smaller and the receive sensitivity of each coil may become unsatisfactory to image the relevant ROI. However, there are particular situations where the coil utility may be improved without sacrificing SNR. For example, in spine imaging the phased array may be precisely defined to suit the whole ROI [2]. The phased array has been further developed in the last decade [11] leading to parallel arrays and to the concept of Parallel Imaging [12, 13, 14]. In parallel arrays, the individual coil elements should be free of magnetic interactions to make the complex sensitivities of each coil sufficiently distinct from the others. This means that large overlap between coils (as seen in most phased-array configurations) is generally avoided and a coil decoupling circuitry is essential. In parallel imaging, it is possible to apply different weights of signals from the multiple small surface coils composing the parallel array, determining the spatial origin of the signal. This process allows to obtain satisfactory images even with a considerable k-space undersampling, thus reducing the need for time-consuming gradient-encoding steps.

Volume coils are tailored to encompass the whole sample volume. The most common clinical examples are limb, head and body coils [1]. With such coils it is possible to obtain very homogeneous transmit and/or receive sensitivity even for large body parts at the expenses of higher power deposition, if they are used in transmission, and lower SNR,

---

[2] Being the receiver sensitivity equal to $\hat{B}_1^-$ (see Appendix A), the aim is to arrange the received signals to maximize this quantity.

if they are used as receivers, with respect surface coils. For these reasons, they should be prevalently used when there is the need to image deeply inside an anatomical part where a surface coil transmit/receive sensitivity would be too weak. For convenience, body coils are often used in transmission mode in conjunction with receive-only surface coils. As already anticipated, the downfall of this approach is represented by an high whole-body SAR generated during the imaging scan.
The trend towards higher static magnetic field values[3], leads to a Larmor frequency that increases accordingly. This process inevitably brings to wavelengths of the RF electromagnetic field that are, in human tissues, comparable with the dimension of several anatomical parts of the human body. In particular, wavelengths that are around 52 cm at 1.5 T decrease to 26 cm at 3 T or to 11 cm at 7 T. In such situations, standing waves may rise inside the ROI leading to brighter and darker areas in the image. Such artefacts are commonly referred to as “dielectric artefacts” and their importance is also dependent on the tissue conductivity due to a “skin-depth” term that represents a damping factor for the standing wave phenomena [16, 17]. To compensate for this problem, so-called “multi-transmit” techniques are employed [18, 19] taking advantage of the spatial distribution of the volume coils. In particular, the entire RF coil is considered as being composed by several “sub-coils”. Each sub-coils is therefore independently supplied and rigorously controlled over timing, phase, power and amplitude to generate its own $\boldsymbol{B}_1$ RF magnetic field. Thanks to the constructive and destructive interference between the several $\boldsymbol{B}_1$ sub-fields, it is possible to carefully control the homogeneity of RF excitation together with the distribution of the magnetic and electric fields generated inside the tissues [20].

There exist a plethora of different RF surface/volume coils that principally differ in their shape, in the operation mode they are designed for (receive/transmit-only or transceiver) and in the application for which they are proposed [21, 22, 23, 24, 25, 26, 27, 28, 29, 30, 31, 32, 33, 34, 35, 36, 37]. In the following, maybe the three most common RF MRI coils are described together with their main features.

Loop coils They represent the simplest RF surface coil for MRI applications such that they have been employed in early MR studies regarding blood flow [38]. They consist of a single turn of sheet or wire conductor and can be easily molded and/or combined to fit different human anatomical shapes. Due to their versatility, they are typically the basic elements that compose the phased array or parallel array coils. They are generally used for imaging of relatively superficial structures providing low SAR deposition or high SNR values if they are used as transmitters or receivers respectively. In fact, a prominent and important feature of such coils is their relatively restricted volume of sensitivity. Whereas this inevitably limits their capability to receive the MR signal from deep structures, it also limits their

---

[3] It can be proved that there is a direct proportionality between the value of the static magnetic field and the maximum signal that is possible to achieve. [15]

response to noise generated by the body. Since such a noise may represent an important fraction of the total noise, particularly at higher frequencies, the limited sensitivity region of the loop coils permits a considerable improvement of SNR for imaging of structures within the sensitive region [21];

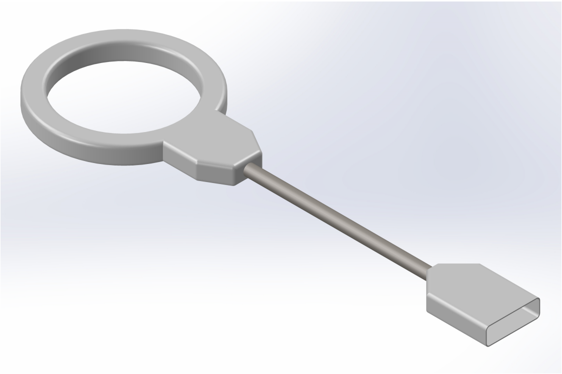

Figure 1.1: 3D CAD model of a genreic loop coil.

Birdcage coils Originally conceived as transceiver head or body volume coils, today they represent the most widely employed body coils in clinical scanner to excite a uniform field over a large ROI [1]. Since their introduction over three decades ago, they have become a mainstay of MR imaging thanks to its highly homogeneous transverse RF magnetic field and to the ease with which they may be driven in quadrature operation mode to produce a circularly polarized field [36, 39].
They are made by several conductive rungs, named “legs”, (typically from about 8 to 32 depending also on the coil size [40]) organized at equally spaced angular interval over a cylindrical surface. The rungs are connected at both ends to their closest neighbors to form the so-called “end-rings”. Moreover, some capacitors are generally positioned on the end-rings and/or on the legs to guarantee the RF magnetic field homogeneity at the desired frequency. The process of selecting the proper capacitance values to reach this goal, is commonly referred as “birdcage tuning” (see also Chapter 2). Different needs together with the arrival of new techniques, such as parallel transmission, stimulate the design of a large number of birdcage variants. These include spiral, double-spiral, woven, multiple-ring and degenerate birdcage types [32, 41, 42, 43, 44, 45];

TEM coils They are essentially composed by an array of transmission line elements that surround a volume or are adjacent to a surface. Such a structure keeps the inherent field homogeneity of the birdcage coils gaining the benefits of an array with independent element operation [1]. They are indeed particularly suitable to be operated in parallel transmission mode, demonstrating to be able to generate an highly homogeneous magnetic field even at higher frequencies where the field

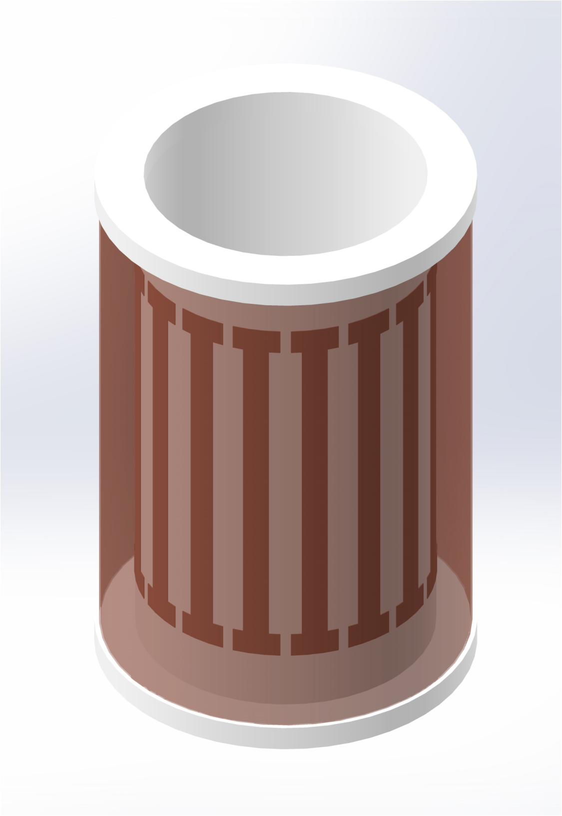

Figure 1.2: 3D CAD model of a 16-leg birdcage coil. The endrings are interrupted by gaps to leave the space for capacitors in case of an high-pass coil is considered. The conductive shield is made transparent to make the rungs and the endrings visible.

> produced by the birdcage coil may be problematic due to a significant coupling between the patient and the coil [22].
> The TEM coils typically adopt foil microstrips fixed to the inner surface of a nonconducting cylinder. Their ends are therefore connected to a thin metallic shield placed on the outer surface of the nonconducting cylinder. The shield becomes an essential element of the system since it provides a return path for currents from the inner conductor strips. Unlike birdcage coils, the inner conductors of the TEM coils are not directly connected each other but connect directly to the shield by means of tunable capacitive elements which can be adjusted to achieve the best field homogeneity [46].

In addition to the surface and volume coils, there exist the so-called "internal coils". Internal coils are specifically designed to be inserted into peripheral orifices of the human body [47]. Among these there are, for example, the catheter coils, designed to be inserted into a blood vessel, the intraoral coils, the endovaginal coils and the endoanal coils [48, 49, 50]. Thanks to their enhanced local sensitivity, such coils permit to obtain,

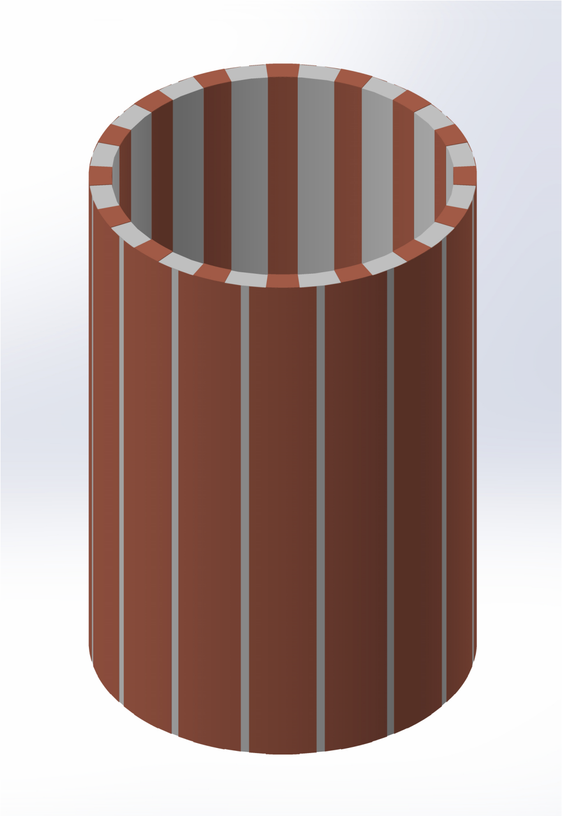

Figure 1.3: 3D CAD model of a 16-rung TEM coil. Capacitors and supply circuits are omitted for simplicity.

within their ROI, a SNR higher than that obtained with standard volume coils, at the expense of an unpleasant feeling for the patient due to their typical invasiveness.

The improper use of coils, a wrong coil configuration, improper patient positioning and poor FOV selection (compared with the RF coil sensitivity) is a major cause of artefacts in the MR image. There exist different types of artefacts that are related to the transmission and reception of the RF signal in MRI. They are usually divided according to their etiology and aspect on the MR image. The most frequent are listed and described below [2, 51]:

Shading artefacts They reveal as areas with reduced signal intensity or bands with signal cancellation. They are often due to improper coil or patient positioning;

Non-uniformity of Signal artefacts These artefacts are a direct result of the spatially inhomogeneity of the RF coil complex sensitivity. Since the RF coil transmit/receive the MR signal most efficiently closest to it, they may appear areas of non-uniform signal in the image. Such effects are more pronounced when surface coils are employed;

RF Inhomogeneity These artefacts are caused by the failure of a coil element or by the presence of a conductive object inside or near the ROI. Conductive implants represent one such instance. Usually, they are revealed as an abnormal signal intensity variation across the MR image;

Zipper artefacts These artefacts often appear as a band of spurious signal that passes through the image [52]. They are due to RF signals leaking (*e.g.* hardware electronic noise) into the receiver of the MR scanner. If the bandwidth of the interfering RF signal is narrower than the readout one, such artefacts appear as a bright line oriented along the phase encoding direction. Its position within the MR image depends, among others, on the frequency of the RF source that causes the artefact.
A similar bright line oriented along the frequency encoding direction may be caused by an imperfect slice-selection profiles in echoes stimulation or from improper RF-transmitter adjustments. Increasing the interslice gap or applying lengthened dephasing and rephasing portions of the read gradient may reduce their effects [53];

Annefact/Star artefacts The annefact artefacts are extremely similar to the zipper artefacts but they are due to an unwanted signal generated outside the FOV and accidentally detected by the receiver (*e.g* by a distant array coils element that has not been properly deactivated). Sometimes, they may be reduced to a single cluster of points near the image centre and they are defined “Star artefacts”.

Thesis programme and original contributions

In this thesis, several electromagnetic aspects related to MRI RF coils are discussed. Whereas some chapters are mainly experimentally based and other chapters approach the specific issues by means of numerical simulations and analytical considerations, they all contribute to explore problems and to investigate solutions in the field.
From a general perspective, four different topics are examined in the thesis:

- The realization and characterization of a dosimetric experimental set-up to perform electromagnetic measurements of the field generated by MRI RF coils inside tissue-mimicking phantoms;
- The design and realization of a 128 MHz tuned, 16-leg high-pass birdcage coil conceived to be integrated inside the dosimetric set-up;
- The study of the interaction between a generic birdcage coil and an elongated metallic implants together with the proposal of a possible solution to the resulting RF inhomogeneity artefacts;

- The investigation of possible safety issues related to the presence of body-art tattoos in MRI. This study straight followed a request from an MRI medical staff and focuses on a systematic procedure to experimentally characterize the electrical and magnetic properties of tattoo inks and pigments.

The topics above are discussed according to the following structure:

- Chapter 2 summarises and elaborates the basic knowledge about the birdcage coil. The discussion is preparatory to the birdcage design and realization described in the next chapter. This chapter mainly reviews well-known results in the field proposing ad-hoc analyses by means of an original code;

- Chapter 3 describes the realization of a dosimetric experimental set-up together with its validation, characterization and employement with a double-tuned loop coil designed for 7 T MRI applications. Furthermore, the chapter presents the design and realization of a 128 MHz tuned, 16-leg high-pass birdcage coil. The experimental activities described in this chapter have been carried out in the laboratory of the Istituto Nazionale di Ricerca Metrologica (INRIM) for a specific MRI dosimetric purpose. As such, they represent an original work;

- Chapter 4 analyzes the RF inhomogeneity artefacts generated inside a birdcage coil by the presence of elongated conductive objects. The case of a realistic hip prosthesis stem model is studied and a solution, based on the application of a suitable low permittivity dielectric coating, is presented to address the issue. An equivalent lumped element circuit is proposed to describe the problem and electromagnetic numerical simulations have been employed to find reliable results. Both the study method and the coating solution represent an original contribution to the field;

- Chapter 5 deals with the possible safety issues related to the presence of body-art tattoos in MRI. A systematic procedure aimed to experimentally characterize the electrical and magnetic properties of tattoo inks and pigments is presented. In this framework, five different commercial tattoo inks are accounted for and simulations are ultimately performed to explore possible thermal interaction with the RF electromagnetic field generated by a birdcage coil. Despite of the numerous research activities available in literature which examine the interaction between body-art tattoos and MRI, none of them seem to involve a systematic characterization of the electromagnetic properties of the inks/pigments. For this reason, the experimental procedure proposed in this chapter, together with the obtained results, represents an original work;

- Chapter 6 draws the conclusion of the thesis summarizing the main achievements and providing some ideas for future developments.

In addition to the above chapters, two appendices are provided to integrate and contextualize the material discussed in the main body of the thesis. In particular:

- Appendix A gives the mathematical framework behind the definition of basic parameters related to the RF coils and employed throughout the thesis;
- Appendix B introduces the first order degenerate perturbation theory considered in chapter 2.

Chapter 2

Birdcage coil theory

2.1 Introduction

Birdcage coils are a particular type of resonators invented in the early 1980s [36]. Due to the highly uniform, circularly polarized transverse magnetic field that they can generate, they have become a mainstay of NMR imaging [54].
In the next chapter (chapter 3), the design and fabrication of such a coil, conceived to be integrated in a dosimetric experimental set-up, will be described. For this reason and considering the large application of this particular coil, a detailed theory describing its behaviour is reported below.

Birdcage coils are made up of two rings, called "end-rings", connected to a finite number of vertical conductive bars called "legs" equally spaced along the perimeter of the end-rings. During their normal quadrature operation (*e.g.* supplying the coil at two ports 90° degrees spaced with a 90° phase shift), each leg is distinguished by a sinusoidal current I_n that is phase shifted with respect to the current in the previous leg by an angle of $2\pi/N$ where N is an even number representing is the total number of legs. This concept can be easily expressed in phasor notation as:

$$I_n = I_0 e^{j2\pi n/N} \tag{2.1}$$

where I_0 represents the maximum current, n is an integer running from 1 to N and j is the imaginary unit.

To properly tune the coil, some capacitors can be positioned on the end-rings or on the legs. In the first case the birdcage will be a high-pass birdcage whereas, in the second case, it will be a low-pass birdcage. Finally there are some birdcages called band-pass birdcages that present capacitors both on the legs and on the end-rings. The importance and specific advantages of each of these structures will be clear in the conclusion of the chapter.

In the following sections, firstly, some general results deriving from the solution of the birdcage coil lumped elements circuit equations are reported. After that the basic

theory of the driven birdcage is summarized and the effect of a perturbation on the birdcage behaviour is investigated. Results are proposed both for the low- and high-pass birdcage. The former have been deeply discussed by Tropp [55] and results are here summarized and expanded by means of additional analyses. The latter are here derived applying the same method used for the low-pass birdcage coil leading to well-known results in litterature [39]. The application of the same study approach both for the low- and high-pass birdcage allows for a reasonable and useful comparison between the structures behaviour. Finally, even the results related to the high-pass birdcage are employed as a starting point for further considerations.
Different codes have been developed in Python language to carry out calculations and to show the graphical results presented in the following sections both for the low- and high-pass birdcage.

2.2 Low-pass birdcage theory

2.2.1 Circuit equations

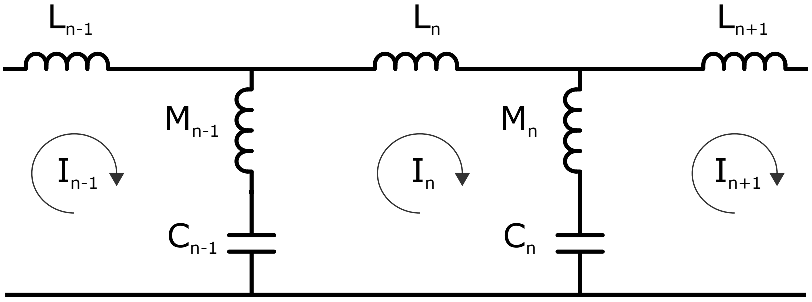

Figure 2.1: A segment of the low-pass birdcage elementary circuit. Three among N total meshes are represented. The self-inductances L, the mutual inductances M, the legs capacitances C and the mesh currents I are also reported.

Let Figure 2.1 represent the lumped elements circuit referred to the nth mesh of an N legs (i.e. N meshes) low-pass birdcage. In the given circuit, L_n takes into account the self inductance of the ring segments of the nth mesh, M_n accounts for both the mutual coupling between the nth and $(n+1)$th meshes and the self inductance of the nth leg, C_n is the nth leg capacitor and I_n is the nth mesh current. Before starting to write the Kirchoff voltage equation for the nth mesh, we have to do some remarks. Firstly, we are neglecting both the resistive terms (they will be considered in a second stage) and the capacitive couplings between different legs and opposite end-rings. Furthermore, we are approximating the mutual flux coupling to be only between two adjacent meshes. However, these approximations do not frustrate the theory proposed here since it is mainly based on the circular simmetry of the structure [55]. Indeed, the purpose of this section is to provide some basic results about the operation of the birdcage coil whilst more detailed lumped elements circuits are employed in chapter 3 dealing with the description of the coil design.

Finally, we have to highlight the limitations behind the lumped elements circuit applied to the study of birdcage coils. Considering the frequencies involved in the birdcage operation together with their spatial dimensions, it turns out that the fundamental assumption behind the adopted lumped elements circuit model (i.e. wavelength much bigger than the circuit dimensions) is not always satisfied. That means that, even if the results obtained with the lumped elements approximations give an almost comprehensive idea about the working principles of the birdcage coil, more reliable results can be obtained by using numerical simulations as it will be shown in chapter 3.

The voltage equation for the nth mesh will be:

$$\left[s(L_n + M_n + M_{n-1}) + s^{-1}\left(\frac{1}{C_n} + \frac{1}{C_{n-1}}\right)\right] I_n - \left(sM_n + \frac{1}{sC_n}\right) I_{n+1} - \left(sM_{n-1} + \frac{1}{sC_{n-1}}\right) I_{n-1} = 0 \quad (2.2)$$

where $s = j\omega$ represents the complex frequency with ω being the considered working angular frequency. Due to the birdcage symmetry, it is reasonable to consider all the self-inductances to be equal to a generic self-inductance L, all the mutual inductances to a generic mutual inductance M and all the leg capacitors to a generic capacitor C. The previous equation can be easily rewritten defining $\omega_a^2 = [(L + 2M)C]^{-1}$ and $\omega_b^2 = (MC)^{-1}$:

$$(s^2 + 2\omega_a^2) I_n - \omega_a^2 \left[\left(\frac{s}{\omega_b}\right)^2 + 1\right](I_{n+1} + I_{n-1}) = 0 \quad (2.3)$$

The relation (2.3) can be written for all the N meshes giving rise to a system of N independent equations. Such system can be viewed as an eigenvalue problem for the variable s^2. That means that the eigenvalues of the system will represent the possible resonant frequencies of the coil whereas the associated eigenvectors are representative of the admissible current phasors circulating in the N meshes [55]. Due to the symmetry of the coil, the system matrix is a circulant matrix. The ith element of the normalized kth eigenvector of a circulant matrix can be generally written as [56]:

$$(\boldsymbol{V_k})_i = \frac{1}{\sqrt{N}} e^{j\frac{2\pi}{N}ki} \quad (2.4)$$

with i and k running from 1 to N. The above relation gives rise to several considerations:

1. The normalized eigenvectors are orthonormal each other:

$$\langle \boldsymbol{V_n}, \boldsymbol{V_m} \rangle = \delta_{n,m} \quad (2.5)$$

   where the angular braket denote the dot product;

2. The whole set of eigenvectors $\boldsymbol{V}$ represents a complete basis for $\mathbb{R}^N$ since:

$$\boldsymbol{e_n} = \sum_{k=1}^{N} (\boldsymbol{V_k})_n^* \boldsymbol{V_k} \tag{2.6}$$

   with $\boldsymbol{e_n}$ being the vector whose only nonzero entry is a "1" in the nth position and the raised asterisk is used to denote complex conjugate;

3. $\boldsymbol{V_k}$ and $\boldsymbol{V_{N-k}}$ are complex conjugate for $k = 1$ to $N/2$. The $(N/2)$th and Nth eigenvectors are real;

4. The sum over the eigenvector elements is zero for all the eigenvectors except for the k=N eigenvector:

$$\sum_{i=1}^{N} (\boldsymbol{V_k})_i = \begin{cases} \sqrt{N} & \text{if } k = N \\ 0 & \text{if } k \neq N \end{cases} \tag{2.7}$$

In order to obtain the eigenvalues of the system matrix, the easiest solution is to substitute to the mesh currents in (2.3) their expressions obtained through (2.4). Considering that for a given k:

$$I_{n+1} + I_{n-1} = \frac{2}{\sqrt{N}} e^{j\frac{2\pi}{N}kn} \cos\left(\frac{2\pi}{N}k\right) \tag{2.8}$$

we obtain:

$$\omega_k^2 + s^2 = \omega_k^2 - \omega^2 = 0 \tag{2.9}$$

where ω_k^2 represents the kth eigenvalue associated to the kth eigenvector and it is:

$$\omega_k^2 = 2\omega_a^2 \frac{1 - \cos(\frac{2\pi}{N}k)}{1 - 2(\frac{\omega_a}{\omega_b})^2 \cos(\frac{2\pi}{N}k)} \tag{2.10}$$

From (2.10) we can observe that the system gives $N/2-1$ double-degenerate eigenvalues (ω_k^2 and ω_{N-k}^2 for $k = 1$ to $N/2$) and two different eigenvalues for $k = N/2$ and $k = N$. It results that the conjugate eigenvectors pair shares the same double-degenerate eigenvalue. Here we have a first general result concerning the birdcage coils. A generic N-legs (with N even) birdcage coil is characterized by $k = N/2 - 1$ different degenerate operational modes. Each of these modes is distinguished by a unique frequency ω_k associated with the current distributions among the meshes $\boldsymbol{V_k}$ and $\boldsymbol{V_{N-k}}$. The mesh currents $\boldsymbol{V_k}$ can be read as a current wave propagating along the birdcage circumference. In this perspective, k denotes the number of full wavelengths across the circumference. The $k = 1$ (or $k = N - 1$) mode gives the most homogeneous magnetic field inside the coil and it is therefore named "fundamental mode". Generally speaking, the tuning process of a birdcage coil consists in making the fundamental mode frequency of the birdcage coil matching with the operational frequency (typically the "Larmor frequency") [39, 54]. This procedure represents an important step that will be followed dealing with the birdcage design in chapter 3. Finally, there are two other non-degenerate operational modes associated with $k = N/2$ and $k = N$. The $k = N/2$ mode is distinguished by the meshes currents to be dephased of π from one mesh to the next. The $k = N$ mode is distinguished by the meshes currents to be the same for all the meshes. Since the generic leg current $\mathbb{I}_n$ is equal to $I_n - I_{n+1}$, it turns out that there will not be any current along the legs and they will circulate only along the end-rings. Finally, equation (2.3) is obtained considering the lossless circuit of Figure 2.1. The effect of losses can be easily taken into account considering the same circuit of Figure 2.1 adding resistive terms ($\boldsymbol{R}$) on each leg. Forcing the circuit currents to be equal to the generic eigenvector $\boldsymbol{V_k}$ (*i.e.* the solution of the lossless system related to the frequency ω_k), we obtain the following equation:

$$\omega_k^2 - \omega^2 + j\omega\omega_k/Q_k = 0 \tag{2.11}$$

where an ad hoc "quality factor" $\boldsymbol{Q}_k$ has been defined and it is equal to $(RC\omega_k)^{-1}$. That is the same equation of (2.9) with a damping term that is frequency dependent. The lossy circuit solution do not bring anymore to a standard eigenvalue problem and the solutions of equation (2.11) represent the frequencies that guarantee the mesh currents of the lossy circuit to have the same shape of those of the lossless circuit. From a deeper insight into equation (2.11) it results that it isn't solved for any non-zero $\omega \in \Re$. That means that the mesh currents of the lossy circuit will not be the same of the mesh currents of the lossless circuit for any physical frequency value.

2.2.2 Driven birdcage

Let us write the equation relative to the nth mesh of the lossy circuit with a time harmonic voltage Φ_n applied to it[1]:

$$(s^2 + 2s\omega_a^2 CR + 2\omega_a^2)I_n - \omega_a^2\left[\left(\frac{s}{\omega_b}\right)^2 + sCR + 1\right](I_{n+1} + I_{n-1}) = \frac{s\Phi_n}{L + 2M} \tag{2.12}$$

The above equation can be rewritten in matrix form as it follows:

$$s^2\mathbb{A}_1\boldsymbol{I} + s\mathbb{A}_2\boldsymbol{I} + \mathbb{A}_3\boldsymbol{I} = \frac{s\boldsymbol{\Phi}}{L + 2M} \tag{2.13}$$

where:

---

[1] There are many different strategies that can be adopted to supply a birdcage coil. Each strategy is generally aimed to adress specific problems which are not related to the theory proposed in the present chapter. For simplicity, here we imagine that the electromotive force is induced in the considered mesh by means of a proper coupling coil supplied at a given frequency. The relative position of the coil with respect to the meshes determines the supply conditions.

$\boldsymbol{I}$ represents the mesh currents vector;

$\boldsymbol{\Phi}$ represents the mesh voltages vector;

$\mathbb{A}_1, \mathbb{A}_2, \mathbb{A}_3$ are circulant matrices;

It has been shown that the eigenvectors $\boldsymbol{V}_k$ represent a complete orthonormal basis for $\mathbb{R}^N$(see (2.6)). Therefore, we can express the generic mesh currents vector as a linear combination of the eigenvectors $\boldsymbol{V}_k$ as it follows:

$$\boldsymbol{I} = \sum_{k=1}^{N} \lambda_k \boldsymbol{V}_k \tag{2.14}$$

where λ_k are appropriate complex coefficients. Considering that $\mathbb{A}_1, \mathbb{A}_2, \mathbb{A}_3$ are circulant matrices, $\boldsymbol{V}_k$ also represent their eigenvectors [56]. Equation (2.13) becomes:

$$\sum_{k=1}^{N} \left[\lambda_k \left(s^2 \alpha_{1_k} + s\alpha_{2_k} + \alpha_{3_k} \right) \boldsymbol{V}_k \right] = \frac{s\boldsymbol{\Phi}}{L + 2M} \tag{2.15}$$

where $\alpha_{1_k}, \alpha_{2_k}, \alpha_{3_k}$ are the eigenvalues, associated to the eigenvector $\boldsymbol{V}_k$, of $\mathbb{A}_1, \mathbb{A}_2, \mathbb{A}_3$ respectively. Considering that the eigenvectors $\boldsymbol{V}_k$ are orthonormal, we can obtain the coefficients λ_k by simply multiplying both members of the above equation by $\boldsymbol{V}_k^\dagger$ where the dagger operator denotes Hermitian transpose:

$$\begin{aligned} \lambda_k &= \frac{s\langle \boldsymbol{V_k}, \boldsymbol{\Phi} \rangle}{(L + 2M)(s^2 \alpha_{1_k} + s\alpha_{2_k} + \alpha_{3_k})} = \\ &\qquad \frac{s\langle \boldsymbol{V_k}, \boldsymbol{\Phi} \rangle}{(L + 2M)\left[1 - 2\left(\frac{\omega_a}{\omega_b}\right)^2 \cos\left(\frac{2\pi}{N}k\right)\right]\left(\omega_k^2 - \omega^2 + j\omega\omega_k/Q_k\right)} \end{aligned} \tag{2.16}$$

The mesh currents can be directly computed using (2.14):

$$\boldsymbol{I} = \sum_{k=1}^{N} \frac{j\omega\langle \boldsymbol{V_k}, \boldsymbol{\Phi} \rangle}{(L + 2M)\left[1 - 2\left(\frac{\omega_a}{\omega_b}\right)^2 \cos\left(\frac{2\pi}{N}k\right)\right]\left(\omega_k^2 - \omega^2 + j\omega\omega_k/Q_k\right)} \boldsymbol{V}_k \tag{2.17}$$

Now we will examine the currents distribution with four different supply configurations (see Figure 2.2). Each supply is intended to be at the fundamental frequency ω_1. We notice that among the N terms of (2.17), those with $k = 1$ and $k = N - 1$ are predominant. This is because both correspond to $\omega_k = \omega_1$ minimizing the denominator of (2.17). We will therefore neglect all off-resonants terms in the sum[2].

---

[2] This approximation allows to obtain quite simple explicit expressions for the driven birdcage problem. A more rigorous result, where also the off-resonance term are considered in the summation, will be given in section 2.2.4.

Firstly we consider $\mathbf{\Phi}$ to be zero everywhere except in the Nth position which has the value Φ_N. It corresponds to supply the Nth mesh of the birdcage coil with a voltage equal to Φ_N (Figure 2.2a). We obtain by means of (2.17) the current for the nth mesh[3]:

$$I_n = \left(\frac{2\Phi_N Q_1}{N\omega_1(L+2M)\left[1-2\left(\frac{\omega_a}{\omega_b}\right)^2\cos\left(\frac{2\pi}{N}\right)\right]} \right) \cos\left(\frac{2\pi n}{N}\right) \tag{2.18}$$

The current along the nth leg can be computed as:

$$\mathcal{I}_n = I_n - I_{n+1} = \left(\frac{2\Phi_N Q_1}{N\omega_1(L+2M)\left[1-2\left(\frac{\omega_a}{\omega_b}\right)^2\cos\left(\frac{2\pi}{N}\right)\right]} \right) \sin\left(\frac{\pi}{N}\right) \sin\left(\frac{\pi(2n+1)}{N}\right) \tag{2.19}$$

By inspection of the above equation, it turns out that with this kind of supply the current distribution along the birdcage legs is such that it would generate a linearly polarized magnetic field whose polarization plane bisects the driven mesh and the coupling coil (see Figure 2.2a).

Now we examine the mesh currents driving the Nth and the first meshes of the birdcage coil (Figure 2.2b). Each mesh is driven by a voltage equal to $\Phi_N/2$. It means that $\mathbf{\Phi}$ will be equal to zero everywhere except in the first and Nth position where it is equal to $\Phi_N/2$. Applying equation (2.17) we obtain for the nth mesh current:

$$I_n = \left(\frac{2\Phi_N Q_1}{N\omega_1(L+2M)\left[1-2\left(\frac{\omega_a}{\omega_b}\right)^2\cos\left(\frac{2\pi}{N}\right)\right]} \right) \cos\left(\frac{\pi}{N}\right) \cos\left(\frac{\pi(2n-1)}{N}\right) \tag{2.20}$$

Again, we can compute the nth leg current as:

$$\mathcal{I}_n = I_n - I_{n+1} = \left(\frac{2\Phi_N Q_1}{N\omega_1(L+2M)\left[1-2\left(\frac{\omega_a}{\omega_b}\right)^2\cos\left(\frac{2\pi}{N}\right)\right]} \right) \sin\left(\frac{2\pi}{N}\right) \sin\left(\frac{2\pi n}{N}\right) \tag{2.21}$$

The polarization plane of the magnetic field generated by the currents distribution keeps to bisect the coupling coil but, in this case, it bisects a leg rather than a mesh of the birdcage coil (see Figure 2.2b).

The next examined scenario contemplates the Nth leg driven with a voltage equal to Φ_N. To obtain that, we drive the Nth and the first meshes of the birdcage coil with a voltage equal to $-\Phi_N/2$ and $+\Phi_N/2$ respectively (Figure 2.2c). It means that $\mathbf{\Phi}$ will be equal to zero everywhere except in the first and Nth position where it is equal to $-\Phi_N/2$ and $+\Phi_N/2$. Applying equation (2.17) we obtain for the nth mesh current:

$$I_n = \left(\frac{2\Phi_N Q_1}{N\omega_1(L+2M)\left[1-2\left(\frac{\omega_a}{\omega_b}\right)^2\cos\left(\frac{2\pi}{N}\right)\right]} \right) \sin\left(\frac{\pi}{N}\right) \sin\left(\frac{\pi(2n-1)}{N}\right) \tag{2.22}$$

---

[3] When the temporal dependence is not explicit in the text, all the proposed currents and voltages are to be intended as phasors. Being $X(\omega)$ the phasor, it can be expressed in time domain as: $X(t) = \Re[X(\omega)e^{j\omega t}]$.

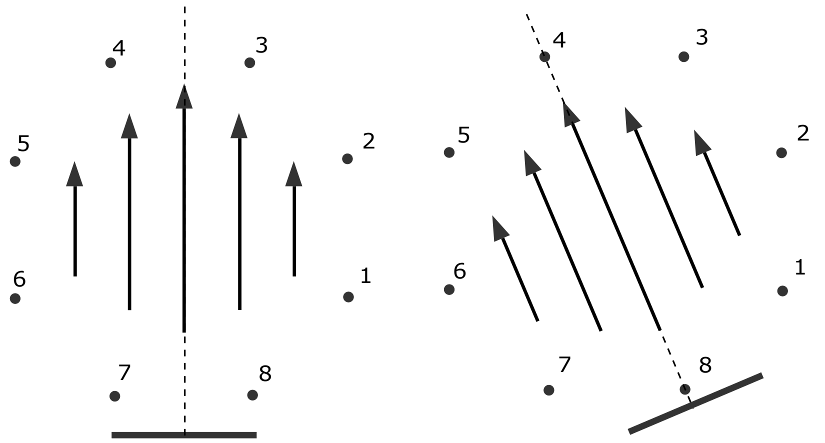

(a) *Supply voltage for the Nth mesh.*

(b) *Supply voltage for the Nth and first mesh.*

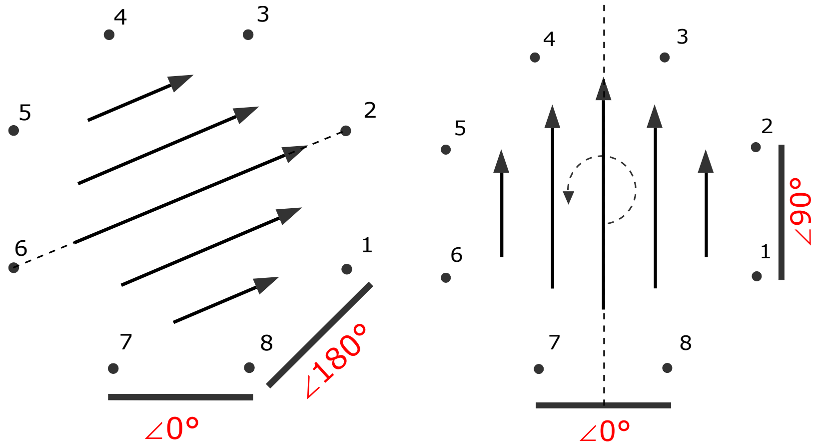

(c) *Supply voltage for the Nth and first mesh in counterphase.*

(d) *Quadrature supply.*

Figure 2.2: Four different supply schemes for an 8-leg birdcage. The black dots represent the legs, the arrows represent the magnetic field direction and the dashed line identifies its polarization plane. The thick line represents the coupling coil responsible for the supply.

Again, we can compute the nth leg current as:

$$\mathcal{I}_n = I_n - I_{n+1} = \left(\frac{2\Phi_N Q_1}{N\omega_1(L+2M)\left[1-2\left(\frac{\omega_a}{\omega_b}\right)^2\cos\left(\frac{2\pi}{N}\right)\right]}\right)\cos\left(\frac{2\pi n}{N}\right)\left[\cos\left(\frac{2\pi}{N}\right)-1\right] \tag{2.23}$$

obtaining a polarization plane of the magnetic field generated by the currents distribution that bisects a leg placed $N/4$ far from the driven one (see Figure 2.2c).
Finally, we investigate the effects of a quadrature supply. We assume the voltage vector

to be:

$$\mathbf{\Phi} = \begin{cases} \Phi_N & \text{if } n = N \\ \Phi_N e^{-j\frac{\pi}{2}} & \text{if } n = \frac{N}{4} \\ 0 & \text{elsewhere} \end{cases} \tag{2.24}$$

By means of (2.17) we obtain the expression for the nth mesh current. In order to make some considerations, we propose below the key passage for the calculation:

$$\begin{aligned} I_n = \left(\frac{\Phi_N}{R}\right)\Big[&\underbrace{\left(e^{-j\frac{2\pi}{N}N} + e^{-j\frac{2\pi}{N}\frac{N}{4}}e^{-j\frac{\pi}{2}}\right)e^{j\frac{2\pi}{N}n}}_{k=1} \\ &+ \underbrace{\left(e^{j\frac{2\pi}{N}N} + e^{j\frac{2\pi}{N}\frac{N}{4}}e^{-j\frac{\pi}{2}}\right)e^{-j\frac{2\pi}{N}n}}_{k=N-1}\Big] = \left(\frac{2\Phi_N}{R}\right)e^{-j\frac{2\pi}{N}n} \end{aligned} \tag{2.25}$$

where $R = N\omega_1(L + 2M)\left[1 - 2\left(\frac{\omega_a}{\omega_b}\right)^2 \cos\left(\frac{2\pi}{N}\right)\right]/Q_1$. We notice that the mesh currents represent a wave propagating along the birdcage legs. As anticipated above, since we stimulate the mode (i.e. $\omega = \omega_1$), this wave is characterized by having only one wavelength across the birdcage coil circumference. We can easily compute the nth leg current as previously done:

$$\mathscr{I}_n = I_n - I_{n+1} = \left(\frac{\Phi_N}{R}\right)\left(1 - e^{-j\frac{2\pi}{N}}\right)e^{-j\frac{2\pi}{N}n} \tag{2.26}$$

A part from a scaling and dephasing term, the considerations carried out for the mesh currents are still valid for the leg currents. This currents distribution give rise to a rotating magnetic field inside the birdcage coil as highlighted in Figure 2.2d.

2.2.3 Perturbed birdcage

In this section we investigate the effects of perturbing the birdcage coil symmetry. In order to obtain this result, we apply to the value of the capacitor of the nth leg a small perturbation factor. The results are here obtained applying the first order degenerate perturbation theory (see Appendix B).

Let us suppose to perturb the nth leg capacitor in such a way its value becomes equal to $C_n/(1 - \delta)$. The nth capacitor is shared between the nth and $n + 1$th legs. So, it enters in the nth and $n + 1$th equations as it follows:

$$[s^2 + \omega_a^2(2 - \delta)]I_n - \omega_a^2[(1 - \delta)I_{n+1} + I_{n-1}] = 0 \tag{2.27a}$$

$$[s^2 + \omega_a^2(2 - \delta)]I_{n+1} - \omega_a^2[I_{n+2} + (1 - \delta)I_n] = 0 \tag{2.27b}$$

Where, for simplicity, we consider all the mutual inductances equal to zero[4]. Due to this approximation, the generic kth unperturbed eigenvalue becomes $\omega_k^2 = 2\omega_a^2[1 - \cos(2\pi k/N)]$ with $\omega_a^2 = (LC)^{-1}$ and the perturbation matrix $\widetilde{\mathbb{A}}$ can be directly obtained from equations (2.27). $\widetilde{\mathbb{A}}$ will be zero everywhere except for:

$$\widetilde{\mathbb{A}}_{n,n} = -\omega_a^2, \qquad \widetilde{\mathbb{A}}_{n,n+1} = \omega_a^2$$
$$\widetilde{\mathbb{A}}_{n+1,n} = \omega_a^2, \qquad \widetilde{\mathbb{A}}_{n+1,n+1} = -\omega_a^2$$

The perturbed system matrix will be:

$$\mathbb{P} = \mathbb{A} + \delta\widetilde{\mathbb{A}} \tag{2.28}$$

We are interested in the perturbed eigenvalues of $\mathbb{P}$ associated to the mode (*i.e.* k=1 and k=N-1). Following the degenerate perturbation theory, we compute the matrix $\mathbb{W}$ whose element pq is equal to:

$$\mathbb{W}_{pq} = \boldsymbol{V_p}^{\dagger}\widetilde{\mathbb{A}}\boldsymbol{V_q} \tag{2.29}$$

for p and q equal to 1 and N-1. This give rise to a 2×2 complex matrix:

$$\mathbb{W} = \begin{pmatrix} \frac{\omega_a^2}{N}\left(1 - e^{j\frac{2\pi}{N}}\right)\left(e^{-j\frac{2\pi}{N}} - 1\right) & -\frac{\omega_a^2}{N}\left(e^{-j\frac{2\pi}{N}(n+1)} - e^{-j\frac{2\pi}{N}n}\right)^2 \\ -\frac{\omega_a^2}{N}\left(e^{j\frac{2\pi}{N}(n+1)} - e^{j\frac{2\pi}{N}n}\right)^2 & \frac{\omega_a^2}{N}\left(1 - e^{j\frac{2\pi}{N}}\right)\left(e^{-j\frac{2\pi}{N}} - 1\right) \end{pmatrix} \tag{2.30}$$

Considering the Nth capacitor to be perturbed (*i.e* n=N in (2.30)) the eigenvalues $\widetilde{\omega}_{1,2}^2$ of $\mathbb{W}$ become:

$$\widetilde{\omega}_1^2 = 0 \tag{2.31a}$$

$$\widetilde{\omega}_2^2 = \frac{-2\omega_1^2}{N} \tag{2.31b}$$

The perturbed mode eigenvalues ${\omega^2}^P_{1,2}$ of the perturbed system matrix $\mathbb{P}$ become[5]:

$${\omega^2}^P_1 = \omega_1^2 + \widetilde{\omega}_1^2 = \omega_1^2 \tag{2.32a}$$

$${\omega^2}^P_2 = \omega_1^2 + \widetilde{\omega}_2^2 = \omega_1^2 - \delta\frac{2\omega_1^2}{N} \tag{2.32b}$$

---

[4] This simplification makes the computation extremely simpler. We will see that, dealing with the high-pass birdcage coil, this approximation would be too severe and the calculations will be carried out solving the complete equations.

[5] It can be shown, using a similar approach to that applied for the high-pass coil in section 2.3.3, that all the obtained results are still valid even considering the presence of the mutual inductances. In this case, the expression for ω_1 is given by (2.10) with $k = 1$.

We observe that, due to the capacitance perturbation, the two eigenvalues are no more degenerate. Let us now consider the perturbed eigenvectors. The normalized eigenvectors of $\mathbb{W}$ perturbing the Nth capacitor are:

$$\boldsymbol{\beta}_1 = \frac{1}{\sqrt{2}}\begin{pmatrix} 1 \\ e^{j\frac{2\pi}{N}} \end{pmatrix} \tag{2.33a}$$

$$\boldsymbol{\beta}_2 = \frac{1}{\sqrt{2}}\begin{pmatrix} 1 \\ -e^{j\frac{2\pi}{N}} \end{pmatrix} \tag{2.33b}$$

The perturbed eigenvectors $\boldsymbol{V}_{\boldsymbol{1,2}}^{\boldsymbol{P}}$ can be expressed as it follows:

$$\boldsymbol{V}_{\boldsymbol{1}}^{\boldsymbol{P}} = \frac{1}{\sqrt{2}}\left(\boldsymbol{V}_{\boldsymbol{1}} + e^{j\frac{2\pi}{N}}\boldsymbol{V}_{\boldsymbol{N-1}}\right) + \delta\widetilde{\boldsymbol{V}_{\boldsymbol{1}}} \tag{2.34a}$$

$$\boldsymbol{V}_{\boldsymbol{2}}^{\boldsymbol{P}} = \frac{1}{\sqrt{2}}\left(\boldsymbol{V}_{\boldsymbol{1}} - e^{j\frac{2\pi}{N}}\boldsymbol{V}_{\boldsymbol{N-1}}\right) + \delta\widetilde{\boldsymbol{V}_{\boldsymbol{2}}} \tag{2.34b}$$

where:

$$\widetilde{\boldsymbol{V}_{\boldsymbol{1}}} = \sum_{\substack{k \in I\!N \\ 1<k\leq N, k\neq N-1}} \frac{1}{\sqrt{2}} \frac{\boldsymbol{V}_{\boldsymbol{k}}^{\dagger}\widetilde{\mathbb{A}}\left(\boldsymbol{V}_{\boldsymbol{1}} + e^{j\frac{2\pi}{N}}\boldsymbol{V}_{\boldsymbol{N-1}}\right)}{\omega_1^2 - \omega_k^2}\boldsymbol{V}_{\boldsymbol{k}} \tag{2.35a}$$

$$\widetilde{\boldsymbol{V}_{\boldsymbol{2}}} = \sum_{\substack{k \in I\!N \\ 1<k\leq N, k\neq N-1}} \frac{1}{\sqrt{2}} \frac{\boldsymbol{V}_{\boldsymbol{k}}^{\dagger}\widetilde{\mathbb{A}}\left(\boldsymbol{V}_{\boldsymbol{1}} - e^{j\frac{2\pi}{N}}\boldsymbol{V}_{\boldsymbol{N-1}}\right)}{\omega_1^2 - \omega_k^2}\boldsymbol{V}_{\boldsymbol{k}} \tag{2.35b}$$

It can be shown, with a rather simple calculation, that the perturbation coefficient $\widetilde{\boldsymbol{V}_{\boldsymbol{1}}}$ is equal to zero and $\boldsymbol{V}_{\boldsymbol{1}}^{\boldsymbol{P}}$ becomes:

$$\boldsymbol{V}_{\boldsymbol{1}}^{\boldsymbol{P}} = \frac{1}{\sqrt{2}}\left(\boldsymbol{V}_{\boldsymbol{1}} + e^{j\frac{2\pi}{N}}\boldsymbol{V}_{\boldsymbol{N-1}}\right) \tag{2.36}$$

The perturbed eigenvectors $\boldsymbol{V}_{\boldsymbol{1,2}}^{\boldsymbol{P}}$ now represent possible mesh currents distribution for the perturbed birdcage. We notice that the perturbed structure shares one of the two eigenvalues (${\omega^2}_1^{\boldsymbol{P}}$) and eigenvectors ($\boldsymbol{V}_{\boldsymbol{1}}^{\boldsymbol{P}}$) with the unperturbed birdcage. The latter is because any linear combination of degenerate eigenvectors still represents an eigenvector[6]. An explicit calculation of the eigenvectors, gives the expressions for the admissible

---

[6] Given a square matrix $\mathbb{A}$ with a double degenerate eigenvalue λ associated to two eigenvectors $\boldsymbol{V}_{\boldsymbol{1}}$ and $\boldsymbol{V}_{\boldsymbol{2}}$, we have: $\mathbb{A}\boldsymbol{V}_{\boldsymbol{1}} = \lambda\boldsymbol{V}_{\boldsymbol{1}}$ and $\mathbb{A}\boldsymbol{V}_{\boldsymbol{2}} = \lambda\boldsymbol{V}_{\boldsymbol{2}}$. We can define a linear combination of $\boldsymbol{V}_{\boldsymbol{1}}$ and $\boldsymbol{V}_{\boldsymbol{2}}$ as $\boldsymbol{V} = \alpha_1\boldsymbol{V}_{\boldsymbol{1}} + \alpha_2\boldsymbol{V}_{\boldsymbol{2}}$ with α_1 and α_2 being scalar coefficients. It follows that: $\mathbb{A}\boldsymbol{V} = \alpha_1\mathbb{A}\boldsymbol{V}_{\boldsymbol{1}} + \alpha_2\mathbb{A}\boldsymbol{V}_{\boldsymbol{2}} = \alpha_1\lambda\boldsymbol{V}_{\boldsymbol{1}} + \alpha_2\lambda\boldsymbol{V}_{\boldsymbol{2}} = \lambda\boldsymbol{V}$.

nth mesh currents:

$$\boldsymbol{I}_n = \frac{1}{\sqrt{2N}}\left(e^{\frac{j2\pi}{N}n} + e^{-\frac{j2\pi}{N}(n-1)}\right) \qquad \text{(for } \boldsymbol{V}_1^{\boldsymbol{P}}\text{)} \tag{2.37a}$$

$$\boldsymbol{I}_n = \frac{1}{\sqrt{2N}}\left(e^{\frac{j2\pi}{N}n} - e^{-\frac{j2\pi}{N}(n-1)}\right) + \delta\widetilde{\boldsymbol{V}_{2n}} \qquad \text{(for } \boldsymbol{V}_2^{\boldsymbol{P}}\text{)} \tag{2.37b}$$

The leg currents can be easily obtained as:

$$\mathscr{I}_n = \boldsymbol{I}_n - \boldsymbol{I}_{n+1} = j\sqrt{\frac{2}{N}}\left(1 - e^{\frac{j2\pi}{N}}\right)\sin\left(\frac{2\pi}{N}n\right) \qquad \text{(for } \boldsymbol{V}_1^{\boldsymbol{P}}\text{)} \tag{2.38a}$$

$$\mathscr{I}_n = \boldsymbol{I}_n - \boldsymbol{I}_{n+1} = \sqrt{\frac{2}{N}}\left(1 - e^{\frac{j2\pi}{N}}\right)\cos\left(\frac{2\pi}{N}n\right) + \delta(\widetilde{\boldsymbol{V}_{2n}} - \widetilde{\boldsymbol{V}_{2n+1}}) \qquad \text{(for } \boldsymbol{V}_2^{\boldsymbol{P}}\text{)} \tag{2.38b}$$

Few considerations can be proposed from the obtained results. Both modes possess leg current distributions which are sinusoidal in first order. Indeed, even for the $\boldsymbol{V}_2^{\boldsymbol{P}}$ eigenvector, the term multiplied by δ has a minor role in defining the distribution shape. This is clearly visible in Figure 2.3 where the $\mathscr{I}_n$ for the normalized $\boldsymbol{V}_2^{\boldsymbol{P}}$ are shown for different δ values. We notice that the current distribution among the legs is almost sinusoidal also for δ different from zero. Some differences from the sinusoidal behaviour are due to the perturbed leg where the current value increases due to the decrease of the capacitive impedance of the leg.

2.2.4 Driven perturbed birdcage

Now we want to examine the birdcage behaviour when it is driven at the fundamental mode frequency after that the Nth leg capacitor has been perturbed. To do that we follow the same method adopted in section 2.2.2 taking into account the presence of the perturbation in (2.27). An equation, analogous to (2.13), can be written:

$$s^2\mathbb{A}_1\boldsymbol{I} + s\mathbb{A}_2\boldsymbol{I} + \mathbb{A}_3\boldsymbol{I} + \delta\omega_a^2\widetilde{\mathbb{A}}_3\boldsymbol{I} = \frac{s\boldsymbol{\Phi}}{L + 2M} \tag{2.39}$$

where:

$\boldsymbol{I}$ represents the mesh currents vector;

$\boldsymbol{\Phi}$ represents the mesh voltages vector;

$\mathbb{A}_1$, $\mathbb{A}_2$, $\mathbb{A}_3$ are circulant matrices;

$\widetilde{\mathbb{A}}_3$ is a matrix whose entries, if the Nth capacitor is perturbed, are zero everywhere except for the (1,1) and (N,N) position where they are equal to -1 and for the (1,N) and (N,1) position where they are equal to 1;

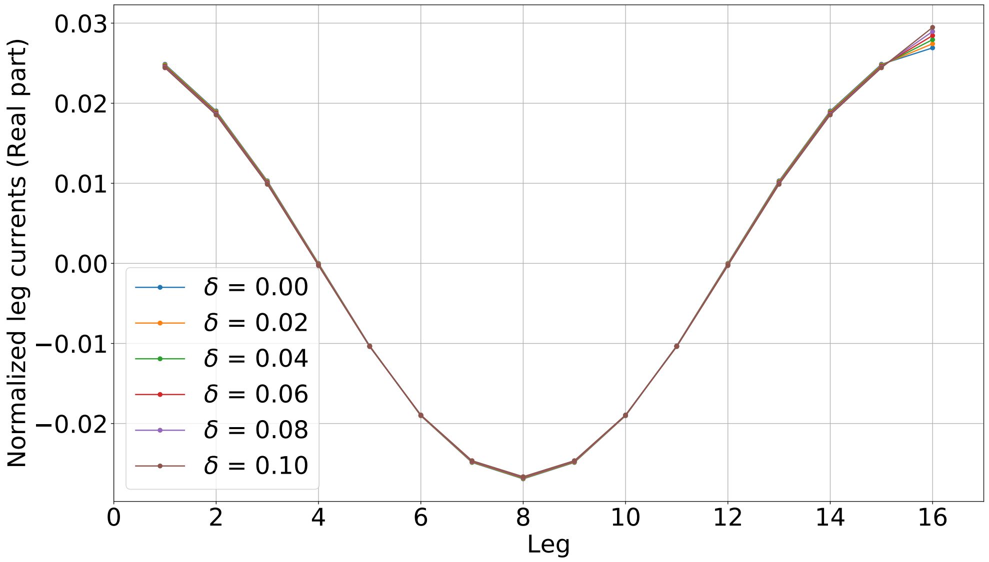

(a) *Real part of the acceptable leg currents obtained from the normalized* $\boldsymbol{V_2^P}$ *eigenvector.*

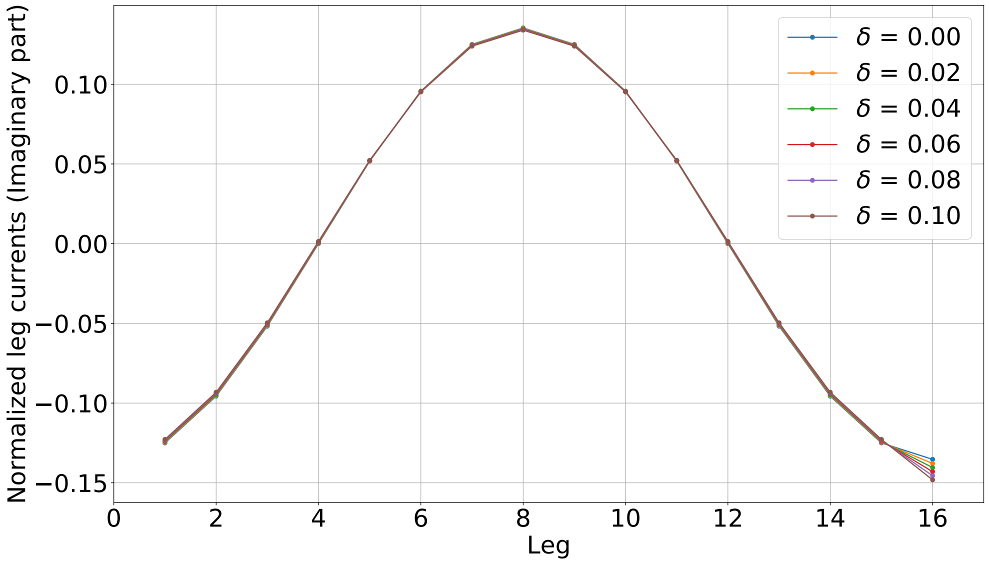

(b) *Imaginary part of the acceptable leg currents obtained from the normalized* $\boldsymbol{V_2^P}$ *eigenvector.*

Figure 2.3: Acceptable leg currents obtained from the normalized $\boldsymbol{V_2^P}$ eigenvector evaluated for a 16-leg low-pass birdcage.

Table 2.1: Low-pass birdcage parameters considered in the evaluation of the leg currents generated by the considered driven conditions. The listed parameters are described in section 2.2.1.

Parameter	Value
C	9 pF
L	100 nH
M	33 nH
R	1 Ω

Expressing the mesh currents as in (2.14) and multiplying both members by $\boldsymbol{V}_k^\dagger$, it is possible to obtain the following expression:

$$\lambda_k\left(s^2\alpha_{1_k} + s\alpha_{2_k} + \alpha_{3_k}\right) + \delta\frac{\omega_a^2}{N}\sum_{k'=1}^{N}\lambda_{k'}\boldsymbol{V}_k^\dagger\widetilde{\mathbb{A}}_3\boldsymbol{V}_{k'} = \frac{s\langle\boldsymbol{V_k},\boldsymbol{\Phi}\rangle}{L+2M} \tag{2.40}$$

Writing an analogous expression for all the k from 1 to N, gives rise to the following matrix equation:

$$\alpha\lambda = \frac{s}{L+2M}\begin{pmatrix}\langle\boldsymbol{V_1},\boldsymbol{\Phi}\rangle\\ \vdots\\ \langle\boldsymbol{V_k},\boldsymbol{\Phi}\rangle\\ \vdots\\ \langle\boldsymbol{V_N},\boldsymbol{\Phi}\rangle\end{pmatrix} \tag{2.41}$$

where:

α is an $N \times N$ circulant matrix;

λ is the column vector consisting of the λ coefficients;

By inverting the matrix α it is possible to obtain the coefficients λ and, through (2.14), to obtain the leg currents.

Now, by means of the results obtained, we will examine the special driven conditions of Figure 2.4. The results proposed in this section are obtained considering the parameters reported in Table 2.1. Such parameters lead to a fundamental unperturbed resonance frequency equal to 63.85 MHz. In the first case (Figure 2.4a) the voltage is equally distributed among the meshes adjacent to the perturbed leg. With this driving set-up the current distribution among the legs (Figure 2.5) does not depend on the perturbation amount and it is the same as for the unperturbed case. The polarization plane of the generated magnetic field bisects the driven leg. This behaviour can be explained considering that, with this driving scheme, the current along the perturbed leg is forced to be zero leading the currents distribution to be not influenced by the perturbation.

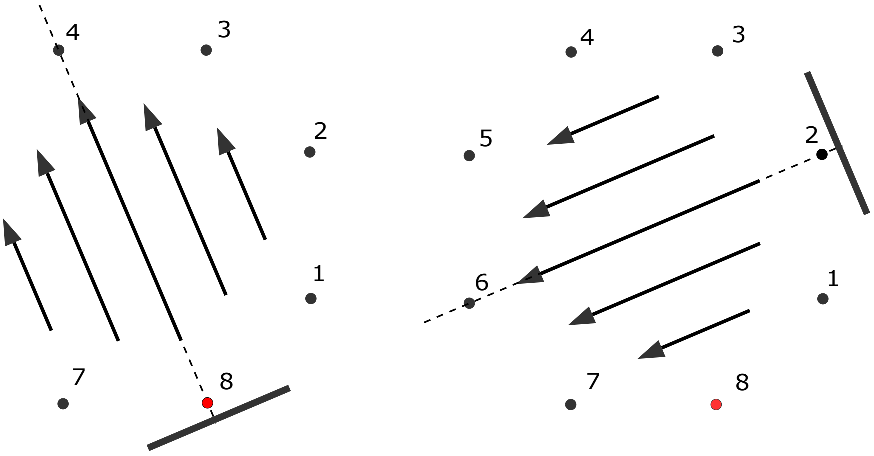

(a) *Supply voltage for the* N*th and first mesh.*

(b) *Supply voltage for the* $N/4$*th and* $(N/4+1)$*th mesh.*

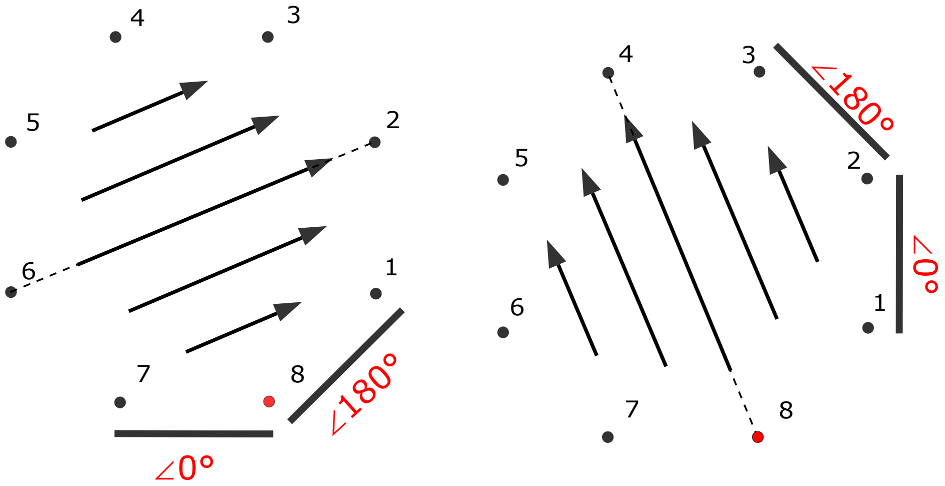

(c) *Supply voltage for the* N*th and first mesh in counterphase.*

(d) *Supply voltage for the* $N/4$*th and* $(N/4+1)$*th mesh in counterphase.*

Figure 2.4: Four different supply schemes for 8-leg birdcage where the Nth leg (represented in red) capacitor has been perturbed. The black dots represent the legs, the arrows represent the unperturbed magnetic field direction and the dashed line identify its polarization plane. The thick line represents the coupling coil responsible for the supply.

Next, we consider the case where the meshes adjacent to the leg $\pi/2$ far from the perturbed one are symmetrically supplied (Figure 2.4b). Several considerations can be done considering the results shown in Figure 2.6. Differently from the previous driving setup, here both the real and imaginary part of the currents distribution among the legs

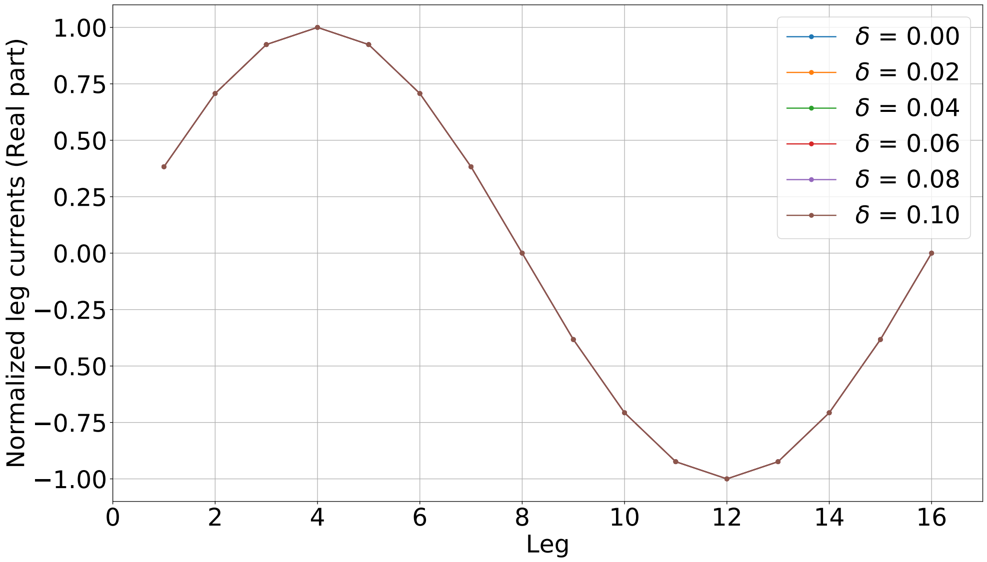

Figure 2.5: Real part of the leg currents obtained supplying a 16-leg birdcage coil symmetrically on the Nth and $N + 1$th meshes. The imaginary part is negligible on all the legs. The currents are normalized to the modulus of the maximum leg current of the unperturbed case.

are influenced by the perturbation δ. In particular, the real part of the leg currents decreases as the perturbation increases. On the other hand, the imaginary part follows a non-monotonic behaviour. In fact, it is null almost everywhere in the unperturbed birdcage increasing for very small perturbations[7]. As soon as the perturbation becomes higher, it starts to decrease tending towards zero. This phenomenon is analogous to the non-monotonic current behaviour of a voltage supplied RLC series circuit as soon as the frequency shifts from the resonance value.

The same behaviour is appreciable when the low-pass birdcage is supplied in counterphase on the Nth and $N + 1$th meshes. Also in this case, the leg currents decrease as the perturbation δ increases (see Figure 2.7). Finally, Figure 2.8 shows the leg currents obtained when the birdcage coil is supplied on the $N/4$th and $N/4 + 1$th meshes in counterphase (Figure 2.4b). The result is analogous to that obtained for the set-up represented in Figure 2.4a. Also in this case, the leg currents are not influenced by the perturbed capacitor.

---

[7] To avoid possible confusion, the perturbation values that lead to an increase of the imaginary part of the leg currents are not reported in Figure 2.6b whereas they are slightly appreciable in Figure 2.7b.

Several considerations can be proposed on the basis of the obtained results. It is interesting to notice that the sensitivity of the leg currents to the perturbation strongly depends on the way the coil is driven. In particular, the sensitivity results to be reduced when, considering the unperturbed scenario, the driving set-up leads to a zero current on the leg that is perturbed (see for example Figures 2.5 and 2.8). In order to explore in a deeper way this behaviour, let us compute the magnitude of the leg current generated by two mesh voltages applied in counterphase on the meshes adjacent to the aforementioned leg. Figure 2.9 shows the result obtained for the perturbed leg (Figure 2.9a), the leg $N/4$ apart from the perturbed one (Figure 2.9b) and a leg that is $N/8$ from the perturbed one (Figure 2.9c). The same birdcage parameters reported in Table 2.1 have been considered except for R that has been decreased to 0.001 Ω to better identify the resonance peaks in Figure 2.9. In Figure 2.9a the resonance peak at 63.85 MHz obtained for the unperturbed birdcage and corresponding to the fundamental mode frequency, moves to 63.69 MHz that is exactly $\sqrt{1-2\delta/N}$ times the unperturbed resonance frequency. Such a shift of the resonance frequency is consistent with the results expected from the perturbation theory (see section 2.2.3) and accounts for the Nth leg current variation already observed in Figure 2.7[8]. Figure 2.9b do not show any resonance shift when the unperturbed birdcage is perturbed. Even in this case, the insensitivity of the resonance peak to the perturbation, accounts for the results obtained in Figure 2.8. Finally, something remains to be said when the low-pass coil is driven on a leg within the perturbed one and that $N/4$ apart. In this scenario (Figure 2.9c) it is appreciable the split of the degenerate modes of the unperturbed coil. In particular, the unperturbed resonance peak at 63.85 MHz splits in two resonance peaks; one fixed at 63.85 MHz and the other at 63.69 MHz. The different resonance peak intensities is attributable to the frequency span resolution and to the normalization and it has not any physical implication. The results shown in Figure 2.9 give reason for those obtained by Tropp [55] with experimental measurements.

All these considerations have some consequences on the birdcage coil final behaviour. For limited perturbation values, such those considered in the proposed results, the leg currents distribution are still sinusoidal. However, the maximum current intensity among the legs depend on the perturbation and on the supply voltage position with respect to the perturbed leg. That means that, with a standard quadrature supply, the circular polarization of the magnetic field will not be ensured.

Finally, it is worth noting that the results in this section are not limited to small perturbations only; as they where those in section 2.2.3. Furthermore, all the contributions in (2.14) have been considered in evaluating the leg currents distributions. The optimum agreement between the unperturbed curves and the analytic expressions obtained in section 2.2.2 prove the reliability of the adopted approximation.

---

[8] Due to the higher value of R considered in Figure 2.7, the Nth leg current tends smoothly towards zero differently from how it would have done if a lower resistance have been considered.

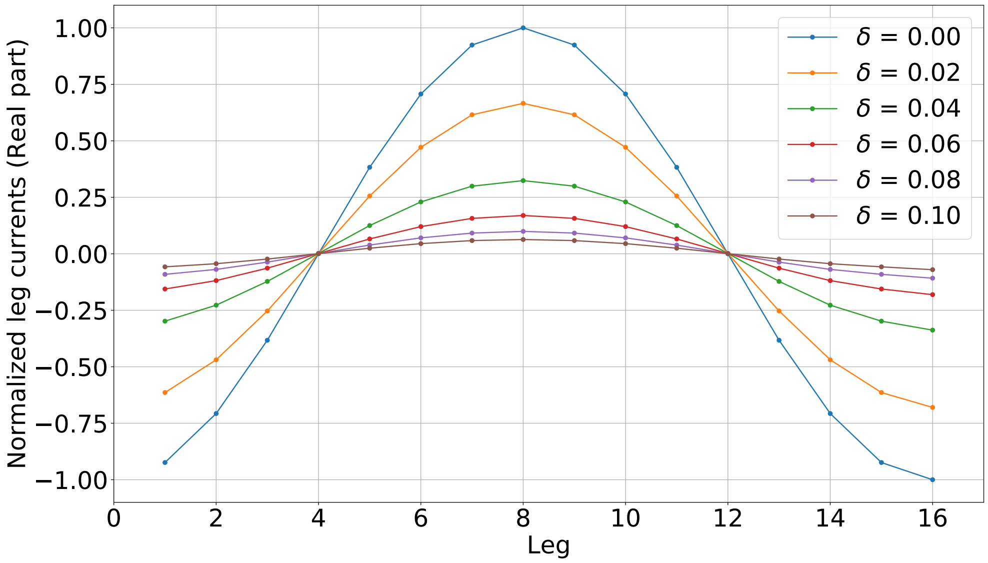

(a) *Real part of the leg currents obtained supplying a 16-leg birdcage coil symmetrically on the $N/4$th and $N/4+1$th meshes.*

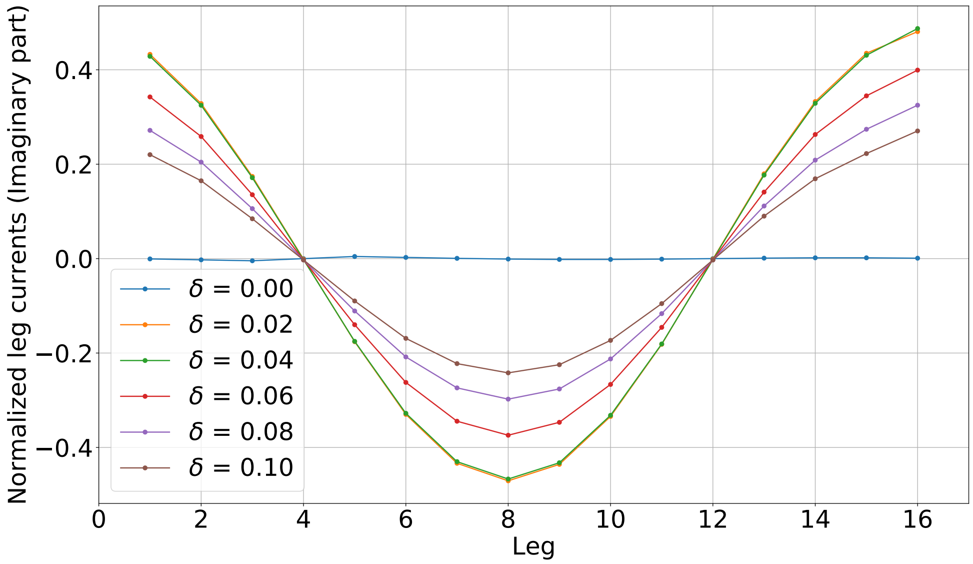

(b) *Imaginary part of the leg currents obtained supplying a 16-leg birdcage coil symmetrically on the $N/4$th and $N/4+1$th meshes.*

Figure 2.6: Leg currents obtained supplying a 16-leg birdcage coil symmetrically on the $N/4$th and $N/4+1$th meshes.

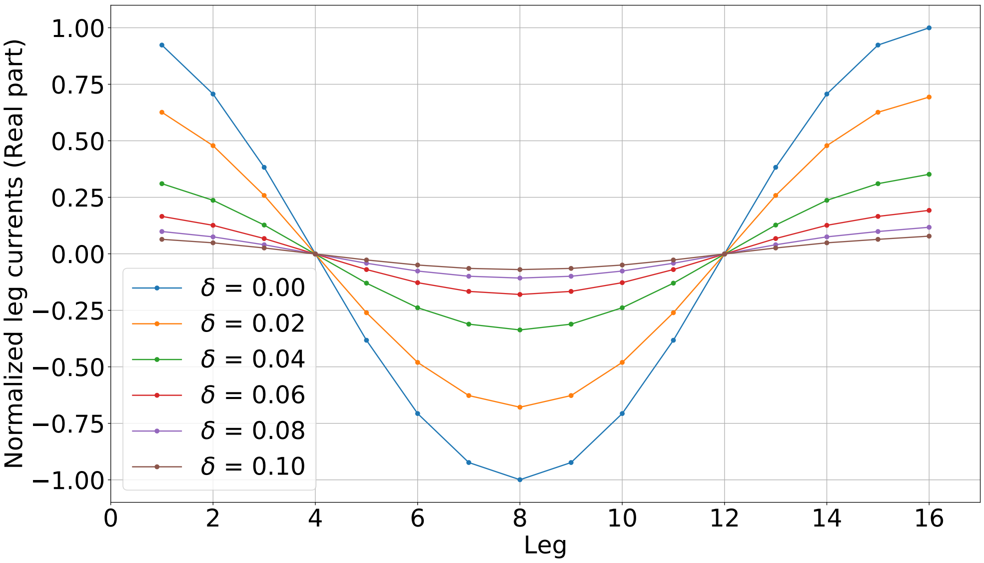

(a) *Real part of the leg currents obtained supplying a 16-leg birdcage coil in counterphase on the* N*th and* $(N+1)$*th meshes.*

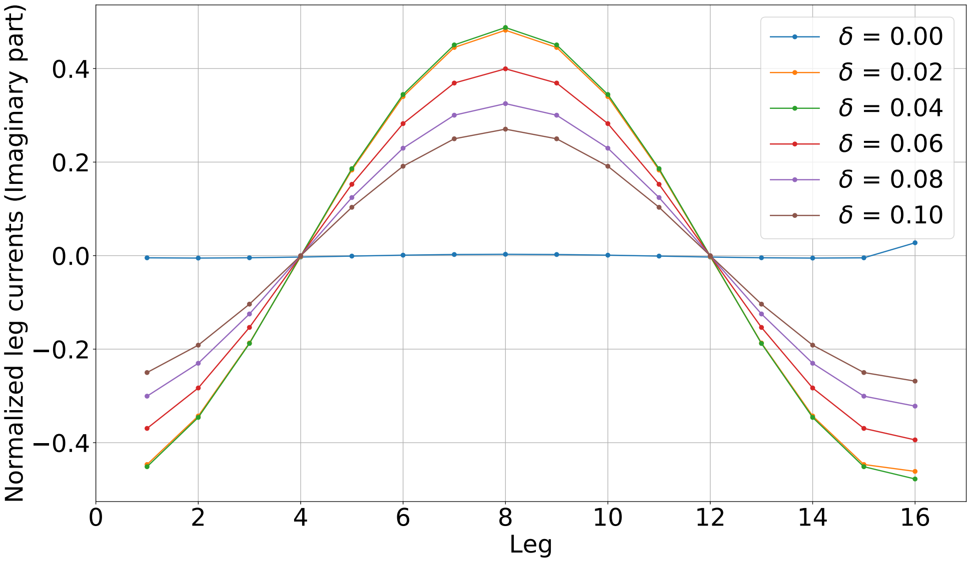

(b) *Imaginary part of the leg currents obtained supplying a 16-leg birdcage coil in counterphase on the* N*th and* $(N+1)$*th meshes.*

Figure 2.7: Leg currents obtained supplying a 16-leg birdcage coil in counterphase on the Nth and $N+1$th meshes.

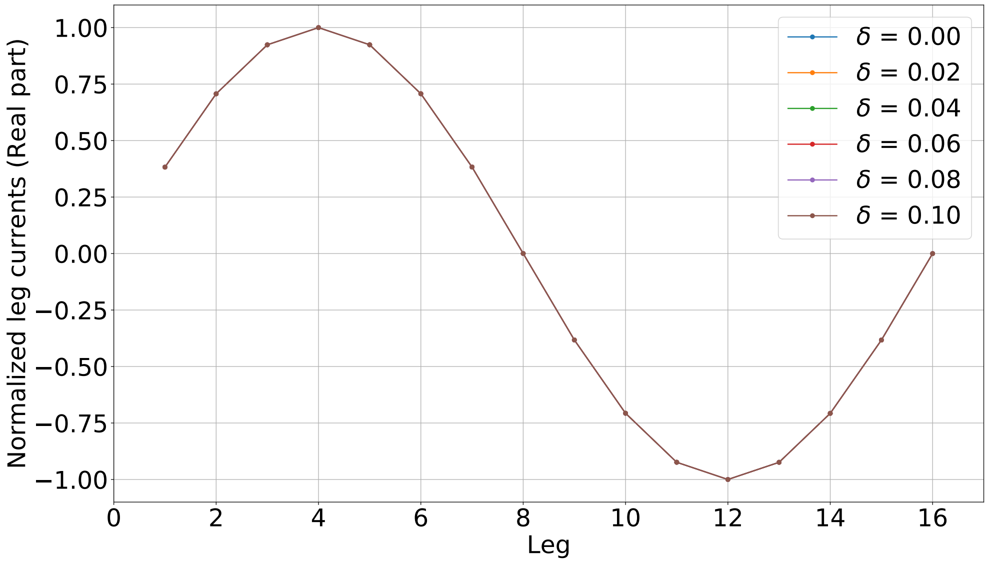

Figure 2.8: Real part of the leg currents obtained supplying a 16-leg birdcage coil in counterphase on the $N/4$th and $N/4+1$th meshes. The imaginary part is negligible on all the legs. The currents are normalized to the modulus of the maximum leg current of the unperturbed case.

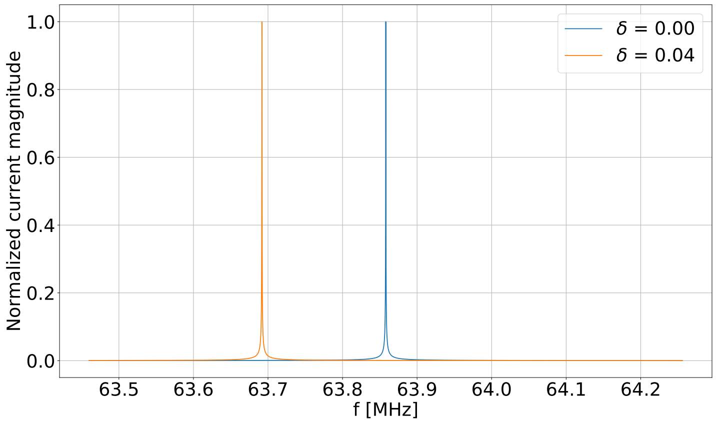

(a) *Magnitude of the Nth leg current due to a supply voltage applied to the Nth and first mesh in counterphase.*

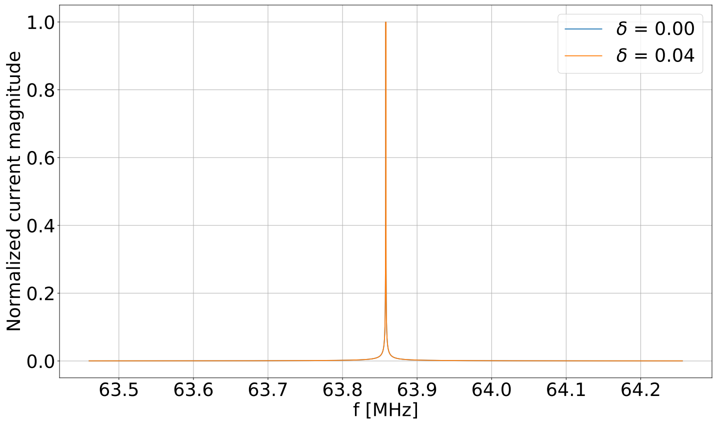

(b) *Magnitude of the $N/4$th leg current due to a supply voltage applied to the $N/4$th and $(N/4+1)$th mesh in counterphase.*

Figure 2.9: Frequency behaviour of the leg current magnitude generated by two mesh voltages applied in counterphase on the meshes adjacent to the leg. The current is normalized to its maximum value and it is reported for the unperturbed scenario and for a capacitor perturbation δ equal to 0.04 (continues on the next page).

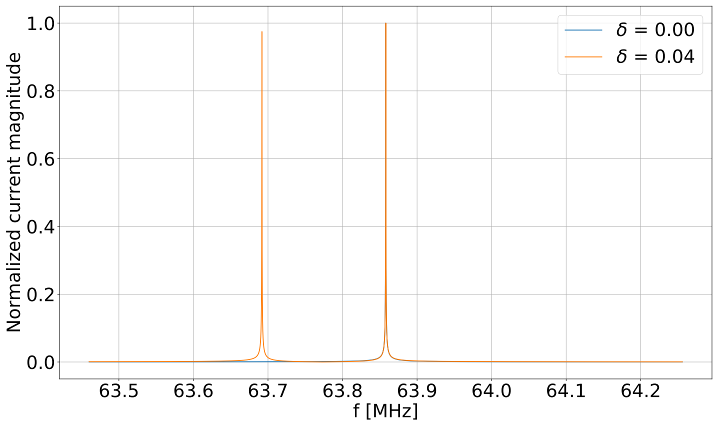

(c) *Magnitude of the $N/8th$ leg current due to a supply voltage applied to the $N/8th$ and $(N/8+1)th$ mesh in counterphase.*

Figure 2.9: Frequency behaviour of the leg current magnitude generated by two mesh voltages applied in counterphase on the meshes adjacent to the leg. The current is normalized to its maximum value and it is reported for the unperturbed scenario and for a capacitor perturbation δ equal to 0.04.

2.3 High-pass birdcage theory

2.3.1 Circuit equations

Figure 2.10 represents the general equivalent circuit relative to the nth mesh of an N-leg birdcage. As for the low-pass birdcage circuit, L_n takes into account the self inductance of the ring segments of the nth mesh and M_n accounts for both the mutual coupling between the nth and $(n+1)$th meshes and the self inductance of the nth leg. C_n^U and C_n^L take into account the capacitors of the upper and lower rings segments respectively.

The voltage Kirchoff law referred to the nth mesh is:

$$(s^2 + \omega_a^2)I_n - \omega_a^2\left[\left(\frac{s}{\omega_b}\right)^2\right](I_{n+1} + I_{n-1}) = 0 \tag{2.42}$$

where:

$$\omega_a^2 = \frac{1/C^L + 1/C^U}{L + 2M} \tag{2.43a}$$

$$\omega_b^2 = \frac{1/C^L + 1/C^U}{M} \tag{2.43b}$$

Again, as already done with the low-pass birdcage, all the auto-inductances are considered to be equal to a generic inductance L and all the mutual inductances to a generic mutual inductance M. Finally, all the capacitors belonging to the upper ring segments are considered equal to a generic capacitor C^U and those belonging to the lower ring segments, to a generic capacitor C^L. Writing equation (2.42) for all the N meshes, gives rise to an eigenvalue problem whose system matrix is circulant. It means that the eigenvectors $\boldsymbol{V}$ have the same expression of those considered for the low-pass birdcage (see (2.4)). Substituting the expression (2.4) for the generic eigenvector $\boldsymbol{V_k}$ into equation (2.42), we obtain the associated eigenvalue ω_k^2 as:

$$\omega_k^2 = \frac{\omega_a^2}{1 - 2(\frac{\omega_a}{\omega_b})^2 \cos(\frac{2\pi}{N}k)} \tag{2.44}$$

Some considerations can be done basing on the comparison of the low-pass birdcage eigenvalues expression (2.10) and those relative to the high-pass birdcage (2.44). Firstly, we noticed that $\omega = 0\,\mathrm{rad\,s^{-1}}$ is a solution in (2.10) but not in (2.44). This is easily explicable considering the different circuital behaviour of the two birdcage types. At this frequency, the capacitors behave like open circuits. This means that, for the low-pass birdcage, currents can circulate on the endrings without involving the legs. In the high-pass birdcage case, the capacitors are placed along the rings segments and, at zero frequency, there are not closed paths and currents can not flow. A second consideration is related to the modes frequency distribution. We noticed that the term ω_a/ω_b is

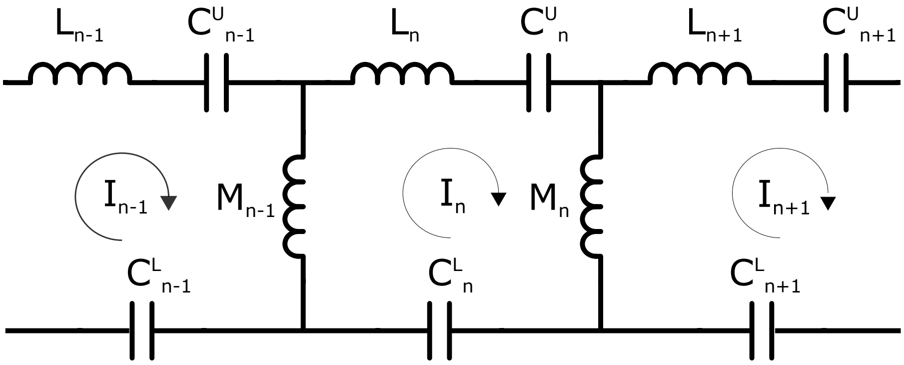

Figure 2.10: A segment of the - birdcage elementary circuit. Three among N total meshes are represented. The self-inductances L, the mutual inductances M, the legs capacitances C and the mesh currents I are then reported.

equal or less than 0.5. It turns out that the frequency of fundamental mode is the lower among all those of the other degenerate modes for the low-pass birdcage. Differently, for the high-pass birdcage, the fundamental mode has the higher frequency. Finally, for the low-pass birdcage, the mode with $k = N$ is the lowest frequency mode ($\omega^2_{k=N}$ = 0 rad s^{-1}) whereas, for the high-pass coil, it represents the highest frequency mode. For both structures, it is associated with a current distribution that involves only the end-rings.

The loss phenomena can be taken into account considering a resistance (R) along each leg in the circuit of Figure 2.10. Substituting in the voltage mesh equation the general currents expression $\boldsymbol{V_k}$, we obtain a relation analogous to (2.11):

$$\omega_k^2 - \omega^2 + j\omega\omega_k/Q_k = 0 \tag{2.45}$$

where the quality factor Q_k is equal to $\frac{(1/C^U+1/C^L)}{2R\omega_k\left(1-\cos\left(\frac{2\pi}{N}k\right)\right)}$.

2.3.2 Driven birdcage

Starting from the Kirchoff voltage law for the nth mesh with a driving term equal to Φ_n:

$$(s^2+2s\omega_a^2\frac{R}{1/C^U+1/C^L}+\omega_a^2)I_n-\omega_a^2\left[\left(\frac{s}{\omega_b}\right)^2+s\frac{R}{1/C^U+1/C^L}\right](I_{n+1}+I_{n-1}) = \frac{s\Phi_n}{L+2M} \tag{2.46}$$

and proceeding in the same way as for the low-pass birdcage, it is possible to write a relation that is formally the same of (2.17):

$$\boldsymbol{I} = \sum_{k=1}^{N} \frac{j\omega\langle \boldsymbol{V_k}, \boldsymbol{\Phi}\rangle}{(L+2M)\left[1-2\left(\frac{\omega_a}{\omega_b}\right)^2\cos\left(\frac{2\pi}{N}k\right)\right]\left(\omega_k^2-\omega^2+j\omega\omega_k/Q_k\right)}\boldsymbol{V}_k \tag{2.47}$$

where the eigenvalues ω_k are expressed by (2.44).
Due to the equivalence between the above equation and (2.17), all the consideration proposed in the previous chapter related to the supplied low-pass birdcage can be applied also for the high-pass coil.

2.3.3 Perturbed birdcage

The behaviour of a perturbed high-pass birdcage can be evaluated in the same way as for the low-pass birdcage. However, here, the mutual inductances can not be neglected. In fact, since in the circuital model of the highpass coil (Figure 2.10) the only element on the legs is the mutual inductance, the system would result in N independent equations if the mutual inductances are replaced by short-circuits. In other words, the coil would consist of N independent meshes with the consequence of N degenerate eigenfrequencies equal to ω_a^2 (the square of the resonance frequency of each mesh) making the discussion meaningless.
Furthermore, the computations reported below, are useful to show that the results obtained for the perturbed high-pass coil are similar to those obtained for the perturbed low-pass coil even if the approximation of neglecting the mutual inductances has been removed.

Without loss of generality[9], let $1/C^U + 1/C^L = 1/C$ perturbed in such a way that the Kirchoff voltage mesh equation related to the perturbed mesh n becomes:

$$(s^2 + (1-\delta)\omega_a^2)I_n - \omega_a^2\left[\left(\frac{s}{\omega_b}\right)^2\right](I_{n+1} + I_{n-1}) = 0 \tag{2.48}$$

Considering the whole set of equations related to the N meshes, it is possible to define the perturbation matrix $\widetilde{\mathbb{A}}$ whose entry $\widetilde{\mathbb{A}}_{pq}$ is:

$$\widetilde{\mathbb{A}}_{pq} = \begin{cases} 0 & \text{if } q \neq n \\ -\omega_a^2 \frac{1}{N} \sum_{i=1}^{N} \frac{e^{j\frac{2\pi}{N}i(p-n)}}{1-\left(\frac{\omega_a}{\omega_b}\right)^2\left(e^{j\frac{2\pi}{N}i}+e^{-j\frac{2\pi}{N}i}\right)} & \text{if } q = n \end{cases} \tag{2.49}$$

Following Appendix B it is possible to write the 2×2 $\mathbb{W}$ matrix (see (B.13)) as:

$$\mathbb{W} = -\frac{1}{N}\omega_a^2 \frac{1}{1-\left(\frac{\omega_a}{\omega_b}\right)^2\left(e^{j\frac{2\pi}{N}} + e^{-j\frac{2\pi}{N}}\right)} \begin{pmatrix} 1 & e^{j2n\frac{2\pi}{N}} \\ e^{-j2n\frac{2\pi}{N}} & 1 \end{pmatrix} \tag{2.50}$$

---

[9] Since the capacitances belonging to opposite ring segments share the same mesh current, any dissymmetric perturbation of C^U and C^L can be reconducted to a symmetric one.

Considering the Nth capacitors to be perturbed (*i.e* $n{=}N$ in (2.50)) the eigenvalues $\widetilde{\omega}^2_{1,2}$ of $\mathbb{W}$ become:

$$\widetilde{\omega}_1^2 = 0 \tag{2.51a}$$

$$\widetilde{\omega}_2^2 = \frac{-2\omega_1^2}{N} \tag{2.51b}$$

It follows that the perturbed fundamental modes eigenvalues ${\omega^2}^P_{1,2}$ of the perturbed system matrix will be expressed as:

$${\omega^2}^P_1 = \omega_1^2 + \widetilde{\omega}_1^2 = \omega_1^2 \tag{2.52a}$$

$${\omega^2}^P_2 = \omega_1^2 + \widetilde{\omega}_2^2 = \omega_1^2 - \delta\frac{2\omega_1^2}{N} \tag{2.52b}$$

which is exactly the same expression of (2.32) where, now, ω_1^2 is expressed by (2.44) with k=1. The normalized eigenvectors of $\mathbb{W}$ evaluated for the Nth perturbed capacitors, are:

$$\beta_1 = \frac{1}{\sqrt{2}}\begin{pmatrix} 1 \\ -1 \end{pmatrix} \tag{2.53a}$$

$$\beta_2 = \frac{1}{\sqrt{2}}\begin{pmatrix} 1 \\ 1 \end{pmatrix} \tag{2.53b}$$

The perturbed eigenvectors $\boldsymbol{V}^{\boldsymbol{P}}_{\boldsymbol{1,2}}$ become:

$$\boldsymbol{V}_{\boldsymbol{1}}^{\boldsymbol{P}} = \frac{1}{\sqrt{2}}\left(\boldsymbol{V}_{\boldsymbol{1}} - \boldsymbol{V}_{\boldsymbol{N-1}}\right) + \delta\widetilde{\boldsymbol{V}_{\boldsymbol{1}}} \tag{2.54a}$$

$$\boldsymbol{V}_{\boldsymbol{2}}^{\boldsymbol{P}} = \frac{1}{\sqrt{2}}\left(\boldsymbol{V}_{\boldsymbol{1}} + \boldsymbol{V}_{\boldsymbol{N-1}}\right) + \delta\widetilde{\boldsymbol{V}_{\boldsymbol{2}}} \tag{2.54b}$$

where:

$$\widetilde{\boldsymbol{V}_{\boldsymbol{1}}} = \sum_{\substack{k\in IN \\ 1<k\leq N, k\neq N-1}} \frac{1}{\sqrt{2}} \frac{\boldsymbol{V}_{\boldsymbol{k}}^{\dagger}\widetilde{\mathbb{A}}\left(\boldsymbol{V}_{\boldsymbol{1}} - \boldsymbol{V}_{\boldsymbol{N-1}}\right)}{\omega^2 - \omega_k^2}\boldsymbol{V}_{\boldsymbol{k}} \tag{2.55a}$$

$$\widetilde{\boldsymbol{V}_{\boldsymbol{2}}} = \sum_{\substack{k\in IN \\ 1<k\leq N, k\neq N-1}} \frac{1}{\sqrt{2}} \frac{\boldsymbol{V}_{\boldsymbol{k}}^{\dagger}\widetilde{\mathbb{A}}\left(\boldsymbol{V}_{\boldsymbol{1}} + \boldsymbol{V}_{\boldsymbol{N-1}}\right)}{\omega^2 - \omega_k^2}\boldsymbol{V}_{\boldsymbol{k}} \tag{2.55b}$$

By means of a direct calculation, it can be obtained that the perturbation coefficient $\widetilde{\boldsymbol{V}_{\boldsymbol{1}}}$ is equal to zero and $\boldsymbol{V}_{\boldsymbol{1}}^{\boldsymbol{P}}$ becomes:

$$\boldsymbol{V}_{\boldsymbol{1}}^{\boldsymbol{P}} = \frac{1}{\sqrt{2}}\left(\boldsymbol{V}_{\boldsymbol{1}} - \boldsymbol{V}_{\boldsymbol{N-1}}\right) \tag{2.56}$$

Again, as for the low-pass birdcage, we notice that the perturbed structure shares one of the two eigenvalues (ω^{2P}_{1}) and eigenvectors $(\boldsymbol{V}_{\boldsymbol{1}}^{\boldsymbol{P}})$ with the unperturbed birdcage.
An explicit computation of the perturbed eigenvectors (2.54) gives the expressions for the admissible nth mesh currents:

$$I_n = \frac{1}{\sqrt{2N}}\left(e^{\frac{j2\pi}{N}n} - e^{-\frac{j2\pi}{N}n}\right) \qquad \text{(for } \boldsymbol{V}_{\boldsymbol{1}}^{\boldsymbol{P}}\text{)} \tag{2.57a}$$

$$I_n = \frac{1}{\sqrt{2N}}\left(e^{\frac{j2\pi}{N}n} + e^{-\frac{j2\pi}{N}n}\right) + \delta\widetilde{\boldsymbol{V}}_{\boldsymbol{2}n} \qquad \text{(for } \boldsymbol{V}_{\boldsymbol{2}}^{\boldsymbol{P}}\text{)} \tag{2.57b}$$

The associated leg currents can be obtained as:

$$\mathcal{I}_n = I_n - I_{n+1} = -2\sqrt{2}j\sqrt{\frac{1}{N}}\sin\left(\frac{\pi}{N}\right)\cos\left(\frac{\pi}{N}(2n+1)\right) \qquad \text{(for } \boldsymbol{V}_{\boldsymbol{1}}^{\boldsymbol{P}}\text{)} \tag{2.58a}$$

$$\mathcal{I}_n = I_n - I_{n+1} = 2\sqrt{2}\sqrt{\frac{1}{N}}\sin\left(\frac{\pi}{N}\right)\sin\left(\frac{\pi}{N}(2n+1)\right) + \delta(\widetilde{\boldsymbol{V}}_{\boldsymbol{2}n} - \widetilde{\boldsymbol{V}}_{\boldsymbol{2}n+1}) \qquad \text{(for } \boldsymbol{V}_{\boldsymbol{2}}^{\boldsymbol{P}}\text{)} \tag{2.58b}$$

As for the low-pass coil case, both modes preserve a sinusoidal shape (neglecting the term multiplied by δ for $\boldsymbol{V}_{\boldsymbol{2}}^{\boldsymbol{P}}$). Figure 2.11 shows the leg currents $\mathcal{I}_n$ for the normalized perturbed eigenvector $\boldsymbol{V}_{\boldsymbol{2}}^{\boldsymbol{P}}$.

2.3.4 Driven perturbed birdcage

The same procedure applied for the low-pass coil, lead to an expression analogous to (2.41). Again, inverting the matrix α evaluated for the high-pass birdcage, it is possible to obtain the coefficients λ and to compute the leg currents induced in the coil by a mesh voltage distribution $\boldsymbol{\Phi}$.

The results proposed in this section are obtained considering the parameters reported in Table 2.2. Such parameters lead to a fundamental unperturbed resonance frequency equal to 128.06 MHz. Let us consider the driving set-ups depicted in Figure 2.12. Since, for an high-pass birdcage, the capacitors are not placed on the legs, we chose to examine the set-ups where the electromotive forces are applied by the coupling coils directly to the meshes. In Figure 2.12a the voltage is applied to the Nth perturbed mesh and in Figure 2.12b to a mesh that is placed $\pi/2$ from the perturbed one.

Figure 2.13 represents the leg currents generated by the driving scheme of Figure 2.12a. The currents distribution is influenced by the value of δ causing the real part of the leg currents distribution to decrease as soon as the perturbation increases (Figure 2.13a). As regards the imaginary part, it increases for small perturbation and starts to decrease for bigger δ values (Figure 2.13b). As highlighted for the low-pass coil, this evolution represents the typical behavior of an RLC series resonant circuit. It is worth

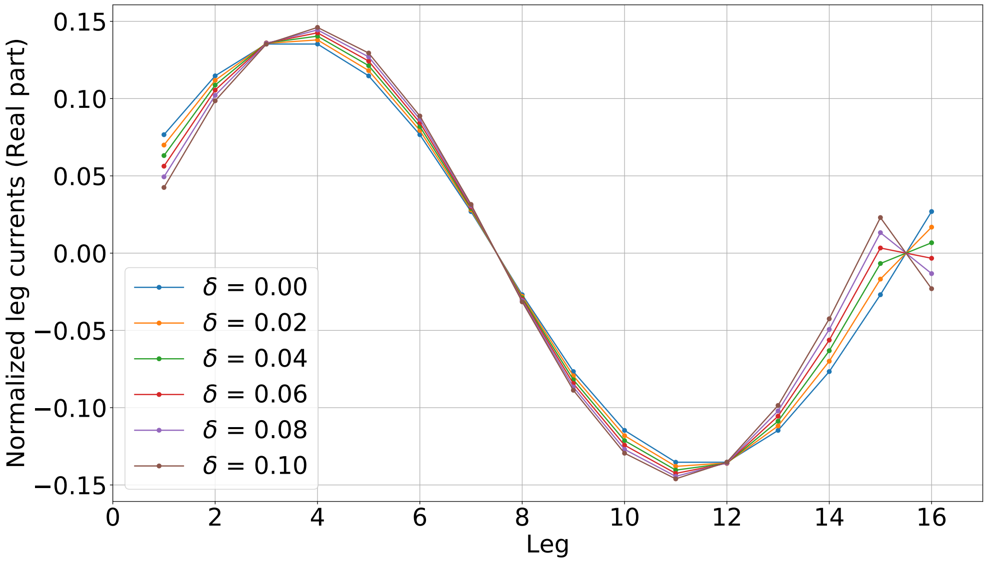

Figure 2.11: Real part of the acceptable leg currents obtained from the normalized $\boldsymbol{V_2^P}$ eigenvector evaluated for a 16-leg high-pass birdcage. The imaginary part is zero on all legs.

Table 2.2: High-pass birdcage parameters considered in the evaluation of the leg and mesh currents generated by the considered driven conditions. The listed parameters are described in section 2.3.1.

Parameter	Value
C	14.7 pF
L	100 nH
M	33 nH
R	1 Ω

noting that the non-sinusoidal distribution of the imaginary part of the leg currents is appreciable in the unperturbed condition and it is due to the presence of the supply applied to the mesh between the Nth and $N - 1$th legs.
A different conditions is met if the coil is driven as represented in Figure 2.12b. In this case the leg currents distribution is not influenced by the capacitors perturbation (Figure 2.14).

The considerations proposed for the low-pass birdcage about the magnetic field polarization in a quadrature operation mode, are still valid. In particular, it results that the sensitivity of the currents distribution to the perturbation results to be muffled when

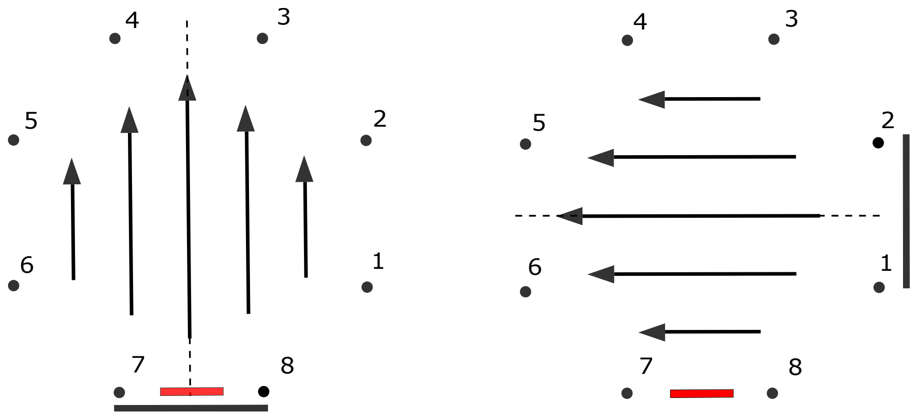

(a) *Supply voltage for the Nth mesh.* (b) *Supply voltage for the $N/4$th mesh.*

Figure 2.12: Two different supply schemes for 8-leg birdcage where the Nth leg (identified by the red thick line) capacitors have been perturbed. The black dots represent the legs, the arrows represent the unperturbed magnetic field direction and the dashed line identify its polarization plane. The thick line represents the coupling coil responsible for the supply.

the driving set-up leads to a zero current on the perturbed mesh for the unperturbed scenario. Furthermore, the presence of a non-null imaginary part of the leg current distributions for both the examined driving set-ups in the unperturbed condition, is attributable to the contribution of the off-resonance terms in (2.17). As regards the real part of the unperturbed leg currents distributions, they are not heavily influenced by the off-resonance terms.

A study of the resonance frequencies excited by mesh voltage generators can be carried out, similarly to the low-pass birdcage case, considering the mesh currents. Also in this case, R equal to 0.001 Ω has been considered to better identify the resonance peaks. Figure 2.15 shows the resonance peaks revealed by a supply voltage applied to the perturbed mesh (Figure 2.15a), to the mesh $N/4$ apart from that perturbed (Figure 2.15b) and to that $N/8$ apart (Figure 2.15c). The results are analogous to those obtained for the low-pass birdcage. A voltage applied to the perturbed mesh (Figure 2.15a), excites the mode whose frequency moves from that of the unperturbed birdcage fundamental mode by $\sqrt{(1-2\delta/N)}$ validating the results obtained in section 2.3.3. The mesh voltage applied to the mesh $N/4$ apart from that perturbed (Figure 2.15b), excites the mode whose frequency do not feel the perturbation. Finally, a mesh voltage applied to the mesh in the middle of the perturbed one and the mesh $N/4$ apart, excites both the modes.

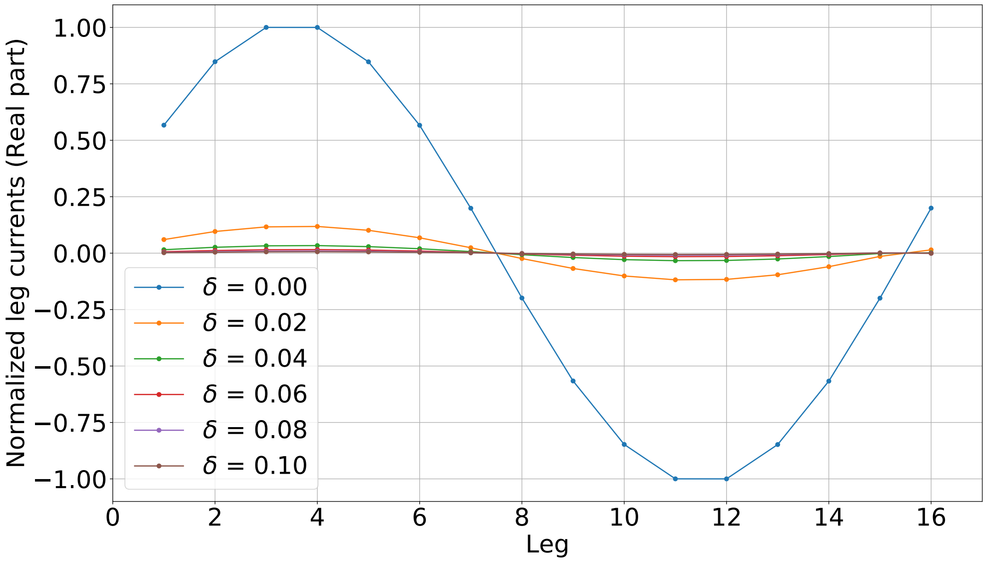

(a) *Real part of the leg currents obtained supplying a 16-leg birdcage coil on the Nth mesh.*

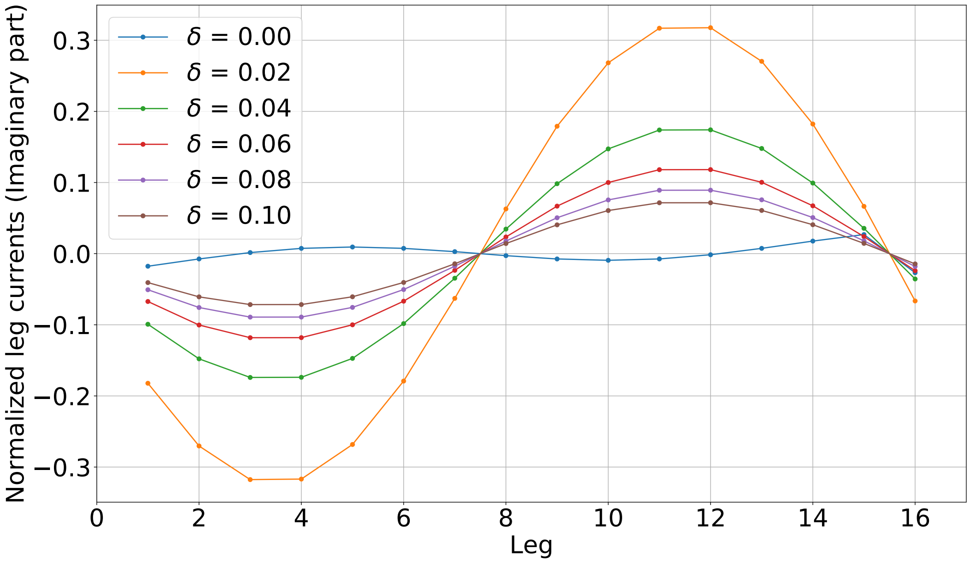

(b) *Imaginary part of the leg currents obtained supplying a 16-leg birdcage coil on the Nth mesh.*

Figure 2.13: Leg currents obtained supplying a 16-leg birdcage coil on the Nth mesh. The currents are normalized to the modulus of the maximum leg current of the unperturbed case.

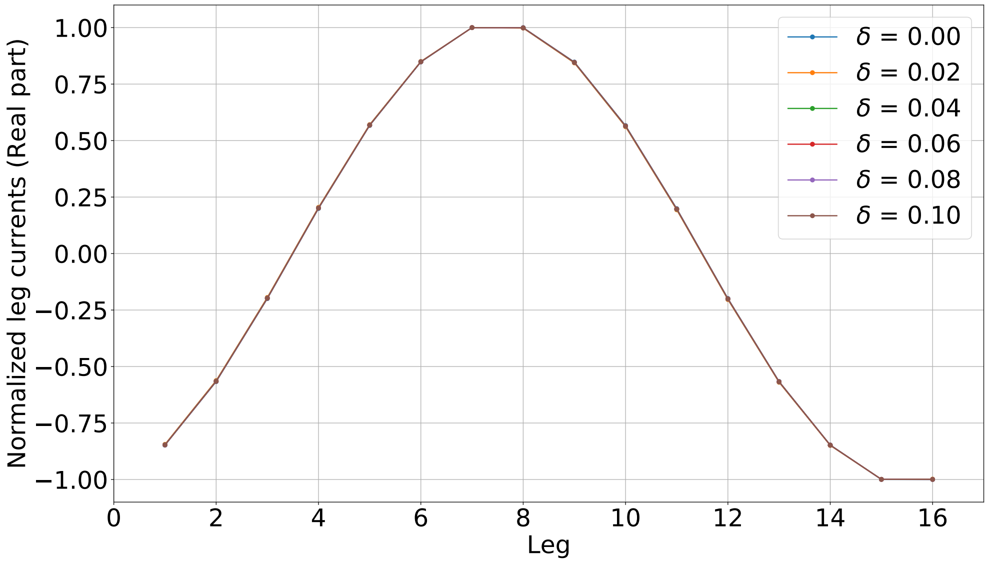

(a) *Real part of the leg currents obtained supplying a 16-leg birdcage coil on the $N/4$th mesh.*

Figure 2.14: Leg currents obtained supplying a 16-leg birdcage coil on the $N/4$th mesh. The imaginary part is negligible on all the legs. The currents are normalized to the modulus of the maximum leg current of the unperturbed case.

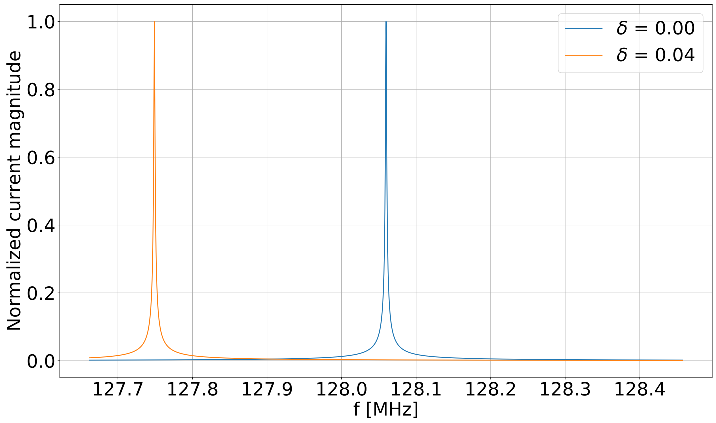

(a) *Magnitude of the Nth mesh current due to a supply voltage applied to the same mesh.*

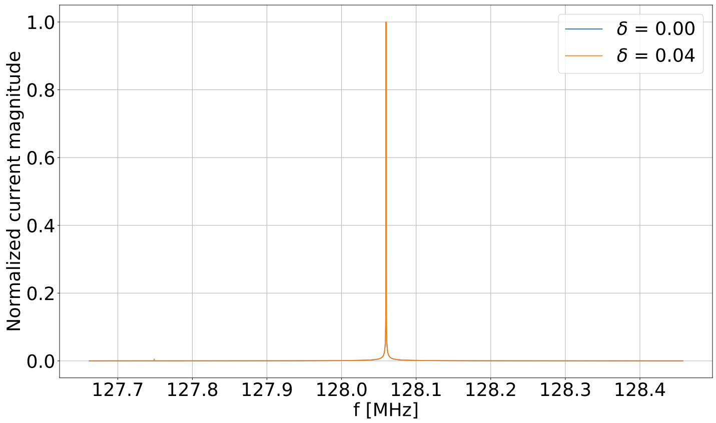

(b) *Magnitude of the $N/4$th mesh current due to a supply voltage applied to the same mesh.*

Figure 2.15: Frequency behaviour of the mesh leg current magnitude generated by a voltage applied to the same mesh. The current is normalized to its maximum value and it is reported for the unperturbed scenario and for a capacitor perturbation δ equal to 0.04 (continues on the next page).

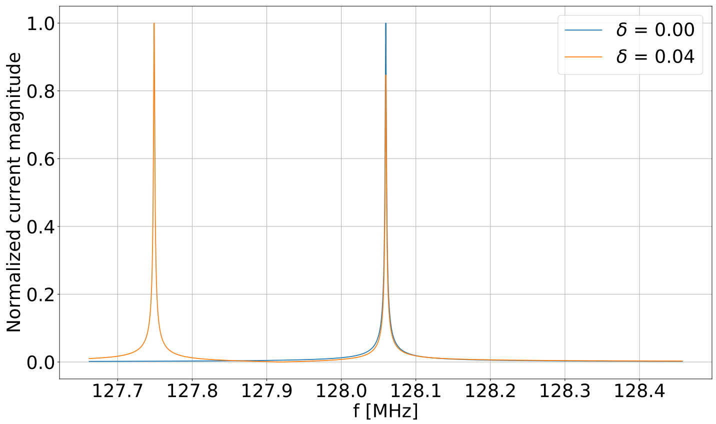

(c) *Magnitude of the $N/8$th mesh current due to a supply voltage applied to the same mesh.*

Figure 2.15: Frequency behaviour of the mesh leg current magnitude generated by a voltage applied to the same mesh. The current is normalized to its maximum value and it is reported for the unperturbed scenario and for a capacitor perturbation δ equal to 0.04.

2.4 Conclusion

On the basis of the results obtained in the previous sections, some main features can be reported together with some general remarks.

We saw that, both the structures (the low-pass and high-pass coils) possess $N/2-1$ degenerate modes and two distinguished modes representing the natural resonance frequencies of the system. Each of the $N/2-1$ modes shares two complex conjugate eigenvectors that represent possible currents distributions among the coil legs. We noticed that the current distributions are sinusoidal and can be seen as current waves with a number of full wavelengths across the coil circumference equal to the mode number k. The $k = 1$ mode is named fundamental mode and leads to the highest homogeneous magnetic field inside the coils. For the low-pass coil, the fundamental mode frequency is the lowest among the $N/2 - 1$ degenerate resonance frequencies whereas, in the high-pass coil, it is identified by the highest one. This aspect represents one of the main differences between the two different structures. A consequence of this behaviour is that the low-pass birdcage coil needs lower capacitance values than those needed by the high-pass coil. For that reason, it is typically preferred at lower operating frequencies since large values capacitors are generally lossy. On the contrary, high-pass birdcage coils are preferred at high frequency where small capacitance values would be affected by the presence of stray capacitances due to the sample. It results that, in the presence of lossy dielectric load of considerable dimensions, in a low-pass birdcage the resonance frequency will tend to be reduced due to the presence of stray capacitances in parallel with those in the coil. In an high-pass birdcage, because of a reduction of the mesh inductances, the resonance frequency tends to increase. A band-pass structure can therefore offer a reduced sensitivity to loading compensating the two effects [54].

In a dedicated section, we showed how it is possible to "stimulate" the resonating modes by means of an electromotive force induced in the structures by an external coupling coil. In particular, it has been shown that, thanks to the double degenerative behaviour of the structures, it is possible to obtain traveling currents waves along the coils circumferences leading to a circularly polarized magnetic field.

Special attention has been paid to the perturbed coil scenario. The case of a single leg (for the low-pass coil) or single mesh (for the high-pass one) perturbation has been considered. This is representative, for example, of a generic driving set-up with the voltage applied to the coil through a balancing and matching capacitive circuit. The first order perturbation theory applied to the aforementioned case, showed that the perturbation causes the degenerate eigenfrequencies to be no more degenerate. In particular, one of them changes from its unperturbed value ω_1^2 to a new value ${\omega^2}_1^P = \omega_1^2(1-2\delta/N)$ highlighting an advantage to increase the number of the legs in a birdcage coil. It can be shown [55] that an identical perturbations of a leg or mesh $\pi/2$ apart from that already perturbed, would result in a perturbation of the other eigenvalue by $-2\omega_1\delta/N$ leading the eigenvalues to be again degenerate. This concept can be extended to the capacitor that is π far from that originally perturbed with the result of restoring the original coil state if it is perturbed by an opposite amount. In the case of single perturbation, whereas the eigenvector associated with the unperturbed eigenvalue still remains equal to that of the unperturbed coil, that associated with the perturbed eigenvalue will not.

The perturbation has several implications on the relation between the leg currents distribution and the supply set-up. We showed that the sensitivity of this distribution to the perturbation δ is strongly related to the driving strategy and position relative to the perturbed capacitor. Furthemore, the analysis of the resonance frequencies excited with different supply strategies, confirmed the results obtained from the first order perturbation theory and experimentally by Tropp [55]. Finally, the single capacitor perturbation theory can be generalized to that of an arbitrary perturbation of the coil [57]. This condition is representative of a human body that enters into the coil. Due to the coupling between the body and the coil, the birdcage results to be perturbed at every reactance leading to a detuning effects comparable, in a first order, to that analyzed in the perturbation theory.

Chapter 3

Dosimetric Experimental Set-up

3.1 Introduction

During an MRI scanning session, some of the parameters related to the RF electromagnetic field can be measured through relatively simple procedures. One such instance is represented by the global SAR. The power accepted by the transmission RF coil, together with the patient weight, is monitored to estimate the average power density deposited in the human body during an MRI exam. These parameters are accounted to limit the maximum active power supplied by the RF amplifiers according to the recommendation of International standards and guidelines [5, 58].

On the other hand, some of the relevant parameters are not straight evaluable and numerical simulations are generally adopted for their estimation. For example, the knowledge of the local SAR would require punctual electric field measurements which are obviously unfeasible inside a human body.

Finally, some parameters can be indirectly evaluated through special MR sequences. For example, the knowledge of the B_1^+ and B_1^- generated by the RF coil allows for the evaluation of parameters such as coil sensitivities (see Appendix A) or transmit efficiency (η_T) which is defined as the ratio between the clockwise rotating magnetic field strength ($|B_1^+|$) and the square root of the active power flowing through the coil (P_{acc}):

$$\eta_T = \frac{|B_1^+|}{\sqrt{P_{acc}}} \tag{3.1}$$

The importance of this information becomes even more significant with Ultra High-Field MRI where the short wavelength of the RF electromagnetic field strongly affects the MR image quality [59, 60]. For these reasons, the so-called B1-mapping sequences have been designed to achieve a quantitative estimation of the B_1^+ and B_1^- distributions [61, 62].

Whereas an experimental validation of the results obtained from numerical simulations is needed to confirm their reliability, even the quantitative evaluations obtained through the MR sequences cannot always replace electromagnetic measurements. Indeed, the complexity of the MR hardware involved in the sequences execution, together with the multi-element measurement chain, reasonably leads to uncertainty values which may be unsatisfactory for some applications.

The previous considerations highlight the importance of a dosimetric experimental set-up aimed to measure the electric and magnetic fields generated by the MR RF coils inside proper phantoms. In the present chapter, the design and realization of the dosimetric experimental set-up available at the Istituto Nazionale di Ricerca Metrologica (Torino, Italy) is described in a devoted section. The first evaluation of the set-up performance, based on the comparison between electromagnetic measurements and numerical simulation results, is described considering a self-made RF planar coil. On that occasion, an accurate measurement model has been defined to evaluate the measurement uncertainties of the system and it is reported in the following section. The same comparison has been hence performed considering a double-tuned (23Na/1H) loop coil provided by the "IMAGO7" foundation (Pisa, Italy) and specifically designed for a 7 T MRI scanner. The previously described measurement model has been considered for the relevant uncertainty budget assessment and the results are reported. Finally, the design and realization of a birdcage type volume coil, conceived to be integrated in the experimental set-up to increase its versatility, is described. Part of the activity and results described in the following sections have been previously published in [63].

3.2 Dosimetric set-up description

Figure 3.1 depicts the dosimetric set-up described in this chapter. The experimental set-up mainly consists of a generation and acquisition system. The former provides to a specific RF coil the power needed to generate electromagnetic fields inside a proper cylindrical phantom. The phantom is intended to mimic the presence of the human body and it is filled with a tissue-simulating liquid (TSL) whose electric properties are comparable to those of some human tissues. The acquisition system is employed to measure the electric and magnetic field inside the phantom. The electromagnetic fields are measured through suitable electric and magnetic field probes whose accurate position is guaranteed by a 3-axial automatic positioning system (gantry) with a spatial movement resolution equal to 1 mm.

Both the RF coil and the cylindrical phantom are held up by a dielectric support whose low-permittivity material does not introduce significative interfererences (if compared to the employed electromagnetic field probes accuracy) to the electromagnetic fields generated by the RF coil. Both the measurement and generation processes are handled through a specifically designed GUI (Graphical User Interface) management software. The software, developed through the so-called "python-QT" bindings, controls the gantry movement inside the measurement area allowing for different measuring paths.

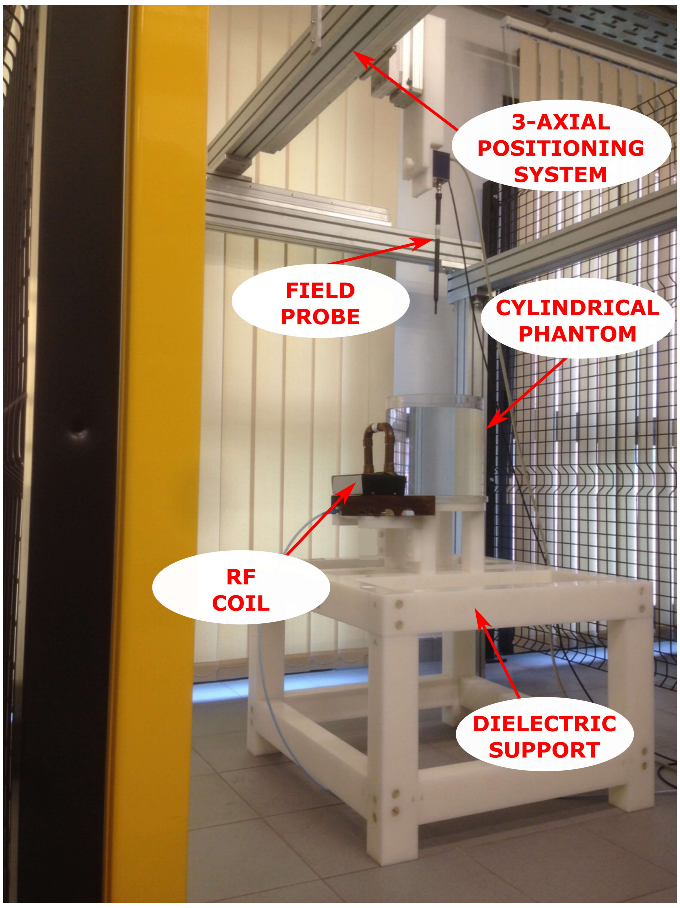

Figure 3.1: View of the dosimetric experimental set-up at the Istituto Nazionale di Ricerca Metrologica laboratory.

3.2.1 Acquisition system

Due to the reduced distance between the RF coil and the measurement area (compared with the wavelengths at the considered frequencies), the electromagnetic field acquisitions are performed in the near-field region where the spatial gradient of the field is expected to be significantly large. For this reason, RMS isotropic RF field probes with very high spatial resolution have been chosen [64].

The main components of the acquisition system are shown in Figure 3.2. The remote unit (Figure 3.2a) is connected to the Data Acquisition Electronics (DAE) (Figure 3.2b) through an optical cable. The optical fiber guarantees very low signal losses without significantly perturb or being influenced by the electromagnetic field generated by the RF sources. The E-field and H-field probes (Figure 3.2c) are directly connected to the DAE which performs the necessary electro-optic conversion to deliver the information from the probes to the remote unit. Finally, the remote unit is connected to the PC by means of a LAN cable to manage the measurement procedures through the designed

(a) “EASY4” Remote Unit.

(b) Data Acquisition Electronics “DAE”.

(c) RMS isotropic electromagnetic field probes. The above probe allows for magnetic field measurements both in air and inside the TSL. The bottom probe allows for electric field measurements in air whereas the middle one is specifically designed for electric field measurements inside the TSL.

Figure 3.2: Exposure Acquisition System (EASY4) employed for the electromagnetic field measurements and provided by SPEAG.

GUI management software.

Being the field-sensitive elements placed in the probe tips, the overall length of the probes is necessary to decouple the effects of the DAE on the measurements. The probes are covered with a black opaque PEEK (polyetheretherketone) coating allowing for their employment inside the TSL. Since the magnetic properties of the TSL correspond to those of air (within a tollerance equal to $-10\,\mathrm{ppm}$ being water-based), the same magnetic field probe can be employed for measurements in both media. Differently, the electric properties of the TSL require the use of a specific probe for electric field measurements inside it. For that reason, two different electric field probes are employed for measurements in air and inside the phantom.

The main features of the electromagnetic field probes are reported in Table 3.1. All

Table 3.1: RMS isotropic electromagnetic field probes features.

	E-Field Air probe	E-Field TSL probe	H-Field probe
Frequency range	20 MHz - 6 GHz	10 MHz - 6 GHz	20 MHz - 3 GHz
Dynamic range	2 V/m - 1000 V/m	5 V/m - 470 V/m	0.01 A/m - 5 A/m
Directivity	$< \pm 0.3$ dB	$< \pm 0.3$ dB	$< \pm 0.2$ dB

Table 3.2: Power supply equipment.

Instrument	Manufacturer	Model	Main characteristics
RF vector signal generator	Rhode&Schwarz	SMW200A	100 kHz - 3 GHz
RF amplifier	Bonn Elektronik	BSA 0110	100 kHz - 400 MHz $P_{MAX} = 100$ W
Bidirectional coupler	Bonn Elektronik	BDC 0125 40-250	9 kHz - 250 MHz *Coupling* = 40 dB *Directivity* = 20 dB
Power meter	Rhode&Schwarz	NRP-Z51	DC - 18 GHz -35 dBm - 20 dBm

the probes have been tested beforehand in a 50 TEM-cell, available at INRIM, to check their reliability up to 128 MHz for some field values of the calibration curves provided by the manufacturer.

3.2.2 Power supply system

The power supply equipment consists of a “Rhode&Schwarz SMW200A” RF dual-channel vector signal generator (Figure 3.3a) whose signal is amplified through a “Bonn Elektronik BSA 0110” RF amplifier (Figure 3.3b). Both the amplitude and phase of the two signals from the generator can be regulated separately to allow for a coil quadrature operation if needed. A “Bonn Elektronik DC 0125 40-250” bidirectional coupler (Figure 3.3c) is employed, together with two “Rhode&Schwarz NRP-Z51” USB power meters (Figure 3.3d), to measure the incident and reflected power at an RF coil port. All the instruments are connected through a GPIB-USB cable to the PC in order to be directly handled through the management software.

The complete list of the instruments devoted to the RF coil power supply is proposed in Table 3.2 together with their main features.

(a) “Rhode&Schwarz SMW200A” RF dual-channel vector signal generator.

(b) “Bonn Elektronik BSA 0110” RF amplifier.

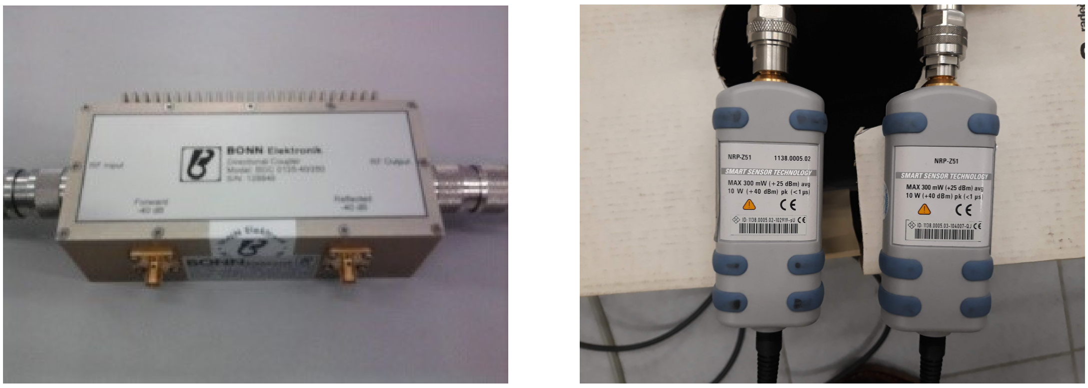

(c) “Bonn Elektronik DC 0125 40-250” bidirectional coupler.

(d) “Rhode&Schwarz NRP-Z51” USB power meters.

Figure 3.3: Power supply equipment employed in the experimental dosimetric set-up.

3.2.3 Phantom and Tissue-simulating liquid

In order to mimic the presence of human tissues, a cylindrical phantom is used (Figure 3.4). The phantom consists of a polymethylmethacrylate cylindrical vessel with a diameter and height equal to 240 mm and thickness equal to 3 mm. The low relative permittivity of the polymethylmethacrylate (2.2) guarantees a negligible effect of the vessel on the electric field generated by the RF coil (if compared to the electromagnetic field probes accuracy). The vessel is filled with a tissue-simulating liquid (TSL) prepared and characterized by SPEAG [65]. The liquid has been prepared following the “ISO/TS 10974” reference standard and it is made of a mixture of water and salt. The electrical properties of the TSL have been tested from 64 MHz to 128 MHz by the manufacturer resulting in a declared 0.47 $\mathrm{S\,m^{-1}}$ electrical conductivity and 78 electric permittivity.
Local SAR evaluations can be obtained from the electric field measurements considering the TSL mass density equal to 1024 $\mathrm{kg/m^3}$.

Figure 3.4: Cylindrical phantom employed in the experimental dosimetric set-up.

3.3 Experimental set-up validation

A preliminary validation of the dosimetric experimental set-up has been achieved at 128 MHz employing a self-made RF shielded loop named "Hydro". The loop is shown in Figure 3.5a and consists of a metallic shield which envelops an inner conductor in a coaxial cable fashion. The shield is divided in two parts by a gap to allow for electromagnetic field radiation and it is welded to the inner conductor at one side of the loop (see Figure 3.5b). The 150 mm × 150 mm loop is placed on the dielectric support with its base in contact with the phantom (see Figure 3.6). The loop has been connected to the power supply system through a BNC connector and it has been supplied with an incident power equal to 15.8 W.

The electromagnetic field measurements have been carried out inside the TSL along four vertical lines. A set of 37 acquisitions, 5 mm spaced, has been performed for each 180 mm length line. In Figure 3.6 a sketch of the relevant measurement set-up is reported. The measurement lines have been selected to highlight the effects of the coil geometry on the electromagnetic fields generated. Furthermore, the chosen measurement lines were close enough to the source to reach detectable field levels even with the limited RF power available from the RF amplifier. To avoid any interference, the stepper motor of the gantry has been stopped and turned off before each acquisition. Thanks

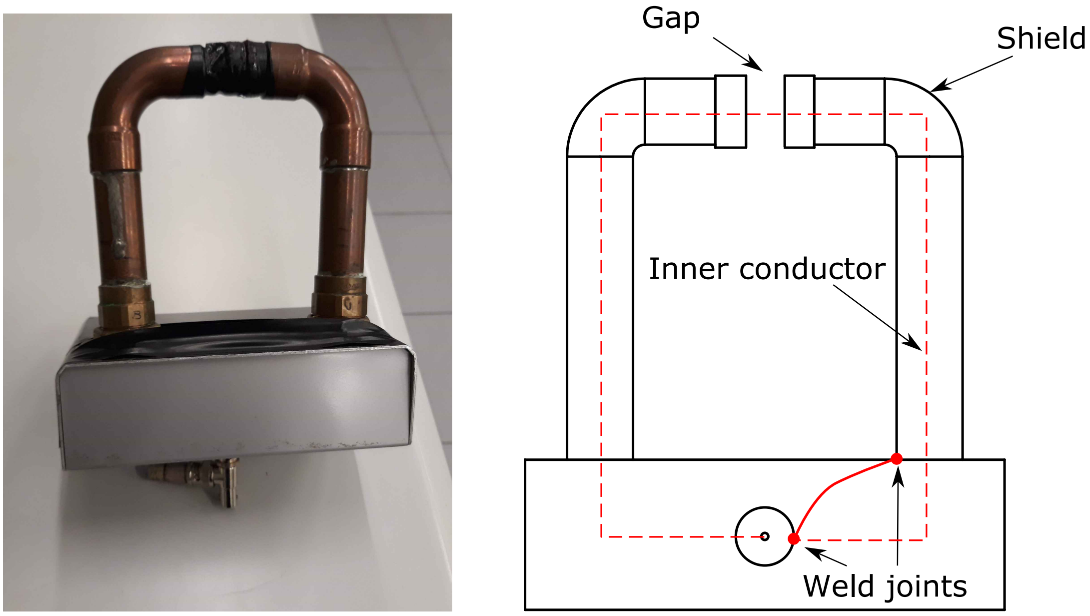

(a) RF loop picture.

(b) RF loop qualitative drawing.

Figure 3.5: “Hydro” RF shielded loop employed for the preliminary set-up validation.

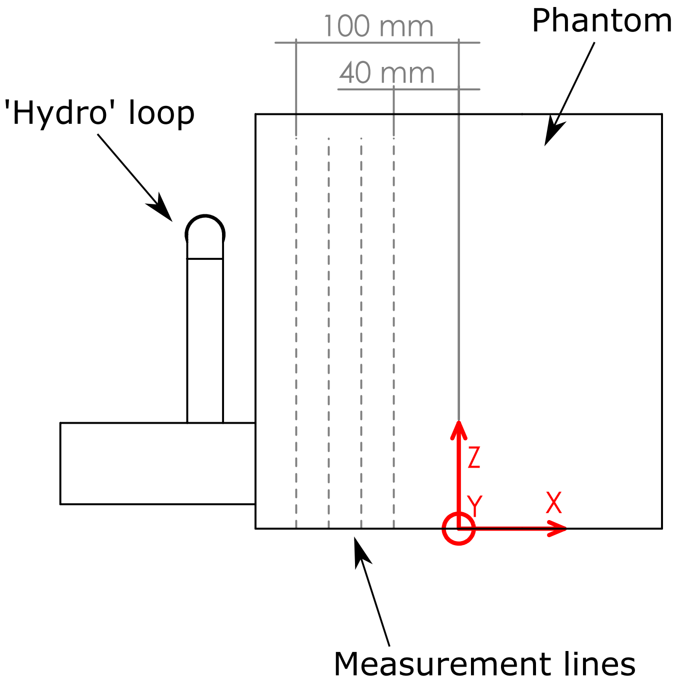

Figure 3.6: Reference coordinate system and measurement lines (dashed lines) considered in the experimental activity.

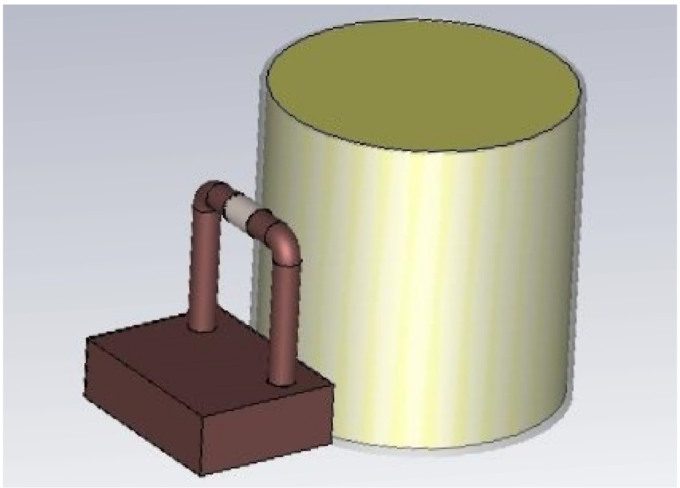

Figure 3.7: Simulation set-up involving "Hydro" and the cylindrical phantom.

to the designed management software, every set of measurements lasted no more than five minutes.

The experimental results have been compared with those obtained through numerical electromagnetic simulations. The simulations have been performed with the frequency domain solver of CST Microwave Studio® (a solver based on the finite element method). Once the physical set-up has been properly modeled in the simulation environment (Figure 3.7), the same lines used for the measurements have been considered for the simulation results extraction. The square root of the average incident power, measured for each line, has been used to rescale the corresponding simulation results.

In Figure 3.8, the results are shown for the nearest "Hydro" line (*i.e.* the line 100 mm far from the phantom centre and named "line-100") and for the furthest one (*i.e.* the line 40 mm far from the phantom centre and named "line-40"). The xy-component of the magnetic field (which is responsible for the spin excitation in MRI) is considered in Figures 3.8a, 3.8c. For completeness, the z-component of the magnetic field is proposed in Figures 3.8b, 3.8d. Finally, the magnitude of the electric field (*i.e.* local SAR) is shown in Figures 3.8e, 3.8f.

The numerical simulations generally led to results which are quite comparable with the experimental measurements for all the considered cases. In particular, the numerical results generally lie within the range defined by the measurement expanded uncertainty. To highlight the influence that the "Hydro" inner conductor shape has on the magnetic field at close distances, in Figures 3.8a, 3.8b and 3.8e two different blend radii (*i.e.* radii of curvature) are considered to represent the conductor path in correspondance of its upper angles in the simulations. Indeed, in "Hydro" the external shield hides the internal conductor making an evaluation of its actual path unfeasible. The blue and red lines represent the results obtained for a blend radius equal to 15 mm and 5 mm respectively. In Figure 3.8a the smaller radius improves the comparability between numerical and experimental results. However, a small opposite effect is shown by the z-component of the magnetic field (Figure 3.8b). As expected, the difference between the numerical results obtained assuming two different radii decreases as soon as the distance from the RF coil increases. Since the results related to line-40 are not significantly affected by the choosen conductor blend radius, they are presented only for the 15 mm one. In Figure 3.8a, a little discrepance between the two curves is appreciable along "line-100" at low z values with a maximum deviation equal to 33 %. This is likely due to model inaccuracies and should be studied further. As regards the electric field results, the smaller blend radius improves the curves similarity along "line-100" (Figure 3.8e) whereas the optimum agreement of the curves in Figure 3.8f suggests the overall accuracy of the model. Finally, it is worth mentioning that, all the numerical results presented in Figure 3.8 have been obtained considering, in the simulations, a more realistic TSL level (estimated considering the amount of TSL available for the relevant measurements) inside the phantom equal to 95 % of its whole capacity. The simulation results are significantly influenced by the level of the TSL and a fully filled phantom, as that simulated in [63], may represent a too strong approximation.

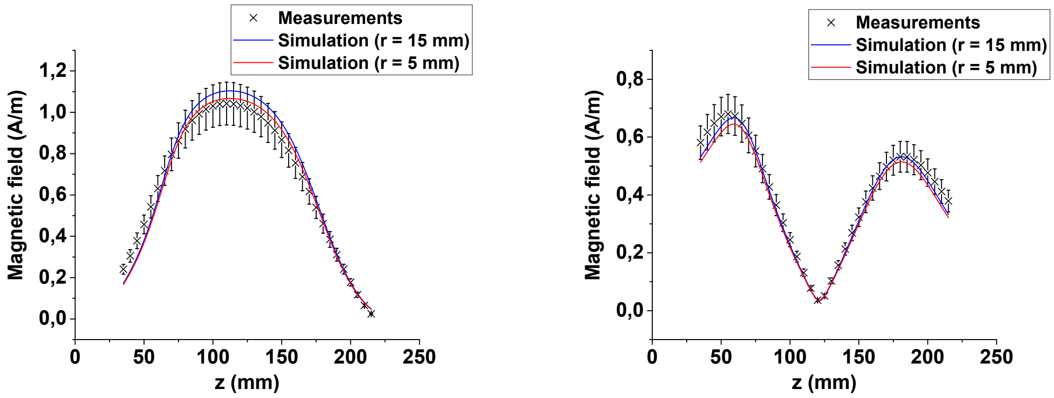

(a) Line-100: Magnetic field *xy*-component.

(b) Line-100: Magnetic field *z*-component.

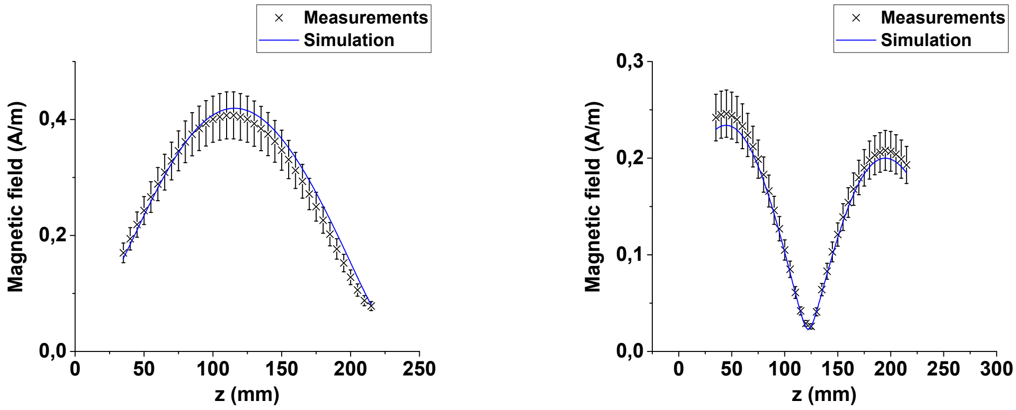

(c) Line-40: Magnetic field *xy*-component.

(d) Line-40: Magnetic field *z*-component.

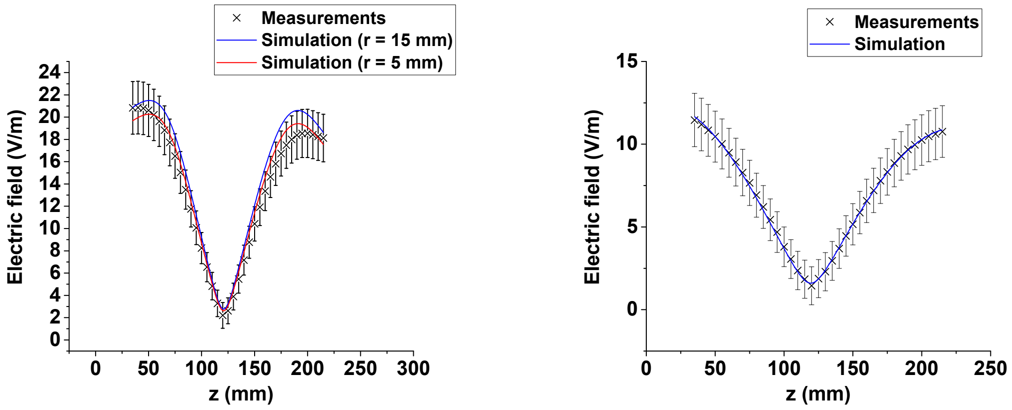

(e) Line-100: Electric field magnitude.

(f) Line-40: Electric field magnitude.

Figure 3.8: Comparison between the experimental measurements obtained with “Hydro” and numerical simulations. The *xy*- and *z*-component of the magnetic field and the magnitude of the electric field are shown in the results. In (a), (b) and (e) two different “Hydro” inner conductor shapes are considered in the simulations.

3.3.1 Measurement uncertainties

In order to estimate the measurement uncertainties associated to the considered experimental method, an accurate measurement model has been defined. The “Hydro” loop has been employed as RF coil for all the model parameters which are computed through an experimental analysis. The considerations below are proposed with reference to the magnetic field measurements. However, the same results keep to be valid for the electric field measurements as well. The uncertainty estimation and propagation comply with the indications provided in the “Guide to the expression of uncertainty in measurement (GUM)” in sections 5 and 6 [66].

The measurement model is defined as:

$$H_{p_0,T_{liq_0},\tilde{P}} = H_{p,T_{liq},P} + C_{cal} + C_{\Delta M} + C_{\Delta T_{liq}} + C_{\Delta P(T_{ins})} \tag{3.2}$$

In (3.2):

$H_{p_0,T_{liq_0},\tilde{P}}$ represents the best estimate of the magnetic field evaluated in the target point p_0 at the expected liquid temperature T_{liq_0} and at the power $\tilde{P}$. $\tilde{P}$ is the average of the values of the incident power at the coil port during the relevant line acquisition;

$H_{p,T_{liq},P}$ represents the observed quantity, read from the instrument display, in the actual point p, at the actual liquid temperature T_{liq} and at the actual incident power P. Since a single reading has been performed for each point of acquisition, its mean value is easily defined as the reading itself (*i.e.* $H_{p,T_{liq},P}$);

C_{cal} accounts for the effects of the specific field probe calibration coefficient on the measurand. It has been evaluated that it does not contribute to systematic errors. Therefore, its estimated value has been considered to be equal to zero;

$C_{\Delta M}$ accounts for the positioning error considered as the difference between the actual acquisition position p and the target position p_0. It has been evaluated that it does not contribute to systematic errors. Therefore, its estimated value has been considered to be equal to zero;

$C_{\Delta T_{liq}}$ accounts for the effect of the difference between the actual liquid temperature T_{liq} and the expected one T_{liq_0} on its electric properties (whose values affect the simulation results). Since a TSL temperature measurement is not involved in the experimental set-up, we cannot consider any systematic effect of $C_{\Delta T_{liq}}$ on the measurand. Therefore, its estimated value has been considered to be equal to zero;

$C_{\Delta P(T_{ins})}$ accounts for the difference between the actual incident power P at the RF coil port and the average power $\tilde{P}$ considered in the simulations. Indeed, during the line acquisition process, the generator is set to provide a specific supply voltage.

> However, the real supply voltage depends, among others, on the instrument temperature T_{ins} and so does the actual incident power at the coil port. It has been evaluated that $C_{\Delta P(T_{ins})}$ does not contribute to systematic errors. Therefore, its estimated value has been considered to be equal to zero.

As prescribed by the GUM, each of the above contributions is associated with a probability density function based on the available knowledge of the quantity itself. In particular:

$H_{p,T_{liq},P}$ is affected by the uncertainty associated with the device resolution. The instrument resolution is equal to 0.001 $\mathrm{A\,m^{-1}}$ and a uniform distribution with limits $a = H_{p,T_{liq},P} - 0.0005\ \mathrm{A\,m^{-1}}$ and $b = H_{p,T_{liq},P} + 0.0005\ \mathrm{A\,m^{-1}}$ has been considered to characterize the quantity. The associated uncertainty is computed as $u(H_{p,T_{liq},P}) = (b-a)/\sqrt{12}$ and it is equal to 0.0003 $\mathrm{A\,m^{-1}}$. The relevant value for the electric field measurements has been evaluated to be equal to 0.58 $\mathrm{V\,m^{-1}}$. Its higher value also accounts for the uncertainty associated with the field noise which resulted to be influential in electric field measurements;

C_{cal} is affected by the uncertainty provided in the probe calibration certificate. The calibration factor influences the read value with a normal probability distribution characterized by a 95 % confidence interval expanded uncertainty equal to 10 % of the read field value. Therefore, the associated uncertainty is obtained as $u(C_{cal}) = (0.1/1.96)H_{p,T_{liq},P}$ and it is equal to $0.05H_{p,T_{liq},P}\ \mathrm{A\,m^{-1}}$;

$C_{\Delta M}$ does not significantly contribute to the measurand uncertainty. This resulted from a set of 100 acquisitions developed as follows. A position inside the phantom, characterized by a high spatial gradient of the relevant field, has been individuated in order to maximize the effect of the positioning on the field reading. At each acquisition the gantry has been forced to return to the origin of its axes and the quantity $H_{p,T_{liq},P}/\sqrt{P}$ has been considered in order to decrease the correlation with the effects described by $C_{\Delta P(T_{ins})}$. The standard deviation of the obtained distribution results to be negligible compared to the other uncertainty contributions;

$C_{\Delta T_{liq}}$ is affected by the uncertainty related to the actual liquid temperature T_{liq}. The controlled laboratory temperature is (24 ± 3) °C and it is foreseeable that the liquid temperature will change in the same range (21 °C to 27 °C). For such a temperature variation, the maximum field amplitude difference has been estimated to be less than 1 %. Hence, a uniform probability distribution with limits $a = -0.005H_{p,T_{liq},P}\ \mathrm{A\,m^{-1}}$ and $b = 0.005H_{p,T_{liq},P}\ \mathrm{A\,m^{-1}}$ has been considered to characterize the quantity. The associated uncertainty is obtainable as $u(C_{\Delta T_{liq}}) = (b-a)/\sqrt{12}$ and it equal to $0.003H_{p,T_{liq},P}\ \mathrm{A\,m^{-1}}$;

Table 3.3: Measurement uncertainty contributions.

Quantity	Estimate	Standard uncertainty	Probability distribution
$H_{p,T_{liq},P}$	$H_{p,T_{liq},P}\,\mathrm{A\,m^{-1}}$	$0.0003\,\mathrm{A\,m^{-1}}$	$R(a,b)$
C_{cal}	$0\,\mathrm{A\,m^{-1}}$	$0.05H_{p,T_{liq},P}\,\mathrm{A\,m^{-1}}$	$N(\mu,\sigma)$
$C_{\Delta M}$	$0\,\mathrm{A\,m^{-1}}$	$0\,\mathrm{A\,m^{-1}}$	*
$C_{\Delta T_{liq}}$	$0\,\mathrm{A\,m^{-1}}$	$0.003\,\mathrm{A\,m^{-1}}$	$R(a,b)$
$C_{\Delta P(T_{ins})}$	$0\,\mathrm{A\,m^{-1}}$	$0.006\,\mathrm{A\,m^{-1}}$	$R(a,b)$

$C_{\Delta P(T_{ins})}$ is affected by the uncertainty related to the incident power at the coil port which is statistically different from its mean value considered in the numerical simulations. The evaluation of this effect has been obtained through 80 consecutive acquisitions (corresponding to acquire two lines consecutively) without moving the probe. Considering the temperature variation of the instruments from the first to the last acquisition, the maximum difference in terms of read field amplitude has been estimated to be less than 2 %. Hence, a uniform probability distribution with limits $a = -0.01H_{p,T_{liq},P}\,\mathrm{A\,m^{-1}}$ and $b = 0.01H_{p,T_{liq},P}\,\mathrm{A\,m^{-1}}$ has been considered to characterize the quantity. The associated uncertainty is obtainable as $u(C_{\Delta P(T_{ins})}) = (b-a)/\sqrt{12}$ and it equal to $0.006H_{p,T_{liq},P}\,\mathrm{A\,m^{-1}}$.

All the uncertainty contributions described above are collected in Table 3.3. In particular, the estimate, standard uncertainty and probability distribution associated to each quantity which contributes to the $H_{p_0,T_{liq0},\tilde{P}}$ measurement uncertainty in (3.2) are reported in the table.

Since the standard deviation $u(C_{cal})$ is much larger than any other from a non-normally distributed quantity, it is possible to apply the central limit theorem in the uncertainty propagation (see section G2 of GUM [66]). It follows that, considering a coverage probability equal to 95 %, the expanded uncertainty, related to the measurand $(H_{p_0,T_{liq0},\tilde{P}})$ is:

$$U(H_{p_0,T_{liq0},\tilde{P}}) = 1.96\,u(H_{p_0,T_{liq0},\tilde{P}}) \tag{3.3}$$

3.4 Double-tuned planar coil

The same dosimetric set-up described above has been involved in the comparison between experimental measurements and numerical results employing a double-tuned planar coil (23Na/1H) provided by the IMAGO7 foundation (Pisa, Italy). The numerical results have been obtained by the IMAGO7 foundation by means of the software and CAD model they employ for the coil characterization (*i.e.* CST Microwave Studio®). In

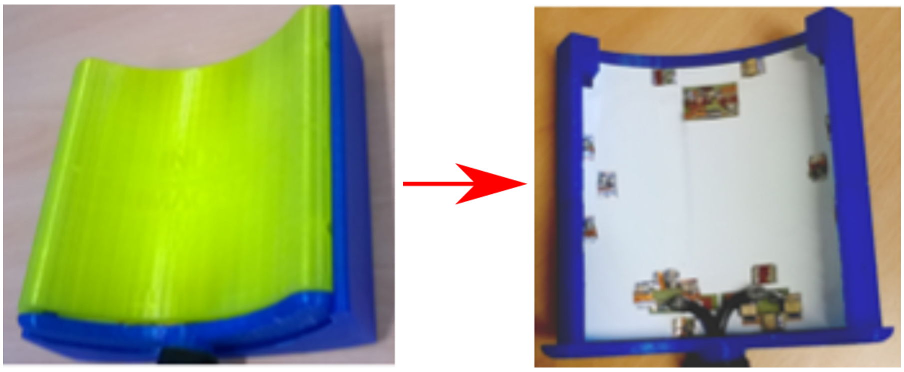

(a) Coil picture with and without the PLA cover.

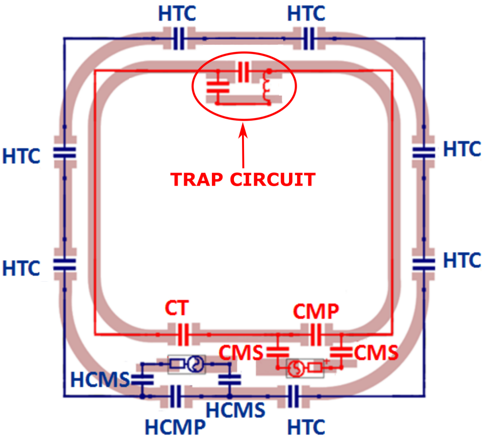

(b) Coil circuit.

Figure 3.9: IMAGO7 Double-tuned planar coil.

this context, the experimental measurements have been considered to verify the reliability of their methods.

Figure 3.9a shows a picture of the double-tuned coil considered in the present section. The coil has been designed to work in a 7 T scanner and to operate at 79 MHz (the Larmor frequency of the 23Na nuclei) and at 298 MHz (the Larmor frequency of the 1H nuclei). Both the loop angles are blended with 28 mm curvature radius. The loops are etched on an FR4 printed circuit board with 200 µm thickness and are plunged in a polylactide (PLA) thermoplastic mechanical support.
Figure 3.9b shows the electrical scheme of the coil. The inner loop (85 mm × 95 mm) is responsible for the 23Na excitation and the outer (110 mm × 110 mm) for that of the 1H nuclei. HTC and CT represent the capacitors employed for the hydrogen and sodium loop tuning respectively. For the hydrogen loop, the tuning capacitors are distributed along its diameter to account for the shorter wavelength at its Larmor frequency. HCMS and HCMP are used for the 50 hydrogen loop impedance matching whereas CMS and CMP guarantee the same matching for the sodium loop. The hydrogen loop impedance

at 79 MHz is high enough to avoid a significant coupling with the sodium coil. Unfortunately, at 298 MHz the impedance of the sodium loop presents a small value and a “trap” circuit is needed for coils decoupling. Such a circuit consists of a 298 MHz LC parallel resonator which opens the circuit of the sodium loop at its resonance frequency avoiding the coupling.

In a clinical practice, the 1H loop is used only as a “localizer”[1]. As a result, there was no practical interest to investigate its behavior in detail. Furthermore, taking into account that a TSL and measuring probes characterization was not available at 298 MHz, only the sodium loop has been considered for the electromagnetic measurements which have been carried out at 79 MHz.

Some paper tape has been used to fix the coil to the phantom being careful to maintain the loop in a vertical and central position with respect to the phantom height. The same measurement lines identified in the previous section (Figure 3.6) have been considered. Also in this case, 37 acquisitions have been carried out for each vertical line. The coil has been supplied with an incident power equal to 9.6 W.

In Figure 3.10, the same field components and lines already considered dealing with the “Hydro” loop are presented for the sodium loop.

Despite the lower incident power, higher field values (about fivefold and twofold magnetic and electric field values respectively) are observed with respect to those obtained with the “Hydro” loop (see Figure 3.8). This is explained by the 50 impedance matching which is optimized in the sodium loop whereas it has not been handled for the “Hydro” loop, considering its different purpose. Also in this case, the numerical simulation results are found to be comparable to the experimental measurements with their uncertainty intervals. A little computational overestimation of the magnetic field up to 14 % and 17 % for the xy- and z-component respectively, is observable for the “line-100” (Figures 3.10a and 3.10b). However, the magnetic field probe accuracy may be influenced, in those points, by the field values which are close to the upper limit of the probe dynamic range and a further analysis should be performed. In addition, some small disagreements (up to 15.4 %) are observed for the z-component of the magnetic field along “line-40” (Figure 3.10d) and for the electric field (up to 14.7 %) at high z coordinates in Figure3.10f. Even if additional investigations are needed, these are likely being influenced by the TSL level inside the phantom in the simulations. Indeed, the numerical results carried out by the IMAGO7 group accounted for a fully filled phantom without exploring other possible configurations. Finally, the maximum disagreements observable in Figures 3.10e and 3.10f are equal to 103 % and 132 % respectively. These stronger discrepances between the results can be attributed to the field values close to the lower limit of the electric field probe dynamic range.

---

[1] In the human body, the signal from 1H atoms is stronger than that from 23Na. For this reason, a preliminary analysis is generally performed by means of the 1H loop to identify the proper image area. When the correct placement is found, the 23Na loop is employed to obtain the required sodium image.

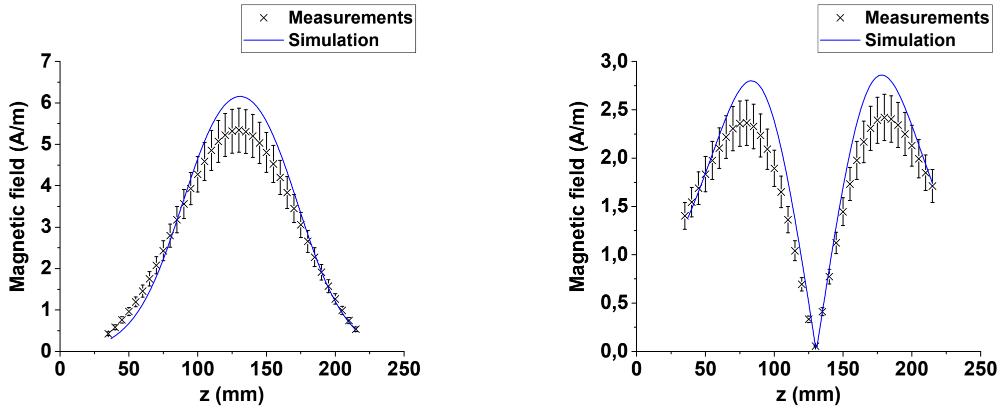

(a) Line-100: Magnetic field xy-component.

(b) Line-100: Magnetic field z-component.

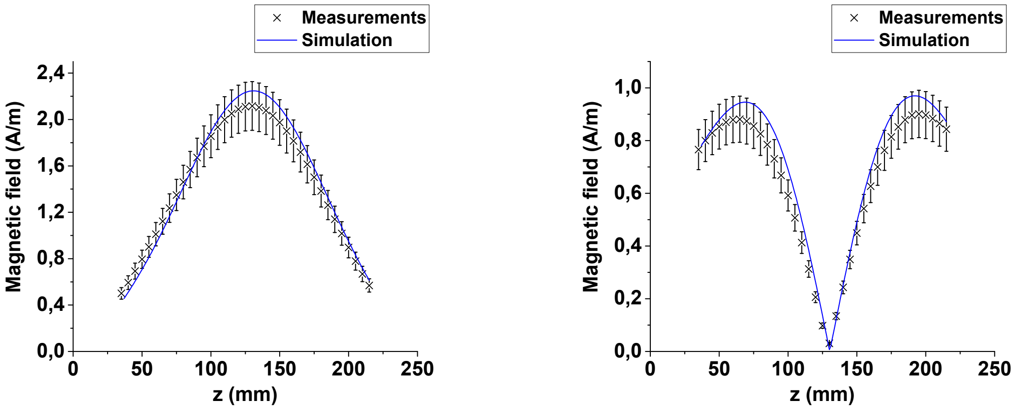

(c) Line-40: Magnetic field xy-component.

(d) Line-40: Magnetic field z-component.

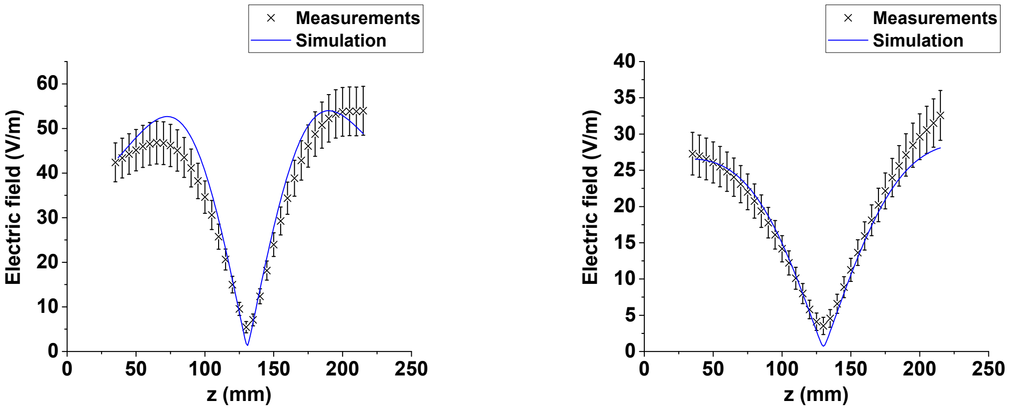

(e) Line-100: Electric field magnitude.

(f) Line-40: Electric field magnitude.

Figure 3.10: Comparison between the experimental measurements obtained with the sodium coil and numerical simulations. The xy- and z-component of the magnetic field and the magnitude of the electric field are shown in the results.

3.5 Birdcage Design

In order to increase the versatility of the experimental dosimetric set-up, the integration of a birdcage coil as an RF transmitter has been conceived. Despite the different dimensions, the coil is representative of a standard body-coil or head coil allowing for evaluations not achievable with the previously described planar loop coil “Hydro”.

The theoretical dissertation provided in chapter 2 gives a comprehensive idea about the working principles of a birdcage type volume coil. In particular, it has been shown that, in order to generate a highly homogeneous, circularly polarized magnetic field, the birdcage coil has to be tuned in such a way as to match the desired working frequency (ω) with that of the fundamental resonance mode (ω_1). To achieve such a goal, once the birdcage coil dimensions have been defined, the value of the capacitors have to be chosen accordingly. Whereas their design values should be selected basing on numerical simulations (where the full-wave Maxwell equations are solved), a first evaluation can be obtained through a lumped element equivalent circuit. However, the circuit provided in chapter 2 is too approximated to be used in the coil design process. In particular, the mutual magnetic coupling between non-adjacent meshes may be influential in determining the proper capacitor values.
Furthermore, chapter 2 does not address some practical issues such as, for example, how to proper supply the coil or how to deal with the common-mode rejection problem.

In the present section, a method proposed by Leifer [39] to obtain an analytical expression for the capacitor values is reported. In the following sub-sections, the design and realization processes of a 128 MHz resonating high-pass birdcage coil are described. The procedures described below represent a first step of the coil realization and do not account for the presence of the phantom inside the coil.

3.5.1 Design Equations

Figure 3.11 shows a section of a generic birdcage coil circuit. The mesh currents I, the mesh self-inductances L_{mesh}, the ring capacitors C_1, the leg capacitors C_2 and the mutual couplings between the generic mesh n and the meshes $n+1$ and $n+2$ are reported. Considering that, due to the birdcage circular symmetry, the flux coupling M_m between any two meshes depends only on their separation m, and defining $M_0 = L_{mesh}$ the self-inductance, the mesh current equation relative to the nth mesh leads to the following homogeneous equation:

$$-\omega^2 \sum_{m=0}^{N-1} I_{n+m} M_m + 2I_n\left(\frac{1}{C_1} + \frac{1}{C_2}\right) - \frac{1}{C_2}(I_{n+1} + I_{n-1}) = 0 \tag{3.4}$$

being ω the working frequency. Writing a similar equation for all the N meshes, it is possible to obtain the following generalized eigenvalue problem:

$$\mathbb{M}^{-1}\mathbb{E}\boldsymbol{I} = -\omega^2 \boldsymbol{I} \tag{3.5}$$

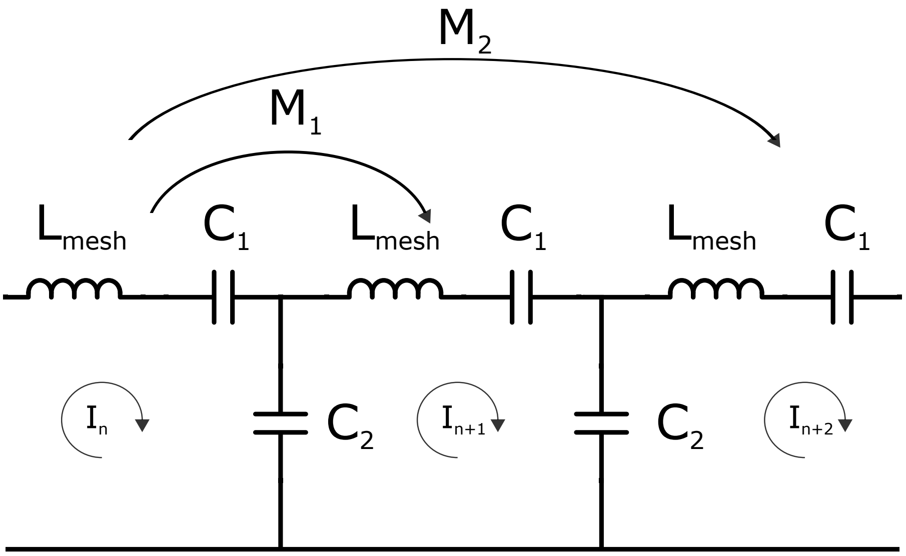

Figure 3.11: A segment of generic birdcage elementary circuit. Three among N total meshes are represented. The self-inductances L_{mesh}, the ring capacitances C_1, the legs capacitances C_2, the mesh currents I and the mutual couplings between the generic mesh n and the meshes $n+1$ and $n+2$ are reported.

where:

$\mathbb{E}$ is a $N \times N$ circulant matrix that contains the electrical coupling terms;

$\mathbb{M}$ is a $N \times N$ circulant matrix that contains the magnetic coupling terms;

$\boldsymbol{I}$ is the mesh currents N-row column vector.

Being $\mathbb{M}^{-1}\mathbb{E}$ still circulant, the ith element of its kth normalized eigenvectors $\boldsymbol{V_k}$ is:

$$(\boldsymbol{V_k})_i = \frac{1}{\sqrt{N}} e^{j\frac{2\pi}{N}ki} \tag{3.6}$$

where j is the imaginary unit. After some manipulations, it is possible to compute the eigenvalue associated with the kth eigenvector and, consequently, the expression for the kth mode resonance frequency ω_k^2:

$$\omega_k = \sqrt{2\frac{\frac{1}{C_1} + \frac{1}{C_2}\left(1 - \cos\left(\frac{2\pi k}{N}\right)\right)}{\sum_{m=1}^{N} M_m e^{-j\frac{2\pi km}{N}}}} \tag{3.7}$$

Considering (3.7), the knowledge of M_m would permit to find possible values of C_1 and C_2 that make the coil fundamental mode resonance frequency (ω_1) corresponding to the desired operating frequency.

Even if, in order to achieve a reliable evaluation of the self-inductances and mutual-inductances, a numerical analysis would be needed, analytic approximated formulas can provide, in a first instance, a satisfactory result. The use and reilability of the following relations has been investigated by Leifer [39] and their derivation is described in detail in [67].
The generic inductance term M_m can be expressed as the sum of mutual couplings between every non-orthogonal pair of conductors in the two meshes m apart:

$$M_m = 2M_{leg_m} - M_{leg_{m-1}} - M_{leg_{m+1}} + 2(M_{r_m} - M_{r'_m}) \tag{3.8}$$

where:

M_{leg_m} is the mutual inductance between two legs m apart. It represents the self-inductance for $m = 0$;

M_{r_m} is the mutual inductance between two ring sections m apart and belonging to the same ring;

$M_{r'_m}$ is the mutual inductance between two ring sections m apart and belonging to the different rings.

With some approximations, it is possible to evaluate each individual term in the previous relation. In particular, the mutual inductance between two legs can be approximated by that between two parallel filaments of length h and relative distance s:

$$M_{leg_m}(s)\Big|_{m\neq0} = \frac{\mu_0 h}{2\pi}\left[ln\left(\frac{h}{s} + \sqrt{1+\left(\frac{h}{s}\right)^2}\right) - \sqrt{1+\left(\frac{s}{h}\right)^2} + \frac{s}{h}\right] \tag{3.9}$$

that can be integrated to obtain the mutual inductance of two legs $2\pi m/N$ apart (with $m \neq 0$) with width $\delta\theta$ on a cylinder with radius r_0 (representing the birdcage radius):

$$M_{cyl_m}\Big|_{m\neq0} = \delta\theta^{-2}\int_0^{\delta\theta}\int_{2\pi m/N}^{(2\pi m/N)+\delta\theta} M_{leg_m}\left(2r_0 \sin\frac{\theta_2-\theta_1}{2}\right)d\theta_1 d\theta_2 \tag{3.10}$$

The self-inductance of a ring or leg in a single mesh can be approximated by that of a flat thin strip of length h and width w:

$$M_{leg_0}(\text{or } M_{r_0}) = \frac{\mu_0 h}{2\pi}\left(ln\frac{2h}{w} + \frac{1}{2}\right) \tag{3.11}$$

The mutual inductance between two non-adjacent ring segments can be obtained directly from Neumann's formula:

$$M_{r_m}(\text{or } M_{r'_m})\Big|_{m\neq0;m\neq1} = \frac{\mu_0 r_0 r_1}{4\pi}\int_0^{\theta}\int_{\theta'}^{\theta'+\theta}\frac{\cos(\theta_2-\theta_1)}{\sqrt{r_0^2+r_1^2-2r_0r_1cos(\theta_2-\theta_1)+s^2}}d\theta_1 d\theta_2 \tag{3.12}$$

where the ring segments are θ long, and (s, θ') distant. $r_0 = r_1$ for the unshielded birdcage (the different radii are discussed below). The mutual inductance between adjacent ring segments is approximated by that of two joined straight filaments of length $h = 2r_0 \sin(\pi/N)$ inclined at an angle $\phi = \pi - 2\pi/N$:

$$M_{r_1} = -\frac{\mu_0 h \cos\phi}{\pi} \tanh^{-1}\left[\frac{1}{1 + \sqrt{2(1-\cos\phi)}}\right] \tag{3.13}$$

Finally, the effects of an RF conducting shield surrounding the coil should be mentioned. In fact, even if its employment decreases both the field homogeneity and strength inside the birdcage volume [39, 54] , they are widely used[2] to prevent unwanted couplings between the coil and the environment. Due to magnetic couplings between the shield and the coil, the resonance frequencies increase in its presence. Indeed, the mutual inductance contributions due to the presence of the shield decrease the value of M_m in (3.8) leading to the increase of ω_k in (3.7).
To take into account the shield effects in the resonance frequencies evaluation, the image principle can be applied [68]. To do that, the shield is approximated as an infinite conductive plane in the vicinity of each conductor. This gives an image located a distance from the birdcage coil centre r_1 equal to $2r_s - r_0$, being r_s the shield radius.
The calculations for the shielded coil follow those for the unshielded one considering in (3.8) the presence of the image currents. In particular, the mutual inductance between a leg or a ring segment to its own image, is obtained, considering (3.9), through:

$$M_{imm} = w^{-2} \int_0^w \int_s^{s+w} M_{leg_m}\left(\sqrt{(x_2 - x_1)^2 + (r_1 - r_0)^2}\right) dx_2 dx_1 \tag{3.14}$$

which identifies the mutual inductance between parallel flat strips of width w where $s = r_1 - r_0$ represents their distance. Equation (3.9) is used to compute the mutual inductances with other leg images and (3.12) with other ring images, except for the images of contiguous ring segments which can be more easily expressed through (3.13) substituting r_0 with r_1 in the expression for h.

3.5.2 Birdcage coil description

A 16-leg high-pass structure has been selected for the relevant volume coil and a 128 MHz working frequency has been considered as a design constraint. The total number of legs have been choosen to guarantee a satisfying stability to perturbation (see chapter 2, section 2.3.3) still employing a reasonable number of capacitors. The adopted

---

[2] Usually, inside an MRI scanner, the body coil is shielded. However, sometimes (*e.g* to improve the transmit and receive sensitivity in a particular scanned zone) smaller local coils are used. These coils, such as the head coils, are generally not equipped with their own shield taking advantage from that of the body coil.

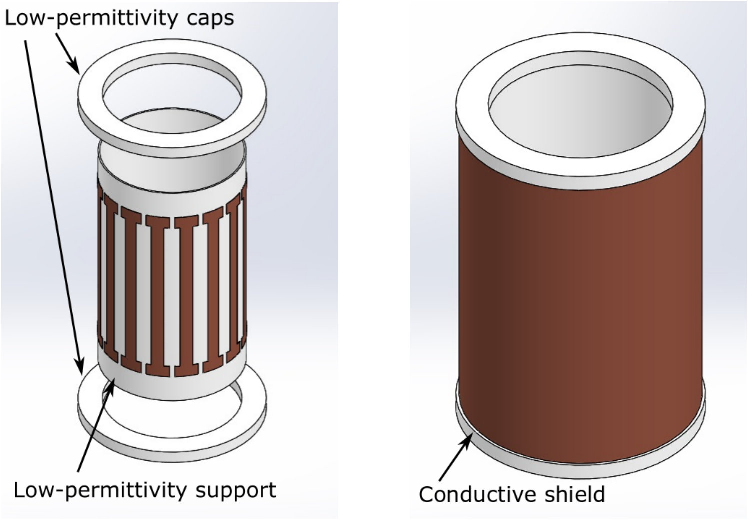

(a) 3D model of the unshielded birdcage coil.

(b) 3D model of the shielded birdcage coil.

Figure 3.12: 3D model of the designed birdcage coil. In (a) the conductive shield is not depicted to show the coil conductors. In (b) the low-permittivity caps fix the relative positions of the inner support and the shield.

structure followed from the choosen working frequency [54] which has been determined to be that typical of 3 T MRI scanner.
The birdcage coil dimensions have been decided according to the size of the phantom and the dielectric support. Indeed, the coil has been designed to be placed on the dielectric support and to allow for the phantom positioning inside its volume. Furthermore, the birdcage radius has been selected to leave enough space for electromagnetic field measurements (probe placing) even outside the phantom but inside the coil volume. Finally, a cylindrical conductive shield has been conceived to make the coil less influenced by the presence of external objects such as the measuring probes and the metallic positioning system.

A 3D model of the designed birdcage coil, developed through SolidWorks$^{\circledR}$, is depicted in Figure 3.12. In Figure 3.12a the shield is not shown to make some of the legs visible. A low-permittivity cylindrical support has been used to fix the birdcage legs position. Two removable caps, of the same low-permittivity material, have been designed to secure the legs and shield relative positions (Figure 3.12b).

The most important dimensions of the designed structure are presented in the dimensioned drawings of Figure 3.13 for the coil legs and end-rings (Figure 3.13a) and the conductive shield (Figure 3.13b).

Figure 3.14 shows the realized birdcage coil. In Figure 3.14a the shield has been removed to visualize the birdcage conductors and inner support. The conductors have

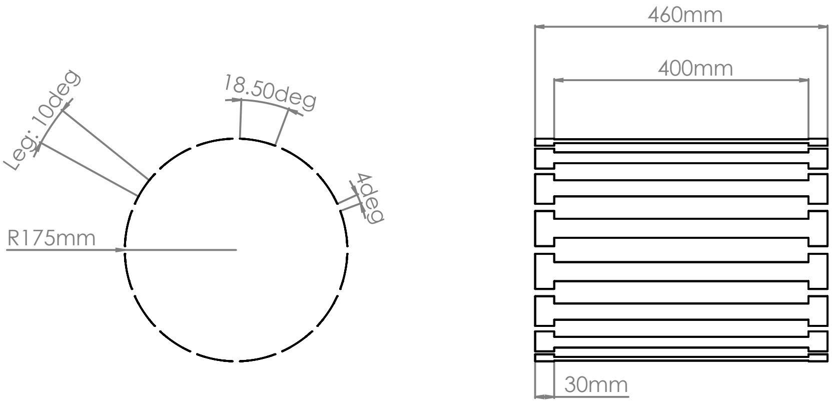

(a) Dimensioned drawing of the birdcage coil conductors.

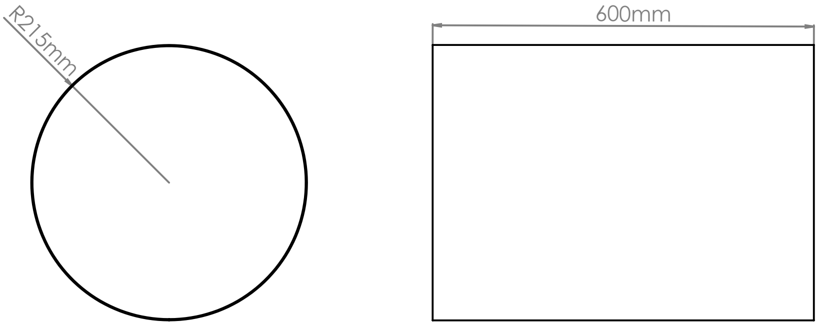

(b) Dimensioned drawing of the birdcage shield.

Figure 3.13: Dimensioned drawings of the designed birdcage volume coil.

been realized through flexible printed circuits of electrolitic copper traces whose thickness (~70 µm) is more than tenfold the skin depth at the considered working frequency. The copper traces have been insulated by means of Kapton® film except for the end-ring zones where the capacitors have to be welded and for a central leg portion. The latter has been conceived to allow for the placement of mid-leg capacitors to obtain a band-pass structure if needed (*e.g.* allowing for the working frequency increase still employing the same conductive device), and to connect the shield to the legs (see section 3.5.4).

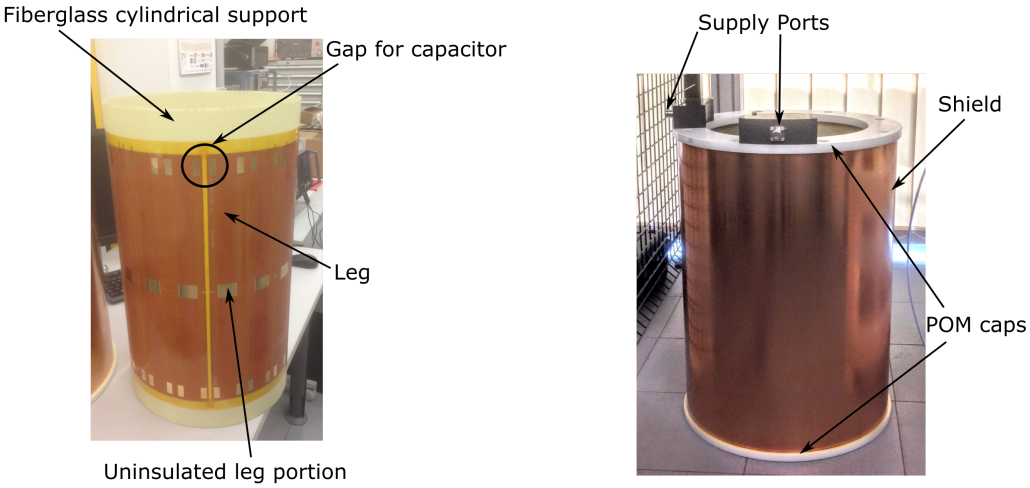

(a) Unshielded birdcage coil.

(b) Shielded birdcage coil.

Figure 3.14: Pictures of the fabricated birdcage coil. In (a) the conductive shield and fiberglass caps have been removed to allow for the legs and inner support visibility. In (b) the shield position is guaranteed by the polyoxymethylene (POM) caps.

The cylindrical support has been built in fiberglass and fixed to the polyoxymethylene (POM) caps by means of 8 fiberglass rods (not shown in Figure 3.14 to improve the legs and inner support visibility). The conductive shield is shown in Figure 3.14b and has been made by means of a 1.5 mm sheet of copper. Finally, two N-ports (panel connectors) have been provided for the coil supply. The two ports have been placed 90° apart to simplify the procedures for the coil quadrature operation. Each port has been screwed to a plastic box through metallic bolts making available a connection with the coaxial cable shield even inside the box. The boxes have been designed to contain the impedance matching circuit boards allowing for matching regulations (if needed) without removing the birdcage shield.

3.5.3 Birdcage tuning

The 3D model of Figure 3.12 has been imported into the electromagnetic simulation environment (CST Microwave Studio®) to identify the proper value of the capacitors to tune the birdcage coil at 128 MHz. Thirty-two lumped capacitors have been employed to connect the adjacent legs and a lumped port has been placed in series to one of the capacitors to evaluate the coil resonances. A 0.1 Ω resistance has been considered in series to each capacitor to help the numerical solver convergence. Both the birdcage legs and shield have been simulated as Perfect Electric Conductors (PEC) and open boundary conditions have been applied.

A first estimation of the proper capacitance value has been obtained through (3.7) imposing $1/C_2$ equal to zero for an high-pass structure. This value has been assumed in the

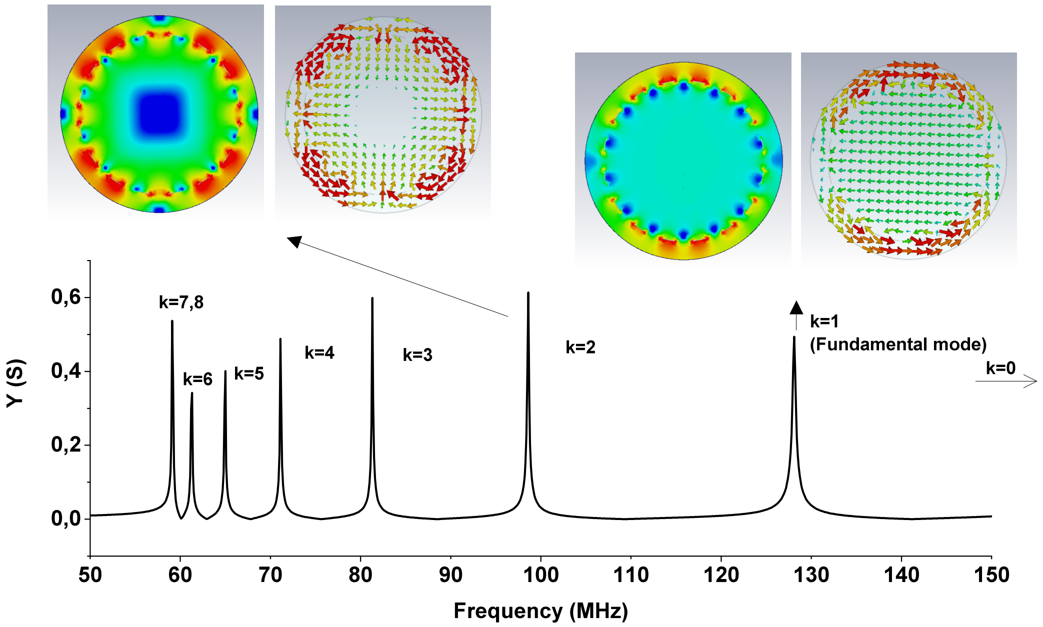

Figure 3.15: Amplitude of the admittance computed at the simulation lumped port in a frequency range from 50 MHz to 150 MHz. The results have been obtained considering a capacitance value equal to 26.4 pF. Each resonance peak is associated to the corresponding mode expected from the theory. The $k = 0$ mode results to be at higher frequency as indicated by the arrow in the figure. The magnetic field distributions inside the shield, relative to the central axial slice of the coil, are reported for the fundamental ($k = 1$) and $k = 2$ modes. The cromatic maps show the magnetic field amplitude and direction expressed in decibel with reference to its maximum value on the same slice in a range from -50 dB to -30 dB.

first simulation and some iterations have been required to assess the final capacitance value C_1 equal to 26.4 pF.

The amplitude of the admittance computed at the simulation lumped port is shown in Figure 3.15 in a frequency range from 50 MHz to 150 MHz. Each admittance peak corresponds to a resonance and is associated to the corresponding mode expected from the theory (chapter 2). The $k = 0$ mode results to be at a frequency higher than 150 MHz whereas the $k = 7$ and $k = 8$ modes are very close and, practically, not distinguishable. As a consequence of the tuning process, the fundamental mode frequency results to be equal to 128 MHz. Such a mode is characterized by a homegenous and equally oriented magnetic field distribution inside the coil as proved by the maps reported in the figure (more information about the color map is reported in the caption). As a comparison, the same results are shown for the next ($k = 2$) mode. In this case, the magnetic field distribution is strongly inhomogeneous and the field direction is correlated with the position within the slice. Finally, the field peaks near the birdcage legs are representative of the current distribution among them. As expected, the $k = 1$ and $k = 2$ modes lead to a single and double wavelength leg current distribution along the coil circumference, respectively.

It is worth recalling that the aim of the relevant coil was to have a device similar to those employed in a 3 T scanner but without the need to cause the nuclear resonance. Furthermore, considering that additional capacitors adjustment will be likely needed when the presence of the phantom will be accounted for and that 26.4 pF capacitors were not available at INRIM laboratory, 24 pF surface mount multilayer ceramic Vishay capacitors (*p/n*: VJ3838D240FCGMW) were employed. Such capacitors present a 1000 V nominal voltage with a high Q-factor and highly stable capacitance values at the frequencies of interest. To weld the capacitors to the birdcage coil, two copper ribbon leads have been soldered to each capacitor. The resulting capacitance has been measured through an Agilent 4294A Precision Impedance Analyzer for each component (*i.e.* capacitor with ribbon leads) obtaining values ranging from 24.7 pF to 24.9 pF and an average value equal to 24.8 pF.

The same simulation set-up described above has been simulated considering the measured capacitance average value leading to the result shown in Figure 3.16. The same comments provided for Figure 3.15 are still valid, but, in this case, the fundamental mode frequency is equal to about 131.5 MHz. Such a value is not too far from the 3 T Larmor frequency, making the results provided by the experimental dosimetric set-up still representative of a real MRI scanner situation. Finally, differently from Figure 3.15, the $k = 7$ and $k = 8$ modes are now distinguishable.

Among the 32 capacitors of birdcage coil, 8 Vishay trimmerable capacitors (*p/n*: BFC280908003) have been employed for the driven birdcage meshes (90° apart to account for quadrature supply) and for those in the opposite positions. The capacitance of the trimmerable capacitors can be regulated from 5 pF to 57 pF. The trimmerable capacitors have been disposed in such an arrangement to allow for the coil fine tuning. In particular, as explained by the theory (see chapter 2), the adopted arrangement permits to change both the degenerate fundamental mode frequencies independently[3].

Once all the trimmerable capacitors have been regulated to the same capacitance of 24.8 pF, all the capacitors have been welded to the coil. A loosely coupled shielded loop has been employed to measure the birdcage resonance frequencies. The shielded loop structure with a central shield gap has been selected to reduce the common-mode currents allowing for balun avoidance [69]. The loop (approximately 45 cm × 6.5 cm) is shown in Figure 3.17 and presents a shape similar to that of the birdcage meshes. This guaranteed a satisfying magnetic coupling with the birdcage mesh when the loop was moved closed to it to perform the relevant measurement.

---

[3] Even if for the specific application and at the current state the fundamental mode frequency do not represent a constraint strong enough to require a coil fine tuning, the trimmerable capacitors keep to be useful dealing with the impedance matching process.

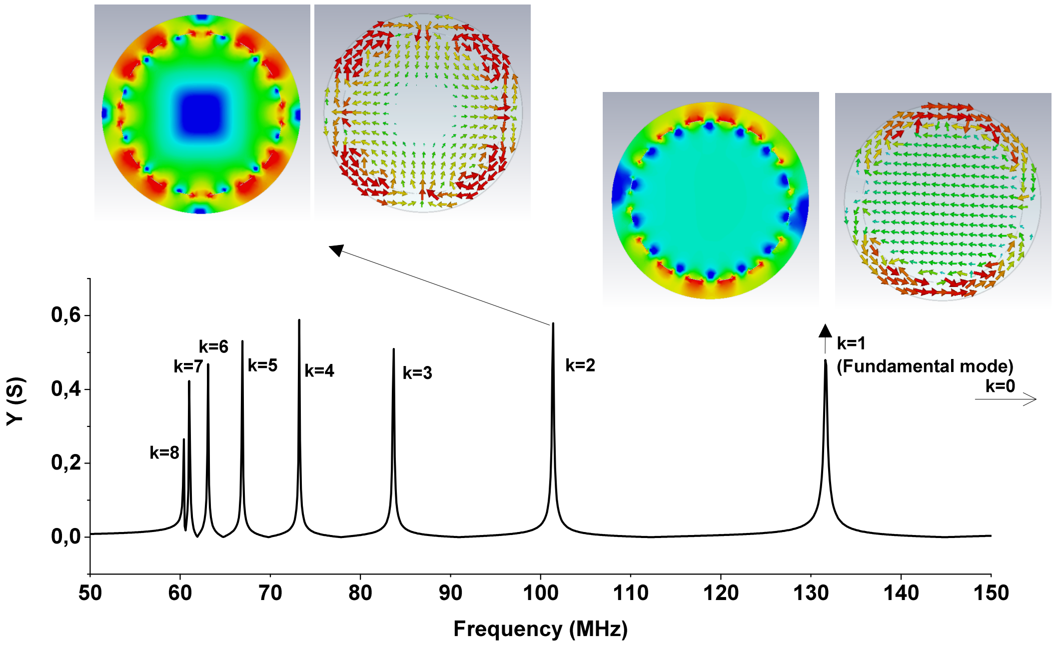

Figure 3.16: Amplitude of the admittance computed at the simulation lumped port in a frequency range from 50 MHz to 150 MHz. The results have been obtained considering the measured capacitance value equal to 24.8 pF. Each resonance peak is associated to the corresponding mode expected from the theory. The $k = 0$ mode results to be at higher frequency as indicated by the arrow in the figure. The magnetic field distributions inside the shield, relative to the central axial slice of the coil, are reported for the fundamental ($k = 1$) and $k = 2$ modes. The cromatic maps show the magnetic field amplitude and direction expressed in decibel with reference to its maximum value on the same slice in a range from −50 dB to −30 dB.

Figure 3.17: Picture of the shielded loop employed for the birdcage resonance frequencies measurement.

Loosely coupled loops are commonly adopted in MRI coil construction [**keil1**, 39, 55] to obtain an easy and flexible estimation of the coil resonance frequencies. The basics behind this type of measurement can be easily understood analyzing the behaviour of

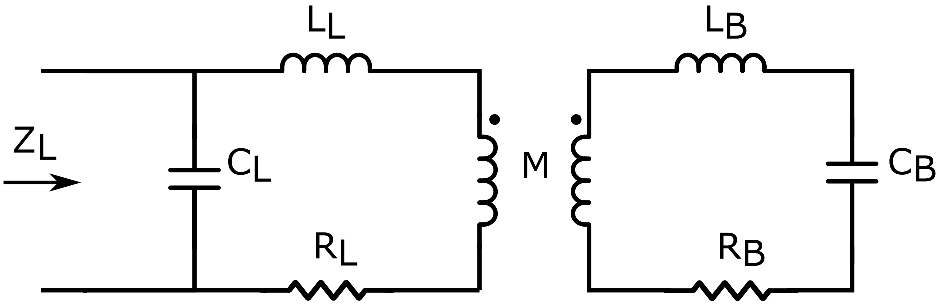

(a) Lumped element description of the magnetic coupling between a resonating circuit and a generic loop.

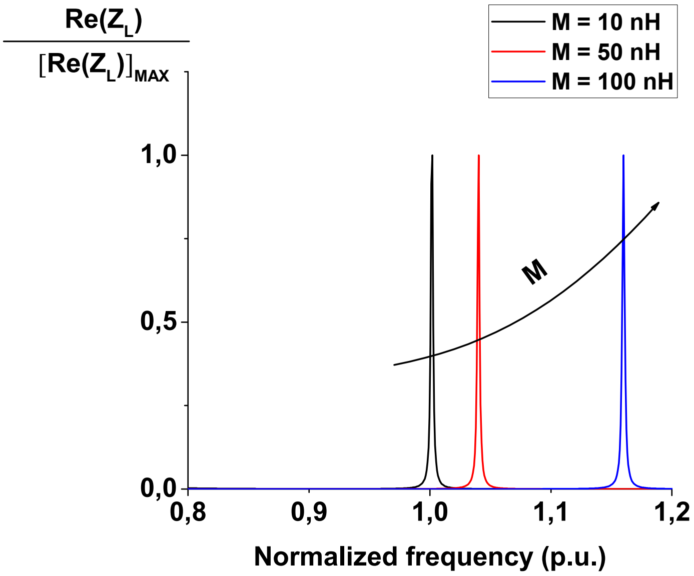

(b) Real part of the impedance measured at the coupled loop port normalized to its maximum value as a function of frequency. The frequency is normalized with respect the resonance frequency of the resonating circuit.

Figure 3.18: Simplified description of the magnetic coupling between a loop and a resonating circuit. A lumped equivalent circuit is proposed in (a). Some results obtained from the analysis of such a circuit are proposed in (b).

the lumped element circuit of Figure 3.18a which gives a simplified but useful description of the magnetic coupling phenomenon. The birdcage is here replaced by a generic resonating circuit with a capacitance C_B equal to 24.8 pF and an inductance L_B equal to 60 nH (*i.e.* the capacitance value considered for the birdcage and the inductance value that leads to a resonance frequency of 131.5 MHz). The loop is modeled by an inductance L_L equal to 1 μH and a parallel stray capacitance C_L equal to 3 pF. The inductance has been computed considering a loop with dimensions similar to those of the employed

Figure 3.19: "Rohde Schwarz R&S ZND" Vector Network Analyzer used, together with the coupling loop, to measure the resonance frequencies of the birdcage coil.

one (Figure 3.17), whereas the capacitance has been selected to avoid self resonances of the loop in the proximity of that of the resonating circuit. The mutual magnetic coupling between the circuits is described by M and a resistance equal to 0.1 Ω is considered both for the loop R_L and resonating circuit R_B.

Figure 3.18b shows the real part of the impedance Z_L computed, by means of the equivalent circuit of Figure 3.18a. The real part of the impedance is normalized to its maximum value as a function of frequency. The frequency is normalized with respect to the resonance frequency of the resonating circuit. The results are shown considering three different values of M (*i.e.* different coupling degrees) properly selected to emphasise the phenomenon. It is evident a relation between the real part of Z_L and the resonance frequency of the coupled circuit. In particular, the result suggests that for low magnetic couplings (*i.e.* if the measuring loop is not placed too close to the birdcage mesh) the real part of the loop impedance shows a peak which is representative of the coupled circuit resonance. For higher M values, the loop and the resonating circuit significantly influence each other affecting the measurement reliability.

The results obtained through this simple analysis have been confirmed by full-wave simulations, carried out with CST Microwave Studio$^{®}$, considering the realistic birdcage coil model of Figure 3.12. In the interest of conciseness, such results are not reported but paved the way for the experimental measurements described below.

The measuring loop has been connected to a calibrated "Rohde & Schwarz R&S ZND" Vector Network Analyzer (VNA) (Figure 3.19) and the real part of the loop impedance has been measured in a frequency range from 50 MHz to 150 MHz placing the measuring loop near a birdcage mesh.

The measurement results are shown in Figure 3.20 as displayed by the VNA screen. The agreement with the simulation results (Figure 3.16) makes easy to identify the birdcage fundamental mode with the impedance peak which occurs at about 131.5 MHz. Furthermore, all the other birdcage modes are labeled in the figure to have a term of

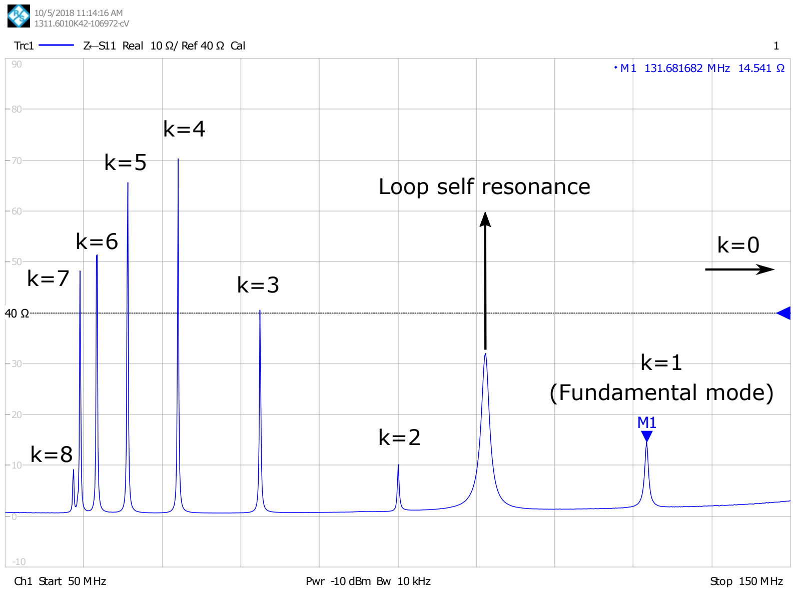

Figure 3.20: Real part of the loop impedance as measured by the "Rohde & Schwarz R&S ZND" VNA. The frequency range is 50 MHz to 150 MHz and each impedance peak is associated to the corresponding birdcage resonance mode. The measuring loop self resonance appears at about 110 MHz and is marked in the figure by an arrow.

comparison with the simulation results. The impedance peak at about 110 MHz corresponds to the self resonance of the measuring loop and it is not significantly affected by the birdcage proximity.

3.5.4 Birdcage power supply

Once the fundamental mode resonance frequency has been identified, a proper power supply strategy has been selected. The followed supply method has been suggested by an US Patent released by Leifer *et al.* [70]. The method has been designed to efficiently drive the shielded birdcage coil, even considering capacitive balancing circuits to reduce the mutual interactions between the quadrature channels due to unwanted common-mode currents. In particular, the balancing circuits have been conceived to avoid the need of baluns and an interpretation for their working principle is given below.

Even if the realized birdcage coil has been prepared to be supplied in quadrature operation mode, the first supply arrangement described in the present chapter has been limited to a single channel only. In this framework , as suggested by the patent, the shield of the coaxial cable coming from the RF amplifier output has been connected to the birdcage coil shield. To link the birdcage shield potential to that of the inner birdcage conductors without perturbing the axial symmetry of the structure, the shield has

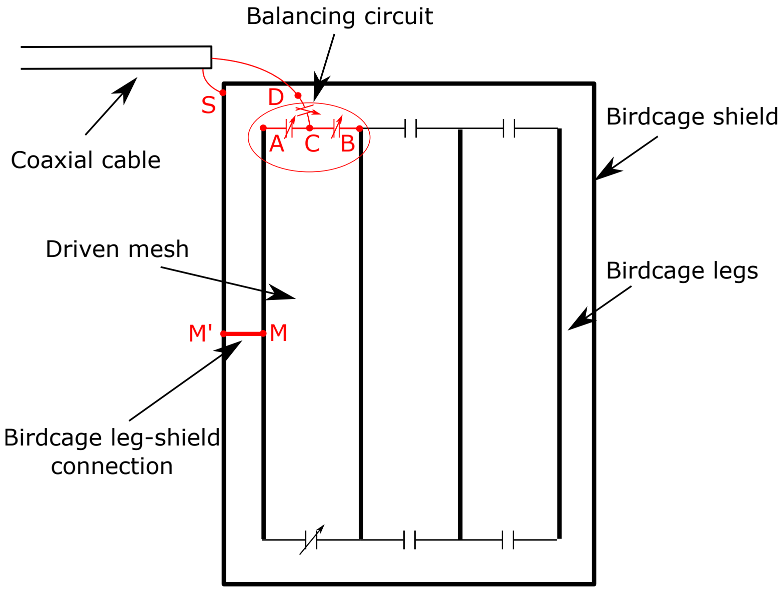

Figure 3.21: Sketch of the supply scheme applied to the birdcage coil. For simplicity, only four of the sixteen legs are depicted in the figure. The coaxial cable shield is connected to the birdcage shield in S. The inner coaxial conductor is connected to the balancing circuit in D which is in turn connected to the birdcage coil in A and B. The connection of the mid-point of a leg adjacent to the supplied mesh (M) and the shield (M′) is also represented by a red line.

been connected to the mid-point of one of the leg adjacent to the supplied mesh. Finally, the inner coaxial conductor is connected, through the balancing circuit, to the birdcage legs enclosing the driven mesh replacing one of the trimmerable capacitors already implemented in the coil.
In Figure 3.21 the supply topology described above is illustrated schematically. The shield of the coaxial cable is connected to the birdcage shield in S. The balancing circuit is connected to the inner coaxial conductor in D and to the birdcage coil in A and B. Finally, the red line from M′ to M represents the connection between the mid-point of the leg adjacent to the supplied mesh and the coil shield.

In Figure 3.22 the discussed constructive solutions are shown. In Figure 3.22a a copper strip has been welded to the birdcage leg to provide the connection (M-M′) to the shield. Indeed, the strip has been shaped to be pressed by the presence of the birdcage shield and the proper contact is guaranteed by the strip elasticity. Figure 3.22b shows the copper strip employed to connect the coaxial shield to the coil shield (S) providing a proper coaxial cable shield termination.

The capacitive balancing circuit is represented in Figure 3.23. It is made of three

(a) Copper strip which is pressed by the birdcage shield to guarantee the connection with the birdcage leg.

(b) Copper strip which connects the outer contact of the N-port to the birdcage shield.

Figure 3.22: Constructive solutions adopted for the birdcage leg and shield connection (a) and for that between the coaxial and birdcage shields (b).

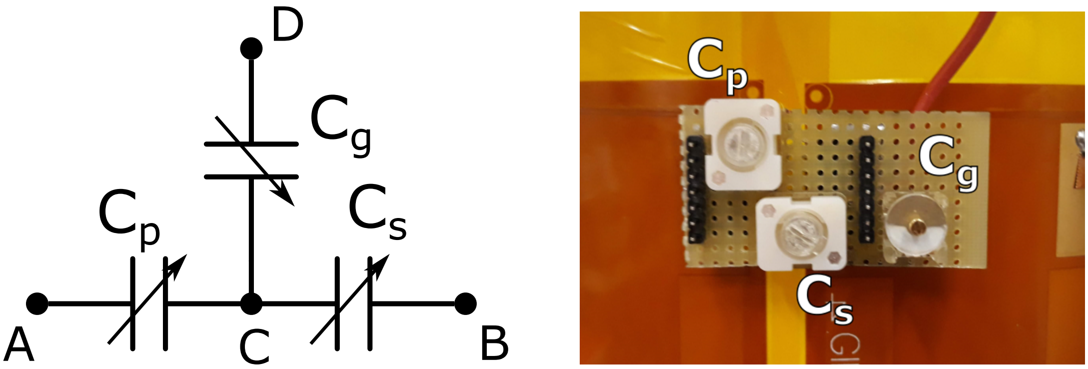

(a) Circuital scheme of the capacitive balancing circuit.

(b) Picture of the capacitive balancing circuit connected to the birdcage coil.

Figure 3.23: Capacitive balancing circuit scheme (a) and picture (b). In (a) the circuit node letters are compliant with the notation employed in Figure 3.21.

trimmable capacitors named C_p, C_s and C_g. In Figure 3.23a a circuital scheme is reported where the node letters are compliant with those employed in Figure 3.21. Figure 3.23b shows the realized circuit connected to the birdcage coil. The connection is guaranteed by pin headers plugged into suitable pin sockets welded to the birdcage. In case modifications were needed, this type of connection simplified the removal process of the stripboard on which the capacitors were soldered. The capacitor C_g (Vishay, *p/n*: BFC280908003, 5 pF to 57 pF) is connected to the inner connector of the N-port placed above the upper POM cap. C_p and C_s (Vishay, *p/n*: BFC280907015, 7 pF to 100 pF) are connected to the legs enclosing the supplied mesh.

To give an interpretation for the role of the capacitive balancing circuit proposed in

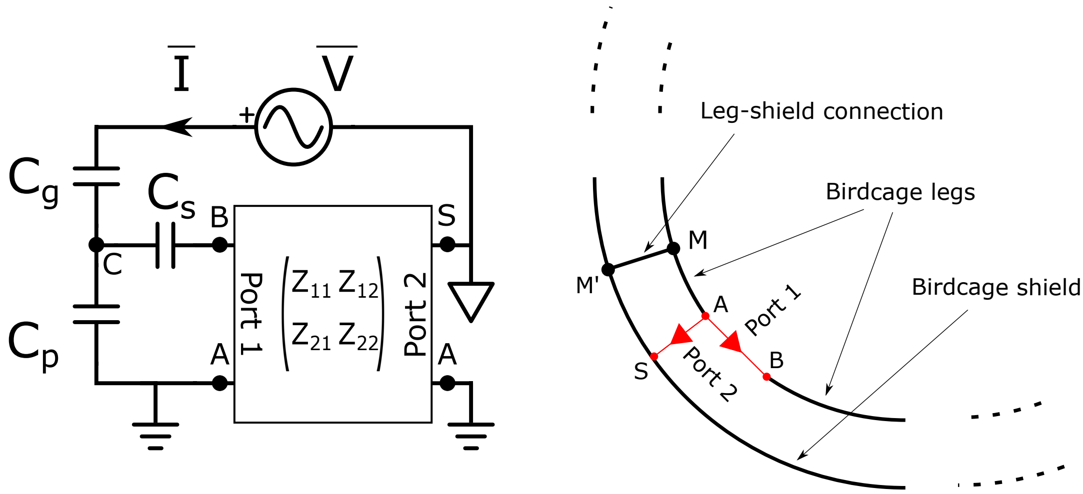

(a) Equivalent circuit describing the connection between the capacitive balancing circuit and the birdcage coil (represented by the 2×2 Z-matrix).

(b) Sketch representing the lumped ports connection considered in the 3D full-wave simulation to evaluate the birdcage coil Z-matrix.

Figure 3.24: Equivalent circuit and 3D full-wave simulation ports set-up considered to evaluate the capacitive circuit role and behaviour.

[70] and to analyze its behaviour, the equivalent circuit of Figure 3.24a has been considered. The birdcage coil is described by its 2×2 Z-matrix evaluated through a 3D full-wave simulation carried out with the frequency domain solver of CST Microwave Studio®. The lumped ports connection considered in the simulation is sketched in Figure 3.24b. A first port named “Port 1” connects the legs enclosing the driven mesh through the nodes A and B (see also Figure 3.21). A second port named “Port 2” connects the leg, whose mid-point is joined to birdcage shield (M-M′), to the shield itself through the nodes A and S.

From the circuit of Figure 3.24a it is possible to obtain an expression for the differential V_d and common-mode V_o voltages evaluated as:

$$V_d = V_{B-S} - V_{A-S}$$
$$V_o = \frac{V_{B-S} + V_{A-S}}{2}$$

and to look for the minimum ratio between V_o and V_d as a function of C_S, C_P and C_g to analyse their role in the structure balancing.

The results are presented in Figure 3.25 assuming C_S and C_P in a range from 1 pF to 100 pF and four different values for C_g. The results have been obtained considering a frequency equal to 131.5 MHz (*i.e.* the resonance frequency of the fundamental mode). The results suggest that a minimum of the ratio V_o/V_d, as a function of C_S and C_P, exists for all the C_g examined values. In particular, for each C_g, the minimum of V_o/V_d can be found for the maximum considered value of C_S and for a lower value of C_P (about 35 pF).

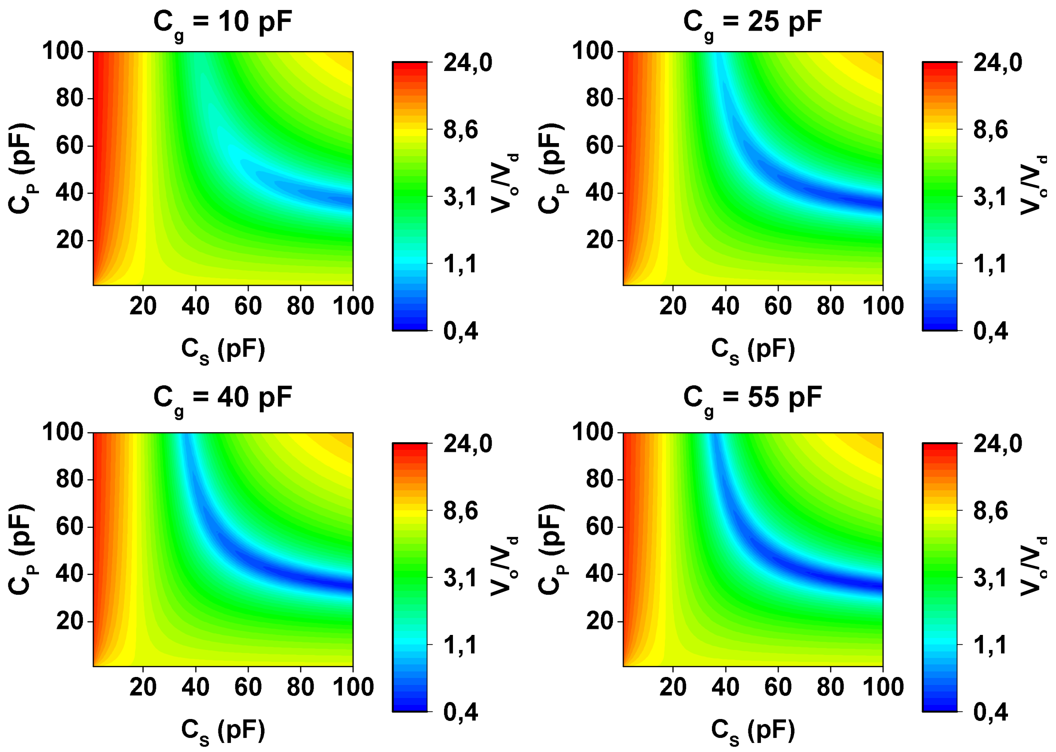

Figure 3.25: Chromatic maps showing the value of the ratio between V_o and V_d as a function of C_S and C_P (considered in a capacitance range from 1 pF to 100 pF). Each map is relative to a specific value of C_g and the results are obtained considering the 131.5 MHz frequency (*i.e.* the resonance frequency of the fundamental mode).

Furthermore, the absolute value of the minimum V_o/V_d is slightly influenced by C_g and decreases monotonously from 0.69 to 0.43 for C_g values of 10 pF and 55 pF respectively. It is worth noting that, even if the absolute value of the V_o/V_d minimum is influenced by the considered frequency and Z-matrix parameters, its qualitative behaviour has been found to be unaffected by the values of C_S, C_P and C_g. This suggests that a C_S much higher than C_P should be employed together with a high value of C_g. Even if more accurate simulations should be performed to obtain more reliable quantitative results (*e.g.* considering the real distance between the point C in Figure 3.24 and the actual N-port of the structure) the analysis revealed to be valuable as an operative method for the capacitive balancing circuit regulation. In particular, trying to obtain the relative values of the capacitors as suggested by the analysis, C_S and C_P have been trimmed to minimize the common-mode currents maintaining the fundamental mode resonance frequency of the driven mesh (measured through the coupling loop of Figure 3.17) equal to a value about 131.5 MHz to ensure the coil electrical symmetry.

To evaluate the effect of the common-mode currents, the experimental procedure

Figure 3.26: “Keysight E5061B ENA” employed in the birdcage coil impedance matching procedure.

suggested in [70] has been followed. Manually grasping the coaxial cable connected to the birdcage supply port and to the VNA, the resonance frequency of fundamental mode has been measured on the mesh 90° apart the driven one by means of the coupling loop. The balancing circuit capacitors have been regulated to minimize such a frequency variation, due to the cable grasping, below 1.5 ‰. During this stage, several coaxial cable types and lengths have been used trying to maximize the common-mode current drawbacks enhancing the balancing circuit effects.

3.5.5 Impedance matching

After the capacitive balancing circuit has been properly adjusted, the complex impedance of the coil has been measured directly from the N-port at 131.5 MHz. Since the VNA previously employed (”Rohde & Schwarz R&S ZND”) was not available anymore, a “Keysight E5061B ENA” VNA (Figure 3.26) has been used in the 50 Ω impedance matching procedure.

A complex impedance equal to (20 − 202j) Ω has been measured and the matching circuit of Figure 3.27a has been considered. A 30 pF C_m capacitance and a 274 nH L_m inductance represented the values needed to properly transform the measured impedance. Since the presence of the matching circuit likely modify the impedance to be matched, a variable capacitor (Vishay, *p/n*: BFC280907015, 7 pF to 100 pF) and a variable inductor (Coilcraft, *p/n*:144-06J12L, 193 nH to 306 nH) have been employed. Considering the maximum power available from the RF amplifier (100 W), the inductor maximum nominal current (8.1 A) does not represent a limit which is still imposed by the maximum nominal voltage of the trimmerable capacitors (200 V to 250 V). In Figure 3.27b a picture of the matching circuit soldered on a stripboard is shown inside the specific plastic box. The N-port is fixed to the box through metallic bolts which make also available the

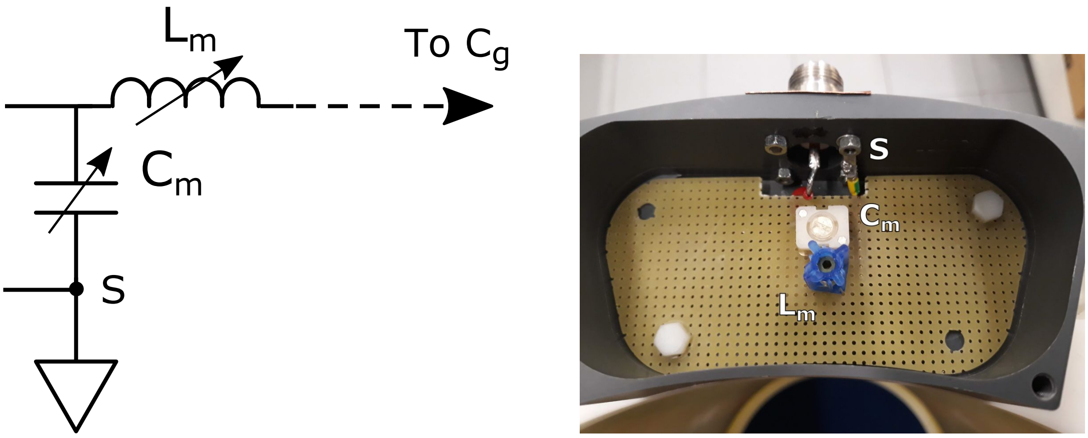

(a) Circuital scheme of the matching circuit.

(b) Picture of the matching circuit soldered on a stripboard and connected to the birdcage coil.

Figure 3.27: Circuital scheme (a) and picture of the circuit employed for the 50 Ω birdcage coil impedance matching.

connection to the shield (identified by letter "S" in the figure) inside the box itself.

The scattering parameter (S11) has been measured through the VNA and the matching circuit components have been fine regulated to achieve the best matching at 131.5 MHz. The result of this procedure is proposed in Figure 3.28 which shows the scattering parameter expressed in decibel from 120 MHz to 150 MHz. The minimum value of S11, equal to about −35 dB, is noticeably close to the fundamental mode resonance frequency, ensuring a good impedance matching at the desired operating frequency.

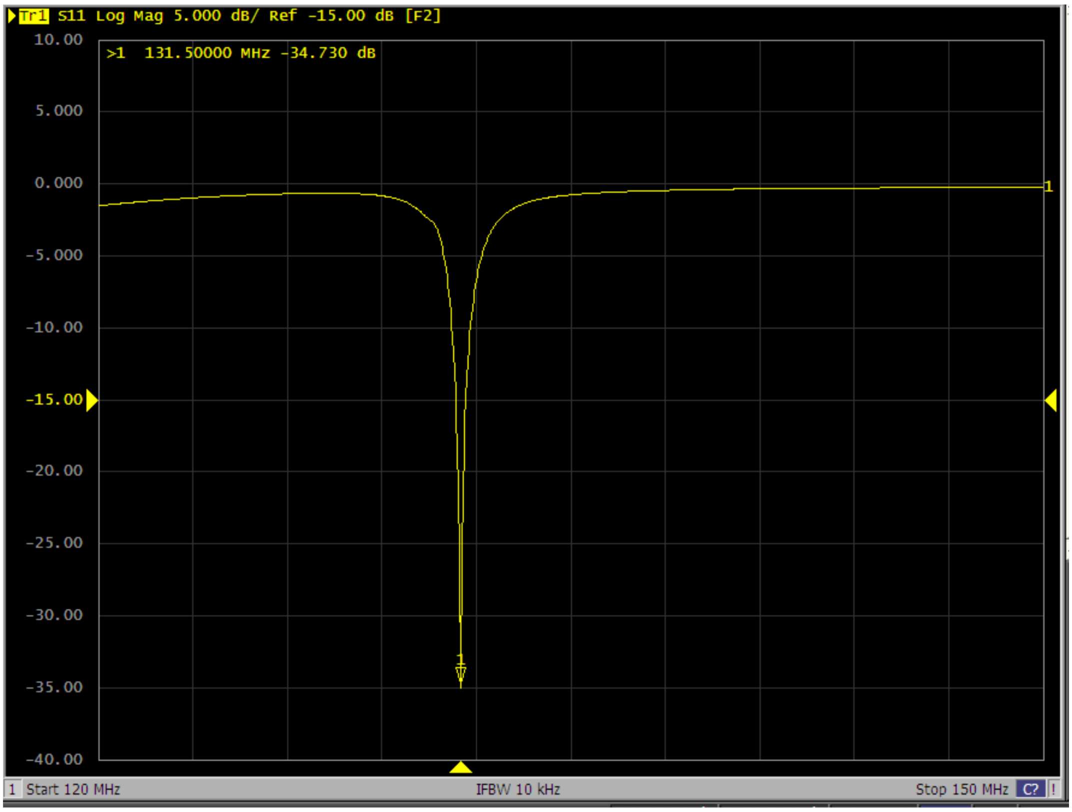

Figure 3.28: Scattering parameter (S11) expressed in decibel measured through the "Keysight E5061B ENA" VNA after the matching circuit fine regulation.

3.6 Conclusion

The realization of an experimental set-up devoted to MRI dosimetry measurements has been described. The set-up consists of a generation system employed to supply the RF coil responsible for the electromagnetic fields radiation. The electromagnetic fields are measured through suitable probes, whose accurate position inside a human tissues mimiking phantom is guaranteed by an automatic tri-axial positioning system. Both the generation and measurement processes are managed by means of a python software.

A home-made RF coil named "Hydro" has been employed for the first experimental set-up characterization and validation. A 3D model of the coil has been drawn in an electromagnetic simulation environment and numerical results have been compared to those obtained experimentally.

In this framework, an uncertainty budget related to the dosimetric set-up has been carried out. Once a suitable measurement model has been defined, the RF coil "Hydro" has been used to obtain the standard deviation of the model parameters which required multiple measurements to be characterized.

The satisfactory agreement between the experimental and numerical results achieved with "Hydro", where more than 93 % of the results obtained from simulations are within the the measurements uncertainty range, paved the way to a similar activity involving a planar double-tuned (23Na/1H) coil provided by the IMAGO7 foundation (Pisa, Italy). The coil was conceived to work into a 7 T MRI scanner and experimental measurements have been performed in the pursuit of validating the results obtained from their electromagnetic simulations.

Finally, a detailed description of the design and realization of an RF MRI volume coil is proposed in the last section. The coil (*i.e.* a 16-leg high-pass birdcage) has been conceived to be integrated in the experimental dosimetric set-up to generate electromagnetic fields similar to those generated by standard body-coils or head-coils inside the MRI scanners. A preliminary discussion suggested a method to define a reference value of the capacitors needed to the coil to resonate at the desired frequency. After the birdcage structure design has been accomplished through a 3D CAD software (SolidWorks®), electromagnetic simulations have been performed to investigate the behaviour of the coil. Even if a resonance frequency equal to 128 MHz has been adopted as a first design constraint, for the sake of concreteness, a resonance frequency equal to 131.5 MHz has been finally achieved. Indeed, considering the relevant application, this choice allowed for the employement of available capacitors without leading to substantial changes with respect to the results obtainable with a 128 MHz resonating coil.
After the capacitors have been properly welded to the birdcage, a loosely coupled loop has been used to measure the actual resonance frequencies finding satisfactory agreements with the expectations from the numerical results. Such a measurement represented a flexible mean to investigate the coil resonance frequencies highlighting possible criticism due to defective capacitors or problematic weldings. However, as shown in section 3.5.3, the resonance frequency measured through the loop is slightly perturbed with respect to the natural resonance frequency of the structure. Even if this perturbation can be neglected at the present stage, a more rigorous value of the resonance frequency can be obtained by means of a direct measurement of the birdcage impedance across a capacitor. Obviously, this requires additional coil arrangements making the procedure much more elaborated than that involving the loosely coupled loop.
Particular attention is dedicated to the coil power supply. A linear excitation has been considered as a first stage and a capacitive balancing circuit has been connected to the coil to address the common-mode current issue, potentially avoiding the needs for baluns. Finally, the 50 Ω impedance matching of the birdcage coil has been achieved at the fundamental mode resonance frequency (131.5 MHz) and the relevant methods and results are presented.

Future work will deal with the improvement of the dosimetric set-up capability and with the birdcage coil completion. The former provides the employement of time-domain electromagnetic probes [71] for electromagnetic field amplitude and phase measurements. The knowledge of the phase represents a key point in the investigation of the electromagnetic field polarization allowing for the estimation of parameters such as transmit/receive sensitivities (*i.e.* $\boldsymbol{B}_1^+$ and $\boldsymbol{B}_1^-$).

Furthermore, the extension of the frequency range of the dosimetric set-up is envisaged. In particular, the RMS probes reliability will be investigated up to 300 MHz to allow for measurements employing RF coils designed for 1H nuclei excitation inside 7 T MRI scanners. For the same purpose, also the Tissue Simulating Liquid characterization will be extended up to 300 MHz.

On the other hand, also the birdage coil gives the opportunity for several additional work. Firstly, electromagnetic field measurements can be performed considering a linear excitation and the absence of the phantom inside the coil. This type of excitation would allow for evaluations, such as field polarization, that would be otherwise unfeasible. After that, the coil can be arranged to be supplied in quadrature operation mode and further measurements can be performed. Finally, the birdcage coil tuning and matching should be considered in the presence of the phantom inside its volume. The presence of the phantom represents a strong constraint for standard birdcage coil design. This is because, due to the different human body shapes and dimensions, various phantoms should be considered in the coil design process trying to achieve a coil behaviour which is affected as little as possible by the phantom shape. This leads potentially to the requirement of modifications which even involve the coil topology (*e.g.* a band-pass structure may be needed with several capacitors distributed along the birdcage legs). This is particularly true when the dimensions of the designed coil are comparable with the electromagnetic wavelength at Larmor frequency. In the specific application described in the present chapter, the phantom shape and properties are defined and are likely to remain unchanged. Therefore, the effects of the phantom which have to be addressed are expected to be reduced to a shift of the coil resonance frequencies. If the same resonance frequency of the unloaded coil has to be achieved even in the presence of the phantom, a modification of the value of the capacitors will be probably needed. Considering such a requirement, attention will be paid to tune the birdcage coil at 128 MHz to be compliant with the RF volume coils employed in 3 T MRI scanners for 1H nuclei excitation.

Chapter 4

RF Inhomogeneity Artefacts in Presence of Elongated Prostheses

4.1 Introduction

It is widely recognized that a joint replacement procedure may lead to several orthopaedic issues [72, 73]. Such complications may occur throughout the metallic implant life, not being limited to the perioperative period only [74, 75]. In particular, the wear between the primary bearing surfaces, with the consequent release of prosthetic particles, as well as aseptic loosening, may induce an immune response in the periprosthetic vicinity. Over time, these processes could result in an excessive accumulation of bone-resorbing factor leading to osteolysis which represents one of the fundamental causes for implant revisions [76].

The increase of the total joint replacement procedures [77, 78], such as hip or knee arthroplasty, highlights the importance of a diagnostic tool able to determine and recognize the presence of perioperative and/or postoperative diseases. Thanks to the potentially achievable high tissues contrast, spatial resolution, sensitivity and specificity, MRI is recognised as the optimum candidate in the evaluation of the different pathologies related to a total joint arthroplasty [79] emerging over other clinical techniques (*e.g.* computerized tomography, conventional radiography, aspiration arthrography or nuclear scintigraphy). In fact, avoiding the use of ionizing radiations, MRI demonstrated to be the most sensitive tool to estimate the location and extent of osteolysis as well as the optimal method to perform imaging of nerves surrounding hip arthroplasty [80].

The presence of metallic objects has been recognized to be one of the most important causes for artefacts in MRI [81]. Metal artefacts, if not properly addressed, may easily lead to a strong degradation of the MR image making the interpretation of the results sometimes a challenge for many physicians. The interaction between the RF coil and the metallic object, which degrades the homogeneity of the RF coil transmit/receive sensitivity, has been already briefly described in chapter 1 as a possible source of artefacts and will be the subject of the following chapter. However, such an interaction is not the only cause for metal artefacts rise. In particular, the presence of a metallic object, whose magnetic susceptibility differs from that of the human body, generally compromises the static field homogeneity leading to a spatial dependent Larmor frequency even in absence of external gradient magnetic fields. Such effects may strongly affect the MR image resulting in the so-called "susceptibility artefacts". Since, given the proton density of an isochromat,[1] the associated net magnetization is proportional to the static field amplitude [15], an unwanted spatially dependence of such a field inevitably compromises the desired relation between the tissue proton density and the MR signal. A second effect associated with the static field amplitude spatial variation, may be recognized in a decrease of T_2^* in the tissues most affected by the static field perturbation. Finally, the spatial dependent Larmor frequency may have a strong impact on the MR image spatial encoding. In fact, deformed slice profiles may result from the slice excitation process together with a geometric distortion along the readout direction if a cartesian k-space filling technique is adopted [82, 83]. Whereas some general precautions may be adopted, using standard sequences, in order to decrease the aforementioned effects (*e.g.* spin-echo or "Filtered Back-Projection" sequences to compensate for the T_2^* decrease, limited RF excitation bandwidths with limited slice excitation gradient amplitudes associated with high readout bandwidths or full phase encoding to limit the in-slice distortion). In addition, several "metal suppression" techniques have been specifically designed to face the susceptibility artefact issues [84]. Among those, the most promising are "View Angle Tilting" (VAT) (where the slice selective gradient is switched on during the readout phase), "Slice Encoding for Metal Artefact Correction" (SEMAC) (which is similar to VAT with the addition of a phase encoding along the direction normal to the slice) and "Multiple-acquisition with Variable Resonances Image Combination" (MAVRIC) (which is a 3D technique where the final image is obtained by a combination of sub-images each obtained applying different RF excitation pulses with limited bandwidths at different resonance frequencies) [82].

Finally, a further cause for artefacts seems to be due to gradient switching [85, 86]. In particular, gradient switching may induce eddy currents that, circulating within non-zero conductivity objects, perturb the original gradient field spatial distribution. Such artefacts are heavily influenced, among others, by the adopted MR sequence and by imaging parameters such as FOV and matrix size.

The static field amplitude, together with the associated Larmor frequency, is recognised to have a strong influence on the metal artefacts prominence. In particular, considering the same difference of magnetic susceptibility between an implant and the periprosthetic tissues, the static field spatial distortion increases linearly with its amplitude. This results in susceptibility artefacts to be more and more important as the static field amplitude grows. Furthermore, also the artefacts due to the coupling between a

---

[1] With "isochromat" is meant a continuous volume of tissue that is subjected to a homogeneous static field.

conductive implant and the RF coils are influenced by the static field amplitude. In fact, such couplings are strongly dependent on the frequency involved which is related to the static field amplitude by the gyromagnetic ratio [87]. Finally, also the relative importance of the different types of metal artefacts can be influenced by the level of the static field amplitude [88].

Currently, the most common alloys employed in the realization of metallic prostheses are cobalt-chromium (CoCr), titanium (Ti) and MR-compatible stainless steel [89]. Whereas cobalt-chromium is generally preferred for joint implants characterized by considerable wear-induced movements, titanium is often involved for structural integrity and stainless steel is applied for a combination of both purposes [84]. It is worth noting that the magnetic susceptibility of the titanium is fivefold lower than that of cobalt-chromium alloys [84] resulting in the consequent reduction of the influence of susceptibility artefacts in imaging of titanium implants.

Whereas metal suppression techniques may be employed to address susceptibility artefacts and some imaging parameters may be modified in order to decrease the prominence of the artefacts due to gradient switching, very few solutions have been proposed in order to mitigate RF inhomogeneity artefacts. Recently, Bachschmidt *et al.* [90] demonstrated that RF inhomogeneity artefacts, due to the presence of a hip prosthesis, are influenced by the polarization of the RF magnetic field generated by the body coil inside a 3 T scanner. In particular, they showed that such a polarization may be properly chosen to minimize the artefacts rise leading to a beneficial impact on the MR image. However, the right polarization is strongly affected by the implant position with respect to the body coil, making the method suffering from the need to perform a preliminary $\boldsymbol{B}_1$-map on the patient to evaluate the optimal RF magnetic field polarization.

In the following sections, the electromagnetic coupling between a metallic cylinder and a generic birdcage coil is examined and described by means of an equivalent lumped elements circuit. The effects of the presence of the metallic cylinder on the $\boldsymbol{B}_1^+$ component generated by an 8-leg birdcage coil, have been computed with numerical simulations at 128 MHz and are highlighted by means of chromatic maps. Special attention is addressed to the $\boldsymbol{B}_1^+$ homogeneity whose corruption is related to the RF inhomogeneity artefacts rise. An original near-field cloaking approach is hence proposed to restore the $\boldsymbol{B}_1^+$ homogeneity covering the metallic cylinder with a low-loss dielectric coating. The optimum relation between the coating electric permittivity and thickness is studied and discussed. The findings are therefore extended to a realistic hip prosthesis model both at 128 MHz and 64 MHz. Finally, some considerations about SAR are also reported investigating the effects of the coating on the power deposition. All the results are obtained by means of the frequency-domain solver of COMSOL Multiphysics® (more details related to the simulation set-ups are reported in the germane sections).

Some of the results proposed in the present chapter have been previously published in [91, 92].

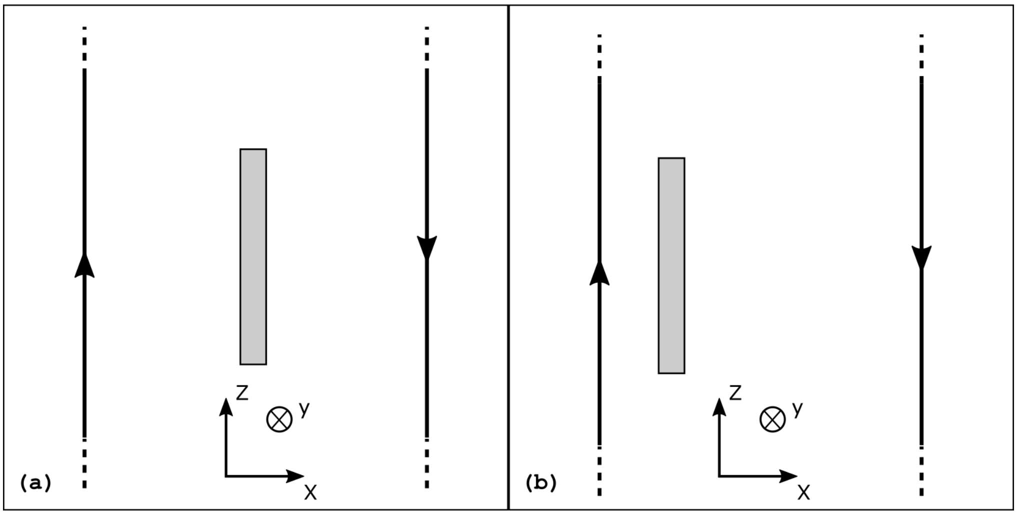

Figure 4.1: The simplified version of the set-up involving the metallic cylinder surrounded by the birdcage coil. In (a) the cylinder is placed in the centre of the coil and, in (b), in a lateral position.

4.2 EM Couplings

Let us start considering a metallic cylinder (representing a generic elongated metallic prosthesis) surrounded by an N-leg birdcage coil whose height is much larger than that of the cylinder. If properly quadrature supplied and tuned (see chapter 2), the current flowing in the n leg of the birdcage coil can be expressed in phasor notation as:

$$\overline{I_n} = I_{MAX} e^{j\frac{2\pi}{N}n} \tag{4.1}$$

From the above relation, it results that the currents flowing in two opposite legs of the birdcage coil have opposite phase angles. As a consequence, the system can be simplified considering $N/2$ planar coils, of infinite height[2], rotated by an angle $2\pi/N$ from the previous one. Thanks to the linearity of the problem, it is possible to consider each of the $N/2$ planar coils separately and superpose their effects at the end. Figure 4.1 reports a representation of the simplified problem. In Figure 4.1(a) the metallic cylinder is placed in the centre of the birdcage coil whereas, in Figure 4.1(b), in a lateral position.

The electromagnetic couplings between the planar coil and a generic metallic external object can be, in principle, both inductive and capacitive[3] [93, 94, 95]. The former are

---

[2] If the birdcage height is much larger than that of the metallic cylinder, the effect of the end-rings currents can be neglected in the analysis of the electromagnetic couplings between the antenna and the cylinder.

[3] Such a distinction of the two phenomena represents, at the considered frequencies, a useful approximation. Indeed, despite its limits that have to be taken into account, it allows to manage a qualitative and simple description of a complex problem.

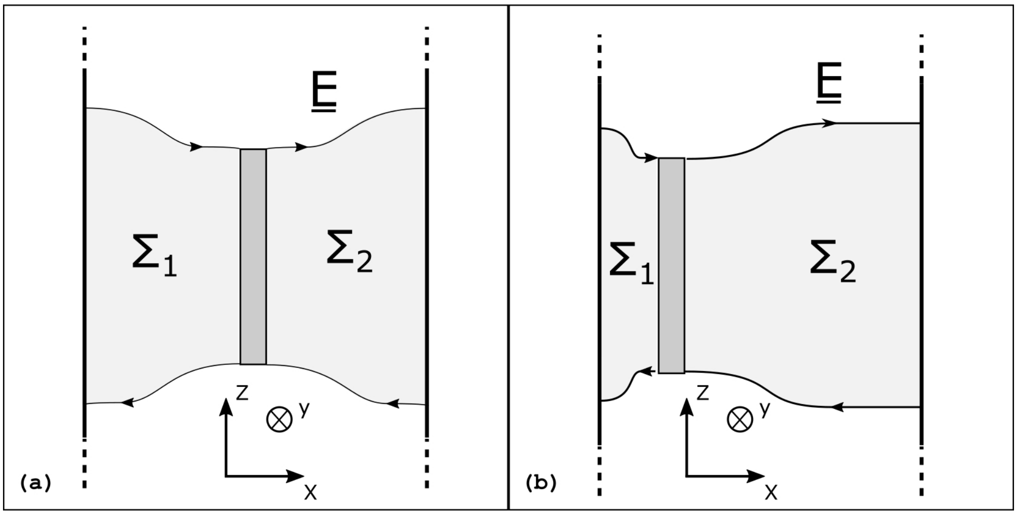

Figure 4.2: Simplified layout of the capacitive coupling between the central cylinder and the loop coil (a) and between the lateral cylinder and the loop coil (b). The electric field lines, responsible for the coupling, are qualitatively represented. The peripheral field lines enclose two surfaces Σ_1 and Σ_2 represented in light gray color. The couplings with the top and the bottom of the cylinder are not represented in the figure.

due to a transformer effect between the coil and the object. The time-varying magnetic field, generated by the currents flowing in the coil conductors, induces currents inside the object. If the object electrical conductivity is much higher than that of the background in which it is placed, those conductive currents are prevalently bounded within the object itself. Capacitive couplings are due to the capacitance between the conductors and the metallic object. In this case, dielectric currents are induced in the material surrounding the object flowing from the source to the object itself. Both the current generated by the inductive and capacitive couplings represent the source of a scattered time-varying magnetic field. Such a field overlaps the original one (*i.e.* that originated by the empty planar coil) potentially downgrading its homogeneity and leading to the RF Inhomogeneity artefact in MRI. If a metallic elongated object is considered, the conductive currents bounded within the object itself have a limited space to flow with the consequence that the generated scattered magnetic field goes to zero very rapidly with the distance from the object. It is hence reasonable to consider the effects on the $\boldsymbol{B}_1$ homogeneity especially due to the capacitive coupling neglecting, in a first instance, those due to the inductive one.

Figure 4.2 shows a qualitative representation of the capacitive coupling between the coil and the metallic cylinder. The electric field lines are orthogonal both to the conductors and to the metallic cylinder and identify two surfaces Σ_1 and Σ_2. Such an electric field configuration is confirmed by Figure 4.3 where a generic cylinder, simulated as Perfect Electric Conductor (PEC) has been placed laterally inside an 8-leg birdcage coil supplied in quadrature operation. The electric field distribution in Figure 4.3 represents

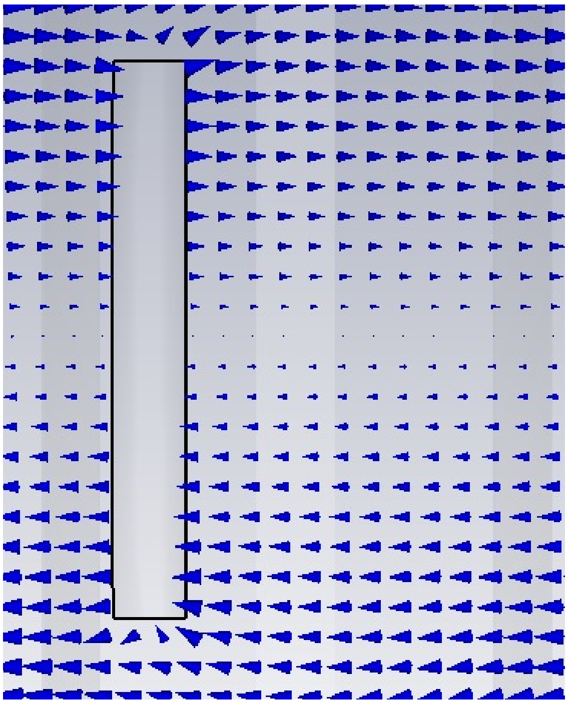

Figure 4.3: Electric field distribution, obtained with an electromagnetic 3D numerical simulation, when the Birdcage coil is ideally supplied in quadrature operation mode (see next section for more details) and the metallic cylinder is placed laterally inside the coil.

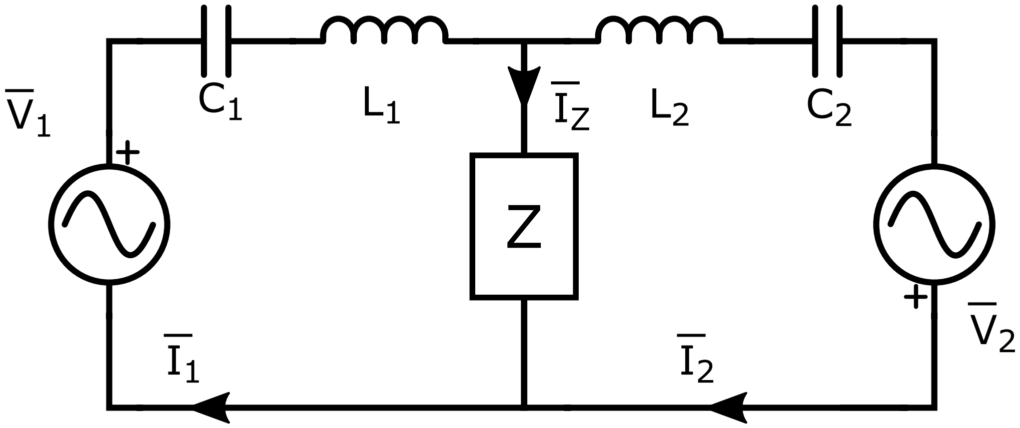

Figure 4.4: Simplified lumped element circuit representative of the coupling between the metallic cylinder and the planar coil.

a snapshot of the field lines obtained when the current flowing on the legs that lay on the figure plane reaches its maximum amplitude. Such a field distribution gives also reason for the planar loop simplification employed in the present dissertation.

To go further in the study of the phenomenon, let us consider the lumped element circuit in Figure 4.4 which represents a simple but effective description of the problem. In the circuit, C_1 and C_2 account for the capacitive coupling between the metallic cylinder and the left and right conductors respectively. L_1 and L_2 represent the inductive reactions relative to Σ_1 and Σ_2 respectively, Z represents the generic impedance of the cylinder, $\bar{V}_1$ and $\bar{V}_2$ are the induced voltages obtained as:

$$\bar{V}_k = -j\omega \int_{\Sigma_k} \bar{B}_y d\Sigma \tag{4.2}$$

where k denotes the surface ($k = 1{,}2$), $\bar{B}_y$ is the phasor of the y-component (refer to the coordinate system depicted in Figure 4.2) of the magnetic field generated by the empty planar coil and ω is the angular frequency. The opposite signs of the induced voltages is explained considering that they both generate a clockwise current for a magnetic field oriented along the direction opposite to the y-axis.
Introducing the inductive and capacitive reactances, defined as $X_L^{1,2} = \omega L_{1,2}$ and $X_C^{1,2} = 1/(\omega C_{1,2})$ respectively, due to the geometric dependence of the circuital parameters, the following relations hold:

$$X_L^1 + X_L^2 = X_L^{TOT} \tag{4.3a}$$

$$X_C^1 + X_C^2 = X_C^{TOT} \tag{4.3b}$$

$$\bar{V}_1 + \bar{V}_2 = \bar{V}_{TOT} \tag{4.3c}$$

where X_L^{TOT}, X_C^{TOT}, $\bar{V}_{TOT}$ do not depend, as a first approximation, on the cylinder position along the x-axis. Solving the circuit, we obtain the following relations:

$$\bar{I}_1 = \frac{\bar{V}_{TOT} Z + j\bar{V}_1 \left(X_L^2 - X_C^2\right)}{jZ\left(X_L^{TOT} - X_C^{TOT}\right) - \left(X_L^1 - X_C^1\right)\left(X_L^2 - X_C^2\right)} \tag{4.4a}$$

$$\bar{I}_2 = \frac{\bar{V}_{TOT} Z + j\bar{V}_2 \left(X_L^1 - X_C^1\right)}{jZ\left(X_L^{TOT} - X_C^{TOT}\right) - \left(X_L^1 - X_C^1\right)\left(X_L^2 - X_C^2\right)} \tag{4.4b}$$

$$\bar{I}_Z = j\frac{\bar{V}_1 \left(X_L^2 - X_C^2\right) - \bar{V}_2 \left(X_L^1 - X_C^1\right)}{jZ\left(X_L^{TOT} - X_C^{TOT}\right) - \left(X_L^1 - X_C^1\right)\left(X_L^2 - X_C^2\right)} \tag{4.4c}$$

Moreover, it is useful to define an “unbalanced” current $\bar{I}_u$ as:

$$\bar{I}_u = \frac{\bar{I}_1 - \bar{I}_2}{2} = \frac{\bar{I}_Z}{2} \tag{4.5}$$

which represents an indicator of the lack of balance between the two meshes and therefore an unwanted effect strictly related to the presence of the metallic cylinder. By extending the lumped element circuit concept to the whole birdcage coil, the presence of

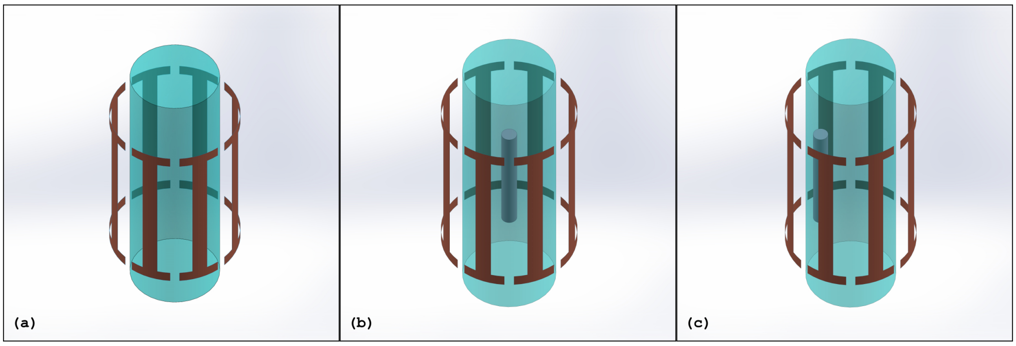

Figure 4.5: Three different simulation set-ups involving the empty phantom (a), the central (b) and lateral (c) metallic cylinder.

a non-zero current $\bar{I}_u$ in the circuit is representative of a lack of balance of the standard coil operation. Since the coil symmetry is one of the most important constraints for ensuring homogeneous coil transmit/receive sensitivities (B_1^+ and B_1^- respectively), the presence of the unbalanced current is found to be responsible for the RF inhomogeneity artefacts rise[4] and should be, therefore, reduced.

Substituting the expressions (4.4) in (4.5), the unbalanced current can be expressed as a function of the circuital parameters:

$$\bar{I}_u = \frac{j}{2}\left[\frac{\bar{V}_1\left(X_L{}^2 - X_C{}^2\right) - \bar{V}_2\left(X_L{}^1 - X_C{}^1\right)}{jZ\left(X_L{}^{TOT} - X_C{}^{TOT}\right) - \left(X_L{}^1 - X_C{}^1\right)\left(X_L{}^2 - X_C{}^2\right)}\right] \tag{4.6}$$

In order to have a comparison between the results expected from the equivalent circuit analysis and those obtained from full-wave simulations involving a whole birdcage coil, three set-ups are considered in Figure 4.5 and are described below.

An 8-leg birdcage coil, simulated as PEC, is ideally supplied in quadrature operation at 128 MHz by means of sixteen voltage ports (two per mesh with opposite phases) connecting the ring segments each other. Each voltage has a phase difference of $\pi/4$ with respect to those immediately adjacent and belonging to the same ring. All the ports share the same voltage amplitude able to generate a 2.5 μT magnetic field in the centre of the coil. Such a supply configuration allows to focus on the field distortion due, exclusively, to the interaction among the electromagnetic fields generated by the coil and the metallic object, leaving aside the effects due to the coil detuning. The birdcage is 460 mm high with a 175 mm radius. The leg and ring widths are equal to 30 mm and the gap between each couple of ring segments is equal to 14°. The birdcage dimensions, which are clearly smaller than those of a body coil, have been chosen to stress the effects of the metallic object presence and to be comparable with those of the coil designed in

---

[4] One of the aims of the several numerical simulations presented in the next sections is to give reasons for this assumption.

our laboratory (see chapter 3). A cylindrical phantom (radius: 120 mm, height: 730 mm, turquoise blue in Figure 4.5), which accounts for the presence of the human body, is placed in the centre of the coil. The electrical properties of the phantom (relative permittivity equal to 61.5 and electrical conductivity equal to 0.87 $\mathrm{S\,m^{-1}}$) are comparable to those of some human tissues [96] and have been selected to be equal to those of the phantom available in our laboratory. Even if the cylindrical shape and homogeneous electrical properties represent a strong approximation of a human body, this configuration allows to put in evidence that the metallic object is the only cause of significant distorsions. In the lumped parameters circuit of Figure 4.4, the presence of the phantom is easily accounted considering C_1 and C_2 as the series of the capacitance between the conductors and the phantom and that between the phantom and the metallic cylinder. Simulations have been carried out by means of the frequency-domain solver of COMSOL Multiphysics®. In particular, a boundary scattering condition has been applied on the external surface of a sphere (containing the entire simulation domain), whose radius is ten fold that of the birdcage. A layer of 300 mm, internal to the sphere boundary, has been simulated as perfectly matched layer (PML) in spherical coordinates. The whole domain has been discretized with tetrahedral elements and an iterative solver has been employed.
In Figure 4.5(a) the empty phantom scenario is considered and it is termed "ideal" case. After that, a metallic cylinder, whose radius is equal to 20 mm and height to 300 mm, is simulated as PEC and placed in the centre of the phantom (Figure 4.5(b)) and in a lateral ($x = -80$ mm) position (Figure 4.5(c)).

The simulation results are presented in Figure 4.6 both for the axial slice at $z = 0$ and for the coronal one at $y = 0$. The chromatic maps show the amplitude of the B_1^+ component of the magnetic field generated by the birdcage coil. To better identify the field inhomogeneity, the B_1^+ component is normalized with respect to the maximum B_1^+ on the relevant slice:

$$B_1^+(P)\Big|_{dB_{MAX}} = 20\log_{10}\left(\frac{B_1^+(P)}{max(B_1^+)\big|_{slice}}\right) \tag{4.7}$$

A quantitative information about the B_1^+ homogeneity over a slice is given by its spatial standard deviation evaluated as the second central moment of the field values over that slice. In particular, the standard deviation is provided with respect to the whole slice (for the coronal plane, it is limited in the z direction from $z = -200$ mm to $z = 200$ mm to remove from the analysis the B_1^+ inhomogeneities due to the finite length of the coil) and is termed σ_{WS}. When present, σ_{RA} represents the standard deviation evaluated in the reduced area delimited by the black rectangle circumscribing the metallic object. In the computations of both σ_{WS} and σ_{RA}, the area occupied by the metallic object has not been included in the standard deviation computation.
Figures 4.6(a),(b) show the results relevant to the ideal case. The considered electric permittivity and electrical conductivity values of the phantom justify the slight variation

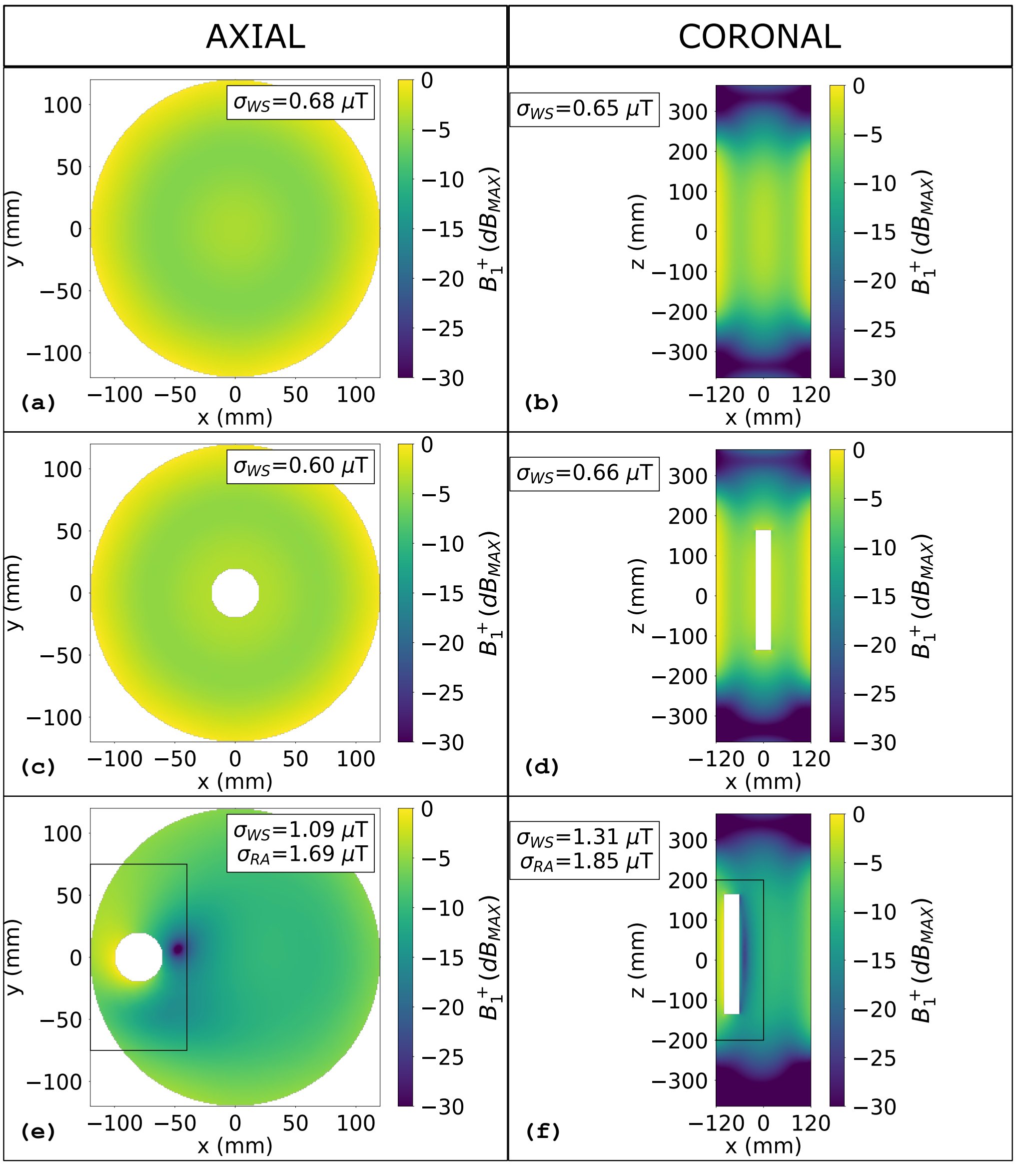

Figure 4.6: $B_1^+(\mathrm{dB}_{\mathrm{MAX}})$ evaluated with the empty phantom ((a) and (b)), with the metallic cylinder placed in the phantom centre ((c) and (d)) and in a lateral position ((e) and (f)). The results are shown both for the axial plane $z = 0$ ((a), (c) and (e)) and for the coronal plane $y = 0$ ((b), (d) and (f)). The rectangles represent the reduced areas in which the standard deviation (σ_{RA}) is computed. σ_{WS} represents the standard deviation computed on the whole slice.

of the B_1^+ component appreciable through the slices. In fact, at this frequency, the electromagnetic wavelength inside the phantom is comparable to the phantom dimensions and the propagation effects become noticeable.

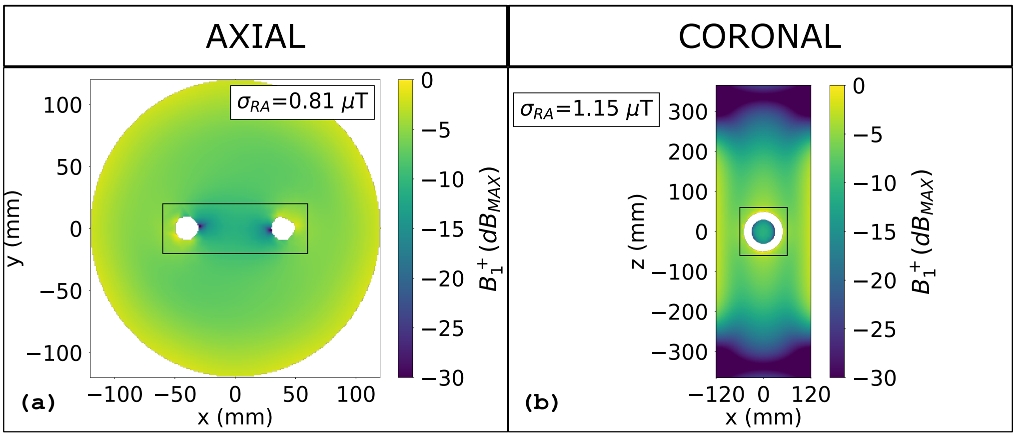

Figure 4.7: B_1^+($\mathrm{dB_{MAX}}$) evaluated when a metallic toroid is placed into the centre of the phantom. Results are shown both for the axial plane $z = 0$ (a) and and for the coronal plane $y = 0$ (b). The rectangles represent the reduced areas in which the standard deviation (σ_{RA}) is computed.

A deeper insight into (4.6) reveals that a zero unbalanced current is obtained if the induced voltages and both the inductive and capacitive reactances are equal each other. This condition is verified when the metallic cylinder is placed in the centre of the coil as shown in Figure 4.5(b). Such a theoretical prediction is confirmed by the numerical results presented in Figure 4.6(c) and Figure 4.6(d). The B_1^+ distribution is very close to that obtained in the ideal case both for the axial and coronal slices. Also the standard deviations are comparable with a maximum variation about 10 % for the axial slice. Such a difference can be ascribed to the area occupied by the cylinder which is excluded from the standard deviation computation.

As soon as the metallic cylinder moves laterally (Figure 4.5(c)), both the reactances and the voltages start to differ each other. The presence of a non-zero unbalanced current (according to (4.6)) suggests the rise of B_1^+ inhomogeneities as confirmed by Figure 4.6(e) and Figure 4.6(f). A zone where the B_1^+ component is severely reduced (*i.e.* an area where with a weak coil transmit sensitivity) appears both in the axial and coronal slice. The standard deviations, computed on the whole slices, increase by 60 % for the axial slice and about 100 % for the coronal one. Such a B_1^+ distribution results in the coil sensitivity to be strongly affected by the presence of the metallic object and inevitably leads to a degraded MR image quality.

In order to confirm that such behaviours are relative only to elongated metallic objects, the case of a metallic toroid is examined in Figure 4.7. The toroid has an inner and external diameters equal to 60 mm and 100 mm respectively. Due to the toroidal shape, the B_1^+ distortions imputable to an inductive coupling with the coil are expected to be predominant and no longer negligible. In Figure 4.7 the toroid axis lays on the xy-plane to maximize the flux of the magnetic field generated by the birdcage coil. As expected, even if the metallic object is placed in the central position, the B_1^+ distribution results to be distorted both in the axial (Figure 4.7(a)) and coronal (Figure 4.7(b)) slices. The standard deviation, computed for the reduced area represented in Figure 4.7(a), results to be threefold higher than that evaluated in the same area of the axial ($x = 0$) slice in the ideal case. The same comparison highlights an increase of the standard deviation of about 450 % if the coronal slice of Figure 4.7(b) is considered.

4.3 Dielectric coating

A further analysis of the expression for the unbalanced current (4.6) and of the lumped element circuit of Figure 4.4, reveals that another condition for $\bar{I}_u$ to be zero, is represented by the impedances X_C^1 and X_C^2 tending towards infinite. Obviously, such a condition is not physically affordable but a strong reduction of the value of the unbalanced current can be achieved by adding an adequately small capacitance in series to C_1 and C_2 in the equivalent circuit of Figure 4.4. This would result in an equivalent capacitance C_{eq} which is smaller than the smallest capacitance in the series and it is given by:

$$C_{eq} = \left(\frac{1}{C_{Bc-Ph}} + \frac{1}{C_{Ph-Co}} + \frac{1}{C_{Co-Obj}} \right)^{-1} \tag{4.8}$$

where C_{Bc-Ph} is the capacitance between the birdcage coil and the phantom, C_{Ph-Co} is the capacitance between the phantom and the dielectric coating and C_{Co-Obj} is the capacitance between the coating and the metallic object.

In the set-ups of Figure 4.5 this corresponds to cover the metallic cylinder with a low-losses dielectric coating whose electric permittivity is much lower than that of the phantom and selected accordingly to the coating thickness.

Once a coating thickness has been identified, several simulations have been carried out to identify a suitable value of the coating electric permittivity to properly cloak the metallic object restoring the B_1^+ homogeneity to that obtained in the ideal scenario. Otherwise specified, in all the simulations a zero electrical conductivity has been considered for the coating.

In Figure 4.8 three different coating thickness/permittivity combinations are examined. In Figures 4.8(a),(b),(c),(d) a 1 mm thickness coating is considered with a relative permittivity equal to 0.1 in Figures 4.8(a),(b) and to 0.4 in Figures 4.8(c),(d). Finally, a 10 mm coating with a relative permittivity equal to 1 (*i.e.* that of vacuum) is examined in Figures 4.8(e),(f). In Figures 4.8(a),(b) the B_1^+ homogeneity is restored to values fully comparable with that of the ideal case depicted in Figures 4.6(a),(b) both for the axial and coronal planes. The whole slice standard deviations decrease by 40 % considering the axial slice and by 45 % considering the coronal one with respect to the uncoated cylinder set-up of Figure 4.6(e),(f). The improvement (*i.e.* the decrease) of the standard deviations become even more appreciable if the reduced area is considered. The standard deviations decrease with respect to the uncoated cylinder case by approximately 55 % for

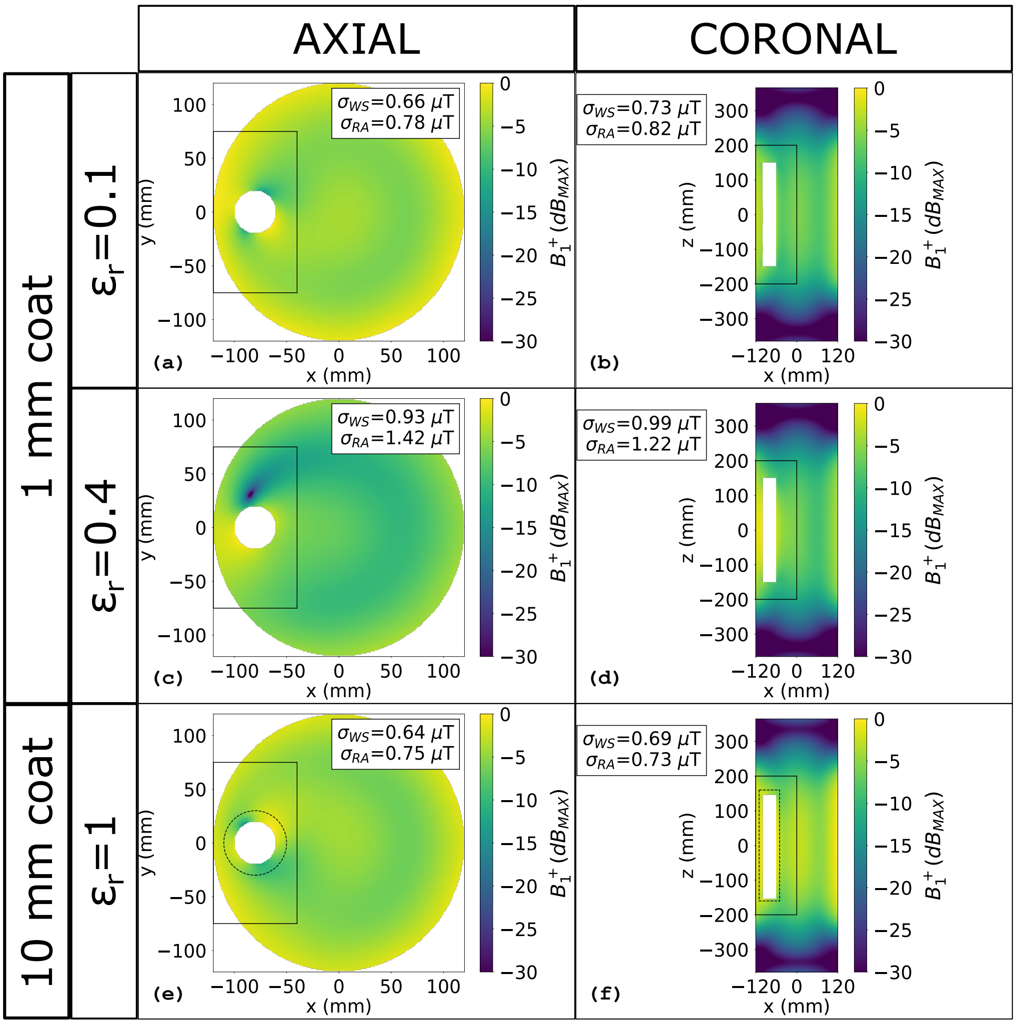

Figure 4.8: $B_1^+(\mathrm{dB_{MAX}})$ evaluated with the coated metallic cylinder placed in a lateral position ($x = -80$ mm). The results are shown both for the axial plane $z = 0$ ((a), (c) and (e)) and for the coronal plane $y = 0$ ((b), (d) and (f)). In (a) and (b) a 1 mm coating with a relative electric permittivity equal to 0.1 is considered. In (c) and (d) the same coating thickness with a relative electric permittivity equal to 0.4 is considered. Finally in (e) and (f), the distribution is relative to a 10 mm coating with a relative electric permittivity equal to 1. The dashed lines in (e) and (f) are representative for the coating. The continuous line rectangles represent the reduced areas in which the standard deviation (σ_{RA}) is computed. σ_{WS} represents the standard deviation computed on the whole slice.

both the axial and coronal slice. The result is analogous when a 10 mm coating with the electric permittivity of vacuum (Figure 4.8(e),(f)) is considered. In this case, the coating permittivity needed to achieve a proper cloaking result, can be increased with respect to the previous case at the expenses of a thicker coating. Finally, Figures 4.8(c),(d) show an “intermediate” case where the thickness of the coating has been kept to 1 mm with an electric permittivity that is fourfold that considered in Figures 4.8(a),(b). The results show that, even if an improvement of the standard deviations is appreciable with respect to the uncoated cylinder scenario of Figures 4.6(e) and (f), the $\boldsymbol{B}_1^+$ homogeneity is not fully satisfactory. In particular, a zone where the $\boldsymbol{B}_1^+$ component is strongly reduced appears in the axial slice near the cylinder. The last case is useful to give a qualitative idea about the sensitivity of the dielectric coating effectiveness as a function of the selected permittivity value.

The proportionality between the coating thickness and relative permittivity needed to achieve a specific improvement of the standard deviations (see Figures 4.8(a),(b) and Figures 4.6(e),(f)) seems to confirm the capacitive behaviour of the coating. In fact, let us consider the following approximated expression of the coating capacitance:

$$C \approx \frac{\int_S \boldsymbol{D} \cdot \boldsymbol{dS}}{\int_R \boldsymbol{E} \cdot \boldsymbol{dr}} \tag{4.9}$$

where $\boldsymbol{D}$ is the dielectric induction, $\boldsymbol{S}$ represents the surface separating the coating from the phantom, $\boldsymbol{E}$ is the electric field and $\boldsymbol{R}$ may be, theoretically, a generic line going from the metal surface to the phantom.

In a linear, isotropic and homogeneous medium, the above equation can be written as:

$$C \approx \frac{\epsilon \int_S \boldsymbol{E} \cdot \boldsymbol{dS}}{\int_R \boldsymbol{E} \cdot \boldsymbol{dr}} \tag{4.10}$$

where ϵ represents the electric permittivity of the coating. Focusing on the integral in the denominator some considerations can be made. Firstly, if we suppose that the dielectric phantom is replaced with a metallic object, the line integral value would be the same for any line going from one metallic surface to the other. Actually, since the phantom is not metallic, it is not guaranteed that the points along the phantom-coating interface are equipotential. However, the phantom permittivity is much higher than that of the coating and, due to the boundary conditions between the phantom and the coating, the electric field inside the coating and near the phantom-coating surface tends to be almost normal to such a surface. It follows that, a surface parallel to the phantom-coating boundary and slightly moved toward the prosthesis may be approximated to be equipotential[5]. As a consequence of the mean-value theorem[6], the capacitance may be expressed as:

$$C \approx \frac{\epsilon \int_S \boldsymbol{E} \cdot \boldsymbol{dS}}{s\,\widetilde{E}} \tag{4.11}$$

where s represents the coating thickness and $\widetilde{E}$ is the the electric field multiplied by the cosine of the angle between the electric field and a line directed along the coating thickness. Even if approximated, relation (4.11) gives reason for the opposite roles of the coating thickness and electric permittivity observed in Figure 4.8 and confirmed by the simulation results presented below.

To further investigate the behaviour of the coating, the standard deviations of the B_1^+ component obtained for the axial slice ($z = 0$) when the metallic cylinder is placed laterally ($x = -80$ mm) inside the phantom, are reported in Figure 4.9 for different values of coating thickness and electric permittivity. In Figure 4.9(a) the standard deviations are relative to the whole slice and, in Figure 4.9(b), only to the reduced area embracing the cylinder. In the lower parts of the panel, a relative permittivity from 0.1 to 1 is considered together with a coating thickness from 1 mm to 10 mm and some combinations are reported. The curves in the upper part of the panel are relative to a coating with a 1 mm thickness whose relative permittivity changes from 0.1 to 61.5 (*i.e.*, the phantom permittivity).

Some considerations can be made analyzing the data reported in the bottom matrices. Both for the whole slice (a) and the reduced area (b), the standard deviations on the main diagonal keep almost constant. This represents a further confirmation for the opposite role that coating thickness and permittivity values play in cloaking the metallic object.

Another interesting standard deviation behaviour is obtained considering a fixed coating thickness and increasing the relative permittivity value. The uncoated scenario can be considered as the coated case where the coating electric permittivity is equal to that

---

[5] These considerations are valid in electrostatic. At radiofrequency, the electric field is no longer irrotational and the time derivative of the magnetic vector potential should be taken into account in order to make the integral along $\boldsymbol{R}$ depending only on the starting and ending point of the integration path. Furthermore, the orthogonality of the electric field to the phantom-coating surface, do not represent anymore a condition for equipotentiality. Neglecting this aspect leads to an approximation that may, theoretically, invalidate the physical meaning of a lumped capacitor and a lumped element circuit in general. However, full-wave simulations showed that, for the specific application, this approximation may be considered, at first instance, suitable.

[6] The result derives from: $\int_R \boldsymbol{E} \cdot \boldsymbol{dr} = \int_{r_1}^{r_2} E(r) \cos\phi(r) dr$ where $\phi(r)$ is the angle between $\boldsymbol{E}$ and the integration curve $\boldsymbol{R}$. Defining $\widetilde{E}$ as the average of $E(r)\cos\phi(r)$ evaluated over $\boldsymbol{R}$, for the mean value theorem for integrals [97], we have that the previous intergal is equal to $(r_2 - r_1)\widetilde{E}$. Selecting a curve $\boldsymbol{R}$ normal both to the metal surface and the phantom, the relation is equal $s\widetilde{E}$ where s is the coating thickness.

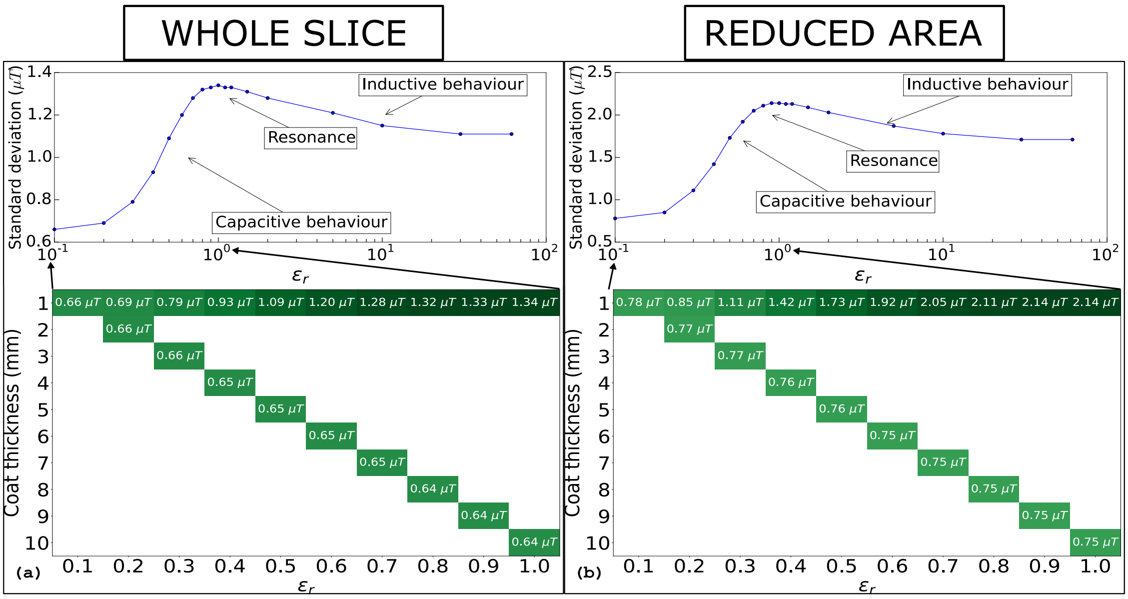

Figure 4.9: Standard deviations of the B_1^+ component evaluated for the metallic cylinder placed laterally ($x = -80$ mm) inside the phantom. The axial slice ($z = 0$) is considered both in (a) and in (b). The whole slice and reduced area standard deviations are reported in (a) and (b) respectively (see the maps in the bottom part of the figure). In the maps, different values of coating permittivity and thickness are considered. The curves in the upper part of the figure refer to the same standard deviations but accounting for a 1 mm coating thickness and for a permittivity range which is larger than that reported in the maps below.

of the phantom[7]. In this framework, the curves in the upper part of Figure 4.9 show that, for a coating thickness equal to 1 mm, the standard deviation reaches values which are higher than those obtained with the uncoated cylinder. This particular trend is observed both dealing with the whole slice standard deviations and with those relative to the reduced area.

An easy qualitative explanation for the non-monotonic trend can be obtained considering the generic series of a capacitance (whose value is proportional to a generic electric permittivity value) and an inductance supplied by an AC voltage generator. For low values of electric permittivity, the capacitive reactance predominates over the inductive one. In particular, when a zero permittivity value (*i.e.* zero capacitance) is considered, the series behaves like an open circuit with a zero current flowing from the voltage generator. If the permittivity value increases, the capacitive reactance approaches the inductive one. When they become equal, a resonance occurs and the series behaves like

---

[7] The differences between the two cases are due to the different values of electrical conductivity of the coating (*i.e.* 0 S m^{-1}) and of the phantom (*i.e.* 0.87 S m^{-1}) considered in the simulations.

a short circuit. In this condition, an infinite current is potentially supplied by the voltage generator. Finally, if the permittivity value increases further, the circuit becomes inductive and the value of the current that flows in the circuit is mainly determined by the value of the inductive reactance.

The behaviour of the lumped element circuit of Figure 4.4 can be comparable with that described above for specific choices of its parameters. Considering the correlation identified between the standard deviation of the B_1^+ component and the unbalanced current (4.6) (which is proportional to I_Z), the lumped element circuit is found to be able to give a reason for the particular standard deviation trends depicted in Figure 4.9. The damped behaviour of the standard deviation curves can be described by (4.6) provided that the non-zero electrical conductivity of the phantom is considered in the lumped element equivalent circuit. To this end, two resistances have to be parallel connected to C_1 and C_2 in the circuit of Figure 4.4.

Figure 4.10 reports the same standard deviation values already shown in the upper panels of Figure 4.9 together with the trend of the unbalanced current amplitude as a function of the coating relative electric permittivity ϵ_r. The parameters of the equivalent circuit of Figure 4.4 have been estimated through a fitting procedure by means of the "Curve Fitting Tool" of MATLAB® using a the non-linear least squares method. In particular, two generic capacitive reactances, proportional to $1/\epsilon_r$, have been considered in series to L_1 and L_2 to describe the effect of the coating relative permittivity. In the upper part of Figure 4.10, the whole slice standard deviation is considered. The values of the parameters of the equivalent circuit that led to the unbalanced current trend reported in the figure are the following: $V_1 = 1.69\,\mathrm{V}$; $V_2 = 1.54\,\mathrm{V}$; $L_1 = 2.38\,\mathrm{nH}$; $L_2 = 4.73\,\mathrm{nH}$; $C_1 = 0.557\,\mathrm{nF}$; $C_2 = 0.474\,\mathrm{nF}$; $R_1 = 3\,\Omega$; $R_2 = 5.95\,\Omega$; $Z = 0.04\mathrm{i}\,\Omega$. R_1 and R_2 represent the resistances in parallel to C_1 and C_2 respectively and are not depicted in Figure 4.4.

The same procedure has been applied to obtain the result shown in the lower part of Figure 4.10 where the standard deviation relative to the reduced area embracing the metallic cylinder is considered. The values of the equivalent circuit parameters are for the relevant case: $V_1 = 3.95\,\mathrm{V}$; $V_2 = 3.47\,\mathrm{V}$; $L_1 = 1.18\,\mathrm{nH}$; $L_2 = 5.81\,\mathrm{nH}$; $C_1 = 0.31\,\mathrm{nF}$; $C_2 = 0.37\,\mathrm{nF}$; $R_1 = 1.35\,\Omega$; $R_2 = 9\,\Omega$; $Z = 0.09\mathrm{i}\,\Omega$.

Differently from the unbalanced current value, the standard deviation does not tend to zero for near-zero coating relative permittivities. In order to account this difference, obtaining the comparable trends of Figure 4.10, a costant current value equal to 0.66 A and 0.78 A has been summed to the unbalanced current amplitude when it is compared to the whole slice and reduced area standard deviations respectively.

Some considerations are needed considering the results shown in Figure 4.10. The good agreement between the unbalanced current trend and the data obtained by means of full-wave numerical simulations (root mean squared error equal to 1.2×10^{-2} and 1.7×10^{-2} for the whole slice and reduced area respectively), suggests that the lumped element circuit proposed in Figure 4.4 is suitable to give a qualitative description of the phenomenon. However, it is worth saying that analogous fitting results could be obtained

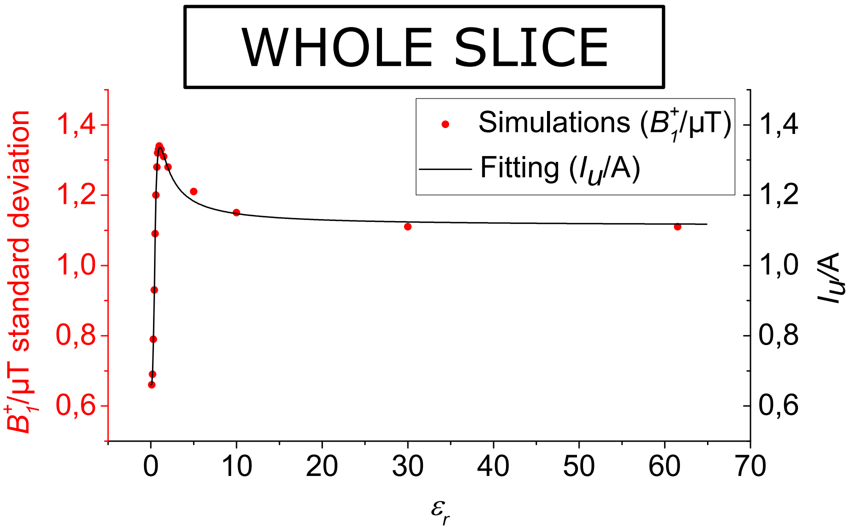

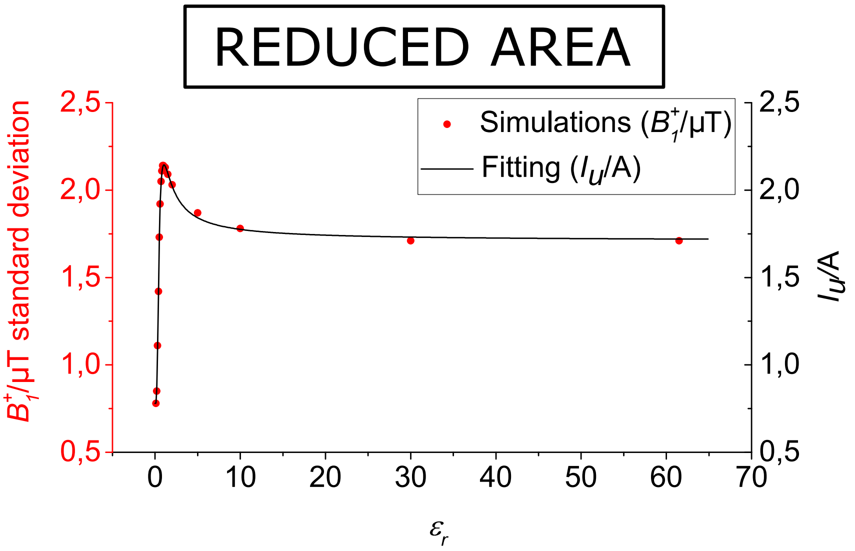

Figure 4.10: Axial slice ($z = 0$) numerical value of the standard deviation of the B_1^+ component evaluated for the metallic cylinder placed laterally ($x = -80$ mm) inside the phantom. The numerical value of the unbalanced current behaviour, obtained through a fitting procedure, is also reported as a function of the coating relative permittivity.

considering different circuital parameters. Furthermore, the considered circuit accounts for the capacitive coupling of only one among the four planar loops in which the 8-leg birdcage coil is decomposed. It turns out that, as already specified, the equivalent circuit should not be intended as an alternative to numerical simulations able to return quantitative results but as a qualitative tool to give a simple and intuitive description

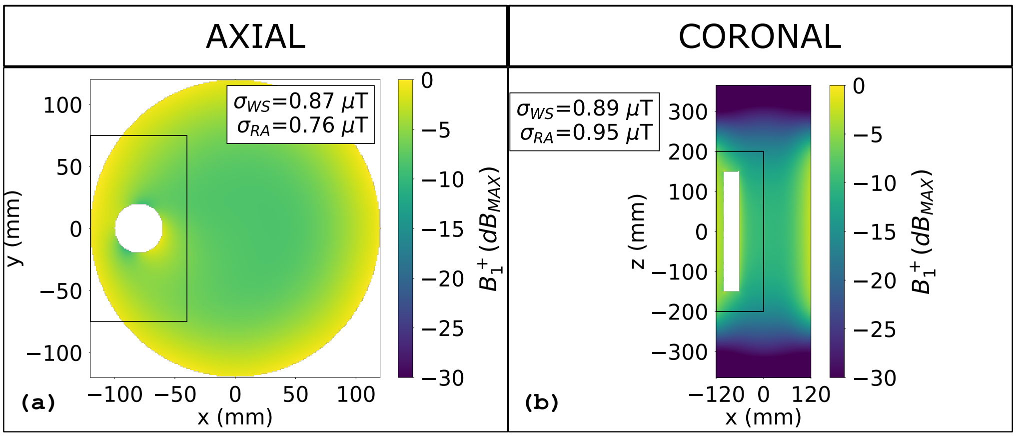

Figure 4.11: B_1^+(dB$_{\text{MAX}}$) evaluated with the coated cylinder placed laterally into the phantom. Results are shown both on the axial plane $z = 0$ (a) and on the coronal plane $y = 0$ (b). The object is covered by a 1 mm thick, anisotropic coating. The coating relative permittivity is equal to 0.1 along the direction normal to the cylinder surface and 2.5 along the other directions.

of a complex physical phenomenon.

To further study the coating electromagnetic behaviour in the pursuit of defining the required constraints of a possible coating material (see also conclusion), an anisotropic permittivity has been examined. Figure 4.11 shows the B_1^+ component distribution when the metallic cylinder is placed laterally inside the phantom and it is covered by a coating with an anisotropic electric permittivity. The relative electric permittivity is assumed to be 0.1 along the direction normal to the covered cylinder faces and to 2.5 (a value observable in some common dielectric materials) along the other two main directions. All the tensor off-diagonal terms have been settled to zero. As usal, the B_1^+ component distribution is proposed both for the axial ($z = 0$) and coronal ($y = 0$) slices. In spite of the twenty-five fold higher electric permittivity along the axial and tangential directions, the effectiveness of the coating keeps to be noticeable. In particular, the standard deviations relative to the reduced areas embracing the metallic cylinder decrease by approximately 50 % for both planes with respect to the uncoated cylinder case. This result gives reason for the hypothesis of a capacitive coupling between the coil and the metallic cylinder whose effects, in terms of B_1^+ homogeneity, are attenuated by the presence of the coating. The differences appreciable comparing Figure 4.11 with the results obtained with the 0.1 relative permittivity isotropic coating (Figures 4.8(a) and (b)) may be originated by the distribution of the electric field near the coating edges. In these zones, due to the particular coating geometry and permittivity tensor, the direction of the electric field does not correspond to that along which the relative permittivity is equal to 0.1.

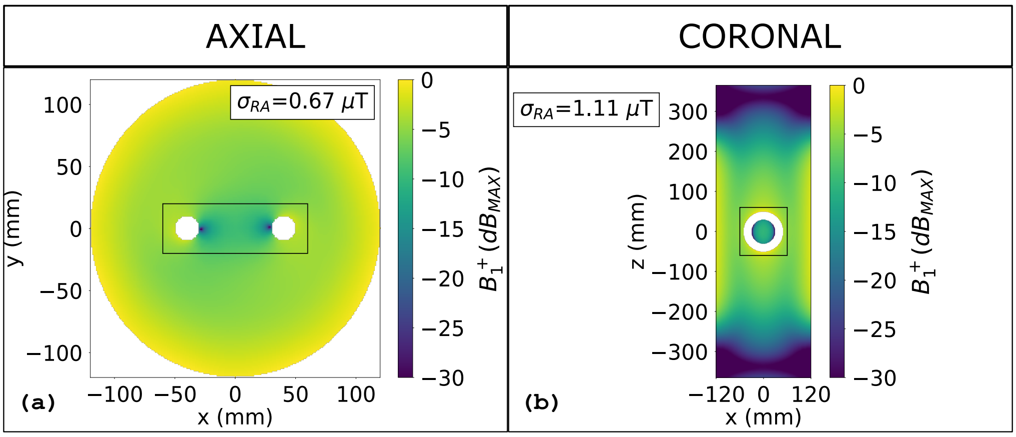

Figure 4.12: $B_1^+(\mathrm{dB}_{\mathrm{MAX}})$ evaluated when a metallic toroid is placed into the centre of the phantom. The toroid is covered by a 1 mm dielectric coating with an electric permittivity equal to 0.1. Results are shown both for the axial plane $z = 0$ (a) and and for the coronal plane $y = 0$ (b). The rectangles represent the reduced areas in which the standard deviation (σ_{RA}) is computed.

Finally, to verify that the coating effect is prevalently related to the capacitive coupling between the metallic object and the antenna, the case of a metallic toroid is considered again. Figure 4.12 shows the B_1^+ component distribution when the same toroid considered in Figure 4.7 is coated by a 1 mm dielectric coating with an isotropic relative permittivity equal to 0.1. Neither for the reduced area considered on the axial slice nor for that in the coronal one, a significant standard deviation improvement is appreciable. In particular, they keep to be far from those measured in the ideal case being 170 % and 430 % higher considering the axial and coronal slice respectively, demonstrating that the coating effects on the inductive couplings are negligible.

4.4 Hip prosthesis

In order to explore and extend the results obtained considering the metallic cylinder to a more practical case, the model of the femoral stem of a realistic hip prothesis (220 mm height) has been considered (Figure 4.13(a)). As for the metallic cylinder, the prosthesis has been simulated as PEC and the same simulation set-up described in the previous sections has been adopted (Figure 4.13(b)). The particular shape of the considered prosthesis leads to two main differences with respect to the cylindrical one. The first is relative to the asymmetrical shape of the prosthesis. In principle, such an asimmetry may lead to a variation of the coating effectiveness which should be investigated. Secondly, as the coating thickness increases, the prosthesis shape is inevitably modified. This aspect can potentially lead to a variation of the standard deviation sensitivity to

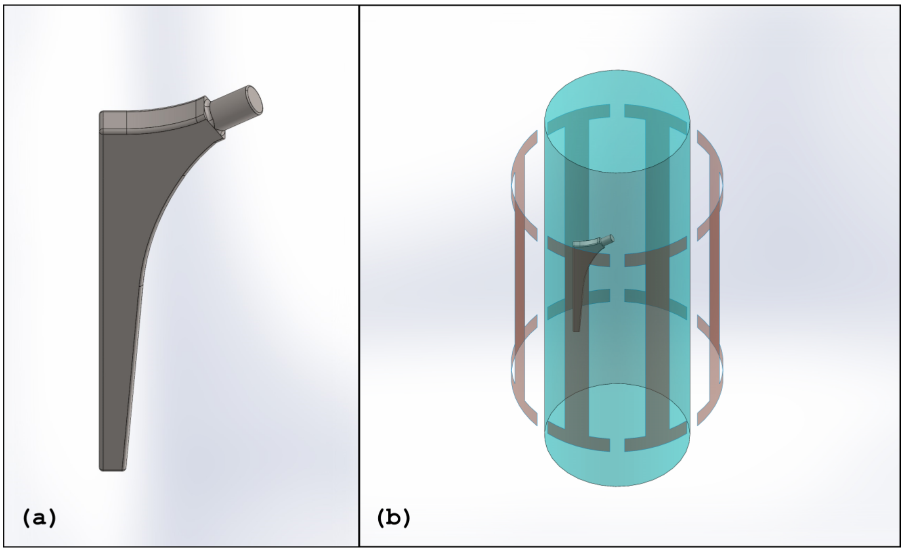

Figure 4.13: Model of a realistic hip prosthesis stem (a). Simulation set-up involving the realistic hip stem model placed laterally ($x = -80\,\text{mm}$ from the phantom centre to the prosthesis base centre) into the cylindrical phantom.

the coating thickness changing the mutual roles of coating thickness and electric permittivity.

In Figures 4.14(a),(b) the B_1^+ component distribution is reported for the axial ($z = 0$) and coronal ($y = 0$) slices when the uncoated hip prosthesis model is placed laterally ($x = -80\,\text{mm}$) inside the phantom. Even if the presence of the metallic prosthesis leads to a B_1^+ perturbation that is less significant with respect to that relevant to the uncoated metallic cylinder (Figures 4.6(e),(f)), the standard deviation still shows a significant increase if compared to those of the ideal case (Figures 4.6(a),(b)). In particular, an increase up to about 50 % and 70 % of the whole slice standard deviations is appreciable for the axial and coronal slices respectively.
In order to have a term of reference with the metallic cylinder scenario, Figures 4.14(c),(d) depict the B_1^+ component distribution when the prosthesis is coated with the 1 mm, 0.1 relative permittivity lossless coating. As for the cylinder case, such a coating restores the B_1^+ homogeneity to that obtained in the ideal case (Figures 4.6(a),(b)) with an improvement up to 60 % of the standard deviation evaluated in the reduced areas.

Other results are shown in Figure 4.15 considering the lateral realistic hip prosthesis model. In particular, for a coating thickness equal to 1 mm and 3 mm, the maximum relative permittivity values that lead to standard deviation values within ±5 % of those obtained in the ideal case, are reported. In Figures 4.15(a) and (b) the prosthesis is covered by a 1 mm coating with a 0.4 relative permittivity. Even if the relative permittivity is fourfold higher than that used in Figures 4.14(c) and (d), the standard deviations keep to be comparable to those obtained in the ideal scenario. Such a result puts in evidence that the sensitivity of the coating effectiveness to the relative permittivity results to be

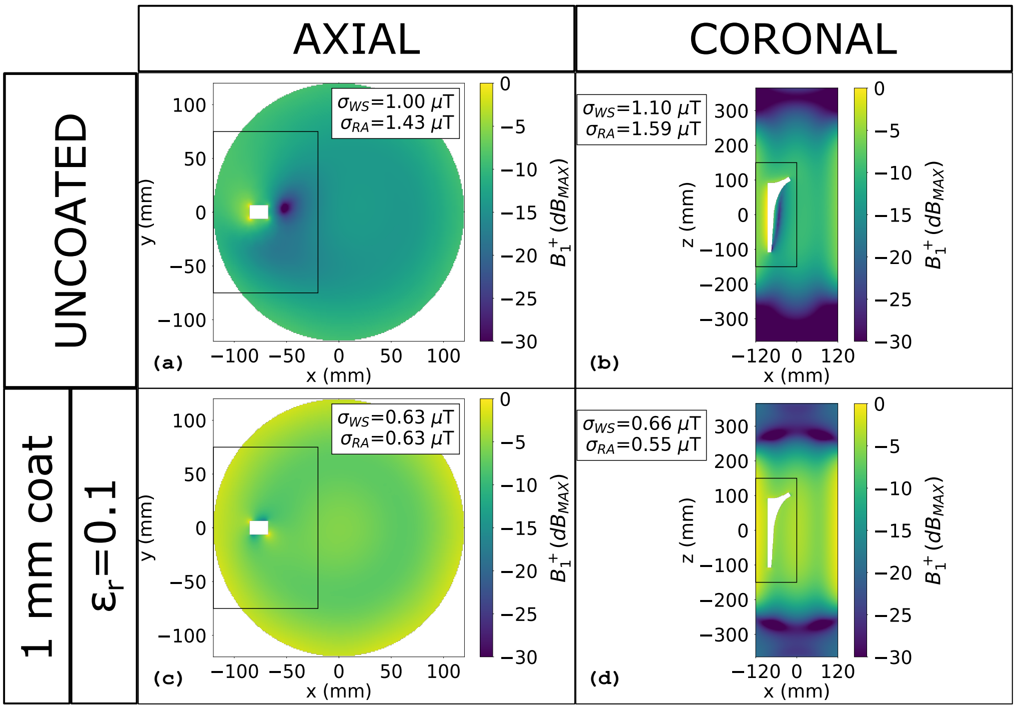

Figure 4.14: B_1^+(dB$_{\mathrm{MAX}}$) evaluated with the realistic hip prosthesis stem placed laterally ($x = -80$ mm) inside the phantom. In (a), (c) the $z = 0$ axial slice and, in (b), (d), the $y = 0$ coronal one are considered. (a), (b) are relevant to the uncoated hip prosthesis and (c), (d) to the coated (relative permittivity equal to 0.1, coating thickness equal to 1 mm) one. The rectangles represent the reduced areas in which the standard deviation (σ_{RA}) is computed. σ_{WS} represents the standard deviation computed on the whole slice.

strongly reduced with respect that of the metallic cylinder (Figures 4.8(c),(d)). Indeed, a relative permittivity increase from 0.1 to 0.4 caused a standard deviation increase up to 82 % for the cylinder which is reduced to 6 % for the prosthesis.
Figures 4.15(c),(d) also show that, considering a 3 mm thick coating, a relative permittivity equal to 1.3 is enough to restore the standard deviations to those obtained in the ideal case.
Further simulations confirmed, even for the prosthesis model, that the proportionality between the coating thickness and relative permittivity bring to comparable cloaking results. However, the absolute values of coating permittivity and thickness, needed to restore the B_1^+ homogeneity, is no longer the same identified for the cylinder. This aspect confirms the influence of the geometrical shape of the metallic object on the coating optimum parameters.

In a practical application, the prosthesis surface would be placed close to different tissues with different electrical properties. Furthermore, the uncertainty with which

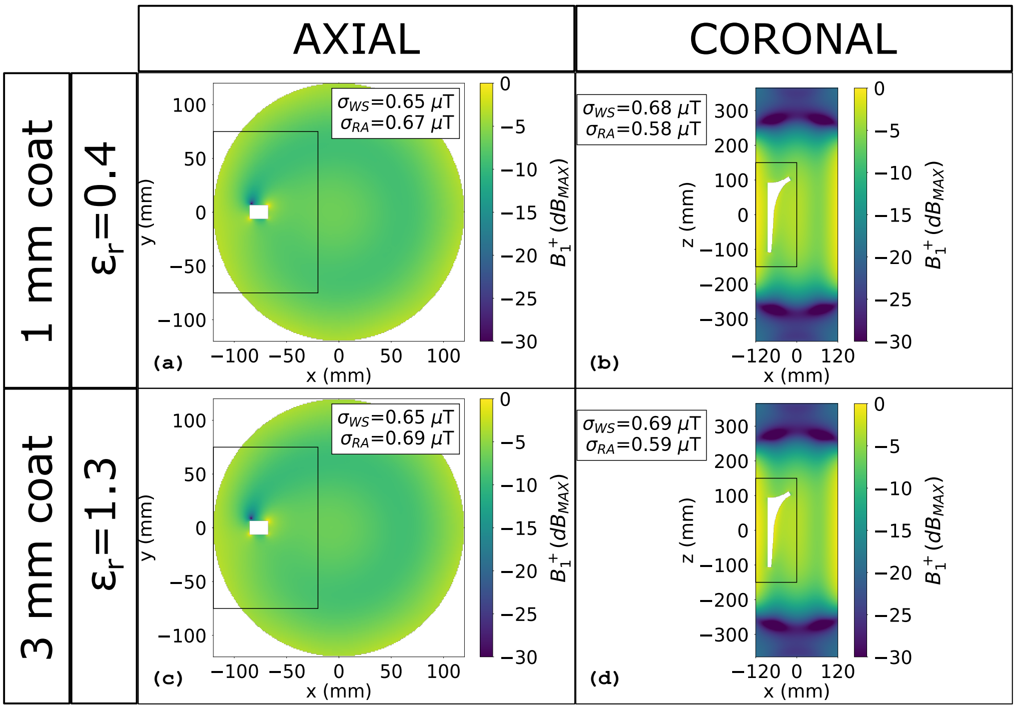

Figure 4.15: B_1^+(dB$_{\text{MAX}}$) evaluated with the realistic hip prosthesis stem placed laterally ($x = -80$ mm) inside the phantom. Results are shown both for the $z = 0$ axial slice and for the $y = 0$ coronal one. In (a) and (b) the prosthesis model is covered by a 1 mm coating with a 0.4 relative permittivity. In (c) and (d) the prosthesis model is covered by a 3 mm coating with a 1.3 relative permittivity. The rectangles represent the reduced areas in which the standard deviation (σ_{RA}) is computed. σ_{WS} represents the standard deviation computed on the whole slice.

such parameters are measured suggests the importance of the investigation of the coating behaviour in phantoms with different electrical properties. To achieve this result, the phantom permittivity has been varied by ±30 % and the results are proposed in Figures 4.16 and 4.17. In Figure 4.16, the relative permittivity of the phantom is equal to 43. In Figures 4.16(a) and (b), the ideal case is reported both for the axial ($z = 0$) and coronal ($y = 0$) slices. A slight increase of the standard deviation with respect to Figures 4.6(a),(b) is appreciable for both the slices. This represents an effect of the different wavelength in the phantom due to its lower electric permittivity and proves that propagation effects cannot be neglected to have accurate results.
Figures 4.16(c) and (d) show the B_1^+ component distribution when the uncoated hip prosthesis stem is placed laterally ($x = -80$ mm) into the phantom. An increase of the standard deviation computed on the whole slice with respect those of the empty phantom (Figures 4.16(a),(b)) of about 40 % and 60 % is appreciable for the axial and coronal slice respectively. The presence of a 1 mm coating with a relative permittivity equal to

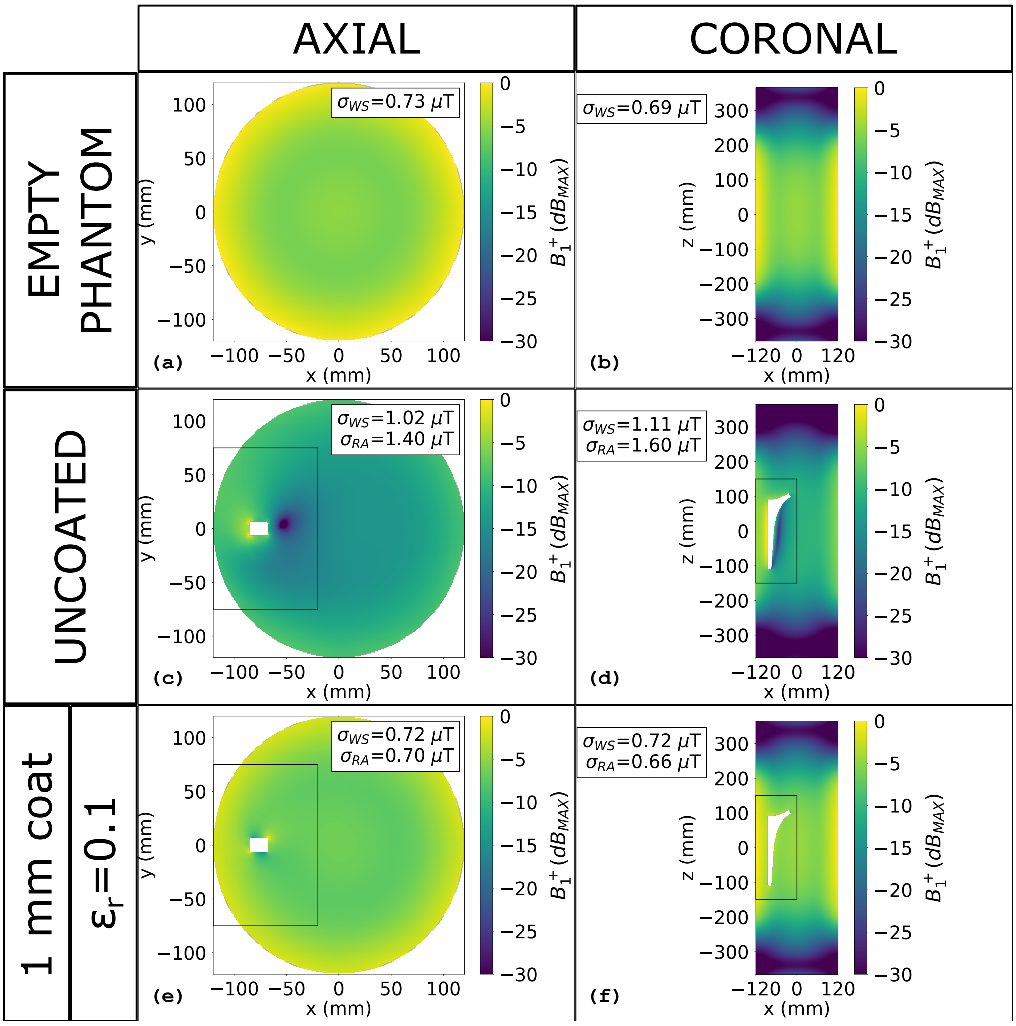

Figure 4.16: $B_1^+(\mathrm{dB_{MAX}})$ evaluated with the empty phantom (a),(b), with the uncoated hip prosthesis stem placed laterally ($x = -80$ mm) inside the phantom (c),(d) and with the coated (coating relative permittivity equal to 0.1 and coating thickness equal to 1 mm) hip prosthesis stem placed in the same position (e),(f). The phantom relative electric permittivity is equal to 43. Results are shown both for the $z = 0$ axial slice and for the $y = 0$ coronal one. The rectangles represent the reduced areas in which the standard deviation (σ_{RA}) is computed. σ_{WS} represents the standard deviation computed on the whole slice.

0.1 (Figures 4.16(e),(f)) brings the standard deviations to be again comparable to those obtained for the empty phantom confirming the behaviour of the coating even for a lower phantom permittivity. In particular, the standard deviations evaluated in the reduced areas decrese by 50 % and around 60 % with respect to those relative to the uncoated case for the axial and coronal slice respectively.

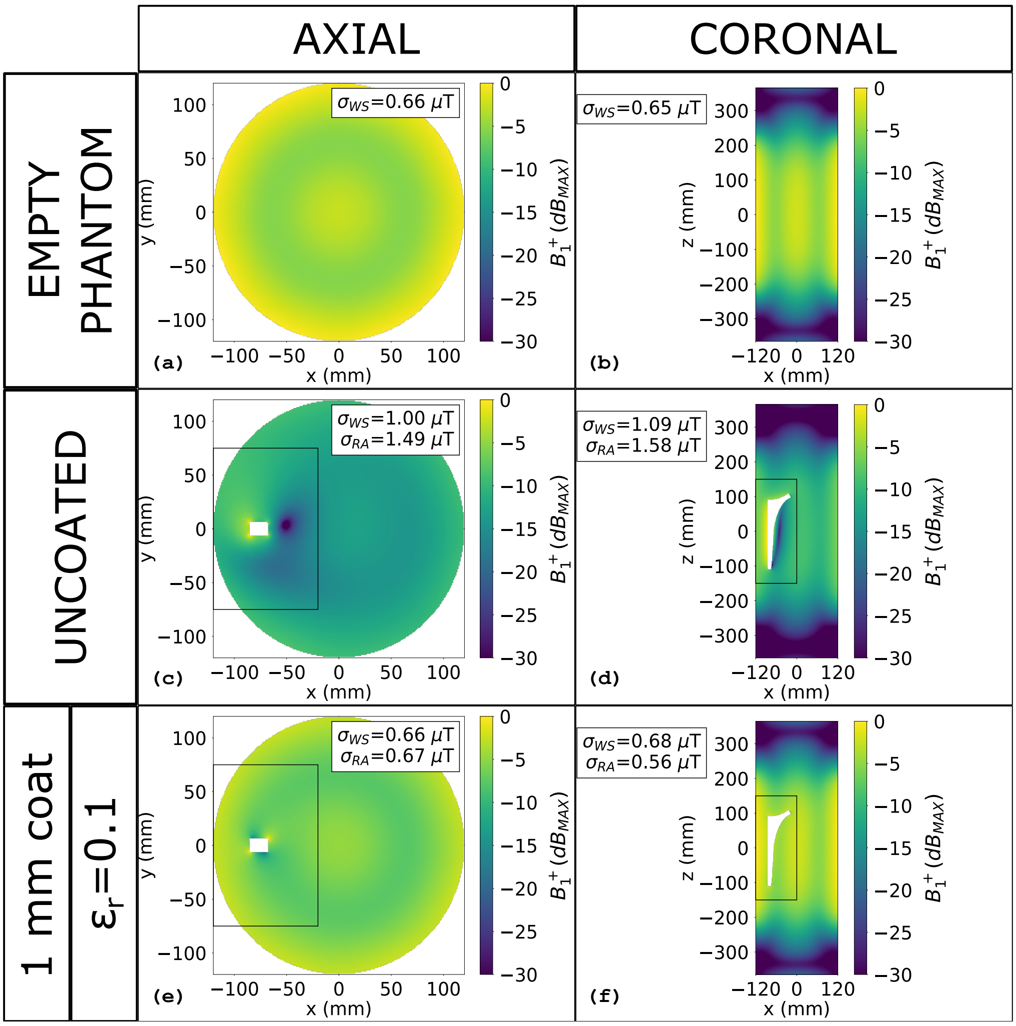

Figure 4.17: $B_1^+(\mathrm{dB}_{\mathrm{MAX}})$ evaluated with the empty phantom (a),(b), with the uncoated hip prosthesis stem placed laterally ($x = -80$ mm) inside the phantom (c),(d) and with the coated (coating relative permittivity equal to 0.1 and coating thickness equal to 1 mm) hip prosthesis stem placed in the same position (e), (f). The phantom relative electric permittivity is equal to 81. Results are shown both for the $z = 0$ axial slice and for the $y = 0$ coronal one. The rectangles represent the reduced areas in which the standard deviation (σ_{RA}) is computed. σ_{WS} represents the standard deviation computed on the whole slice.

The same set-ups are considered in Figure 4.17 with a relative permittivity of the phantom equal to 81. In Figures 4.17(a) and (b) the empty phantom scenario is reported. Also in this case the propagation effects can be appreciated considering the slight decrease of the standard deviations with respect to those of Figures 4.6(a) and (b). The standard deviations increase, obtained when the uncoated hip prosthesis stem is placed laterally into the phantom, is comparable to that observed in the previous case. In particular, they increase by around 50 % and 65 % with respect to the empty phantom case (Figures 4.17(a),(b)). The coating efficacy is demonstrated also in this case, leading the $\boldsymbol{B}_1^+$ distribution to be again comparable to that obtained with the empty phantom (Figures 4.17(e),(f)). In fact, the 1 mm coating with 0.1 relative permittivity reduces the standard deviation up to 37 % and 65 % for the whole slices and the reduced areas respectively.

Finally, in order to account for a possible variation of the antenna-prosthesis couplings due to a metallic shield sorrounding the coil, in Figure 4.18 the $\boldsymbol{B}_1^+$ component distribution is considered for a shield radius equal to 225 mm. The shield height is equal to 750 mm and it has been simulated as PEC. Figures 4.18(a) and (b) show the empty phantom $\boldsymbol{B}_1^+$ distribution both for the $z = 0$ axial slice and for $y = 0$ coronal one. The effects of the shield are appreciable considering the standard deviation decreases with respect to the unshielded coil scenario (Figures 4.6(a),(b)). The presence of the hip prosthesis stem, laterally placed into the phantom, leads to a whole slice standard deviation increase equal to 50 % and 70 % with respect to the empty phantom case for the axial and coronal slices respectively (Figures 4.18(c),(d)). The effectiveness of the 1 mm thick, 0.1 relative permittivity dielectric coating is confirmed also in this last case (Figures 4.18(e),(f)). The standard deviations in the whole slice are close to those computed with the empty phantom. Furthermore, a standard deviation decrease up to 65 % is observed if the reduced areas are considered.

All the results presented above are relative to the birdcage coil supplied at 128 MHz which approximately represents the Larmor frequency associated with a static magnetic field of 3 T for 1H nuclei excitation. Even if all the evaluations conducted at such a frequency are particularly interesting because of the strong couplings between the coil and the external metallic object, today, the majority of installed MRI clinical scanners are associated with a static magnetic field of 1.5 T and operate at 64 MHz. For this reason, an analysis of the coating behaviour at this frequency represents an important contribution as well.

Figures 4.19(a) and (b) show the $\boldsymbol{B}_1^+$ component distribution evaluated into the same phantom of Figures 4.6(a),(b) when the birdcage coil is supplied at 64 MHz. In order to account for the different coil load due to the different frequency values, the power ingoing to the coil has been modified to obtain the same magnetic field in the empty phantom centre. As expected, the $\boldsymbol{B}_1^+$ component presents more homogeneous distributions than those obtained at 128 MHz both considering the $z = 0$ axial slice and the $y = 0$ coronal one. In particular, the standard deviations computed on the whole slices are about 50 % and 70 % of those obtained at the higher frequency (Figures 4.6(a),(b)) considering the axial and coronal slice respectively. This result is due to the longer wavelength which is no more comparable with the phantom dimensions. This reflects on the central and lateral brightenings of the chromatic maps of Figures 4.6(a),(b) which become no more appreciable in Figures 4.19(a) and (b).

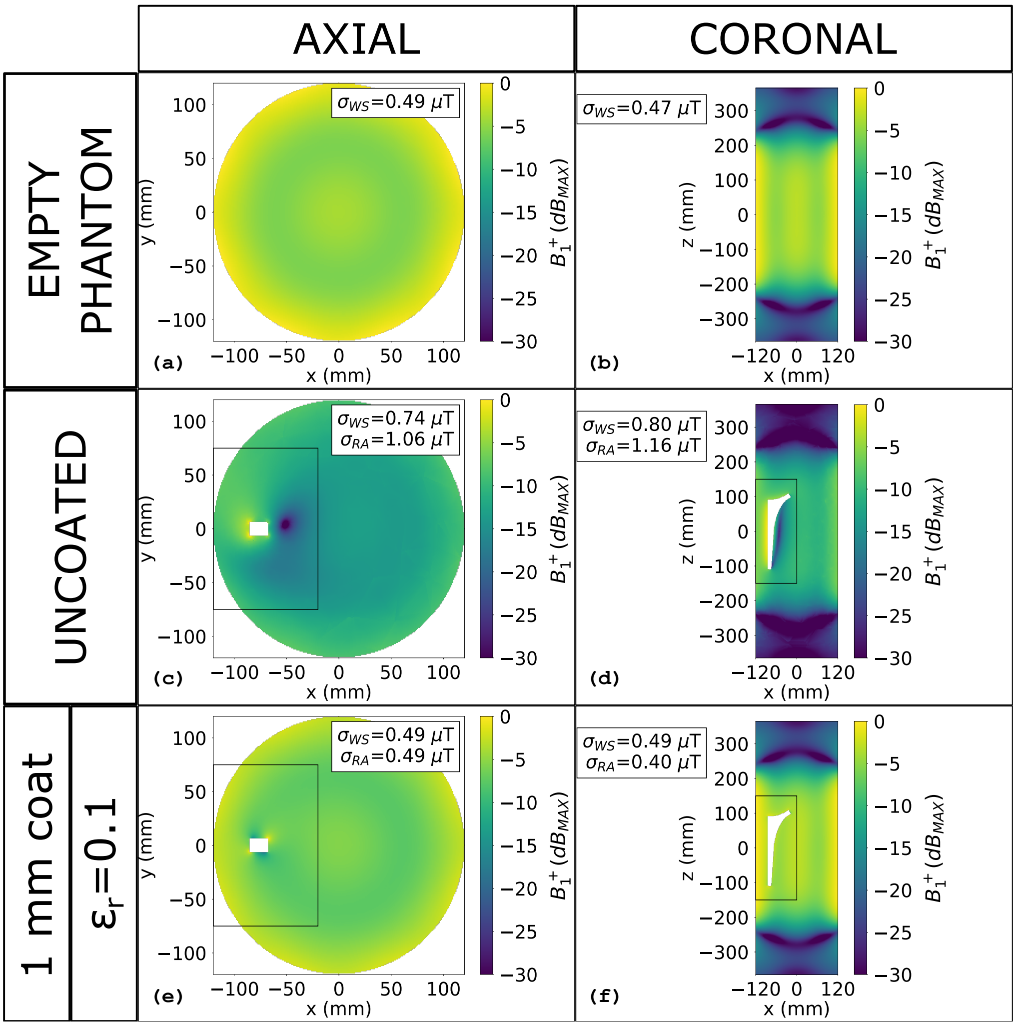

Figure 4.18: B_1^+(dB$_{\text{MAX}}$) evaluated with the empty phantom (a),(b), with the uncoated hip prosthesis stem placed laterally ($x = -80$ mm) inside the phantom (c),(d) and with the coated (coating relative permittivity equal to 0.1 and coating thickness equal to 1 mm) hip prosthesis stem placed in the same position (e),(f). The birdcage coil is surrounded by a metallic shield (simulated as PEC) with a radius equal to 225 mm and an height equal to 750 mm. Results are shown both for the $z = 0$ axial slice and for the $y = 0$ coronal one. The rectangles represent the reduced areas in which the standard deviation (σ_{RA}) is computed. σ_{WS} represents the standard deviation computed on the whole slice.

The standard deviation values increase by about 300 %, in the axial slice, and by about 95 %, in the coronal one, if the hip stem model is placed laterally ($x = -80$ mm) inside the phantom.

With reference to the equivalent circuit of Figure 4.4, both the induced voltages and

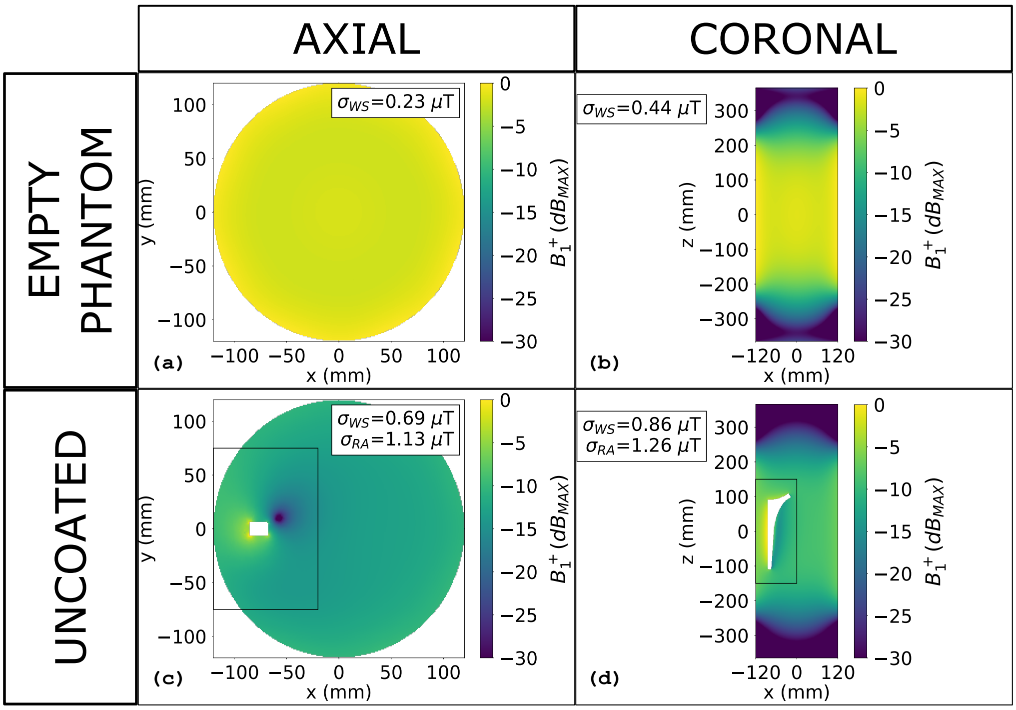

Figure 4.19: B_1^+(dB$_{\text{MAX}}$) evaluated at 64 MHz with the empty phantom ((a) and (b)) and with the uncoated hip prosthesis stem model placed in a lateral position ($x = -80$ mm) into the phantom ((c) and (d)). The results are shown both for the axial plane $z = 0$ ((a), (c)) and for the coronal plane $y = 0$ ((b), (d)). The rectangles represent the reduced areas in which the standard deviation (σ_{RA}) is computed. σ_{WS} represents the standard deviation computed on the whole slice.

the reactances depend on frequency. In particular, when the frequency value decreases from 128 MHz to 64 MHz, the induced voltages V_1 and V_2 and the inductive reactances halve whereas the capacitive reactances double. When the coating capacitance is considered, the inductive reactances become smaller than the capacitive ones (see “Capacitive behaviour” zone of Figure 4.9) and can be neglected. It turns out that the same current $\bar{I}_Z$ (*i.e.* the artefacts reduction) is expected to be achievable, at this frequency, with a coating permittivity much higher than that needed at 128 MHz. Such a prediction is confirmed by Figure 4.20 which shows some results relative to the coated hip stem model. In particular, for two different coating thickness values (1 mm and 2 mm) the maximum values of electric permittivity which bring to whole slice standard deviations 20 % higher than those of the empty phantom (Figures 4.19(a),(b)) are investigated. In both cases, the coating relative permittivity results to be higher than one bringing to cloaking results that were not achievable at 128 MHz employing the same coating thickness. Furthermore, also for this working frequency value, the opposite roles of coating thickness and permittivity are confirmed.

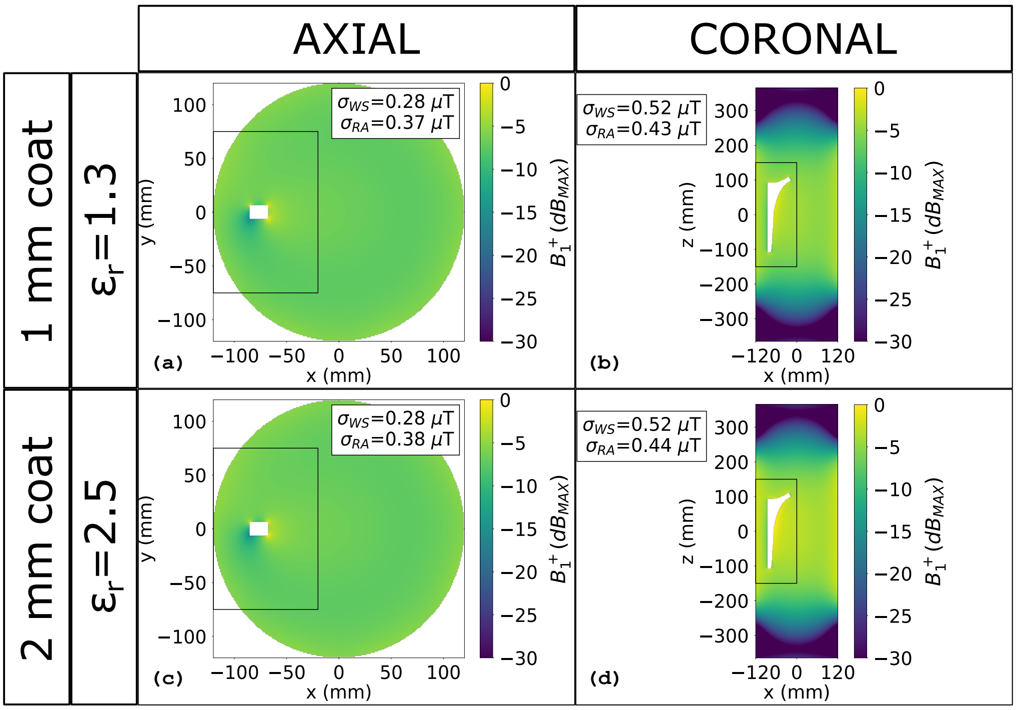

Figure 4.20: B_1^+(dB$_{\text{MAX}}$) evaluated at 64 MHz with the coated hip prosthesis stem model placed in a lateral position ($x = -80$ mm) into the phantom. The results are shown both for the axial plane $z = 0$ ((a), (c)) and for the coronal plane $y = 0$ ((b), (d)). The 1 mm thickness coating with a relative permittivity equal to 1.3 ((a),(b)) and the 2 mm thickness coating with a relative permittivity equal to 2.5 ((c),(d)) cases are examined. The rectangles represent the reduced areas in which the standard deviation (σ_{RA}) is computed. σ_{WS} represents the standard deviation computed on the whole slice.

The results of Figures 4.20(c) and (d) are found to be particularly interesting. Indeed, whereas most of the other results deal with coating electric properties which are not immediately achievable (refer to the conclusive section of this chapter), those obtained in Figures 4.20(c),(d) can be observed in existing dielectric materials. For example, TEFLON™ is a low-losses and low-permittivity material with a dissipation factor (DF) equal to 2×10^{-4} and a relative electric permittivity equal to 2.1 at 64 MHz [98]. Figure 4.21 shows the B_1^+ component distribution considering a 2 mm coating of TEFLON™ both for the $z = 0$ axial slice and for the $y = 0$ coronal one. Despite the non-zero conductivity, such a material demostrated to be suitable to restore the B_1^+ homogeneity leading to standard deviations comparable with those obtained in the ideal case of Figures 4.19(a) and (b).

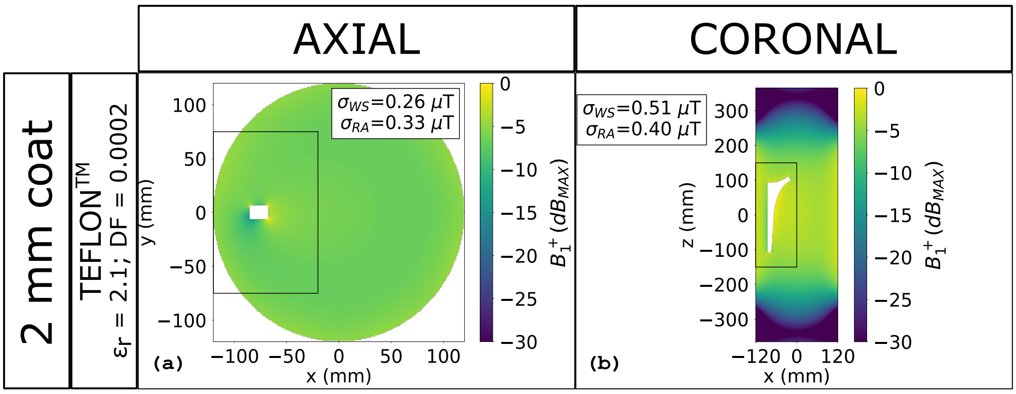

Figure 4.21: B_1^+(dB$_{\mathrm{MAX}}$) evaluated at 64 MHz with the coated hip prosthesis stem model placed in a lateral position ($x = -80$ mm) into the phantom. The results are shown both for the axial plane $z = 0$, (a), and for the coronal plane $y = 0$,(b). A 2 mm thickness TEFLON™ coating (relative permittivity equal to 2.1 , dissipation factor equal to 2×10^{-4}) is examined. The rectangles represent the reduced areas in which the standard deviation (σ_{RA}) is computed. σ_{WS} represents the standard deviation computed on the whole slice.

4.5 SAR

So far, the dielectric coating behaviour has been evaluated in terms of the homogeneity of the B_1^+ magnetic field component. In the current section, the effects on the Specific Absorbtion Rate (SAR) are considered both at 128 MHz and 64 MHz. In the first case, the 1 mm, 0.1 relative permittivity coating is considered whereas, at the lower frequency, the 2 mm Teflon™ coating is examined. In both instances, the SAR distribution is normalized to a whole phantom average SAR equal to 2 W kg^{-1} (*i.e.* the whole body SAR limit relative to a normal operation mode [5]) and compared with those obtained with the empty phantom and with the uncoated prosthesis.

Figure 4.22 shows the SAR distribution at 128 MHz. Figures 4.22(a) and (b) are relative to the empty phantom. The presence of the uncoated prosthesis (Figures 4.22(c) and (d)) results in a slight variation of the SAR along the prosthesis side of the phantom introducing a SAR asimmetry which is particuarly evident for the axial slice (Figure 4.22(c)). The most noticeable effect of the presence of the uncoated prosthesis, is appreciable on the coronal plane (Figure 4.22(d)), where, due to edge effects, there is a significant SAR increase near the prosthesis sharpest parts. Since small areas are involved in such SAR increases, the effect is not appreciable on the whole body SAR but may result important if the local SAR is considered. The effects of the 1 mm, 0.1 relative permittivity dielectric coating are presented in Figures 4.22(e) and (f). As for the magnetic field, also in this case the coating restores the conditions to be comparable with those relative to the empty phantom. In particular, the SAR distribution symmetry is restablished both for the axial and coronal slices. Furthermore, the SAR increases in the

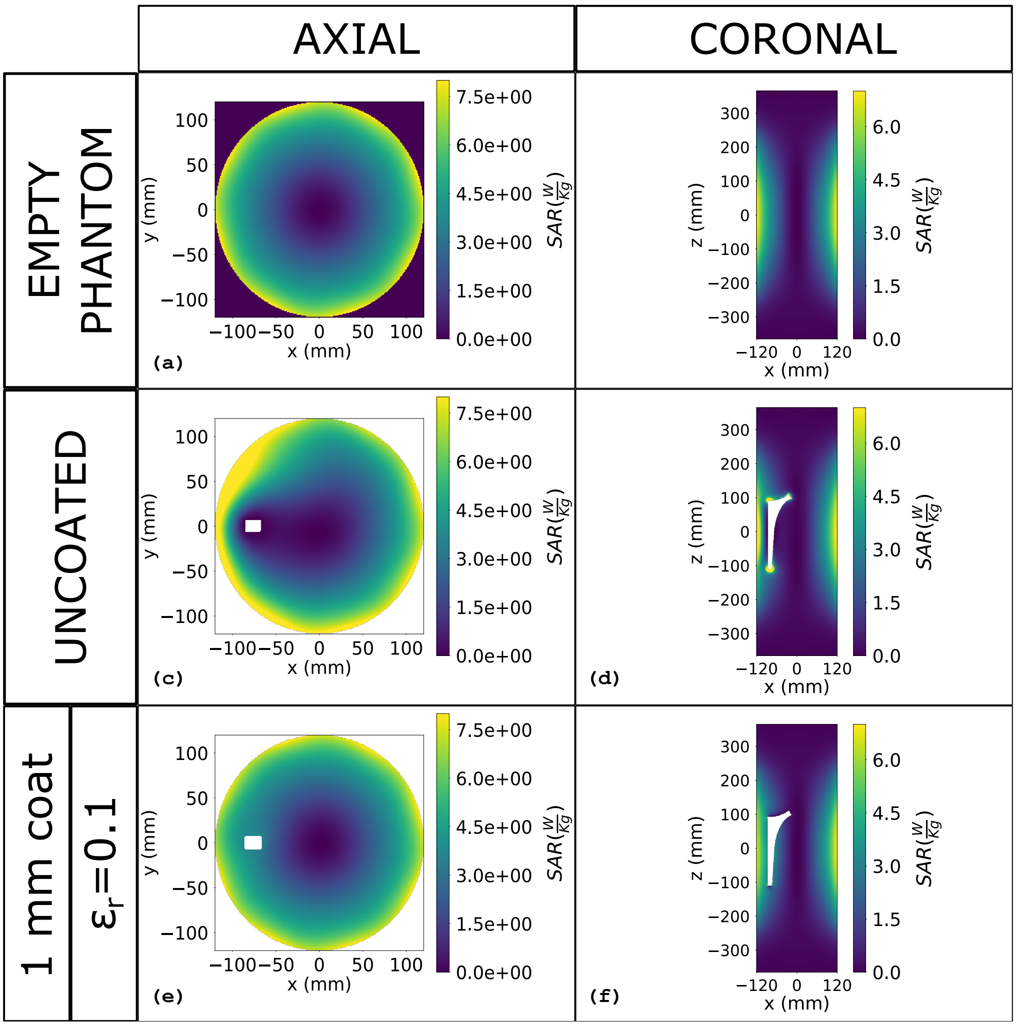

Figure 4.22: SAR distribution normalized to a whole phantom average SAR equal to 2 W kg^{-1}. The distributions are relative to 128 MHz and are shown both for the $z = 0$ axial ((a),(c),(e)) and $y = 0$ coronal ((b),(d),(f)) slices. The empty phantom is considered in (a) and (b) and the laterally placed ($x = -80$ mm) uncoated prosthesis in (c) and (d). In (e) and (f) the hip prosthesis is covered with the 1 mm, 0.1 relative permittivity dielectric coating.

prosthesis edges proximity result to be strongly reduced.

Figure 4.23 shows the analogous set-up at 64 MHz. The SAR distribution in the empty phantom is proposed for the $z = 0$ axial and $y = 0$ coronal planes in Figures 4.23(a) and (b) respectively. Such distributions are comparable with those observed at 128 MHz in Figures 4.22(a) and (b). Also in this case (Figures 4.23(c) and (d)), the uncoated prosthesis introduces an assimmetry in the SAR distribution which is again particularly appreciable considering the $z = 0$ axial slice. Furthermore, the SAR increases near the prosthesis

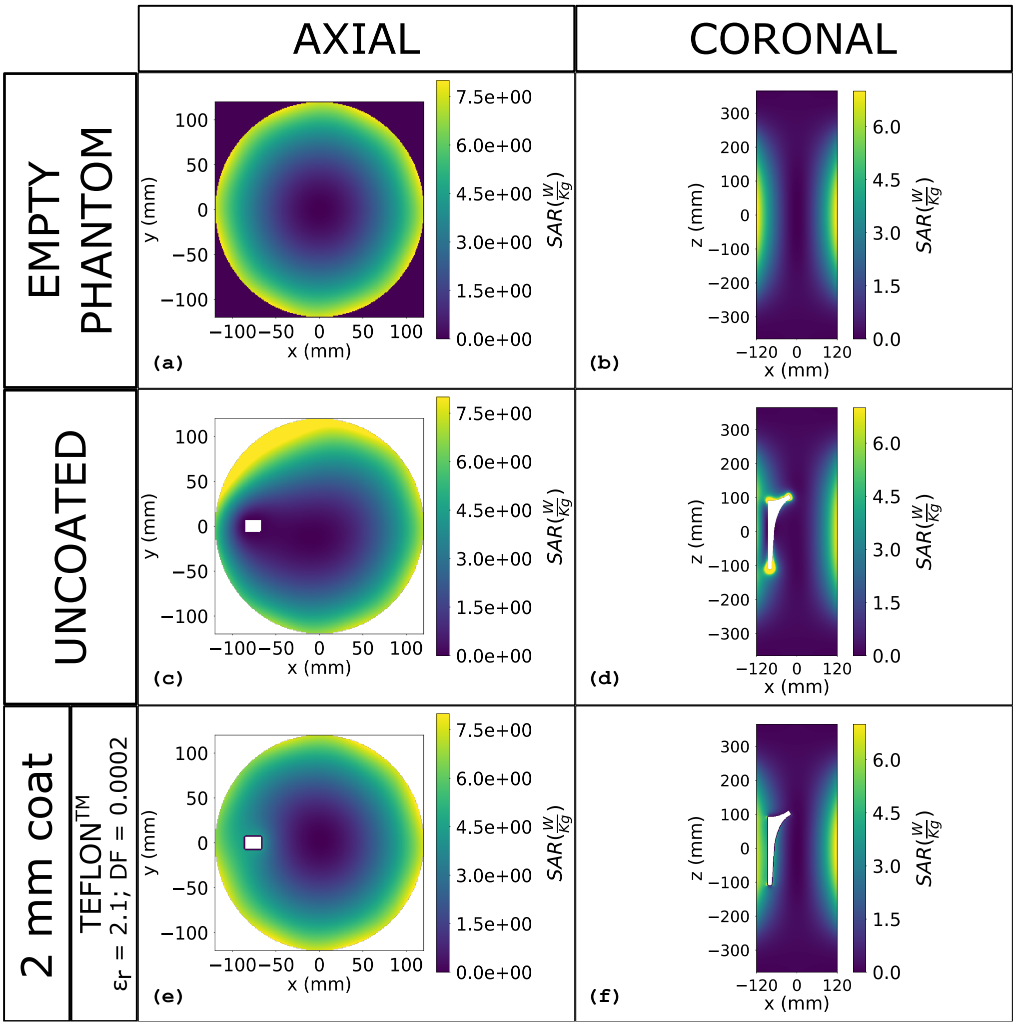

Figure 4.23: SAR distribution normalized to a whole phantom average SAR equal to 2 W kg^{-1}. The distributions are relative to 64 MHz and are shown both for the $z = 0$ axial ((a),(c),(e)) and $y = 0$ coronal ((b),(d),(f)) slices. The empty phantom is considered in (a) and (b) and the laterally placed ($x = -80$ mm) uncoated prosthesis in (c) and (d). In (e) and (f) the hip prosthesis is covered with 2 mm, of Teflon™.

edges, result to be even more remarked with respect the previous case. Figures 4.23(e) and (f) shows the effects of a 2 mm of Teflon™ coating. Again, the presence of the coating restores the SAR distribution to be comparable with that obtained for the empty phantom reducing the SAR increase near the prosthesis edges and confirming a beneficial effect of the coating even on the SAR.
Finally, a brief consideration should be made about the SAR distribution inside the coating. Due to the lower electric permittivity of the coating and to the boundary conditions

between coating and phantom, the amplitude of the electric field inside the coating results to be significantly higher than that inside the phantom. However, from a SAR perspective, this does not represent a problem since the higher electric field amplitude effects are damped by the low electrical conductivity of the coating. This is purposely remarked in Figures 4.23(e) and (f) where the coating is included in the SAR calculations to take into account the non-zero conductivity of Teflon™.

4.6 Conclusion

All the results proposed suggest the efficacy of the dielectric coating in hiding an elongated prosthesis from the radiating antenna. Such a cloaking effect is appreciable both dealing with the magnetic field ($\boldsymbol{B}_1^+$) and with the electric field (SAR). The predictions provided by a rough model based on the lumped elements equivalent circuit, have been confirmed by full-wave simulations. In this perspective, considering the strong approximations in employing a circuital modelling of high frequency phenomena, the circuit demostrated to be suitable to offer a qualitative and immediate description of a complex problem.

The theoretical analysis of the coating has been carried out considering a generic metallic cylinder. Indeed, the cylinder shape allows to arbitrarily increase the coating thickness being sure that the shape of the coated object remains a cylinder. Nevertheless, the results relative to the realistic hip prosthesis stem showed that all findings remain valid.

The effects of the coating, related to the magnetic field, have been presented considering the transmit sensitivity $\boldsymbol{B}_1^+$. Obviously, due to the symmetry of the problem, the same benefits can also be appreciated with the receive sensitivity, $\boldsymbol{B}_1^-$, whose distribution can be easily obtained from the simulations inverting the phase of the supply.

The concept of making a generic object "invisible" to the surrounding electromagnetic field has been extensively studied in the last years. Several cloaking techniques have been proposed depending on the particular application and frequencies. One of the smarter and versatile ideas has been proposed by A. J. Ward and J. B. Pendry [99, 100]. The method is based on the fact that Maxwell equations are invariant to a coordinate transformation if the constitutive parameter tensors are properly redefined. The idea is to use this information to compute the constitutive parameter tensors to control the electromagnetic field. One of the key strength of this approach is that it is extremely general and it can be applied, theoretically, to all problems and frequencies. The critical issue is that, usually, it requires to employ materials with strong anisotropic and spatially dependent magnetic permeability and electric permittivity. Despite this constraint, several theoretical and practical applications have been proposed for different frequency ranges [101, 102, 103, 104, 105, 106, 107, 108, 109].

Another problem related to this technique is inherent in the coating spatial dimensions.

Indeed, the amount of space required by the coating to be effective results to be incompatible with the constraits imposed by the specific application.
This technique and the majority of the studies related to electromagnetic cloaking proposed in literature consider a far-field operation. In such conditions, the object to be cloaked does not significantly interact with the electromagentic field source and the field perturbations are due to the fact that the object represents an obstacle to the electromagnetic field propagation. On the contrary, in the discussed MRI application, the metallic proshtesis necessarily couples with the antenna making the far-field approximation no more reliable. The solution introduced in the present chapter takes advantage from this concept, specifically acting on the object-source couplings responsible for the electromagnetic field distortion. In other words, this no longer correspond to hide the object directly from the whole electromagnetic radiation but to make the object "invisible" to the antenna. Since, as explained in the above sections, such couplings depend, among others, on the geometry of the involved components, the cloaking results are valid only for a specific set-up. The loss of generality, with respect other cloaking applications, is compensated by the possibility to adopt simple coating parameters which are compatible with the application requirements.

Whereas at 64 MHz an existing biocompatible material (already employed in implantable antennas [110]) demostrated to be suitable for the problem purposes, at 128 MHz a material with a relative electric permittivity lower than one is needed to avoid an excessive coating thickness. Despite Epsilon Near Zero (ENZ) materials may be directly found in nature with different forms at specific frequencies [111], considering the requirements of the coating, such a material should be, in principle, synthesized as metamaterial or meta-composite. The narrowband nature of metamaterials (*i.e.* the frequencies at which they present a desired electromagnetic behaviour) matches particularly well with an MRI application where the frequency of the RF magnetic field $\boldsymbol{B}_1$ is univocally determined and restrained in a range of a few tens of kilohertz. This consideration represents one of the reasons why the employement of metamaterials in MRI has been more and more investigated in the last years [30, 112, 113, 114, 115, 116, 117]. However, the constraints led by the considered coating make the metamaterial design even more a challenge. Indeed, the coating thickness, conductivity and biocompatibility have to be taken into account. In particular, it has been shown that the coating thickness can be increased to "relax" the needed electric permittivity. Nevertheless, such a thickness should be reduced as much as possible to ensure that the coating does not influence the original shape and dimensions of the prosthesis.

Future work will be divided in two parts. A first part will deal with the experimental validation of the results obtained at 64 MHz with the Teflon™ coating. A second part will deal with the realization of a proper metamaterial able to cloak the prosthesis at 128 MHz while respecting the application constraints. Most of the metamaterials proposed in litterature present anisotropic electromagentic properties. In particular, their properties can be are engineered only along specific directions which depend on the selected structure. In this framework, the results obtained examining the anisotropic coating clearly showed the direction along which the permittivity value shoud be stressed and will represent the starting point for this last activity.

Chapter 5

MRI & Tattoos

5.1 Introduction

Even if the number of tattooed individuals definitely increased in the last years [118, 119], a reliable assessment of the safety issues related to a possible interaction between tattoo inks and the MRI electromagnetic fields has never been considered. Indeed, such effects are still not clear leading, sometime, to an exaggerated reaction from physicians such as the avoidance of the MR exam for tattooed patients. Furthermore, due to the lack of knowledge in the relevant field, even the U.S. Food & Drug Administration included MRI among the possible safety issues related to tattooing [120]. Indeed, whereas some patients reported burning sensation during the exam or explicit mild swelling and erythema in the proximity of tattoos [121, 122, 123], several others did not report any noticeable consequences.

The abundance of variables which may be crucial in defining the phenomenon (*e.g.* tattoo position, shape and spatial extents, adopted MRI sequence) together with the amount of different tattoo inks commercially available, makes the analysis of such effects really a challenge. In fact, it is extremely difficult, if not impossible, to achieve a satisfying description of all the possible scenarios relative to tattooed individuals submitted to an MRI exam. These considerations highlight the importance to define a systematic procedure which allows for the evaluation of such effects in a way that is as unrelated as possible to each specific scenario.

The aforementioned issues, combined with the cases reporting image degradation due to artefacts rising near tattooed parts or permanent cosmetics [124, 125], may be attributable to the presence of metallic particles which locally perturb the electromagnetic properties of the tissues and, consequently, the MRI electromagnetic fields distribution. This suggests the importance of a proper characterization of the electric and magnetic properties of the tattoo inks usually employed in body tattooing. The experimental quantification of these properties represents the necessary stage to assess a series of electromagnetic and thermal numerical simulations aimed to explore the problem. Indeed, due to the complex chemical composition relative to different tattoo inks, together with the few related information provided by manufacturers, it is extremely difficult, if not impossible, to know at least an order of magnitude of such properties without experimental measurements. In particular, such properties should be investigated in relation to each particular kind of interaction which may rise inside an MR scanner. It turns out that a magnetic characterization is essential to evaluate a possible interaction with the strong static magnetic fields. At the same time, the knowledge of the inks electrical properties (*i.e.* electric permittivity and electrical conductivity) is important considering the interaction with the time-varying gradient fields (usually in a frequency range from 10 Hz to 10 kHz, depending on the imaging sequence employed) and with the radio-frequency electromagnetic fields.

Once the tattoo inks are injected inside the human skin, they follow a complex time evolution which strongly affects their nature and, therefore, can not be neglected [126]. Even if some aspects of such an evolution are still unclear and a detailed biological analysis of the phenomenon exceeds the scope of this chapter, a brief description of the mechanisms regulating the tattoo inks absorption by the human body is worth to be reported.

Generally, tattoo ink consists of pigment and carrier. The pigment is responsible for the relevant color of the tattoo whereas the only role of the carrier is to keep the pigment evenly distributed in a fluid matrix to inhibit the growth of pathogens and to aid the ink application to the skin [127]. It is recognized that tattoo pigment collects in the outer 1/3 of dermis where the basement membrane does not allow its passage out of the skin [126, 128]. There are two different paths for drainage from a tattoo. The first is directly to the venous system and the second is through the lymph tracts and lymph nodes to the bloodstream. They both contribute, together with secondary phenomena, to carry part of the deposited pigment away from the tattoo area resulting in a reduction of about 32 % of the initial dose of the pigment in the skin after only forty-two days after tattooing [126].

Such considerations lead to two main implications. First, they pave the way to assess a reliable analysis of the problem, second they suggest the importance of extending the electromagnetic characterization of the inks to the relevant pigments as well.

In the following sections, special attention is given to the samples preparation. The electric and magnetic properties measurements are hence described both for the ink solutions and pigments and the results are presented. Special care is given to the estimation of the uncertainty related to the aforementioned measurements and a detailed description of the uncertainty budget is given in a dedicated section. Finally, some results relative to the estimation of possible heating effects due the interaction between the tattooed skin and the MR radio-frequency field have been obtained by means of numerical simulation carried out with Comsol Multiphysics® and are reported in devoted sections.

Some of the results proposed in the present chapter have been previously published in [129].

Figure 5.1: Five different commercial tattoo inks, involved in the electric and magnetic characterizations, just before being poured into the magnetic sample holders.

5.2 Sample definition

One of the most critical steps of the magnetic and electric properties characterization is represented by the preparation of the samples. Indeed, all the measurement results are expected to be strongly related to the choices and procedures adopted in such a stage. For this reason, a systematic approach has been defined to develop a standard method to be applied to all the examined inks making the results comparable each other.

The characterization procedures described in the present chapter, has been applied to five different tattoo ink colors (blue, black, white, red and yellow) purchased from a tattoo authorized dealer (Figure 5.1) and selected among the most commonly used colours [130] and brands. After the inks have been thoroughly shaken inside their original pots (as suggested by the manufacturer indications), a weighted amount of each ink solution has been moved into the fixture specific for the relevant measurement.

In order to obtain the ink pigments from the original solutions, a recorded amount (whose weight has been measured by means of a precision balance) of ink has been moved from the original container into a cleaned glass cup. The cup, filled by the liquid ink, has been placed in an oven Figure 5.2 and heated for two hours at 150 °C. A pestle has been employed to mill the dried inks obtaining the pigment powder. The powder has been stored into a specific container after its weight has been recorded. It is worth saying that all the pigments presented as powders except for the black one which looked like a dense paste not modified by a further heating (Figure 5.3). As for the liquid inks, also the tattoo pigments weight have been recorded before they have been moved into

Figure 5.2: Oven employed in the inks exsiccation process.

Figure 5.3: Tattoo pigments obtained from the ink solutions through an exsiccation process. Whereas all the pigments presented as powders, the black one looked like a dense paste.

the specific fixtures to perform the relevant characterization.

(a) Agilent “4294A Precision Impedance Analyzer”.

(b) Agilent “16452A Liquid Test Fixture”.

Figure 5.4: Instrumentation employed for the electric characterization of the liquid inks.

5.3 Electrical parameters measurements

The electric parameters of the ink solutions have been measured by means of an Agilent “4294A Precision Impedance Analyzer” (Figure 5.4a) connected to the Agilent “16452A Liquid Test Fixture” (Figure 5.4b). The liquid test fixture reliability was declared by the manufacturer to be in a frequency range from 40 Hz to 30 MHz limiting that of the Impedance Analyzer which was up to 110 MHz.

The fixture has been filled by 6.8 cm^3 of tattoo inks and the impedance of the cell has been measured. A first estimation of the relative electric permittivity (ϵ_r) and electrical conductivity (σ) has been obtained, as reported in the manufacturer measurement guidelines, through the following expressions:

$$\epsilon_r = \frac{C_p}{C_0} \tag{5.1a}$$

$$\sigma = \frac{\epsilon_0}{R_p C_0} \tag{5.1b}$$

where:

C_p and R_p are the capacitance and resistance values of an equivalent RC parallel circuit, evaluated through the impedance analyzer;

C_0 represents the capacitance value measured with the empty fixture;

ϵ_0 is the permittivity of free space.

Unfortunately, several parasitic phenomena, which are typical of electrochemical measurements [131, 132, 133], occured to complicate the estimation of the electrical parameters. Among these phenomena, the most significant are the so-called double-layer effect

and electrode polarization. The former is due to two layers of polarized ions generated at the electrode interfaces. The two layers, having opposite polarity, are formed by the ions in the electrode and by those distributed in the electrolyte which migrated towards the polarized electrode. The charged electrode and the charged ions are separated by an insulating space forming a capacitor. Due to its time constants, such a phenomenon is particularly important dealing with low frequencies measurements where the double-layer capacitance may strongly affect the whole cell capacitance estimation [134].
The electrode polarization causes the electrode potential to be forced away from its open circuit value. This is responsible for electrochemical reactions induced at the electrode surfaces which cause cathodic and/or anodic currents to flow. The voltage drop gives rise to an increased resistance estimation which may be significant compared to that of the total cell.
These phenomena are generally frequency dependent making a direct estimation of the solution electric permittivity and electrical conductivity by means of (5.1a) and (5.1b) not always reliable. Indeed, considering the measurements relative to the ink solutions, the electrical conductivity estimation is generally reliable only above 20 kHz. As regards the electric permittivity, it is more difficult to resolve even at higher frequencies and its value remains not estimable in the whole frequency range investigated. This is explained considering the significant conductivity values of the ink. Even at the frequencies where the double-layer effects start to be attenuated, the high conductivity values cause the phase angle of the complex permittivity to be large [135]. This results in a low equivalent resistance which prevails in the RC parallel invalidating the estimation of the solution capacitance. At higher frequencies, where the capacitive reactance would prevail, the permittivity resolution remains compromised by the non-ideal behaviour of the liquid test fixture.

Figure 5.5 reports the ink conductivity values, together with the associated uncertainty, measured in a frequency range from 40 Hz to 30 MHz (*i.e.* the whole liquid test fixture frequency range) for the red (Figure 5.5a), blue (Figure 5.5b) and white (Figure 5.5c) inks. The first and the last identify the less conductive and most conductive inks respectively. The blue ink is well representative for a middle ground electrical conductivity. The values have been straight obtained through (5.1b) considering the impedance measurements. All the trends feature a frequency range where the parasitic phenomena do not affect the conductivity estimation making it almost constant (flat linear region). In particular, this frequency range identifies a good reference zone for a first assessment of the ink solution electrical conductivity.

In order to test the reliability of the electrical conductivity values obtained from the measurements through (5.1b), a circuit analogous to the Randles one[1] [132, 136] has been adopted.

---

[1] An equivalent circuit commonly employed in electrochemical impedance spectroscopy as a mean for the interpretation of impedance measurements.

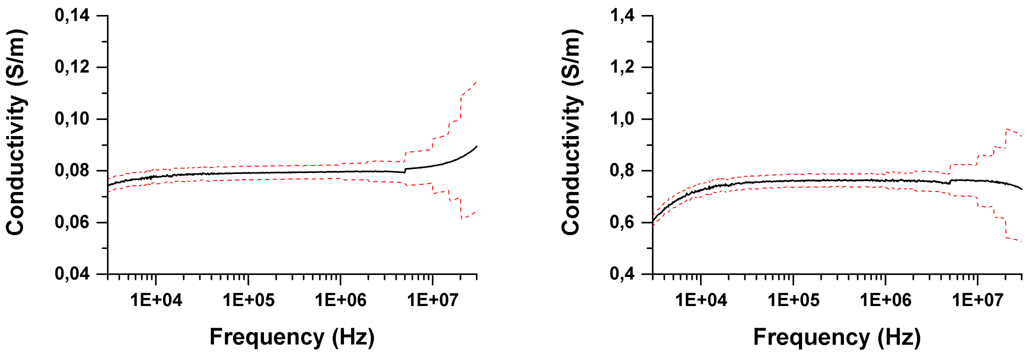

(a) Red Ink.

(b) Blue Ink.

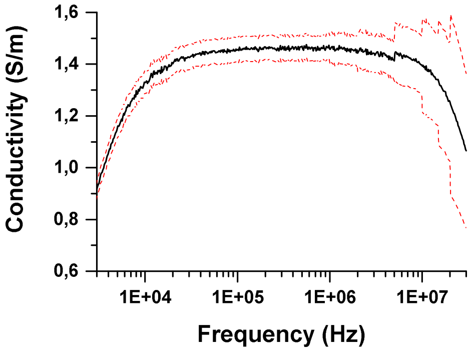

(c) White Ink.

Figure 5.5: Measured electrical conductivity of different inks as a function of frequency. The red dashed lines identify the associated uncertainty interval.

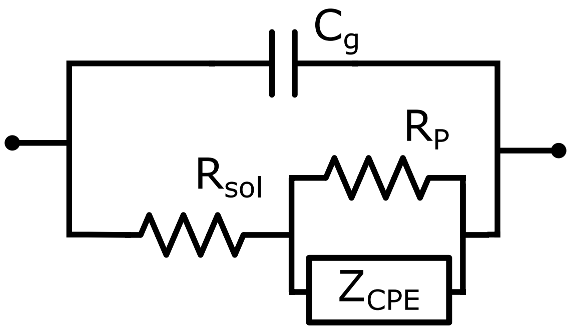

Figure 5.6: Equivalent circuit, analogous to the Randles one, whose parameters are representative of the parasitic phenomena that generally occur in electrochemical measurements.

Table 5.1: Comparison between the inks electrical conductivity values measured at 1 MHz and those obtained through the fitting procedure.

Color	σ (S/m)	
	Measurements	Fitting
Black	0.099 ± 0.004	0.11
Blue	0.76 ± 0.03	0.76
Red	0.079 ± 0.003	0.08
Yellow	0.45 ± 0.02	0.45
White	1.46 ± 0.06	1.46

Figure 5.6 shows the equivalent circuit whose parameters have been estimated through a fitting procedure. In the figure R_{SOL} represents the solution bulk resistance, R_P is the polarization resistance which accounts for the electrode polarization phenomenon, C_g is the capacitance associated with the cell electrodes, and Z_{CPE} is a constant phase element modeling the double-layer capacitance and having electrical impedance equal to:

$$Z_{CPE} = \frac{(\omega/\omega_0)^{-\alpha}}{\omega_0 C_p}\left(cos(\frac{\pi}{2}\alpha) - jsin(\frac{\pi}{2}\alpha)\right) \tag{5.2}$$

where j is the imaginary unit, α is an arbitrary phase parameter and ω_0 represents a normalizing frequency.

Both the real and imaginary parts of the circuit impedance have been optimized to match those measured in a frequency range from 300 kHz to 30 MHz giving rise to a double-objective optimization problem.

Figure 5.7 shows both the real and imaginary part of the measured impedance together with those obtained through the fitting procedure. The results are reported for the red (Figure 5.7a,5.7b), blue (Figure 5.7c,5.7d) and white (Figure 5.7e,5.7f) ink colors. A good agreement between measurement data and the fitting curves is appreciable, especially in the flat linear region, for all the three colors and both for the real and imaginary part of the impedance. This result suggests that the circuit of Figure 5.6 is appropriate to describe the occurring phenomena. In particular, the equivalent impedance of such a circuit optimally describes the impedance behaviour of the red ink (Figure 5.7a and Figure 5.7b). Considering the white and blue inks, the results remain not fully satisfactory for the lower frequency range. However, is worth noting that, whereas a finer optimization may improve the match of the curves, R_{SOL} (*i.e.* the parameter which describes the solution conductivity) is found to be less influenced by this type of refinements. In particular, all the solutions belonging to the Pareto front share the same value of R_{SOL} confirming the reliability of the procedure.

In Table 5.1, the conductivity values computed through R_{SOL} considering the cell dimensions have been compared with those measured at 1 MHz for all the ink colors. The conductivity values, estimated through the fitting procedure, are compatible with

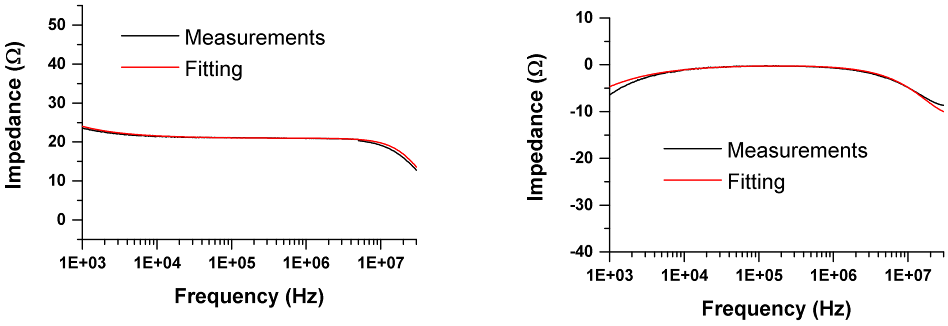

(a) Impedance real part of the red ink (RMSE equal to 0.33 Ω).

(b) Impedance imaginary part of the red ink (RMSE equal to 0.43 Ω).

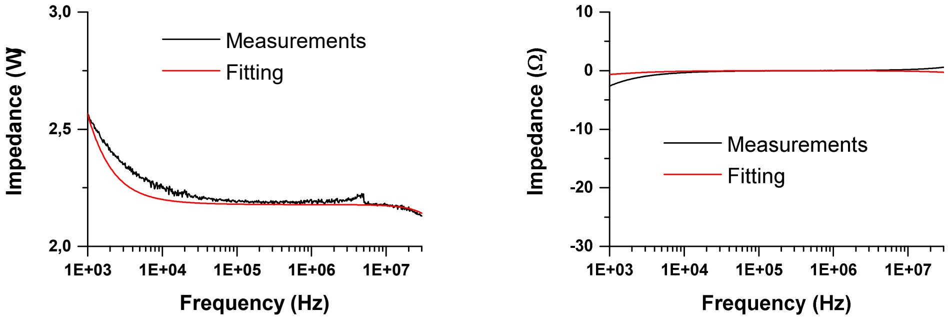

(c) Impedance real part of the blue ink (RMSE equal to 0.036 Ω).

(d) Impedance imaginary part of the blue ink (RMSE equal to 0.48 Ω).

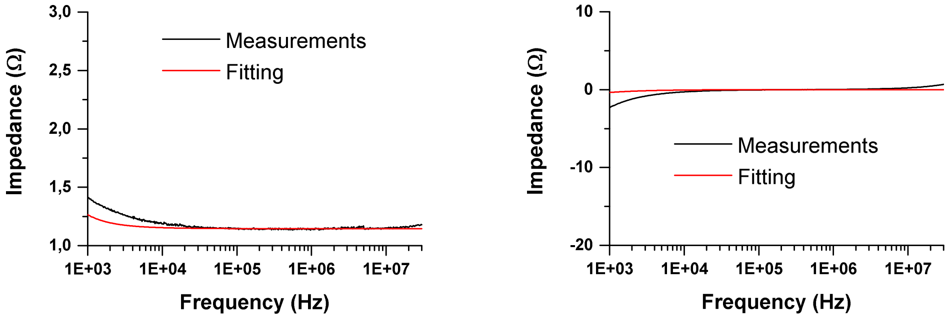

(e) Impedance real part of the white ink (RMSE equal to 0.046 Ω).

(f) Impedance imaginary part of the white ink (RMSE equal to 0.47 Ω).

Figure 5.7: Real and imaginary part of the measured impedance compared to those obtained through the fitting procedure. Data are shown for the red, white and blue inks. The root mean square error is reported in each subcaption as a parameter related to the goodness of the fit.

those measured for all the ink colors also considering their associated uncertainty. Since

Figure 5.8: Agilent "16451B Dielectric Test Fixture" employed for the pigments electric characterization.

the values obtained from the equivalent circuit are not affected by the parasitic effects which affect the impedance measurements, the contained difference between the conductivity values estimated through the two different methods suggests that the flat linear region may be the proper frequency range to be accounted for the conductivity evaluations.

The electrical characterization of the tattoo pigments have been performed through the same impedance analyzer used for the inks (Figure 5.4a) together with the Agilent "16451B Dielectric Test Fixture" (Figure 5.8). In this case, the fixture manufacturer declared the reliability frequency range to be up to 15 MHz further limiting that of the impedance analyzer. A suitable cylindrical frame, made of plastic, has been realized to gather the pigment powder when it was pressed between the fixture electrodes. Particular attention has been paid to consider the same volume of powder in each measure. Thus, fixing the electrodes distance through the fixture micrometer guaranteed almost the same pressure applied by the electrodes to the powders.
The relative electric permittivity and electrical conductivity have been estimated through (5.1a) and (5.1b).

Figure 5.9 shows some measurements carried out on different pigments in the frequency range from 40 Hz to 15 MHz. The proposed results are relative to the pigments obtained from the same ink colors discussed above. The red (Figure 5.9a) and white (Figure 5.9c) pigments show the lower and higher electric permittivity evaluated at 1 MHz respectively. The blue pigment (Figure 5.9b) is representative for a middle permittivity

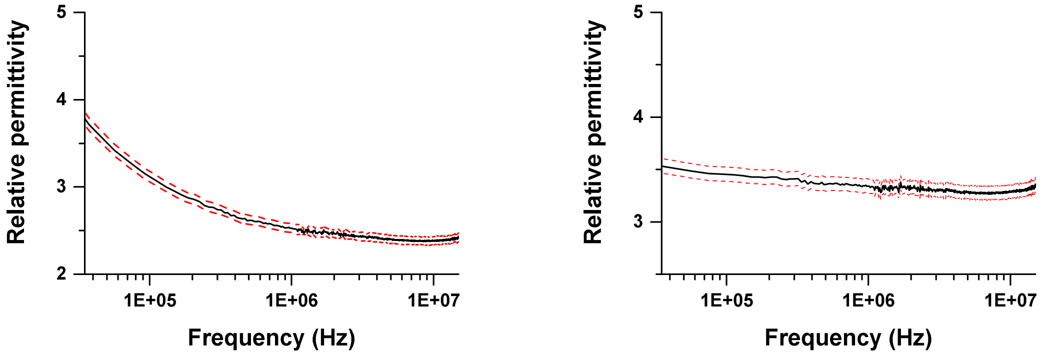

(a) Relative permittivity of the red pigment.

(b) Relative permittivity of the blue pigment.

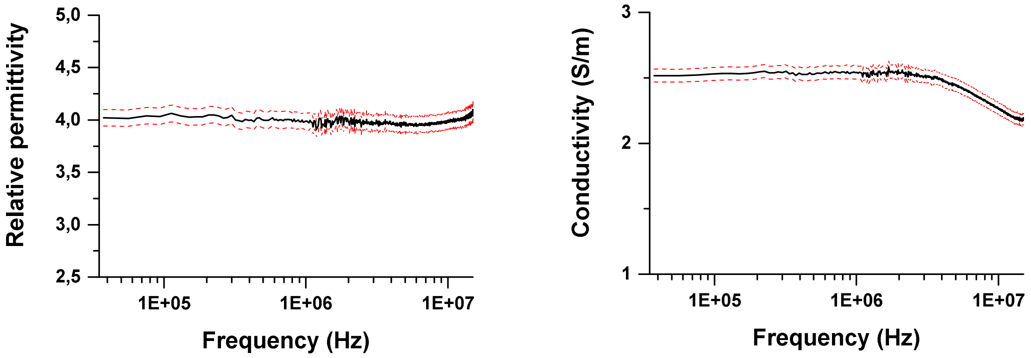

(c) Relative permittivity of the white pigment.

(d) Electrical conductivity of the black pigment.

Figure 5.9: Electric permittivity measured for the red (a) blue (b) and white (c) pigments. The electrical conductivity measured for the black pigment is also reported (d). The red lines identify the associated uncertainty intervals.

value. Finally, the electrical conductivity measured for the black pigment (Figure 5.9d), whose value has been found to be much higher than that of the remaining pigments, is also reported as a function of frequency.

Whereas the electric permittivity of the blue and white pigments only slightly changes with frequency (with a maximum variation equal to 8 % and 5 % for the blue and white pigments respectively), that of the red pigment results to be more influenced (with a maximum variation equal to 43.8 %). Nevertheless, considering the purpose of the described characterization, the permittivity variability is still contained and mainly concerns the low frequency values. Furthermore, Figure 5.9 shows that the variations of the values relative to the pigments are less marked, in the considered frequency range, with respect those measured for the inks. This is due to the parasitic phenomena which are less influential dealing with such kind of measurements. Finally, some consideration relative to the conductivity of the black pigment are needed. Indeed, it is appreciable a

Table 5.2: Pigments electrical conductivity and electric permittivity measured at 1 MHz.

Color	σ (S/m)	ϵ_r
Black	2.54 ± 0.05	–
Blue	$(2.54 \pm 0.06) \times 10^{-4}$	3.34 ± 0.07
Red	$(1.52 \pm 0.03) \times 10^{-5}$	2.52 ± 0.05
Yellow	$(1.88 \pm 0.04) \times 10^{-5}$	2.84 ± 0.06
White	$(5.6 \pm 0.1) \times 10^{-6}$	3.99 ± 0.08

remarkable increase of its values with respect those measured for the relevant ink solution which highlighted a less conductive behaviour for the whole examined frequency range. This aspect suggests the importance of the distinction between ink solutions and pigments when this type of characterizations are considered.

The electrical conductivity and the relative electric permittivity measured for the five pigment colors are reported in Table 5.2. To have a term of comparison with the results relative to the respective ink solutions (Table 5.1), the electrical conductivity and electric permittivity are reported for the same frequency value of 1 MHz. As a general result, the electrical conductivities of the pigments differ from those measured for the inks. In particular, all the pigments, apart from the black one, show a non-conductive behaviour. As regards the relative electric permittivity values, they are limited with respect those typical of the human tissues [96] and are comparable among the different pigments. Finally, it is worth noting that the employed method did not allow for the electric permittivity assessment of the black pigment. As happened for the ink measurements, the higher electrical conductivity led to a parallel resistance R_p in the RC equivalent circuit which was much lower than $1/C_p$. This inevitably resulted in a measured impedance where the capacitive phenomena were overcome by the conductive ones.

5.4 Magnetic parameters measurements

The magnetic properties of both inks and pigments have been investigated by means of a calibrated [137] Lakeshore “7410 Vibrating Sample Magnetometer (VSM)” (Figure 5.10). The VSM working principle is based on the application of a uniform magnetic field to magnetize the sample to be measured. A sinusoidally vibration (80 Hz for the relevant case) is hence applied to the sample. An electromotive force is hence measured on nearby pickup coils due to the time-varying magnetic flux generated by the magnetic moment of vibrating the sample. The induced voltage in the pickup coil is proportional to the sample magnetic moment which represents the measurand.

A weighted amount of solution/pigment has been poured in specific diamagnetic containers which have been firmly tightened through a cap-screw. Such containers were

Figure 5.10: Lakeshore "7410 Vibrating Sample Magnetometer" employed for the magnetic measurements.

in their turn screwed onto the bottom end of the VSM sample holder made of quartz. A magnetic field in the range of ±1 T has been applied to polarize the vibrating samples and the hysteresis loops have been recorded. Even if the maximum magnetic field applied to the samples is much lower than that commonly encountered in clinical scanners, it demonstrated to be sufficient to reach the magnetic saturation in all the examined cases. The diamagnetic response of the empty container has been initially measured and has been subtracted from the magnetic moment measured for each sample. In order to assess comparable results, each measurement has been normalized by the recorded sample weight. Finally, by means of a freeware software named "RockMag Analyzer" [138, 139], the magnetic behaviour of each sample has been considered separately. In particular, each trend has been analyzed in terms of the saturation magnetization, the remanent magnetization and the paramagnetic/diamagnetic slope.

Figure 5.11 shows the normalized magnetic moment hysteresis curves relative to the tattoo inks after subtracting the magnetic moment of the empty container. In this case, due to the particular hysteresis trend associated to each ink, the results obtained for all the considered colors are reported. The diagrams clearly put in evidence the strong correlation between the ink type and the magnetic behaviour. The blue ink (Figure 5.11a) is the only one having a paramagnetic behaviour together with a ferromagnetic one. All the other inks are characterized by an overall diamagnetic response combined to a weak ferromagnetic one for the black (Figure 5.11d), red (Figure 5.11b) and yellow (Figure 5.11e) inks. Finally, it is worth noting that some of the hysteresis loop areas are opened at their ends. Such an effect is appreciable especially for the blue (Figure 5.11a) and black (Figure 5.11d) curves and obviously represents an error associated to the experimental method.

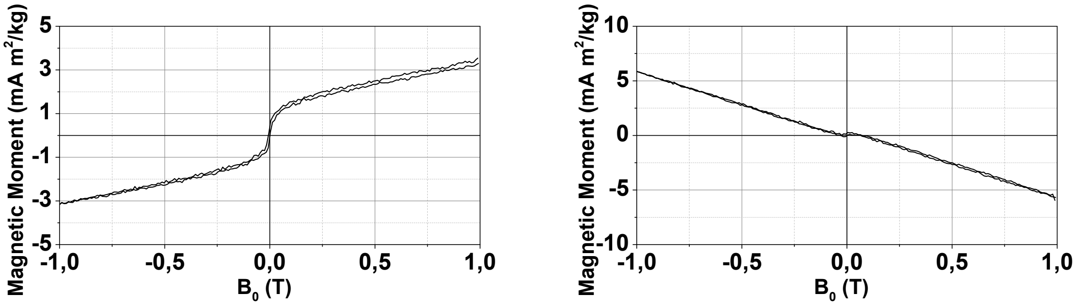

(a) Blue ink. (b) Red ink.

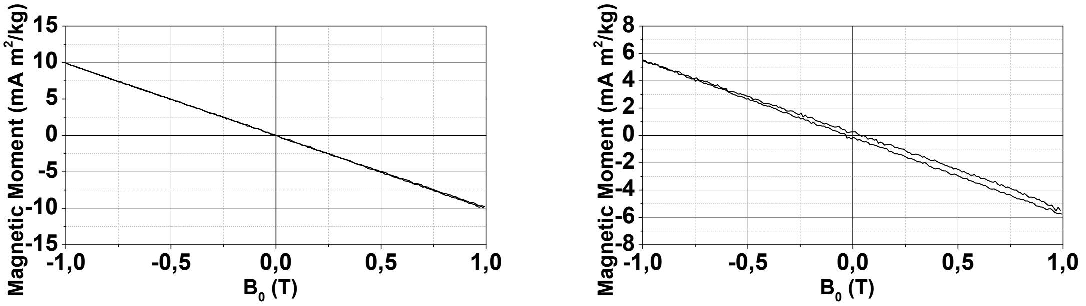

(c) White ink. (d) Black ink.

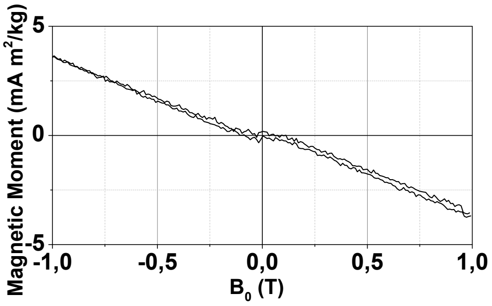

(e) Yellow ink.

Figure 5.11: ±1 T hysteresis loops measured for all the tattoo inks considered.

In Table 5.3, the saturation magnetization, the remanent magnetization and the paramagnetic/diamagnetic slope obtained from the analysis of the magnetic curves of Figure 5.11 are reported [138]. Because of the strict diamagnetic behaviour of the white ink, its saturation and remanent magnetization are not reported in the table. The parameters emphasize the different magnetic behaviour of the blue ink with respect that of the others suggesting, as for the electric properties, a strong correlation between the magnetic parameters and the ink color. However, their values do not generally highlight a significant magnetic reaction of the tattoo inks.

Table 5.3: Magnetic parameters associated to the measured tattoo inks.

Color	Sat. mag. (Am^2/kg)	Rem. mag. (Am^2/kg)	Par/Diam slope ($Am^2/kg/mT$)
Blue	(13.2 ± 0.5) $\times 10^{-4}$	(2.31 ± 0.04) $\times 10^{-4}$	(1.95 ± 0.08) $\times 10^{-6}$
Red	(3.63 ± 0.37) $\times 10^{-4}$	(1.09 ± 0.02) $\times 10^{-4}$	(-6.13 ± 0.12) $\times 10^{-6}$
White	–	–	(-9.9 ± 0.2) $\times 10^{-6}$
Black	(2.74 ± 0.35) $\times 10^{-4}$	(2.39 ± 0.04) $\times 10^{-4}$	(-5.86 ± 0.11) $\times 10^{-6}$
Yellow	(4.77 ± 0.2) $\times 10^{-4}$	(1.85 ± 0.03) $\times 10^{-4}$	(-4.13 ± 0.07) $\times 10^{-6}$

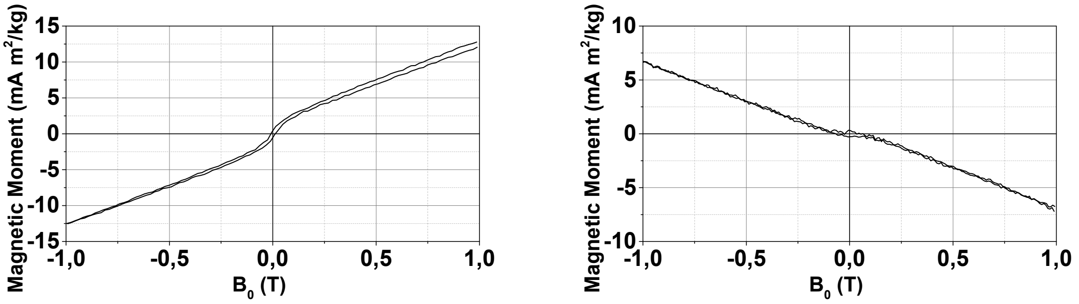

(a) Blue pigment.

(b) Red pigment.

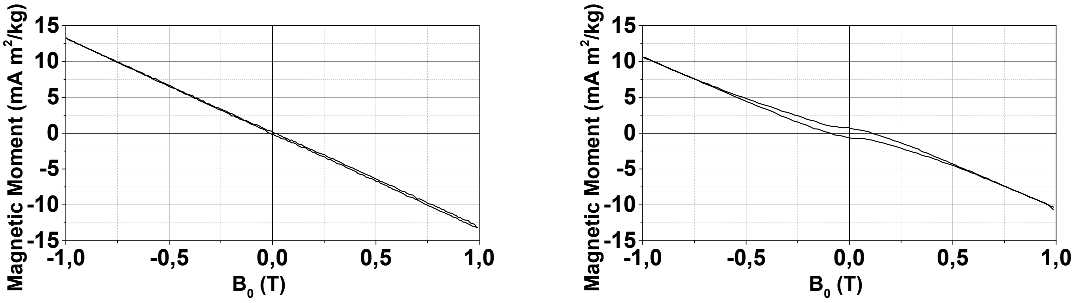

(c) White pigment.

(d) Black pigment.

Figure 5.12: ±1 T hysteresis loops measured for the blue (a), red (b), white (c) and black (d) tattoo pigments.

Figure 5.12 shows the magnetic curves obtained for the blue (Figure 5.12a), red (Figure 5.12b), white (Figure 5.12c) and black (Figure 5.12d) tattoo pigments. Also in this case, the magnetic moment of the empty container have been subtracted from that of the pigments. The results are not reported for the yellow pigment since the measured values resulted to be severely affected by noise. This is probably due to its magnetic response comparable to the instrument limit of detection. The general magnetic behaviors of the pigments remain comparable to those observed for the relevant inks. In particular, the blue pigment is still the only pigment which shows a paramagnetic behaviour

Table 5.4: Magnetic parameters associated to the measured tattoo pigments.

Color	Sat. mag. (Am^2/kg)	Rem. mag. (Am^2/kg)	Par/Diam slope ($Am^2/kg/mT$)
Blue	$(20.8 \pm 0.1) \times 10^{-4}$	$(4.69 \pm 0.07) \times 10^{-4}$	$(10.5 \pm 0.3) \times 10^{-6}$
Red	$(9.39 \pm 0.42) \times 10^{-4}$	$(2.90 \pm 0.04) \times 10^{-4}$	$(-7.80 \pm 0.15) \times 10^{-6}$
White	–	–	$(-13.3 \pm 0.3) \times 10^{-6}$
Black	$(18.2 \pm 0.6) \times 10^{-4}$	$(6.98 \pm 0.10) \times 10^{-4}$	$(-12.4 \pm 0.2) \times 10^{-6}$

whereas all the others keep showing a diamagnetic one. A ferromagnetic behaviour is still observed for the blue, red and black colors. However, their general behaviors seem to be more pronounced with respect those of the relevant inks. Such considerations are confirmed by the parameters reported in Table 5.4. An increased remanent magnetization is appreciable especially for the black pigment highlighting its stronger ferromagnetic behaviour. Furthermore, both the paramagnetic and diamagnetic slope of the blue and black pigments respectively became more important. Finally, even dealing with the pigments, all the measured magnetic parameters are not representative for a strong magnetic reaction.

5.5 Measurement uncertainties

The intrinsic nature of such type of measurements makes them particularly affected by uncertainties. Furthermore, in order to assess worst case simulations to evaluate the possible thermal effects of the presence of tattoos during MRI exams, an uncertainty budget is at least appropriate.

The complexity of the measurements and the different stages in which they have been developed, make such a budget really a challenge. In the study proposed below, the uncertainty related to the sample definition (*e.g.* heating time and temperature, amount of ink/pigment inside the specific measurement fixtures, pigments milling degree) has not been considered. Indeed, even if it likely represents an important contribution to the final budget, it necessarily requires to carry out a statistically significant number of different sample preparations and measurements. Due to the very long time required and to the limited amount of available inks, such a work has not been considered at the actual stage. The evaluation of the uncertainty related to the sample measurements took advantage from the accuracy information reported on the instrument documentations by the manufacturers and from previous calibrations. For this reason, the uncertainty budget is strongly related to the type of instrument employed for the characterization and will be hence discussed below in three different section: Inks electrical measurements, Pigments electrical measurements and Inks/Pigments magnetic measurements. The uncertainty budget has been developed following the indications given by the “Guide to the expression of uncertainty in measurement (GUM)” [66].

5.5.1 Inks electrical measurements

For these measurements, the “16452A Liquid Test Fixture” has been employed with the Agilent “4294A Precision Impedance Analyzer”. The test fixture manufacturer declared that the main uncertainty contributions are introduced by the fixture itself. In particular, the error associated to the relative complex permittivity amplitude is given by:

$$U(|\dot{\epsilon_r}|) = (A + B)|\dot{\epsilon_r}| \tag{5.3}$$

where:

$\dot{\epsilon_r}$ represents the relative complex permittivity equal to $\epsilon_r - j\sigma/\omega\epsilon_0$, being σ the electrical conductivity, ϵ_0 the electric permittivity of void, ϵ_r the relative electrical permittivity and ω the angular frequency;

A is an uncertainty contribution related to the amplitude of the relative complex permittivity whose values are given by the manufacturer;

B is an uncertainty contribution related to the measuring frequency whose values are given by the manufacturer.

In the final uncertainty assessment, the error (5.3) has been interpreted as the expanded uncertainty considering a uniform probability distribution with a 95 % confidence interval.

5.5.2 Pigments electrical measurements

The uncertainty budget for this type of measurements required more elaborations with respect the previous one. The “16451B Dielectric Test Fixture” together with the Agilent “4294A Precision Impedance Analyzer” has been employed for such measurements. The “16451B Dielectric Test Fixture” manufacturer declared that the fixture contributions to the final uncertainty can be neglected with respect to those introduced by the adopted impedance analyzer. The impedance analyzer manufacturer provided an analytic relation to evaluate the relative error of the impedance amplitude and phase as a function of the impedance analyzer settings and measurement conditions. Considering the nonlinearities of the problem, the Monte Carlo method has been applied. In particular, to be conservative, the relative error computed through the manufacturer information has been interpreted as the the expanded uncertainty considering a uniform probability distribution with a 95 % confidence interval. Basing on this result, the limits of a symmetrical rectangular probability distribution, on which ten thousand extractions have been performed, have been defined. Since no further information has been provided by the impedance analyzer manufacturer, the impedance module and phase errors have been considered uncorrelated. The extractions have been hence performed both for the module and phase of the impedance considering the measured values as the average of the aforementioned distributions. Each extraction has been used to evaluate the electric permittivity ϵ_r and electrical conductivity σ through (5.1a) and (5.1b) where the equivalent resistance R and equivalent capacitance C of a parallel RC circuit have been obtained as:

$$R = \frac{|Z|}{\cos\phi} \tag{5.4a}$$

$$C = \frac{\sin\phi}{|Z|\omega} \tag{5.4b}$$

In the above relations, $|Z|$ represents the impedance amplitude and ϕ the impedance phase. Repeating this procedure for all the extractions led to a Rayleigh distribution both for the electric permittivity and electrical conductivity. The 95 % confidence interval limits (U_1 and U_2) for a Rayleigh distribution was obtained as:

$$U_1 = \frac{\sqrt{N}a}{\sqrt{N} + 1.96} \tag{5.5a}$$

$$U_2 = \frac{\sqrt{N}a}{\sqrt{N} - 1.96} \tag{5.5b}$$

where a is the average value of the distribution and N the number of extractions [140]. In the sections above, the uncertainty intervals are reported symmetrically considering the larger value between U_1 and U_2.

5.5.3 Inks/Pigments magnetic characterization

The accuracy of the magnetic moment, measured by the VSM, was achieved by comparisons with a NIST certified Nichel sphere. Furthermore, the reliability of the applied static magnetic field was assessed thanks to the feedback of a calibrated Hall probe.
Basing on these previous evaluations together with the reported instrument specifications, the relative expanded uncertainty value of the measured magnetic moment has been evaluated to be equal to 1.5 %. Such an estimation has been obtained considering a normal probability distribution with a confidence interval equal to 95 %. Both the uncertainty values related to the applied static magnetic field and the measured sample weigh (employed in the normalization of the measured magnetic moment) have been evaluated to be negligible with respect to the other uncertainty contributions. The standard deviations of the magnetic parameters obtained from the hysteresis and discussed in the above relevant section, have been computed through a linear propagation of the

magnetic moment uncertainty. In particular, the following relations have been considered:

$$M_S = \frac{m_L B_{0_U} - m_U B_{0_L}}{B_{0_U} - B_{0_L}} \tag{5.6a}$$

$$Sl = \frac{m_U - m_L}{B_{0_U} - B_{0_L}} \tag{5.6b}$$

where:

M_S represents the saturation magnetization per unit mass;

Sl represents the paramagnetic/diamagnetic slope;

m_L and B_{0_L} represent the lower magnetic moment per unit mass and static magnetic flux density respectively, used for the linearly approximated paramagnetic/diamagnetic contribution evaluation;

m_U and B_{0_U} represent the upper magnetic moment per unit mass and static magnetic flux density respectively, used for the linearly approximated paramagnetic/diamagnetic contribution evaluation.

The reliability of the employed linear method for the uncertainty propagation has been guaranteed by the negligible uncertainty of the denominators of (5.6). A $B_{0_U} = 1$ T and $B_{0_L} = 0.25$ T have been found to be appropriate for all the examined ink/pigment. The expanded uncertainty values reported in the tables above have been obtained considering a normal distribution with a 95 % confidence interval.

5.6 Electromagnetic and Thermal simulations

Even if the tattoo inks and pigments measured property values do not suggest possible significant interactions with the MRI electromagnetic fields, some worst-case simulations have been performed to obtain a reliable confirmation. Considering the measured magnetic properties of the inks/pigments, a strong interaction with the MR static magnetic field (which justifies the slight tingling experienced by a patient before the MRI exam beginning [122]) is not motivated. Furthermore, neither a heating effect at the gradient field frequency or radio frequency seems to be attributable to magnetic losses. Therefore, in this framework, only the electrical parameters of the inks/pigments (*i.e.* electric permittivity and electrical conductivity) have been accounted in the simulations. To stress a possible thermal effect, the higher values of electric permittivity and electrical conductivity measured for the different inks/pigments have been considered as the properties of the simulated tattoo (*i.e.* $\epsilon_r = 4$ and $\sigma = 2.6\,\mathrm{S\,m^{-1}}$). The electrical conductivity value is comparable with those typical of human tissues [96]. At the frequencies considered for the gradient magnetic field, where the conductive effects are

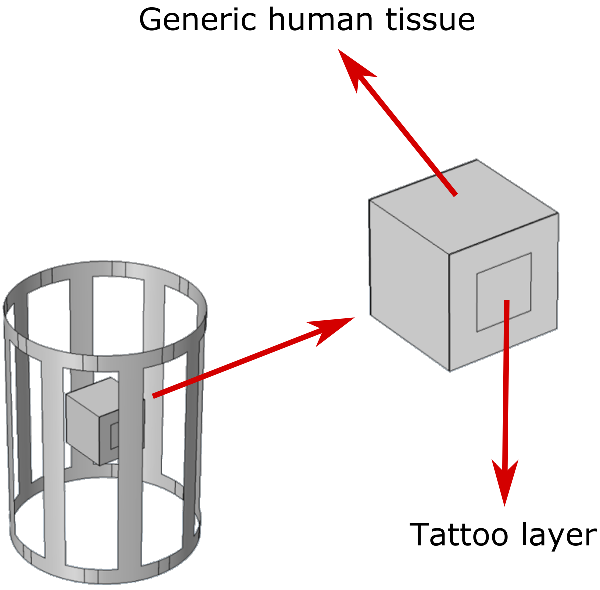

Figure 5.13: Simulation set-up considered for the electromagnetic and thermal simulations in the presence of tattoo.

predominant on the dielectric ones, the tattoo presence is not expected to significantly affect the temperature of the sorrounding tissues. For this reason, the simulations have been performed at 128 MHz where both the electrical conductivity and electric permittivity of the tattoo may influence the thermal behaviour of the system. It should be noted that the above tattoo parameters have been measured at frequencies which are lower than that accounted in the simulations. Even if a different value of these properties measured at 128 MHz can not be excluded a priori, such a difference is unlikely to significantly affect the thermal simulation results.

Figure 5.13 depicts the set-up considered for the electromagnetic and thermal simulations performed with Comsol Multiphysics®. A cube with electric properties comparable with human skin [141] (electric permittivity equal to 66 and electrical conductivity equal to 0.52 $\mathrm{S\,m^{-1}}$) has been radiated by an 8-leg birdcage coil ideally supplied in quadrature operation mode by means of sixteen voltage ports. The tattoo is considered as a 1 mm squared layer centered in one of the lateral cube faces. The tattooed face has been selected to maximize the flux of the magnetic field generated by the RF coil on the tattooed surface. The tattoo thickness is appositely exagerated to enhance the possible effects of its presence. Due to a lack of information about the thermal properties of the tattoo inks/pigments, the same used for the tissue [141] have been considered for the tattoo as well. The detailed values of the parameters employed in the simulation are reported in Table 5.5.

The SAR distribution inside the cube has been obtained solving the electromagnetic problem in frequency-domain. Successively, the steady-state temperature elevation, due

Table 5.5: Tattoo electromagnetic and thermal simulation parameters.

Parameter	Value
ϵ_r tissue	66
ϵ_r tattoo	4
σ tissue	$0.52\,\mathrm{S\,m^{-1}}$
σ tattoo	$2.6\,\mathrm{S\,m^{-1}}$
Birdcage height	460 mm
Birdcage radius	175 mm
Tattoo thickness	1 mm
Cube side length	100 mm
Tattoo side length	50 mm
Tissue thermal conductivity	0.37 W/(mK)
Tissue thermal capacitance	3391 J/(kgK)
Tissue-air heat transfer coefficient	$6\,\mathrm{W/(m^2K)}$
Perfusion coefficient	$7400\,\mathrm{W/(m^3K)}$

to the SAR deposition inside the cube, has been computed assuming as unknown the temperature elevation with respect to the temperature distribution before the exposure [142]. It is worth noting that the relevant description of the problem represents an overestimation of a more realistic situation. Indeed, the limited time RF pulses applied during the most common MR sequences, have been replaced by a continous wave in the simulation. Furthermore, the obtained results are the steady-state solutions of a phenomenon which may be too short, in a realistic application, to reach its equilibrium status.

Finally, particular importance has been reserved to define the thermal problem boundary conditions whose choice significantly influences the solution. Even in this case, a conservative approach has been followed. A Neumann boundary condition (*i.e.* a thermal insulation condition) has been considered for all the cube faces except for that with the tattoo. A Robin boundary condition (*i.e.* a heat flux proportional to the difference between the cube face temperature and the external one) has been applied for the tattoed face instead. Thanks to the temperature elevation formultaion adopted for the thermal problem, both the electromagnetic and thermal equations are linear. This allow for a general result, which is indipendent of the power radiated by the coil, if the SAR and the temperature elevation are properly normalized.

Figure 5.14 shows the SAR values normalized to the maximum value of SAR recorded in the relevant slice. To better identify the SAR distribution in the slice, its maximum value has been investigated in the untattoeed areas only. The results are reported for the xy (Figure 5.14(a)) and yz (Figure 5.14(b)) symmetry planes of the cube. Both for the xy- and yz-slice, the almost symmetrical SAR distribution in the tissues suggests an insignificant contribution of the tattoo in its definition. Furthermore, the higher SAR

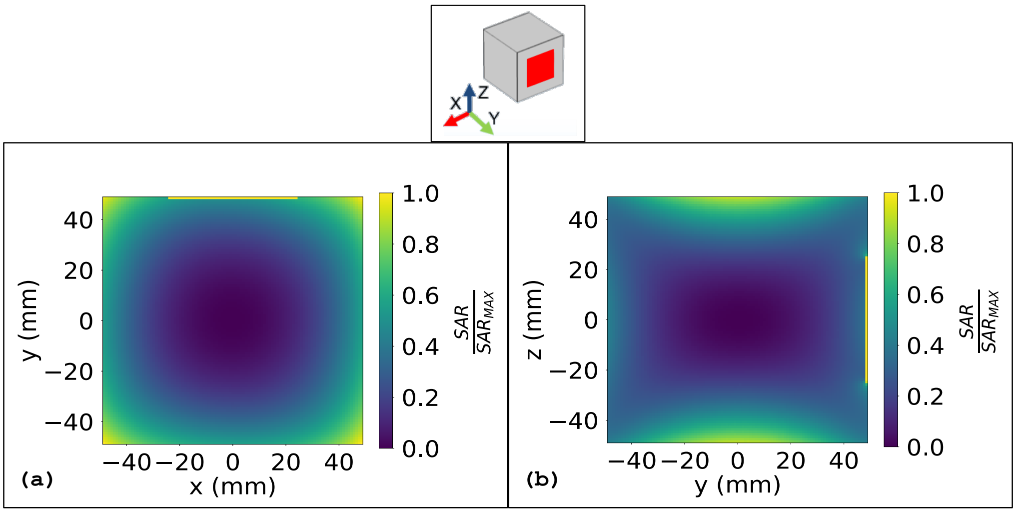

Figure 5.14: SAR values normalized to the maximum value recorded in the untattooed zones of the slice. The results are proposed for the *xy* (a) and *yz* (b) symmetry planes of the cube. In the picture above the chromatic maps, the tattoo is identified by the red surface.

values in the tattooed zone are not imputable to increased values of the electric field, which are only slightly appreciable near the tattoo edges in Figure 5.14(b), but to the higher conductivity value of the tattoo with respect that of the tissue. This is confirmed by the power deposition in the tattoo zone and in an equivalent zone situated on the cube opposite face whose ratio is the same of that between the conductivity values of the tattoo and tissue respectively.

The temperature elevation with respect that before the exposure, is shown in Figure 5.15. Results are normalized to the maximum temperature elevation recorded in the relevant slice. A subtle difference between the temperature elevation in the tattooed zone with respect that in the opposite face is appreciable both considering the *xy* (Figure 5.15(a)) and *yz* (Figure 5.15(b)) symmetry planes of the cube. Even considering the different boundary conditions applied to these faces, such a difference remains too small to hold the analyzed tattoo inks liable for the thermal reactions reported in the germane litterature.

5.7 Conclusion

A reference method to perform the tattoo inks electric and magnetic characterization has been proposed and experimentally demonstrated on five different commercial tattoo inks. The measured parameters have been adopted to define the set-up for the electromagnetic and thermal simulations aimed to to assess MRI safety evaluations.

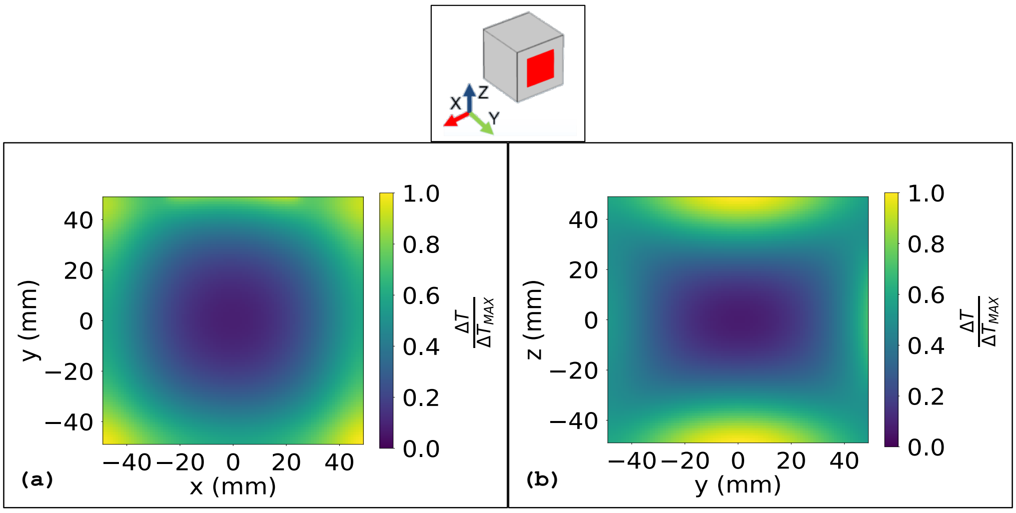

Figure 5.15: Temperature elevation with respect the temperature before the exposure normalized to its maximum value in the slice. The results are proposed for the *xy* (a) and *yz* (b) symmetry planes of the cube. In the picture above the chromatic maps, the tattoo is identified by the red surface.

Whereas the procedure employed for the magnetic measurements did not lead to significant problems, those considered for the electric characterization resulted in several limitations being also complicated by the occurrence of several parasitic phenomena. For these reasons, additional tools, like fitting procedures, have been taken into account to interpret the results obtained from the most critical measurements. Regardless of the efforts dedicated to this operation, some approxiamtions turned out to be necessary. In particular, due to the limited frequency bandwidth of the liquid test fixture and dielectric test fixture, the acquired electrical parameters have been measured at frequencies relatively far from those generally employed in clinical MRI scanner. Even if the knowledge of an order of magnitude of these parameters would be enough to assess the electromagnetic and thermal simulations, different methods [143, 144] may be considered to account for a possible dispersive behavior of the tattoo inks/pigments.
Particular attention has been reserved to the elaboration of an uncertainty budget, specifically formulated for each measurement method, to allow for an estimation of the measurement accuracies. Even if the sample definition is expected to significantly contribute to the final measurement uncertainty budget, the amount of tattoo ink and time needed to achieve a meaningful statistical analysis made this kind of evaluation hardly affordable.

Both the electric and magnetic experimental characterizations did not suggest strong interactions with the MRI electromagentic fields. This expectation is confirmed by the electromagnetic and thermal simulations which did not reveal abnormal temperature elevations attributable to the tattoo presence. However, it is intersting to notice the relation between the electric and magnetic behaviour and the tattoo ink/pigment examined color. This suggest the importance to include in the relevant analysis other ink colors of different commercial brands. Even if, major Europe governments defined proper guidelines [145] which limit, among others, the amount of metallic particles contained in the tattoos or permanent cosmetics, it should be considered the possibility that they are not followed by all the tattoo ink manufacturers. Finally, the described analysis should be extended to consider different tattoo shapes. Even if, given the measured electric and magnetic properties of the examined inks and the kind of evaluations performed, this parameter is unlikely to be an influencial factor, this may not be the case for different inks. Indeed, the shape of the tattoo (*e.g.* particular loops, resonant length segments) may significantly influence possible electromagnetic and thermal tattoo reactions.

Chapter 6

Conclusion

The thesis focused on several aspects related to MRI RF coils exploring and studying some of the relevant issues. Whereas some results have been obtained numerically (by means of electromagnetic simulations), others have been carried out experimentally taking advantage of the measurement facilities available at the INRIM laboratories.
The experimental core of the described activity is represented by the development of a dosimetric set-up aimed to support the integration of different types of RF coils and to measure the electromagnetic fields they generate inside a tissue-mimicking phantom. The validation and characterization of the set-up is described employing a self-made shielded loop and comparing the experimental results to those from numerical electromagnetic simulations. The same approach is repeated using a double-tuned loop coil designed by IMAGO7 foundation, Pisa, and specifically oriented to 7 T MRI applications. The results obtained from the comparison between experimental and numerical data brought the dosimetric experimental set-up to consist of a well characterized environment easy to be modeled inside most electromagnetic simulators. From this perspective, the dosimetric set-up may represent a useful tool to confirm the reliability of numerical results involving RF coil models.

Particular relevance is devoted to the design of a scaled-down birdcage body-coil conceived to be integrated inside the experimental set-up to increase its versatility. The complexity of the working principles associated with this coil structure led to a whole chapter devoted to its theoretical description. The birdcage coil design and realization represent instead a significant part of the chapter related to the dosimetric set-up. The coil is currently optimized for a linear operation in unloaded conditions. Even if these do not represent the normality conditions for the coil inside an MRI scanner, the possibility to operate the birdcage in such a way, allows for kind of evaluations (*e.g.* field orientation, equivalent lumped element circuit limitations) that, differently, may be barely achievable.

The unwanted effects due to the interaction between a generic birdcage coil and elongated conductive passive implants, such as a hip prosthesis, also required specific considerations. In this framework, the problem is analyzed through numerical electromagnetic simulations. A lumped element circuit is proposed to interpret some of the occurring electromagnetic phenomena and a near-field cloaking approach is presented to address the RF inhomogeneity artefacts issue. The results obtained from this specific study have a double value. Firstly, they suggest a possible and easy solution to a well-known MRI problem. This revealed to be particularly true at 64 MHz where an existing material shows the needed requirements. On the other side, the results demonstrated numerically the application of a simple electromagnetic near-field cloaking strategy which is tailored to fit a civil and common area like MRI.

Finally, a systematic procedure to experimentally characterize the electric and magnetic properties of tattoo inks and pigments is described in the final chapter of the thesis. This specific activity has been developed in the pursuit of addressing long-standing discussions related to possible tattoos safety issues in MRI and directly followed an explicit request from MRI radiologists. Even if the procedure is focused on the study of a limited group of tattoo inks, which did not show alarming behaviour, its value lies in the applied methodology, suitable to be easily extended to every kind of tattoo ink.

Each of the results reached in this thesis offers several opportunities for future developments.

Several improvements may be implemented to the birdcage coil. For example, a second supply port may be prepared for quadrature operation and the coil tuning and matching may be regulated in the presence of the phantom. After that, time-domain electric and magnetic field probes could be employed, together with the available RMS probes, to evaluate the field polarization inside the coil and finally assess its spatial sensitivity.

Furthermore, the dosimetric set-up could be also improved in a way which is unrelated to the birdcage coil. Indeed, taking into account the growing interest in high-field MRI and the increasingly availability of 7 T MRI scanners, the upgrading of the experimental set-up capabilities up to 300 MHz could pave the way to even further activities.

The study of the RF inhomogeneity artefacts caused by the presence of elongated conductive objects, led to several promising results. All the findings have been obtained through numerical simulations and an experimental activity represents the natural development needed to check their reliability. This should be performed both with electromagnetic measurements and employing a real MRI scanner to account for secondary effects. In particular, susceptibility artefacts are expected to significantly influence the result and may overcome the potential advantages of the coating. In this context, a preliminary activity could involve an MRI simulation software to be considered in order to separately examine the drawbacks of the two effects; *i.e.* RF inhomogeneity and susceptibility artefacts. Whereas the experimental activity would be already affordable at 64 MHz, where the pursued results are obtained with an existing material, at 128 MHz a further step would be required since a proper metamaterial should be preliminarily designed.

Finally, even the study of the possible interactions between body-art tattoos and MRI suggests the opportunity for future developments. Indeed, the electric measurements range should be expanded at least up to 128 MHz to be compliant with the most common MRI frequencies. Furthermore, the ink colours analyzed have been purchased from an authorized dealer and have been produced by reputable ink manufacturers. This should ensure that they fall within health European guidelines being created in strictly controlled environments. However, the production of counterfeit tattoo inks is increasing worldwide and their electric and magnetic properties can be significantly different from those measured in the presented activity. In this context, it would be interesting and useful to extend the analysis to some of those inks also accounting for a possible relation between the tattoo shapes and heating effects.

Appendix A

RF coil sensitivities

In this appendix, some of the basic concepts related to radio frequency signal transmission and reception in MRI are presented. In particular, the study of the evolution of the transverse magnetization following the application of a generic in-plane magnetic field at Larmor frequency leads to an expression for the so called "transmit sensitivity". On the other hand, the study of the signal induced in a receiving coil by the rotating transverse magnetizations, leads to an expression for the "receiver sensitivity". In the following sections, the static magnetic field $\boldsymbol{B_0}$ is supposed to be oriented along the negative z-direction. From Bloch equations, this results in the transverse component of the magnetization vector $\boldsymbol{M}$ to rotate in the positive direction around the z-axis at the Larmor frequency.

A.1 Field and rotating frames

Given a generic time harmonic vector field $\boldsymbol{A}(t, \boldsymbol{r})$, whose components in the xy-plane are $A_x(t, \boldsymbol{r})$ and $A_y(t, \boldsymbol{r})$ where $\boldsymbol{r}$ is the position vector. They can be expressed as it follows:

$$A_x(t, \boldsymbol{r}) = C_x(\boldsymbol{r}) \cos(\omega t + \alpha(\boldsymbol{r})) = \Re[C_x(\boldsymbol{r}) e^{j\alpha(\boldsymbol{r})} e^{j\omega t}] \tag{A.1a}$$

$$A_y(t, \boldsymbol{r}) = C_y(\boldsymbol{r}) \cos(\omega t + \beta(\boldsymbol{r})) = \Re[C_y(\boldsymbol{r}) e^{j\beta(\boldsymbol{r})} e^{j\omega t}] \tag{A.1b}$$

where $C_x(\boldsymbol{r})$ and $C_y(\boldsymbol{r})$ are position dependent amplitude coefficients, $\alpha(\boldsymbol{r})$ and $\beta(\boldsymbol{r})$ are position dependent phase coefficients, ω is the angular frequency, j the imaginary unit and $\Re$ indicates the real part. Such components can be expressed in phasor notation as:

$$\overline{A}_x = C_x e^{j\alpha} \tag{A.2a}$$

$$\overline{A}_y = C_y e^{j\beta} \tag{A.2b}$$

where the position dependence of the parameters is left understood. Expressing the $\boldsymbol{A}$ components in a positive and negative ω rotating frame, whose rotation axis coincides with the z-axis both of the rotating and of the static frame, gives:

$$A_x^{(+)} \approx \frac{1}{2}[C_x \cos\alpha - C_y \sin\beta] A_y^{(+)} \approx \frac{1}{2}[C_x \sin\alpha + C_y \cos\beta] \tag{A.3a}$$

$$A_x^{(-)} \approx \frac{1}{2}[C_x \cos\alpha + C_y \sin\beta] A_y^{(-)} \approx \frac{1}{2}[-C_x \sin\alpha + C_y \cos\beta] \tag{A.3b}$$

where the terms with a time variation as $2\omega t$ have been neglected since they vary too quickly to have any influence on the system [7].

Involving the formal expression of the component phasors in (A.2), it is possible to express $A_x^{(+)}$ and $A_y^{(+)}$ as:

$$A_x^{(+)} \approx \frac{1}{2}\Re(\overline{A}_x + j\overline{A}_y) \tag{A.4a}$$

$$A_y^{(+)} \approx \frac{1}{2}\Im(\overline{A}_x + j\overline{A}_y) \tag{A.4b}$$

where $\Im$ indicates the imaginary part.

$A_x^{(+)}$ and $A_y^{(+)}$ can be represented in the complex Agrand plane as:

$$A^{+} = A_x^{(+)} + jA_y^{(+)} = \frac{\overline{A}_x + j\overline{A}_y}{2} \tag{A.5}$$

Equation (A.4) can be written in a similar fashion also for $A_x^{(-)}$ and $A_y^{(-)}$ giving the general result:

$$A^{-} = A_x^{(-)} + jA_y^{(-)} = \left(\frac{\overline{A}_x - j\overline{A}_y}{2}\right)^{*} \tag{A.6}$$

where the asterisk implies complex conjugation.

(A.5) and (A.6) represent, therefore, the components of $\boldsymbol{A}(t, \boldsymbol{r})$ in a positive rotating and negative rotating Agrand plane respectively.

A.2 Signal transmission

Being $\boldsymbol{B_1}(t, \boldsymbol{r})$ an RF harmonic magnetic field applied on the xy-plane and being the magnetization vectors equally oriented along the positive z-direction at time zero[1] with an amplitude equal to M_0, the time evolution of the magnetization vectors can be described by Bloch equations. Bloch equation can be written in a Larmor frequency

---

[1] The opposite direction between the relaxed magnetizations and the static field $\boldsymbol{B_0}$ is due to the fact that the considered domain is intended to be diamagnetic. This is justified by the fact that in MRI the most common applications consider the signal emitted from water.

rotating frame, whose rotation axis coincides with the z-axis both of the rotating and of the static frame, as:

$$\frac{\partial M_x^{(+)}}{\partial t} = \gamma B_{1y}^{(+)} M_z^{(+)} \tag{A.7a}$$

$$\frac{\partial M_y^{(+)}}{\partial t} = -\gamma B_{1x}^{(+)} M_z^{(+)} \tag{A.7b}$$

where, for brevity, it has been assumed that only the positive rotating $\boldsymbol{B_1}$ RF magnetic field causes a perturbation of the magnetization vectors. In (A.7), γ represent the gyromagnetic ratio, $M_x^{(+)}$, $M_y^{(+)}$ and $M_z^{(+)}$ represent the components of the magnetization vectors in the aforementioned rotating frame whereas $B_{1x}^{(+)}$ and $B_{1y}^{(+)}$ those of the RF applied magnetic field. Time and space dependence have been omitted and the relaxation terms have been neglected.
If the duration τ of the RF pulse is such that the angles between the z-axis and the magnetization vectors at the end of the pulse (flip angles) are small, $M_z^{(+)} \approx M_0$ represents a good approximation and:

$$M_x^{(+)} \approx \gamma \tau M_0 B_{1y}^{(+)} \tag{A.8a}$$

$$M_y^{(+)} \approx -\gamma \tau M_0 B_{1x}^{(+)} \tag{A.8b}$$

and expressing the magnetization vectors in an Agrand positive rotating frame:

$$M^{(+)} = M_x^{(+)} + jM_y^{(+)} = -j2\gamma\tau M_0 B_1^{+} \tag{A.9}$$

where B_1^+ represent the “transmit sensitivity” and its expression is given by (A.5):

$$B_1^+ = \frac{\overline{B}_{1x} + j\overline{B}_{1y}}{2} \tag{A.10}$$

where $\overline{B}_{1x}$ and $\overline{B}_{1y}$ are the phasors associated with the x- and y-component of $\boldsymbol{B_1}(t, \boldsymbol{r})$.

A.3 Signal reception

Let us consider the Ampere law where the displacement term has been neglected[2]:

$$\nabla \times \boldsymbol{B}(t, \boldsymbol{r}) = \mu_0 \boldsymbol{J}(t, \boldsymbol{r}) \tag{A.11}$$

---

[2] This implies $\boldsymbol{J}(t, \boldsymbol{r}) \ll \frac{\partial \boldsymbol{D}(t,\boldsymbol{r})}{\partial t}$. This assumption is almost never verified in a normal MRI application. However, it permits to obtain in a simple way, general results that keep to be valid, under certain conditions, even if the above approximation would not be considered [146].

where $\boldsymbol{B}(t,\boldsymbol{r})$ can be seen as the magnetic field generated by the current density $\boldsymbol{J}(t,\boldsymbol{r})$. Introducing the magnetic vector potential $\boldsymbol{A}(t,\boldsymbol{r})$ such that:

$$\boldsymbol{B}(t,\boldsymbol{r}) = \nabla \times \boldsymbol{A}(t,\boldsymbol{r}) \tag{A.12}$$

it is possible, considering the Coulomb gauge, to obtain the following Laplace's equation:

$$\nabla^2 \boldsymbol{A}(t,\boldsymbol{r}) = -\mu_0 \boldsymbol{J}(t,\boldsymbol{r}) \tag{A.13}$$

whose solution can be shown to be:

$$\boldsymbol{A}(t,\boldsymbol{r}) = \frac{\mu_0}{4\pi}\int_V \frac{\boldsymbol{J}(t,\boldsymbol{r}')}{|\boldsymbol{r}-\boldsymbol{r}'|} d^3r' \tag{A.14}$$

where V represents the volume out of which $\boldsymbol{J}(t,\boldsymbol{r}) = 0$.
Given a distribution of magnetizations $\boldsymbol{M}(t,\boldsymbol{r})$, it is possible to define an effective magnetic current density as:

$$\boldsymbol{J}_{\boldsymbol{M}}(t,\boldsymbol{r}) = \nabla \times \boldsymbol{M}(t,\boldsymbol{r}) \tag{A.15}$$

Substituting (A.15) in (A.14), it is possible to obtain a relation between the magnetic vector potential and the magnetization distribution:

$$\boldsymbol{A}(t,\boldsymbol{r}) = \frac{\mu_0}{4\pi}\int_V \frac{\nabla' \times \boldsymbol{M}(t,\boldsymbol{r}')}{|\boldsymbol{r}-\boldsymbol{r}'|} d^3r' \tag{A.16}$$

To avoid to excessively weighting down the notation, in the following part the time dependence is omitted.
Considering a generic receiver coil, the flux Φ generated by the magnetic field $\boldsymbol{B}(\boldsymbol{r})$ through its area A is equal to:

$$\Phi = \int_A \boldsymbol{B}(\boldsymbol{r}) \cdot \boldsymbol{n} dS = \int_A \nabla \times \boldsymbol{A}(\boldsymbol{r}) \cdot \boldsymbol{n} dS = \oint_{\partial A} \boldsymbol{A}(\boldsymbol{r}) \cdot \boldsymbol{\tau} dl \tag{A.17}$$

where $\boldsymbol{n}$ is the unit vector normal to A and $\boldsymbol{\tau}$ is the unit vector tangential to ∂A that represents the closed path bounding A. In (A.17) the Stokes' theorem has been applied.
Substituting (A.16) in (A.17) we obtain:

$$\Phi = \oint_{\partial A} \boldsymbol{\tau} dl \cdot \left(\frac{\mu_0}{4\pi}\int_V \frac{\nabla' \times \boldsymbol{M}(\boldsymbol{r}')}{|\boldsymbol{r}-\boldsymbol{r}'|} d^3r' \right) \tag{A.18}$$

Using Einstein notation, the magnetic flux Φ can be written as:

$$\Phi = \frac{\mu_0}{4\pi} \oint_{\partial A} dl \tau_i \left(\int_V \frac{\nabla' \times \boldsymbol{M}(\boldsymbol{r}')}{|\boldsymbol{r}-\boldsymbol{r}'|} d^3r' \right)_i \tag{A.19}$$

where the subscript i indicates the ith component. The previous relation can be written as:

$$\Phi = \frac{\mu_0}{4\pi} \oint_{\partial A} dl\tau_i \left(\int_V \frac{e_{ijk}\partial'_j \boldsymbol{M}(\boldsymbol{r}')_k}{|\boldsymbol{r} - \boldsymbol{r}'|} d^3r' \right) \tag{A.20}$$

where the three-dimensional Levi-Civita tensor is adopted. An integration by parts, leads to:

$$\Phi = \frac{\mu_0}{4\pi} \oint_{\partial A} dl\tau_i \int_V e_{ijk} \left[\partial'_j \left(\frac{\boldsymbol{M}(\boldsymbol{r}')_k}{|\boldsymbol{r} - \boldsymbol{r}'|} \right) - \boldsymbol{M}(\boldsymbol{r}')_k \partial'_j \left(\frac{1}{|\boldsymbol{r} - \boldsymbol{r}'|} \right) \right] d^3r' \tag{A.21}$$

Applying the divergence theorem to the first term of the volume integrals, surface integrals are obtained. Due to the arbitrariness in the choice of V, for finite sources, it is possible to choose a volume delimited by a surface on which the magnetization is zero. For this reason, the surface integral contributions are not considered obtaining:

$$\begin{aligned}\Phi = \frac{\mu_0}{4\pi} \oint_{\partial A} dl\tau_i \int_V -e_{ijk} \boldsymbol{M}(\boldsymbol{r}')_k \partial'_j \left(\frac{1}{|\boldsymbol{r} - \boldsymbol{r}'|} \right) d^3r' = \\ \frac{\mu_0}{4\pi} \oint_{\partial A} dl\boldsymbol{\tau} \cdot \int_V -\nabla' \left(\frac{1}{|\boldsymbol{r} - \boldsymbol{r}'|} \right) \times \boldsymbol{M}(\boldsymbol{r}') d^3r' = \\ \frac{\mu_0}{4\pi} \int_V d^3r' \oint_{\partial A} dl\boldsymbol{\tau} \cdot \left[-\nabla' \left(\frac{1}{|\boldsymbol{r} - \boldsymbol{r}'|} \right) \times \boldsymbol{M}(\boldsymbol{r}') \right]\end{aligned} \tag{A.22}$$

Using the vector identity $\boldsymbol{A} \cdot (\boldsymbol{B} \times \boldsymbol{C}) = \boldsymbol{C} \cdot (\boldsymbol{A} \times \boldsymbol{B})$ we obtain:

$$\Phi = \frac{\mu_0}{4\pi} \int_V d^3r' \oint_{\partial A} -\boldsymbol{M}(\boldsymbol{r}') \cdot \left[-\nabla' \left(\frac{1}{|\boldsymbol{r} - \boldsymbol{r}'|} \right) \times \boldsymbol{\tau} dl \right] \tag{A.23}$$

Considering that, in Einstein notation:

$$\begin{aligned}\left(-\nabla' \left(\frac{1}{|\boldsymbol{r} - \boldsymbol{r}'|} \right) \times \boldsymbol{\tau} \right)_i = e_{ijk}\tau_j \left(\nabla' \frac{1}{|\boldsymbol{r} - \boldsymbol{r}'|} \right)_k = \\ e_{ijk}\tau_j \partial'_k \frac{1}{|\boldsymbol{r} - \boldsymbol{r}'|} = -\left(\nabla' \times \frac{\boldsymbol{\tau}}{|\boldsymbol{r} - \boldsymbol{r}'|} \right)_i\end{aligned} \tag{A.24}$$

the magnetic flux can be written as:

$$\Phi = \frac{\mu_0}{4\pi} \int_V d^3r' \boldsymbol{M}(\boldsymbol{r}') \cdot \left[\nabla' \times \left(\oint_{\partial A} \frac{\boldsymbol{\tau} dl}{|\boldsymbol{r} - \boldsymbol{r}'|} \right) \right] \tag{A.25}$$

The magnetic vector potential in $\boldsymbol{r}'$ that the considered receiver coil would generate if a unitary current run through it, is given by:

$$\hat{\boldsymbol{A}}(\boldsymbol{r}') = \frac{\mu_0}{4\pi} \oint_{\partial A} \frac{\boldsymbol{\tau} dl}{|\boldsymbol{r} - \boldsymbol{r}'|} \tag{A.26}$$

and the associated magnetic field by:

$$\hat{\boldsymbol{B}}(\boldsymbol{r}') = \nabla' \times \hat{\boldsymbol{A}}(\boldsymbol{r}') = \nabla' \times \frac{\mu_0}{4\pi} \oint_{\partial A} \frac{\tau dl}{|\boldsymbol{r} - \boldsymbol{r}'|} \tag{A.27}$$

where the circumflex indicates the field due to unit current.
Recognizing this expression in that of the magnetic flux leads to:

$$\Phi = \int_V d^3r' \; \hat{\boldsymbol{B}}(\boldsymbol{r}') \cdot \boldsymbol{M}(\boldsymbol{r}') \tag{A.28}$$

By means of the Faraday's law, it is possible to compute the electromagnetic force V induced in the coil as:

$$V = -\frac{\partial}{\partial t}\Phi = -\frac{\partial}{\partial t} \int_V d^3r' \; \hat{\boldsymbol{B}}(\boldsymbol{r}') \cdot \boldsymbol{M}(\boldsymbol{r}') \tag{A.29}$$

The above relation is due to David Hoult [7, 147, 148]. It is recognized as an example of the Principle of Reciprocity and represents a milestone in the MRI history. It leads to the fundamental consequence that a receiver coil receives a signal from a point proportionally to the the magnetic field generated in the same point by a unitary current flowing through such a coil.
Now, we suppose that the magnetization vectors have been rotated on on the xy-plane by a proper RF pulse. Due to the presence of a static magnetic field oriented along the negative z-axis, they will precess around the z-axis at the Larmor angular frequency ω_0 in the positive direction. Developing the inner product in (A.29) and making explicit the time dependence, we obtain:

$$V(t) = -\frac{\partial}{\partial t} \int_V d^3r' \hat{B}_x(\boldsymbol{r}') M_x(t, \boldsymbol{r}') + \hat{B}_y(\boldsymbol{r}') M_y(t, \boldsymbol{r}') \tag{A.30}$$

Representing the magnetization on a complex static Agrand plane gives:

$$M_+(t, \boldsymbol{r}') = M_+(0, \boldsymbol{r}') e^{j\omega_0 t + j\phi_0(\boldsymbol{r}')} \tag{A.31}$$

where $\phi_0(\boldsymbol{r}')$ represents the phase of the magnetization at time zero after the application of the RF pulse and corresponds to the phase of B_1^+ in (A.9).
Considering the expression above, the following relations hold:

$$M_x(t, \boldsymbol{r}') = \Re[M_+(t, \boldsymbol{r}')] \tag{A.32a}$$

$$M_y(t, \boldsymbol{r}') = \Im[M_+(t, \boldsymbol{r}')] \tag{A.32b}$$

Taking into account the relations above and developing the time derivative, the electromagnetic force becomes:

$$\begin{aligned} V(t) = \omega_0 \int_V d^3r' \hat{B}_x(\boldsymbol{r}') \Re[j M_+(0, \boldsymbol{r}') e^{j\omega_0 t + j\phi_0(\boldsymbol{r}')}] + \hat{B}_y(\boldsymbol{r}') \Im[j M_+(0, \boldsymbol{r}') e^{j\omega_0 t + j\phi_0(\boldsymbol{r}')}] = \\ \omega_0 \int_V d^3r' M_+(0, \boldsymbol{r}')[-\hat{B}_x(\boldsymbol{r}') \sin(\omega_0 t + \phi_0(\boldsymbol{r}')) + \hat{B}_y(\boldsymbol{r}') \cos(\omega_0 t + \phi_0(\boldsymbol{r}'))] \end{aligned} \tag{A.33}$$

The high frequency oscillations at ω_0 can be removed through a demodulation process which consists of multiplying the signal by a sinusoid or cosinusoid with a frequency at or near ω_0 [149]. Such a procedure corresponds to view the signal from a rotating reference frame and it results in two signals that can be conveniently added together to obtain the MRI useful complex signal. In particular, the multiplication of (A.33) by $\sin(\omega_0 t)$, leads to:

$$V_{Re} = -\omega_0 \Re\left[\int_V d^3r' M_+(0, \boldsymbol{r}')(\hat{B}_1^-)^* e^{j\phi_0(\boldsymbol{r}')}\right] \tag{A.34}$$

Where the fast oscillating terms at $2\omega_0$ are not reported since they are supposed to be eliminated by low pass filtering. $(\hat{B}_1^-)^*$ represents the complex conjugate of the magnetic field, expressed in a negative rotating Agrand plane, that a unitary current would produce if it flowed through the receiver coil (A.6):

$$\hat{B}_1^- = \left(\frac{\hat{B}_{1x} - j\hat{B}_{1y}}{2}\right)^* \tag{A.35}$$

On the other hand, the multiplication of (A.33) by $\cos(\omega_0 t)$ and low-pass filtering, leads to:

$$V_{Imm} = -\omega_0 \Im\left[\int_V d^3r' M_+(0, \boldsymbol{r}')(\hat{B}_1^-)^* e^{j\phi_0(\boldsymbol{r}')}\right] \tag{A.36}$$

For evident reasons, (A.34) and (A.36) are usually referred as “Real” and “Imaginary” channel signals respectively. The forms of (A.34) and (A.36) suggest the definition of a complex signal s that is useful in most MRI application and that is defined as:

$$s = V_{Re} + jV_{Imm} \tag{A.37}$$

Resulting in:

$$s \propto \omega_0 \int_V d^3r' M_+(0, \boldsymbol{r}')(\hat{B}_1^-)^* e^{j\phi_0(\boldsymbol{r}')} \tag{A.38}$$

In the above expression, it is evident the proportionality of the complex signal s with the complex conjugate of $\hat{B}_1^-$ that represents, therefore, the “receiver sensitivity”. It interesting to notice that, whereas the sensitivity in reception is identified with the complex conjugate of (A.35), that in transmission is given by (A.10). Such asymmetry is clearly not a violation of the Principle of Reciprocity but is due to the fact that both (A.9) and (A.38) are derived in a rotating frame. In fact, we have no right to expect that a principle, that is specifically derived in a static frame with its own set of symmetries, would be still valid if those symmetries are broken by imposing handedness [7].
Finally, it is worth noting that (A.6) is a rigorous definition of a generic vector $\boldsymbol{A}(t, \boldsymbol{r})$, defined in a negative rotating Agrand plane, where $\overline{A}_x$ and $\overline{A}_y$ represent the phasors (with a real and imaginary part) of the x- and y-component of $\boldsymbol{A}(t, \boldsymbol{r})$ respectively. In

order to obtain (A.38), the Laplace's equation has been used and the effects of the displacements currents have been neglected. This resulted in $\hat{B}_x(\boldsymbol{r}')$ and $\hat{B}_y(\boldsymbol{r}')$ to be real numbers and to be not influenced by the presence of a subject near the receiver coil. However, under certain conditions, it is possible to derive an expression analogous to (A.38) where $\hat{B}_x(\boldsymbol{r}')$ and $\hat{B}_y(\boldsymbol{r}')$ take also into account an inhomogeneous domain due, for example, to the presence of a human body [146].

Appendix B

First order degenerate perturbation theory

Given an eigenvalue problem, it is possible to investigate the eigenvalues and eigenvectors variation due to a perturbation of the system matrix. The so called "Perturbation theory" allows to find the new eigenvalues and eigenvectors associated with the perturbed matrix. Since in the case of our interest, the system matrix is a degenerate $N \times N$ matrix (i.e. more than one eigenvector per eigenvalue), in this section we focalize on the special perturbation theory named "Degenerate perturbation theory". Since in the following analysis the second order perturbation terms are neglected, the proposed theory is said to be of a "frist order" kind.

Let $\mathbb{A}$ be a $N \times N$ matrix with $\mathbb{A} \in \mathbb{R}^{N\times N}$. Let $\boldsymbol{x_k}$ and λ_k be the k-th eigenvector and eignevalues of $\mathbb{A}$ respectively with k going from 1 to N. This brings to:

$$\mathbb{A}\boldsymbol{x_k} = \lambda_k \boldsymbol{x_k} \qquad k \in \mathbb{N}^+, k \rightarrow 1 : N \tag{B.1}$$

Let's suppose that the generic eigenvalue λ has multiplicity equal to M. It means λ has a set of M associated eigenvectors $\boldsymbol{y_q}$ with q going from 1 to M (with $M \leq N$). That is:

$$\mathbb{A}\boldsymbol{y_q} = \lambda \boldsymbol{y_q} \qquad q \in \mathbb{N}^+, q \rightarrow 1 : M \tag{B.2}$$

Since all the eigenvectors $\boldsymbol{y_q}$ are associated with the same eigenvalue λ, any linear combination of the $\boldsymbol{y_q}$ still represent an eigenvector of the matrix $\mathbb{A}$:

$$\mathbb{A}\sum_{q=1}^{M} \alpha_q \boldsymbol{y_q} = \sum_{q=1}^{M} \alpha_q \mathbb{A}\boldsymbol{y_q} = \sum_{q=1}^{M} \alpha_q \lambda \boldsymbol{y_q} = \lambda \sum_{q=1}^{M} \alpha_q \boldsymbol{y_q} \tag{B.3}$$

It follows that if we define:

$$\boldsymbol{z} = \sum_{q=1}^{M} \alpha_q \boldsymbol{y_q} \tag{B.4}$$

$\boldsymbol{z}$ will represent an eigenvector of $\mathbb{A}$ associated with the eigenvalue λ. Now, let's suppose that the matrix $\mathbb{A}$ is perturbed in such a way that:

$$\mathbb{P} = \mathbb{A} + \delta\widetilde{\mathbb{A}} \tag{B.5}$$

where:

$\mathbb{P}$ represents the matrix of the system after it has been perturbed;

$\mathbb{A}$ represents the matrix of the system after it has been perturbed;

$\widetilde{\mathbb{A}}$ represents the perturbation matrix;

δ represents the degree of perturbation;

We are now interested in investigating the variation of λ and $\boldsymbol{z}$ due to the perturbation. So, we can imagine that the perturbation process gives origine to new eigenvalues $\lambda + \delta\tilde{\lambda}$ associated to new eigenvectors $\boldsymbol{z} + \delta\tilde{\boldsymbol{z}}$. It follows:

$$\left(\mathbb{A} + \delta\widetilde{\mathbb{A}}\right)(\boldsymbol{z} + \delta\tilde{\boldsymbol{z}}) = (\lambda + \delta\tilde{\lambda})(\boldsymbol{z} + \delta\tilde{\boldsymbol{z}}) \tag{B.6}$$

carrying out the multiplications, neglecting the second order δ terms (which is reliable for $\delta \ll 1$) and using (B.4), we obtain:

$$\mathbb{A}\tilde{\boldsymbol{z}} + \widetilde{\mathbb{A}}\boldsymbol{z} = \lambda\tilde{\boldsymbol{z}} + \tilde{\lambda}\boldsymbol{z} \tag{B.7}$$

Now, since the whole set of eigenvectors of $\mathbb{A}$ represents a complete basis of $\mathbb{R}^N$, we can express $\tilde{\boldsymbol{z}}$ as a linear combination of the eigenvectors of the $\mathbb{A}$ matrix. Doing this, we split the contributions of the generic eigenvectors $\boldsymbol{x_k}$ associated with the generic eigenvalues λ_k and the eigenvectors $\boldsymbol{y_q}$ associated to the eigenvalue λ.

$$\tilde{\boldsymbol{z}} = \sum_{k=1}^{N-M} \beta_k \boldsymbol{x_k} + \sum_{q=1}^{M} \gamma_q \boldsymbol{y_q} \tag{B.8}$$

Substituting the last relation in (B.7), we obtain:

$$\left(\mathbb{A} - \lambda\mathbb{I}\right)\left(\sum_{k=1}^{N-M} \beta_k \boldsymbol{x_k} + \sum_{q=1}^{M} \gamma_q \boldsymbol{y_q}\right) + \left(\widetilde{\mathbb{A}} - \tilde{\lambda}\mathbb{I}\right)\left(\sum_{q=1}^{M} \alpha_q \boldsymbol{y_q}\right) \tag{B.9}$$

where $\mathbb{I}$ is the identity matrix. Carrying out the multiplication of the first addend, we get:

$$\underbrace{\sum_{k=1}^{N-M} \beta_k \mathbb{A}\boldsymbol{x_k}}_{\sum_{k=1}^{N-M} \beta_k \lambda_k \boldsymbol{x_k}} + \underbrace{\sum_{q=1}^{M} \gamma_q \mathbb{A}\boldsymbol{y_q}}_{\sum_{q=1}^{M} \gamma_q \lambda \boldsymbol{y_q}} - \sum_{k=1}^{N-M} \beta_k \lambda \boldsymbol{x_k} - \sum_{q=1}^{M} \gamma_q \mathbb{A}\boldsymbol{y_q} + \left(\widetilde{\mathbb{A}} - \tilde{\lambda}\mathbb{I}\right)\left(\sum_{q=1}^{M} \alpha_q \boldsymbol{y_q}\right) = 0 \tag{B.10}$$

So, we get:

$$\sum_{k=1}^{N-M} \beta_k(\lambda_k - \lambda)\boldsymbol{x_k} + \left(\widetilde{\mathbb{A}} - \tilde{\lambda}\mathbb{I}\right)\left(\sum_{q=1}^{M} \alpha_q \boldsymbol{y_q}\right) = 0 \tag{B.11}$$

Now, in the hypothesis of orthonormal eigenvectors, premultipling the first member of the previous relation by the transpose conjugate of $\boldsymbol{y_p}$, we get:

$$\sum_{q=1}^{M} \boldsymbol{y_p}^{\dagger}\widetilde{\mathbb{A}}\boldsymbol{y_q}\alpha_q = \tilde{\lambda}\alpha_p \tag{B.12}$$

This can be expressed in a matrix form as it follows:

$$\mathbb{W}\boldsymbol{\alpha} = \tilde{\lambda}\boldsymbol{\alpha} \tag{B.13}$$

where $\mathbb{W}$ is a $\boldsymbol{M} \times \boldsymbol{M}$ matrix with entries $\mathbb{W}_{pq} = \boldsymbol{y_p}^{\dagger}\widetilde{\mathbb{A}}\boldsymbol{y_q}$. We can see (B.13) as another eigenvalues problem where the eigenvalues $\tilde{\lambda}_q$ (with q from 1 to $\boldsymbol{M}$) are the perturbations to the original degenerate eigenvalue λ and the eigenvectors $\boldsymbol{\alpha_q}$ are the "good" coefficients for the unperturbed $\boldsymbol{z_q}$ from which computing the perturbed eigenvectors. Now we are able to obtain the perturbed eigenvalues:

$$\lambda_q^P = \lambda + \delta\tilde{\lambda}_q \tag{B.14}$$

In order to compute the perturbed eigenvectors $\boldsymbol{z_q}^P$ we need to obtain an expression for the $\widetilde{\boldsymbol{z}}_{\boldsymbol{q}}$. To do this, let's consider again equation (B.10):

$$\sum_{k=1}^{N-M} \beta_k\lambda_k\boldsymbol{x_k} - \sum_{k=1}^{N-M} \beta_k\lambda\boldsymbol{x_k} = -\left(\widetilde{\mathbb{A}} - \tilde{\lambda}\mathbb{I}\right)\boldsymbol{z_q} \tag{B.15}$$

Premultipling both members of the previous equation by $\boldsymbol{x_k}^{\dagger}$ we obtain the β_k coefficient as:

$$\beta_k = \frac{\boldsymbol{x}_{\boldsymbol{k}}^{\dagger}\widetilde{\mathbb{A}}\boldsymbol{z_q}}{\lambda - \lambda_k} \tag{B.16}$$

Regarding the γ_q coefficients of (B.8), we see that they do not give contributions to the perturbation relation (B.7) since they cancel in equation (B.10). This means that the perturbation analysis for $\boldsymbol{z_q}^P$ is neutral to the contribution of the $\boldsymbol{y_q}$. We are thus free to set $\gamma_q = 0$. Finally, the perturbed eigenvector $\boldsymbol{z_q}^P$ will be expressed as:

$$\boldsymbol{z_q}^P = \boldsymbol{z_q} + \delta \sum_{k=1}^{N-M} \frac{\boldsymbol{x}_{\boldsymbol{k}}^{\dagger}\widetilde{\mathbb{A}}\boldsymbol{z_q}}{\lambda - \lambda_k}\boldsymbol{x_k} \tag{B.17}$$

Nomenclature

Acronyms / Abbreviations

BNC	Bayonet Neill–Concelman
CAD	Computer-Aided Design
CoCr	Cobalt-Chromium
DAE	Data Acquisition Electronics
DF	Dissipation Factor
EASY	Electronic Acquisition System
EM	ElectroMagnetic
FOV	Field Of View
GPIB	General Purpose Interface Bus
GUI	Graphic User Interface
GUM	Guide to the expression of Uncertainty in Measurement
H	Hydrogen
INRIM	Istituto Nazionale di Ricerca Metrologica
MAVRIC	Multiple-Acquisition with Variable Resonances Image Combination
MR	Magnetic Resonance
MRI	Magnetic Resonance Imaging
Na	Sodium
NIST	National Institute of Standards and Technology
NMR	Nuclear Magnetic Resonance

PEC	Perfect Electric Conductor
PEEK	polyetheretherketone
POM	polyoxymethylene
POM	polyoxymethylene
RA	Reduced Area
RF	Radio Frequency
RMS	Root Mean Square
RMSE	Root Mean Square Error
ROI	Region Of Interest
SAR	Specific Absorption Rate
SEMAC	Slice Encoding for Metal Artefact Correction
SNR	Signal to Noise Ratio
TEM	Transverse ElectroMagnetic
Ti	Titanium
TSL	Tissue-Simulating Liquid
VAT	View Angle Tilting
VNA	Vector Network Analyzer
VSM	Vibrating Sample Magnetometer
WS	Whole Slice

Bibliography

[1] J. T. Vaughan and J. R. Griffiths. *RF Coils for MRI.* Wiley, 2012.

[2] GE Healthcare. *MR Field Notes - RF Coils... They've Come a Long, Long Way.* Tech. rep. GE Healthcare, 2005.

[3] J. P. Hornak. *The Basics of MRI - IMAGING HARDWARE.* [Online; accessed 13-August-2018]. URL: https://www.cis.rit.edu/htbooks/mri/chap-9/chap-9.htm#9.4.

[4] A. D. Elster. *Questions and Answers in MRI - Radiofrequency Coils.* [Online; accessed 13-August-2018]. URL: http://mriquestions.com/rf-coil-functions.html.

[5] International Electrotechnical Commission (IEC). *Medical electrical equipment - Part 2-33: Particular requirements for the basic safety and essential performance of magnetic resonance equipment for medical diagnosis.* International Standard. International Electrotechnical Commission (IEC), Mar. 2010, p. 219.

[6] R.W. Brown et al. "Magnetic Resonance Imaging: Physical Principles and Sequence Design: Second Edition". In: Whiley, 2014. Chap. 3 - Rotating Reference Frames and Resonance. DOI: 10.1002/9781118633953.

[7] D.I. Hoult. "The principle of reciprocity in signal strength calculations - A mathematical guide". In: *Concepts in Magnetic Resonance* 12.4 (2000), pp. 173–187. DOI: 10.1002/1099-0534(2000)12:4<173::AID-CMR1>3.0.CO;2-Q.

[8] A. D. Elster. *Questions and Answers in MRI - Radiofrequency Coils.* [Online; accessed 14-August-2018]. URL: http://mriquestions.com/lp-vs-cp-quadrature.html.

[9] G.H. Glover et al. "Comparison of linear and circular polarization for magnetic resonance imaging". In: *Journal of Magnetic Resonance (1969)* 64.2 (1985), pp. 255–270. DOI: 10.1016/0022-2364(85)90349-X.

[10] P.B. Roemer et al. "The NMR phased array". In: *Magnetic Resonance in Medicine* 16.2 (1990), pp. 192–225. DOI: 10.1002/mrm.1910160203.

[11] A. D. Elster. *Questions and Answers in MRI - Radiofrequency Coils.* [Online; accessed 16-August-2018]. URL: http://mriquestions.com/array-coils.html.

[12] M.A. Ohliger and D.K. Sodickson. “An introduction to coil array design for parallel MRI”. In: *NMR in Biomedicine* 19.3 (2006), pp. 300–315. DOI: `10.1002/nbm.1046`.

[13] M.A. Griswold et al. “Generalized Autocalibrating Partially Parallel Acquisitions (GRAPPA)”. In: *Magnetic Resonance in Medicine* 47.6 (2002), pp. 1202–1210. DOI: `10.1002/mrm.10171`.

[14] K.P. Pruessmann et al. “SENSE: Sensitivity encoding for fast MRI”. In: *Magnetic Resonance in Medicine* 42.5 (1999), pp. 952–962. DOI: `10.1002/(SICI)1522-2594(199911)42:5<952::AID-MRM16>3.0.CO;2-S`.

[15] R.W. Brown et al. “Magnetic Resonance Imaging: Physical Principles and Sequence Design: Second Edition”. In: Whiley, 2014. Chap. 6 - The Quantum Mechanical Basis of Thermal Equilibrium and Longitudinal Relaxation. DOI: `10.1002/9781118633953`.

[16] C.M. Collins et al. “Central brightening due to constructive interference with, without, and despite dielectric resonance”. In: *Journal of Magnetic Resonance Imaging* 21.2 (2005), pp. 192–196. DOI: `10.1002/jmri.20245`.

[17] A. D. Elster. *Questions and Answers in MRI - Radiofrequency Coils*. [Online; accessed 14-August-2018]. URL: `http://mriquestions.com/dielectric-effect.html`.

[18] P. R. Harvey and R. M. Hoogeveen. *MultiTransmit parallel RF transmission technology*. Tech. rep. Philips, 2009.

[19] L. L. Wald and E. Adalsteinsson. *Parallel Transmit Technology for High Field MRI*. Tech. rep. Siemens, 2009.

[20] A. D. Elster. *Questions and Answers in MRI - Radiofrequency Coils*. [Online; accessed 16-August-2018]. URL: `http://mriquestions.com/multi-transmit-rf.html`.

[21] L. Axel and C. Hayes. “Surface coil magnetic resonance imaging”. In: *Archives of Physiology and Biochemistry* 93.5 (1985), pp. 11–18. DOI: `10.3109/13813458509080620`.

[22] T.S. Ibrahim et al. “Effect of RF coil excitation on field inhomogeneity at ultra high fields: A field optimized TEM resonatior”. In: *Magnetic Resonance Imaging* 19.10 (2001), pp. 1339–1347. DOI: `10.1016/S0730-725X(01)00404-0`.

[23] S.E. Hurlston et al. “A high-temperature superconducting Helmholtz probe for microscopy at 9.4 T”. In: *Magnetic Resonance in Medicine* 41.5 (1999), pp. 1032–1038. DOI: `10.1002/(SICI)1522-2594(199905)41:5<1032::AID-MRM23>3.0.CO;2-X`.

[24] T. Munsat et al. “Two new planar coil designs for a high pressure radio frequency plasma source”. In: *Applied Physics Letters* (1995), p. 2180.

[25] J.P. Hornak, J. Szumowski, and R.G. Bryant. “Elementary single turn solenoids used as the transmitter and receiver in magnetic resonance imaging”. In: *Magnetic Resonance Imaging* 5.3 (1987), pp. 233–237. DOI: `10.1016/0730-725X(87)90024-5`.

[26] J.A. Stringer et al. “Reduction of RF-induced sample heating with a scroll coil resonator structure for solid-state NMR probes”. In: *Journal of Magnetic Resonance* 173.1 (2005), pp. 40–48. DOI: `10.1016/j.jmr.2004.11.015`.

[27] E.A. Marshall et al. “Magnetic resonance imaging using a ribbonator: Hand and wrist”. In: *Magnetic Resonance in Medicine* 9.3 (1989), pp. 369–378. DOI: `10.1002/mrm.1910090308`.

[28] D.K. Sodickson and W.J. Manning. “Simultaneous acquisition of spatial harmonics (SMASH): Fast imaging with radiofrequency coil arrays”. In: *Magnetic Resonance in Medicine* 38.4 (1997), pp. 591–603. DOI: `10.1002/mrm.1910380414`.

[29] P.J. Prado, B. Blümich, and U. Schmitz. “One-Dimensional Imaging with a Palm-Size Probe”. In: *Journal of Magnetic Resonance* 144.2 (2000), pp. 200–206. DOI: `10.1006/jmre.2000.2038`.

[30] M.C.K. Wiltshire et al. “Microstructured magnetic materials for rf flux guides in magnetic resonance imaging”. In: *Science* 291.5505 (2001), pp. 849–851. DOI: `10.1126/science.291.5505.849`.

[31] T.M. Grist and J.S. Hyde. “Resonators for in Vivo 31P NMR at 1.5 T”. In: *Journal of Magnetic Resonance (1969)* 61.3 (1985), pp. 571–578. DOI: `10.1016/0022-2364(85)90201-X`.

[32] F.D. Doty, G. Entzminger Jr., and C.D. Hauck. “Error-Tolerant RF Litz Coils for NMR/MRI”. In: *Journal of Magnetic Resonance* 140.1 (1999), pp. 17–31. DOI: `10.1006/jmre.1999.1828`.

[33] N. Baril et al. “Single-Coil Surface Imaging Using a Radiofrequency Field Gradient”. In: *Journal of Magnetic Resonance* 146.1 (2000), pp. 223–227. DOI: `10.1006/jmre.2000.2130`.

[34] B.H. Suits, A.N. Garroway, and J.B. Miller. “Noise-Immune Coil for Unshielded Magnetic Resonance Measurements”. In: *Journal of Magnetic Resonance* 131.1 (1998), pp. 154–158. DOI: `10.1006/jmre.1997.1335`.

[35] K.L. Meyer and D. Ballon. “A 3 × 3 Mesh Two-Dimensional Ladder Network Resonator for MRI of the Human Head”. In: *Journal of Magnetic Resonance, Series B* 107.1 (1995), pp. 19–24. DOI: `10.1006/jmrb.1995.1053`.

[36] C.E. Hayes et al. “An efficient, highly homogeneous radiofrequency coil for whole-body NMR imaging at 1.5 T”. In: *Journal of Magnetic Resonance (1969)* 63.3 (1985), pp. 622–628. DOI: `10.1016/0022-2364(85)90257-4`.

[37] D.W. Alderman and D.M. Grant. "An efficient decoupler coil design which reduces heating in conductive samples in superconducting spectrometers". In: *Journal of Magnetic Resonance (1969)* 36.3 (1979), pp. 447–451. DOI: 10.1016/0022-2364(79)90123-9.

[38] O.C. Morse and J.R. Singer. "Blood velocity measurements in intact subjects". In: *Science* 170.3956 (1970), pp. 440–441. DOI: 10.1126/science.170.3956.440.

[39] M.C. Leifer. "Resonant Modes of the Birdcage Coil". In: *Journal of Magnetic Resonance* 124.1 (1997), pp. 51–60.

[40] A. D. Elster. *Questions and Answers in MRI - Radiofrequency Coils.* [Online; accessed 17-August-2018]. URL: http://mriquestions.com/birdcage-coil.html.

[41] D.C. Alsop, T.J. Connick, and G. Mizsei. "A spiral volume coil for improved rf field homogeneity at high static magnetic field strength". In: *Magnetic Resonance in Medicine* 40.1 (1998), pp. 49–54. DOI: 10.1002/mrm.1910400107.

[42] M. F. Mueller et al. "Double Spiral Array Coil Design for Enhanced 3D Parallel MRI at 1.5 Tesla". In: *Concepts in Magnetic Resonance Part B (Magnetic Resonance Engineering)* 35B(2).1 (2009), pp. 67–79. DOI: 10.1002/cmr.b.20137.

[43] T. Lanz et al. "Double-tuned four-ring birdcage resonators for in vivo 31P-nuclear magnetic resonance spectroscopy at 11.75 T". In: *Magnetic Resonance Materials in Physics, Biology, and Medicine* 5.3 (1997), pp. 243–246. DOI: 10.1007/BF02594587.

[44] G. Lykowsky et al. "Optimization and comparison of two practical dual-tuned birdcage configurations for quantitative assessment of articular cartilage with sodium magnetic resonance imaging". In: *Quantitative Imaging in Medicine and Surgery* 5.6 (2015). DOI: 10.3978/j.issn.2223-4292.2015.11.06.

[45] V. Alagappan et al. "Degenerate mode band-pass birdcage coil for accelerated parallel excitation". In: *Magnetic Resonance in Medicine* 57.6 (2007), pp. 1148–1158. DOI: 10.1002/mrm.21247.

[46] A. D. Elster. *Questions and Answers in MRI - Radiofrequency Coils.* [Online; accessed 17-August-2018]. URL: http://mriquestions.com/tem-coils.html.

[47] R. R. Harman et al. "Some observations of the design of rf coils for human internal use". In: *Magnetic Resonance in Medicine* 6.1 (), pp. 49–62. DOI: 10.1002/mrm.1910060106.

[48] T. Flügge et al. "Magnetic resonance imaging of intraoral hard and soft tissues using an intraoral coil and FLASH sequences". In: *European Radiology* 26.12 (2016), pp. 4616–4623. DOI: 10.1007/s00330-016-4254-1.

[49] I.L. Tan, J. Stoker, and J.S. Lameris. "Magnetic resonance imaging of the female pelvic floor and urethra: Body coil versus endovaginal coil". In: *Magnetic Resonance Materials in Physics, Biology, and Medicine* 5.1 (1997), pp. 59–63. DOI: `10.1007/BF02592267`.

[50] N.M. DeSouza et al. "Magnetic resonance imaging of the anal sphincter using an internal coil". In: *Magnetic Resonance Quarterly* 11.1 (1995), pp. 45–56.

[51] S. Heiland. "From A as in aliasing to Z as in zipper: Artifacts in MRI". In: *Clinical Neuroradiology* 18.1 (2008), pp. 25–36. DOI: `10.1007/s00062-008-8003-y`.

[52] A. D. Elster. *Questions and Answers in MRI - Radiofrequency Coils.* [Online; accessed 17-August-2018]. URL: `http://mriquestions.com/zipper-artifact.html`.

[53] R.W. Brown et al. "Magnetic Resonance Imaging: Physical Principles and Sequence Design: Second Edition". In: Whiley, 2014. Chap. 16 - A Closer Look at Radiofrequency Pulses. DOI: `10.1002/9781118633953`.

[54] N. De Zanche. In: *RF Coils for MRI.* Ed. by J. T. Vaughan and J. R. Griffiths. Wiley, 2012. Chap. Birdcage Volume Coil Design, pp. 123–136.

[55] J. Tropp. "The theory of the bird-cage resonator". In: *Journal of Magnetic Resonance (1969)* 82.1 (1989), pp. 51–62. DOI: `10.1016/0022-2364(89)90164-9`.

[56] P.J. Davis. *Circulant Matrices.* Wiley, 1970. ISBN: 0471057711.

[57] J. Tropp. "The theory of an arbitrarily perturbed bird-cage resonator, and a simple method for restoring it to full symmetry". In: *Journal of Magnetic Resonance (1969)* 95.2 (1991), pp. 235–243. DOI: `10.1016/0022-2364(91)90214-E`.

[58] International Commission of Non-Ionizing Radiation Protection (ICNIRP). *Exposure to High Frequency Electromagnetic Fields, Biological Effects and Health Consequences (100 kHz–300 GHz).* International Guidelines. International Commission of Non-Ionizing Radiation Protection (ICNIRP), 2009.

[59] W. Mao, M.B. Smith, and C.M. Collins. "Exploring the limits of RF shimming for high-field MRI of the human head". In: *Magnetic Resonance in Medicine* 56.4 (2006), pp. 918–922. DOI: `10.1002/mrm.21013`.

[60] J. Tropp. "Image brightening in samples of high dielectric constant". In: *Journal of Magnetic Resonance* 167.1 (2004), pp. 12–24. DOI: `10.1016/j.jmr.2003.11.003`.

[61] E.K. Insko and L. Bolinger. "Mapping of the Radiofrequency Field". In: *Journal of Magnetic Resonance, Series A* 103.1 (1993), pp. 82–85. DOI: `https://doi.org/10.1006/jmra.1993.1133`.

[62] Laura I. Sacolick et al. "B1 mapping by Bloch-Siegert shift". In: *Magnetic Resonance in Medicine* 63.5 (), pp. 1315–1322. DOI: `10.1002/mrm.22357`.

[63] Umberto Zanovello et al. “Experimental Setup to Compare Measurements and Numerical Simulations in Magnetic Resonance Imaging RF Dosimetry”. In: *IEEE Transactions on Instrumentation and Measurement* 66 (2017), pp. 1208–1216. DOI: 10.1109/TIM.2017.2687138.

[64] *EASY4/MRI.* [Online; accessed 11-December-2018]. URL: https://speag.swiss/products/easy6-mri/easy4mri-discontinued/.

[65] *TLe78c0.47@64.* [Online; accessed 13-December-2018]. URL: https://zmt.swiss/validation-hw/tsm/tle78c0-47-64/.

[66] BIPM. *JCGM 100:2008 - Evaluation of measurement data — Guide to the expression of uncertainty in measurement.* Tech. rep. Sections. 5, 6 and G2. BIPM Joint Committee for Guides in Metrology, Working Group 1, (JCGM/WG 1), 2008.

[67] F.W. Groover. *Inductance calculations, working formulas and tables.* Dover, 1962.

[68] Peter M. Joseph and Dongfeng Lu. “Technique for double resonant operation of birdcage imaging coils”. In: *IEEE Transactions on Medical Imaging* 8.3 (1989), pp. 286–294. DOI: 10.1109/42.34719.

[69] Carlo Carobbi and Luigi M. Millanta. “Analysis of the Common-Mode Rejection in the Measurement and Generation of Magnetic Fields Using Loop Probes”. In: *Instrumentation and Measurement, IEEE Transactions on* 53 (May 2004), pp. 514–523. DOI: 10.1109/TIM.2004.823297.

[70] Mark C. Leifer and Spencer C. Hartman. *Shielded drive for balanced quadrature bird cage coil.* US Patent 6,011,395. Jan. 2000. URL: https://patents.google.com/patent/US6011395.

[71] *TDS/MRI.* [Online; accessed 15-January-2019]. URL: https://speag.swiss/products/tds/tds-time-domain-sensor-systems/tds-standalone/.

[72] W.L. Healy et al. “Complications of Total Hip Arthroplasty: Standardized List, Definitions, and Stratification Developed by The Hip Society”. In: *Clinical Orthopaedics and Related Research* 474.2 (2016), pp. 357–364. DOI: 10.1007/s11999-015-4341-7.

[73] C.T. Talmo, M. Aghazadeh, and J.V. Bono. “Perioperative Complications Following Total Joint Replacement”. In: *Clinics in Geriatric Medicine* 28.3 (2012), pp. 471–487. DOI: 10.1016/j.cger.2012.05.006.

[74] M. Khan et al. “Early postoperative complications after total hip arthroplasty: current strategies for prevention and treatment”. In: *Instructional course lectures* 64 (2015), pp. 337–346.

[75] A.D. Boyd Jr. et al. “Long-term complications after total knee arthroplasty with or without resurfacing of the patella”. In: *Journal of Bone and Joint Surgery - Series A* 75.5 (1993), pp. 674–681. DOI: 10.2106/00004623-199305000-00006.

[76] J. Gallo et al. “Particle disease. A comprehensive theory of periprosthetic osteolysis: a review.” In: *Biomedical papers of the Medical Faculty of the University Palacký, Olomouc, Czechoslovakia* 146.2 (2002), pp. 21–28.

[77] H.M. Kremers et al. “Prevalence of total hip and knee replacement in the United States”. In: *Journal of Bone and Joint Surgery - American Volume* 97.17 (2014), pp. 1386–1397. DOI: 10.2106/JBJS.N.01141.

[78] *13th Annual Report*. Tech. rep. National Joint Registry, 2016. URL: http://www.njrcentre.org.uk/njrcentre/Portals/0/Documents/England/Reports/13th%20Annual%20Report/07950%20NJR%20Annual%20Report%202016%20ONLINE%20REPORT.pdf.

[79] P. Aliabadi et al. “Cemented total hip prosthesis: Radiographic and scintigraphic evaluation”. In: *Radiology* 173.1 (1989), pp. 203–206. DOI: 10.1148/radiology.173.1.2675184.

[80] Hollis G. Potter, Li F. Foo, and Bryan J. Nestor. “What is the Role of Magnetic Resonance Imaging in the Evaluation of Total Hip Arthroplasty?” In: *HSS Journal* 1.1 (Sept. 2005), pp. 89–93. ISSN: 1556-3324. DOI: 10.1007/s11420-005-0112-4.

[81] K. Krupa and M. Bekiesińska-Figatowska. “Artifacts in magnetic resonance imaging”. In: *”Polish journal of radiology* 80 (), pp. 93–106. DOI: 10.12659/PJR.892628.

[82] B.A. Hargreaves et al. “Metal-induced artifacts in MRI”. In: *American Journal of Roentgenology* 197.3 (2011), pp. 547–555. DOI: 10.2214/AJR.11.7364.

[83] J.F. Schenck. “The role of magnetic susceptibility in magnetic resonance imaging: MRI magnetic compatibility of the first and second kinds”. In: *Medical Physics* 23.6 (1996), pp. 815–850. DOI: 10.1118/1.597854.

[84] K.M. Koch et al. “Magnetic resonance imaging near metal implants.” In: *Journal of magnetic resonance imaging : JMRI* 32.4 (2010), pp. 773–787. DOI: 10.1002/jmri.22313.

[85] H. Graf et al. “Metal artifacts caused by gradient switching”. In: *Magnetic Resonance in Medicine* 54.1 (2005), pp. 231–234. DOI: 10.1002/mrm.20524.

[86] A. Shenhav and H. Azhari. “Gradient field switching as a source for artifacts in MR imaging of metallic stents”. In: *Magnetic Resonance in Medicine* 52.6 (2004), pp. 1465–1468. DOI: 10.1002/mrm.20294.

[87] H. Graf et al. “RF artifacts caused by metallic implants or instruments which get more prominent at 3 T: An in vitro study”. In: *Magnetic Resonance Imaging* 23.3 (2005), pp. 493–499. DOI: 10.1016/j.mri.2004.12.009.

[88] U.A. Lauer et al. "Radio frequency versus susceptibility effects of small conductive implants - A systematic MRI study on aneurysm clips at 1.5 and 3 T". In: *Magnetic Resonance Imaging* 23.4 (2005), pp. 563–569. DOI: `10.1016/j.mri.2005.02.012`.

[89] S. Santavirta et al. "Materials in total joint replacement". In: *Current Orthopaedics* 12.1 (1998), pp. 51–57. DOI: `https://doi.org/10.1016/S0268-0890(98)90008-1`.

[90] T.J. Bachschmidt et al. "Polarized multichannel transmit MRI to reduce shading near metal implants". In: *Magnetic Resonance in Medicine* 75.1 (2016), pp. 217–226. DOI: `10.1002/mrm.25621`.

[91] U. Zanovello, L. Matekovits, and L. Zilberti. "An ideal dielectric coat to avoid prosthesis RF-artefacts in Magnetic Resonance Imaging". In: *Scientific Reports* 7.1 (2017). DOI: `10.1038/s41598-017-00215-7`.

[92] Umberto Zanovello, Luca Zilberti, and Ladislau Matekovits. "A Near Field Cloaking Study to Reduce MRI RF-Artefacts in Presence of Elongated Prostheses". In: *IEEE Journal of Electromagnetics, RF and Microwaves in Medicine and Biology* PP (Oct. 2018), pp. 1–1. DOI: `10.1109/JERM.2018.2875248`.

[93] C.R. Camacho, D.B. Plewes, and R.M. Henkelman. "Nonsusceptibility artifacts due to metallic objects in MR imaging". In: *Journal of Magnetic Resonance Imaging* 5.1 (1995), pp. 75–88. DOI: `10.1002/jmri.1880050115`.

[94] V. Ballweg, F. Eibofner, and H. Graf. "RF tissue-heating near metallic implants during magnetic resonance examinations: An approach in the ac limit". In: *Medical Physics* 38.10 (2011), pp. 5522–5529. DOI: `10.1118/1.3637495`.

[95] W.R. Nitz et al. "On the heating of linear conductive structures as guide wires and catheters in interventional MRI". In: *Journal of Magnetic Resonance Imaging* 13.1 (2001), pp. 105–114. DOI: `10.1002/1522-2586(200101)13:1<105::AID-JMRI1016>3.0.CO;2-0`.

[96] S. Gabriel, R.W. Lau, and C. Gabriel. "The dielectric properties of biological tissues: II. Measurements in the frequency range 10 Hz to 20 GHz". In: *Physics in Medicine and Biology* 41.11 (1996), pp. 2251–2269. DOI: `10.1088/0031-9155/41/11/002`.

[97] C. Canuto and A. Tabacco. *Mathematical Analysis I*. Springer International Publishing, 2015.

[98] WS Hampshire Inc. *Teflon*. [Online; accessed 23-October-2018]. URL: `http://catalog.wshampshire.com/Asset/psg_teflon_ptfe.pdf`.

[99] A.J. Ward and J.B. Pendry. "Refraction and geometry in Maxwell's equations". In: *Journal of Modern Optics* 43.4 (1996), pp. 773–793. DOI: `10.1080/09500349608232782`.

[100] J.B. Pendry, D. Schurig, and D.R. Smith. "Controlling electromagnetic fields". In: *Science* 312.5781 (2006), pp. 1780–1782. DOI: 10.1126/science.1125907.

[101] J. Prat-Camps, C. Navau, and A. Sanchez. "A Magnetic Wormhole". In: *Scientific Reports* 5 (2015). DOI: 10.1038/srep12488.

[102] C. Lan et al. "Electrostatic Field Invisibility Cloak". In: *Scientific Reports* 5 (2015). DOI: 10.1038/srep16416.

[103] B. Wood and J.B. Pendry. "Metamaterials at zero frequency". In: *Journal of Physics Condensed Matter* 19.7 (2007). DOI: 10.1088/0953-8984/19/7/076208.

[104] D. Shin et al. "Broadband electromagnetic cloaking with smart metamaterials". In: *Nature Communications* 3 (2012). DOI: 10.1038/ncomms2219.

[105] Y. Ma et al. "First experimental demonstration of an isotropic electromagnetic cloak with strict conformal mapping". In: *Scientific Reports* 3 (2013). DOI: 10.1038/srep02182.

[106] J. Zhu et al. "Three-dimensional magnetic cloak working from d.c. to 250 kHz". In: *Nature Communications* 6 (2015). DOI: 10.1038/ncomms9931.

[107] H.F. Ma and T.J. Cui. "Three-dimensional broadband ground-plane cloak made of metamaterials." In: *Nature communications* 1 (2010), p. 21.

[108] L. Li et al. "Reconfigurable all-dielectric metamaterial frequency selective surface based on high-permittivity ceramics". In: *Scientific Reports* 6 (2016). DOI: 10.1038/srep24178.

[109] X. Wang, F. Chen, and E. Semouchkina. "Implementation of low scattering microwave cloaking by all-dielectric metamaterials". In: *IEEE Microwave and Wireless Components Letters* 23.2 (2013), pp. 63–65. DOI: 10.1109/LMWC.2013.2238914.

[110] P. Soontornpipit, C.M. Furse, and Y.C. Chung. "Design of implantable microstrip antenna for communication with medical implants". In: *IEEE Transactions on Microwave Theory and Techniques* 52.8 II (2004), pp. 1944–1951.

[111] Mario Silveirinha et al. "Overview of Theory and Applications of Epsilon-Near-Zero Materials". In: ().

[112] A.P. Slobozhanyuk et al. "Enhancement of Magnetic Resonance Imaging with Metasurfaces". In: *Advanced Materials* 28.9 (2016), pp. 1832–1838. DOI: 10.1002/adma.201504270.

[113] I.R.O. Connell et al. "Design of a parallel transmit head coil at 7T with magnetic wall distributed filters". In: *IEEE Transactions on Medical Imaging* 34.4 (2015), pp. 836–845. DOI: 10.1109/TMI.2014.2370533.

[114] M.J. Freire et al. "On the applications of mu(r) = - 1 metamaterial lenses for magnetic resonance imaging". In: *Journal of Magnetic Resonance* 203.1 (2010), pp. 81–90. DOI: 10.1016/j.jmr.2009.12.005.

[115] R.R.A. Syms et al. “Magneto-inductive catheter receiver for magnetic resonance imaging”. In: *IEEE Transactions on Biomedical Engineering* 60.9 (2013), pp. 2421–2431. DOI: `10.1109/TBME.2013.2258020`.

[116] A.V. Shchelokova et al. “Experimental investigation of a metasurface resonator for in vivo imaging at 1.5 T”. In: *Journal of Magnetic Resonance* 286 (2018), pp. 78–81.

[117] R. Schmidt et al. “Flexible and compact hybrid metasurfaces for enhanced ultra high field in vivo magnetic resonance imaging”. In: *Scientific Reports* 7.1 (2017).

[118] G.E. Long and L.S. Rickman. “Infectious complications of tattoos”. In: *Clinical Infectious Diseases* 18.4 (1994), pp. 610–619. DOI: `10.1093/clinids/18.4.610`.

[119] A. Stirn, E. Brähler, and A. Hinz. “Prevalence, sociodemography, mental health and gender differences of tattooing and body piercing [Prävalenz, soziodemografie, mentale gesundheit und geschlechtsunterschiede bei piercing und tattoo]”. In: 56.11 (2006), pp. 445–449. DOI: `10.1055/s-2006-951817`.

[120] U.S. Food & Drug Administration. *Think Before You Ink: Are Tattoos Safe?* [Online; accessed 4-December-2018]. URL: `https://www.fda.gov/ForConsumers/ConsumerUpdates/ucm048919.htm`.

[121] J.R. Ross and M.J. Matava. “Tattoo-induced skin ”burn” during magnetic resonance imaging in a professional football player: A case report”. In: *Sports Health* 3.5 (2011), pp. 431–434. DOI: `10.1177/1941738111411698`.

[122] W.D. Tope and F.G. Shellock. “Magnetic resonance imaging and permanent cosmetics (tattoos): Survey of complications and adverse events”. In: *JMRI* 15.2 (2002), pp. 180–184. DOI: `10.1002/jmri.10049`.

[123] W.A. Wagle and M. Smith. “Tattoo-induced skin burn during MR imaging”. In: *American Journal of Roentgenology* 174.6 (2000), p. 1795. DOI: `10.2214/ajr.174.6.1741795`.

[124] N. Kluger. “Tattoos and medical imaging: Issues and myths [Tatouages et imagerie médicale: Problèmes et mythes]”. In: *Presse Medicale* 43.5 (2014), pp. 529–533. DOI: `10.1016/j.lpm.2013.07.031`.

[125] S. Chenji et al. “Hair product artifact in magnetic resonance imaging”. In: *Magnetic Resonance Imaging* 35 (2017), pp. 1–3. DOI: `10.1016/j.mri.2016.08.023`.

[126] E. Jacobsen et al. *Chemical Substances in Tattoo Ink*. Tech. rep. Danish Environmental Protection Agency, 2012.

[127] A. M. Helmenstine. *Tattoo Ink Carrier Chemistry*. [Online; accessed 20-November-2018]. URL: `https://www.thoughtco.com/tattoo-ink-carrier-chemistry-608403`.

[128] A. Humphries et al. “Finite element analysis of thermal and acoustic processes during laser tattoo removal”. In: *Lasers in Surg. and Med.* 45.2 (2013), pp. 108–115. DOI: `10.1002/lsm.22107`.

[129] U. Zanovello et al. “Tattoo Inks EM Characterization for MRI Interaction Evaluation”. In: *2018 Conference on Precision Electromagnetic Measurements (CPEM 2018).* July 2018, pp. 1–2. DOI: `10.1109/CPEM.2018.8500971`.

[130] A. M. Helmenstine. *Tattoo Ink Carrier Chemistry.* [Online; accessed 24-May-2019]. URL: `https://www.thoughtco.com/tattoo-ink-chemistry-606170`.

[131] F. Durbiano et al. “An electrode-matrix cell for electrolytic conductivity measurements”. In: *IEEE Transactions on Instrumentation and Measurement* 56.2 (2007), pp. 321–325. DOI: `10.1109/TIM.2007.890612`.

[132] S. Seitz et al. “Traceability of electrolytic conductivity measurements to the International System of Units in the sub mS m-1 region and review of models of electrolytic conductivity cells”. In: *Electrochimica Acta* 55.22 (2010), pp. 6323–6331. DOI: `10.1016/j.electacta.2010.06.008`.

[133] S Seitz et al. “Electrolytic conductivity at 0.5 S m −1 and 5 mS m −1”. In: 54 (Jan. 2017), pp. 08032–08032.

[134] K.J. Aoki. “Frequency-dependence of electric double layer capacitance without Faradaic reactions”. In: *Journal of Electroanalytical Chemistry* 779 (2016), pp. 117–125. DOI: `10.1016/j.jelechem.2016.04.026`.

[135] T.T. Grove, M.F. Masters, and R.E. Miers. “Determining dielectric constants using a parallel plate capacitor”. In: *American Journal of Physics* 73.1 (2005), pp. 52–56. DOI: `10.1119/1.1794757`.

[136] J. E. B. Randles. “Kinetics of rapid electrode reactions”. In: *Discuss. Faraday Soc.* 1 (0 1947), pp. 11–19. DOI: `10.1039/DF9470100011`.

[137] W.E. Case and R.D. Harrington. “Calibration of Vibrating-Sample Magnetometers”. In: *JOURNAL OF RESEARCH of the National Bureau of Standards* 70C.4 (1966), p. 255.

[138] R. Leonhardt. “Analyzing rock magnetic measurements: The RockMagAnalyzer 1.0 software”. In: *Computers and Geosciences* 32.9 (2006), pp. 1420–1431. DOI: `10.1016/j.cageo.2006.01.006`.

[139] F. Fiorillo. *Measurement and characterization of magnetic materials.* Amsterdam: Elsevier Academic Press, 2005.

[140] M.M. Siddiqui. “Some problems connected with Rayleigh distributions”. In: *Journal of Research of the National Bureau of Standards* 66D.2 (1962), p. 167.

[141] P.A. Hasgall et al. *IT’IS Database for thermal and electromagnetic parameters of biological tissues.* DOI: 10.13099/VIP21000-04-0, [Version 4.0]. May 2018.

[142] L. Zilberti et al. “Collateral Thermal Effect of MRI-LINAC Gradient Coils on Metallic Hip Prostheses”. In: *IEEE Transactions on Magnetics* 50.11 (Nov. 2014), pp. 1–4. DOI: `10.1109/TMAG.2014.2323119`.

[143] Atefeh Kordzadeh and Nicola De Zanche. “Permittivity measurement of liquids, powders, and suspensions using a parallel-plate cell”. In: *Concepts in Magnetic Resonance Part B: Magnetic Resonance Engineering* 46 (Feb. 2016). DOI: `10.1002/cmr.b.21318`.

[144] *DAK - Dielectric Assessment Kit Product Line.* [Online; accessed 4-December-2018]. URL: `https://speag.swiss/products/dak/dielectric-measurements/`.

[145] Ministers’ Deputies. *Resolution ResAP(2008)1 on requirements and criteria for the safety of tattoos and permanent make-up.* Guidelines. Council of Europe, Feb. 2008.

[146] T.S. Ibrahim. “Analytical approach to the MR signal”. In: *Magnetic Resonance in Medicine* 54.3 (2005), pp. 677–682. DOI: `10.1002/mrm.20600`.

[147] D.I. Hoult and R.E. Richards. “The signal-to-noise ratio of the nuclear magnetic resonance experiment”. In: *Journal of Magnetic Resonance (1969)* 24.1 (1976), pp. 71–85. DOI: `10.1016/0022-2364(76)90233-X`.

[148] D.I. Hoult. “The principle of reciprocity”. In: *Journal of Magnetic Resonance* 213.2 (2011), pp. 344–346. DOI: `10.1016/j.jmr.2011.08.005`.

[149] R.W. Brown et al. “Magnetic Resonance Imaging: Physical Principles and Sequence Design: Second Edition”. In: Whiley, 2014. Chap. 7 - Signal Detection Concepts. DOI: `10.1002/9781118633953`.